DOCTORAT ECOLOGIE BRETAGNE GEOSCIENCES LOIRE AGRONOMIE ALIMENTATION

UNIVERSITÉ DE NANTES

THESE DE DOCTORAT DE

L'UNIVERSITE DE NANTES

ECOLE DOCTORALE N° 600
Ecole doctorale Ecologie, Géosciences, Agronomie et Alimentation
Spécialité : Sciences de la Terre et des Planètes

Par

Sneha SINGH

"Wavefield gradients and small-scale heterogeneities"

Thèse présentée et soutenue à Nantes, le 20/11/2020
Unité de recherche : Laboratoire de Planetologie et Geodynamique, Universite de Nantes, CNRS UMR 6112, Nantes, France

Rapporteurs avant soutenance :

Ana Ferreira	Reader, UCL Earth Sciences, University College London
Romain Brossier	Maitre de Conférence HDR, Institut des Sciences de la Terre, Université Grenoble Alpes

Composition du Jury :

Président :

Éric Beucler	Professor, Laboratoire De Planétologie Et Géodynamique, Université de Nantes

Examinateurs :

Céline Hadziioannou	Junior Professor, Institute of Geophysics, Universität Hamburg
Éléonore Stutzmann	Physiscienne, Institut de Physique du Globe de Paris, Université de Paris

Directeur de thèse :

Yann Capdeville	Directeur de Recherche CNRS, Laboratoire De Planétologie Et Géodynamique, Université de Nantes

Invités :

Cédric Schmelzbach	Senior Scientist, Institut für Geophysik, Eidgenössische Technische Hochschule, Zürich
Heiner Igel	Professor, Dept. of Earth and Environmental Sciences, Ludwig-Maximilians-Universität München

Wavefield gradients and small-scale heterogeneities

Sneha Singh

October 2, 2020

Sciences de la Terre et des Planètes

Wavefield gradients and small-scale heterogeneities

Sneha Singh

1. Reviewer Ana Ferreira
UCL Earth Sciences
University College London (UCL)

2. Reviewer Romain Brossier
Institut des Sciences de la Terre (ISTerre)
Université Grenoble Alpes

Supervisor Yann Capdeville

October 2, 2020

Abstract

Local small-scale heterogeneities, like geological inhomogeneities, surface topographies and cavities are known to affect seismic wavefield gradients (stains and rotations). This effect is in fact measurable with current instruments. For example, the agreement between data and synthetics computed in a tomographic model is often not as good for rotation as it is for displacement.

Here, we use the theory of homogenization to explain why small-scale heterogeneities strongly affect wavefield gradients, but not the wavefield itself. We show that at any receiver measuring wavefield gradient, small-scale heterogeneities cause the wavefield gradient to couple with strain through a coupling tensor **J**. Furthermore, we show that this **J** is 1) independent of source, 2) independent of time, but 3) only dependent on the receiver location. Consequently, we can invert for **J** based on an effective model for which synthetics fit displacement data reasonably well. Once inverted, **J** can be used to correct rotations at that receiver for other sources. Results of the correction are shown for synthetic rotational receivers and for the ring laser located in Wettzell, Germany. We find that compared to synthetics, the synthetics corrected through **J** are a better fit to the rotation data. Although results here are derived for rotations, they can be extended to receivers measuring any wavefield gradient.

We show that the full waveform inversions performed with rotations and strains are equivalent to that performed with displacements provided that 1) the number of data is sufficient, and 2) the receivers are placed far away from heterogeneities. They do not bring any substantial improvements to full waveform inversions in terms of accuracy and resolution. In the case that receivers are placed near heterogeneities, we find that an incorrect model is recovered from inversion. Therefore, when the receivers are placed near

heterogeneities, the coupling tensor **J** needs to be taken into account for each receiver to get rid of the effect. This part is a work that is still in progress.

Résumé

Les hétérogénéités locales à petite échelle, comme les inhomogénéités géologiques, les topographies de surface et les cavités sont connues pour affecter les gradients du champ d'onde sismiques (les déformations et les rotations). Cet effet est effectivement mesurable avec les instruments actuels. Par exemple, la concordance entre les données et les synthétiques calculées dans un modèle tomographique n'est souvent pas aussi bonne pour la rotation que pour le déplacement.

Ici, nous utilisons la théorie de l'homogénéisation pour expliquer pourquoi les hétérogénéités à petite échelle affectent fortement les gradients de champ d'onde, mais pas le champ d'onde lui-même. Nous montrons qu'à tout récepteur mesurant un gradient de champ d'onde, les hétérogénéités à petite échelle provoquent un couplage du gradient de champ d'onde avec le déformation par le biais d'un tenseur de couplage **J**. De plus, nous montrons que ce **J** est 1) indépendant de la source, 2) indépendant du temps, mais 3) uniquement dépendant de l'emplacement du récepteur. Par conséquent, nous pouvons inverser pour **J** sur la base d'un modèle effectif pour lequel les synthétiques s'adaptent raisonnablement bien aux données de déplacement. Une fois inversé, **J** peut être utilisé pour corriger les rotations à ce récepteur pour d'autres sources. Les résultats de la correction sont présentés pour les récepteurs rotatifs synthétiques et pour le laser en anneau situé à Wettzell, en Allemagne. Nous constatons que par rapport aux synthétiques, les synthétiques corrigés par **J** correspondent mieux aux données de rotation. Bien que les résultats soient ici dérivés pour les rotations, ils peuvent être étendus aux récepteurs mesurant n'importe quel gradient de champ d'onde.

Nous montrons que les inversions complètes de la forme d'onde réalisées avec les rotations et les déformations sont équivalentes à celles réalisées avec les déplacements à condition que 1) le nombre de données soit suffisant, et 2) les récepteurs soient placés loin des hétérogénéités. Ils n'apportent pas

d'améliorations substantielles aux inversions complètes de la forme d'onde en termes de précision et de résolution. Dans le cas où les récepteurs sont placés près des hétérogénéités, nous constatons qu'un modèle incorrect est récupéré de l'inversion. Par conséquent, lorsque les récepteurs sont placés à proximité d'hétérogénéités, le tenseur de couplage **J** doit être pris en compte pour chaque récepteur afin d'éliminer l'effet. Cette partie est un travail qui est toujours en cours.

Acknowledgement

One. Supervisors. Yann Capdeville and Heiner Igel. For taking me under your wing. For managing to keep a straight face during all my stupid questions. For being encouraging and also nudging at the right times. **Two.** Friends and family that blend into each other. Tobias Schwaiger and Oana Dancan. Adulting is difficult, but you make it doable. Singh(s). For always reminding me about trivial things such as lunch, dinner and sleep. **Three.** Office mates. Chloé Larre. You are amazing. We never made that tally on who is the clumsier one and sometimes I wonder who would have own. Anthony Guimpier. I loved our language lessons. 'I want to escape' will forever be my favorite phrase. Carolina Gil-Lozano. I feel so lucky to have met you and your awesome family. **Four.** Friends who don't judge me for my very weird dreams. Sitraka Randriamamonjy. Three years and I still have to look up if I spelt your last name correctly. I will always remember the night we walked a lost cat all the way to your home because you did not want to leave it alone and because it would not stay in the basket on your bike. Because of you, I am a little scared of petting cats. Ludivine Harrel. I have seen that you always talk to the lonely people at gatherings and go out of your way to make them feel comfortable. This is one of the many qualities that I admire in you. Maï Bordiec. You are so good at everything you do that I envy you sometimes. Maxime Pineau. No matter where in the world I am, if 'Bohemian Rhapsody' starts playing, you will be the first person I think of. Kevin Costard. For all the bêtise. **Five**. People from the land of Shah Rukh Khan. Surbhi Dhingra. For all the tea therapy sessions. Shivangi Sharan. For introducing me to the 'Punjabi Tadka'.

This list misses quite a few names, and I am not sure if I will be able to remember out every one of them. But I thank you for sharing your beautiful stories with me and for letting me practice my broken French with you. The last three years have been extraordinary.

Are the death of all things that are seen and unseen
Not an end, but the start of all things that are left to do

Andrew John Hozier-Byrne (from Wasteland, Baby!)

Notation

General Notation

$A : b$	product of fourth order tensor A and second-order tensor b, i.e. $[A : b]_{ij} = A_{ijkl} b_{kl}$
$A : B$	product of fourth order tensors A and B, i.e. $[A : B]_{ijkl} = A_{ijmn} B_{mnkl}$
$\mathcal{F}^{\varepsilon}$	low-pass filter
${}^{t}.$	transpose of .
d	data
G	differential operator
m	model

Physical Quantities

$\boldsymbol{\epsilon}(\mathbf{u})$	strain tensor, $\epsilon(\mathbf{u}) = \frac{1}{2}(\nabla\mathbf{u} +^{\mathrm{t}} \nabla\mathbf{u})$
$\boldsymbol{\Omega}(\mathbf{u})$	rotation tensor, $\Omega(\mathbf{u}) = \frac{1}{2}(\nabla\mathbf{u} -^{\mathrm{t}} \nabla\mathbf{u})$
$\boldsymbol{\sigma}$	stress tensor
$\mathbf{c}$	elastic tensor
λ, μ	Lamé parameters in isotropic material
ρ	density
$\mathrm{V_p}$	P-wave velocity
$\mathrm{V_s}$	S-wave velocity
λ_m	minimum wavelength in the medium
$\mathbf{u}$	displacement
ω	rotation

Forward problem

Δt	time step of the computation
Δx	mesh size
C	Courant constant
$\mathbf{f}$	external source

Inverse problem

ϕ	misfit functional
ξ	L2 norm
$\mathbf{F}$	Frechlet derivative, $\mathbf{F} = [\frac{\partial \mathbf{s}}{\partial \mathbf{m}}]$
$\mathbf{H}$	Hessian matrix
covar	covariance
R	correlation
σ	standard deviation
σ^2	variance

Homogenization

λ	scale separator
ε	homogenization parameter, $\varepsilon = \frac{\lambda}{\lambda_m}$
$\mathbf{x}$	large-scales
$\mathbf{y}$	small-scales
$\langle . \rangle$	cell average of .
χ	first-order corrector
$.^{\varepsilon}$	true .
$.^{0}$	effective .

Contents

Gradients de champ d'onde et hétérogénéités à petite échelle **xiv**
I Homogénéisation xix
II Effets des hétérogénéités à petite échelle sur les gradients du champ d'onde xxi
III Correction des gradients de champ d'onde pour les effets des structures à petite échelle xxviii
IV Inversions synthétiques de la forme d'onde complète avec gradients de champ d'onde xxxiv
V Conclusions xlii

1 Seismology 101 **1**
1.1 The Forward Problem 1
1.2 The Inverse Problem 6
1.3 Motivation and Problem Statement 9
1.4 Thesis Structure 10

2 Homogenization **11**
2.1 Homogenization in context of the forward problem 11
2.2 Homogenization in context of the inverse problem 13
2.3 Homogenization for the 2D periodic media 15
2.4 Homogenization for 2D non-periodic media 20
2.5 Homogenization for 1D and 3D media 22
2.6 Other homogenization techniques 22

3 Effect of small-scale structures on gradients **24**
3.1 Previous Work 24
3.2 Numerical examples 25
3.2.1 Numerical example 1 25
3.2.2 Numerical example 2 28
3.3 Homogenization to explain the effect 31
3.4 Discussion and Conclusion 35

4 Correcting wavefield gradients for the effects of small-scale structures **36**
4.1 Previous Work . . . 36
4.2 Correction . . . 37
4.3 Synthetic Tests . . . 39
4.3.1 Inversion of **J** for a receiver in a 2D volume . . . 39
4.3.2 Inversion of **J** for a receiver on a 3D surface . . . 41
4.4 Real World Scenario . . . 45
4.4.1 Inversion for **J** at the Ring laser, Wettzell using PREM . 46
4.4.2 Inversion for **J** at the Ring laser, Wettzell using array-derived estimates . . . 48
4.5 Discussion and Conclusion . . . 51

5 Mapping discontinuities **53**
5.1 Previous Work . . . 53
5.2 Mapping discontinuities through the wavefield . . . 54
5.2.1 Numerical Example . . . 54
5.2.2 Real Data . . . 57
5.3 Mapping discontinuities using correctors . . . 66
5.3.1 Numerical Example . . . 67
5.3.2 Real Data . . . 69
5.4 Discussion and Conclusion . . . 69

6 Synthetic Full Waveform Inversion with wavefield gradients **72**
6.1 Previous Work . . . 72
6.2 Inversion Strategy . . . 74
6.3 Numerical Experiments . . . 81
6.3.1 Receivers far away from the heterogeneity . . . 81
6.3.2 Receivers close to the heterogeneity . . . 82
6.3.3 Receivers close to the heterogeneity with correctors . . 83
6.4 Results . . . 84
6.4.1 Receivers far away from the heterogeneity . . . 85
6.4.2 Receivers close to the heterogeneity . . . 89
6.4.3 Receivers close to the heterogeneity with correctors . . 93
6.5 Discussion and Conclusion . . . 94

7 Conclusions and Outlook **99**

Bibliography **101**

A Deriving wavefield gradients from an array **117**

B Corrector for array-derived wavefield gradient **119**

C Translations are in good agreement I **120**

D Source-receiver distribution **123**

E Full Seismograms **125**

F Other Networks **126**

G Translations are in good agreement II **128**

H Inversion with strains **130**
H.1 Receivers far away from the heterogeneity 132
H.2 Receivers close to the heterogeneity 134

Gradients de champ d'onde et hétérogénéités à petite échelle

C'est un dimanche matin tranquille. Quels sons vos oreilles peuvent-elles capter ? Peut-être votre musique préférée jouée à l'autre bout de la pièce, le gazouillis des oiseaux et le bruissement du vent à l'extérieur, ou le tintement des cloches d'une église au loin.

La sismologie consiste essentiellement à écouter ce qui se produit à l'intérieur des planètes. Les sismomètres placés à la surface des corps planétaires sont peuvent être assimilés à des oreilles qui enregistrent les ondes générées par les sources sismiques. Ces mesures aident à comprendre les processus et les cycles sismiques et les déformations de l'écorce terrestre de la planète, à analyser les catastrophes, telles que les glissements de terrain et les éruptions volcaniques, et enfin à quantifier les risques sismiques. La modélisation de cet aspect est appelée le problème direct en sismologie. Et, d'une manière similaire à la façon dont le son enregistré par les oreilles est utilisé pour localiser sa source et sa direction, ces mesures sismiques peuvent être utilisées pour contraindre l'emplacement de la source sismique, pour imager la structure de l'intérieur de la planète et pour explorer les réserves d'hydrocarbures. Cet aspect est appelé le problème inverse en sismologie.

Une brève description de chacun de ces aspects est présentée ci-dessous.

Le Problème Direct

Le problème direct peut être décrit de manière simplifiée par le schéma I, ou par l'équation

$$\mathbf{d} = \mathbf{G}\mathbf{m}. \tag{I}$$

Avec cette équation, nous pouvons déterminer les données ou les observables sismiques $\mathbf{d}$ pour un modèle $\mathbf{m}$ donné via la relation G. En sismologie, cette relation est généralement l'équation de l'onde sismiques.

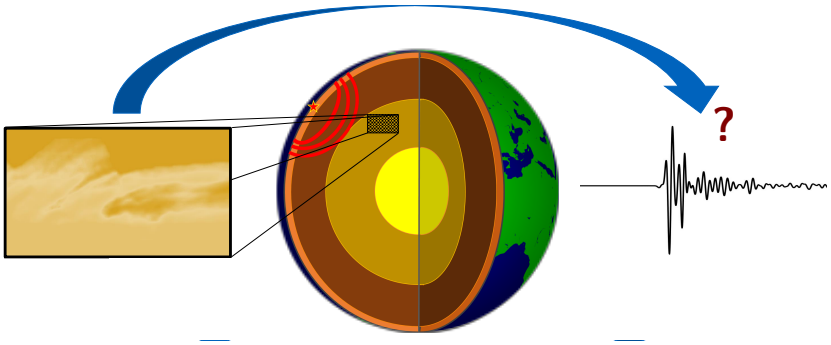

Fig. I.: Le problème direct. [1]

L'équation de l'onde sismique nous permet d'étudier la façon dont les ondes se propagent depuis la source sismique et comment elles peuvent être mesurées aux récepteurs. Selon Aki and Richards (1980, 2002), nous pouvons mesurer les mouvements suivants aux récepteurs.

1. Les translations définissent les mouvements pour lesquels chaque point du corps se déplace selon le même vecteur.

$$u_i$$

2. Les déformations définissent les mouvements dus à la partie symétrique du tenseur de déformation.

$$\epsilon_{ij} = \frac{1}{2}(\partial_i u_j + \partial_j u_i)$$

3. Les rotations définissent les mouvements dus à la partie asymétrique du tenseur de déformation.

$$\omega_{ij} = \frac{1}{2}(\partial_i u_j - \partial_j u_i)$$

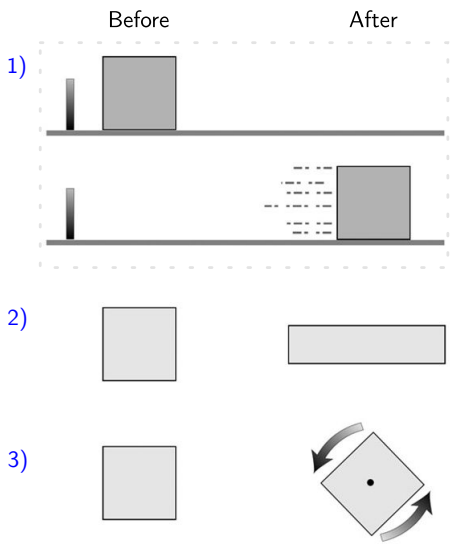

Fig. II.: Les observables sismiques. 1) Translation, 2) Déformation, et 3) Rotation. [2]

Les translations rigides sont des mesures absolues des changements de position alors que les déformations et les rotations rigides sont des mesures relatives. Ces dernières sont donc assemblées à partir des gradients de dé-

[1] Modifié de https://mediatum.ub.tum.de/node?id=1232040; Dernier accès le 29 septembre 2020

[2] Modifié de https://www.slideserve.com/aric/general-geology-crustal-deformation; Dernier accès le 29 septembre 2020

placement. Dans ce travail, j'ai choisi d'utiliser le terme "gradients de champ d'onde" pour les déformations et les rotations.

Pour évaluer complètement tout mouvement du sol, les six composantes de la déformation et les trois composantes de la rotation sont aussi importantes que les trois composantes de la translation (Aki and Richards, 2002). Les mesures simultanées des trois types de mouvements nous aident également à supprimer le couplage qu'un mouvement introduit sur l'autre, par exemple les rotations horizontales en translation (Aki and Richards, 2002, p. 604) et la rotation verticale en translation (Trifunac and Todorovska, 2001; Graizer, 2009). De même, les gradients de champ d'onde sont nécessaires en génie parasismique pour évaluer les risques sismiques (Trifunac, 1982; Abdel-Ghaffar and Rubin, 1984; Castellani and Boffi, 1989; Basu et al., 2015).

Les instruments mesurant les translations ont évolué rapidement, passant de simples instruments à pendule (Milne, 1888) à des sismomètres de fond océanique (Sutton and Duennebier, 1987; Lázaro et al., 2012), des géophones (McCarter, 1956; Lawton and Bertram, 1990), et des sismomètres à large bande (Owens et al., 1993; Wielandt and Steim, 1986). Les déformations et les rotations, quant à elles, ont longtemps été estimées à l'aide de réseaux denses (Spudich et al., 1995; Bodin et al., 1997; Huang, 2003) car les instruments sismiques permettant de les mesurer n'étaient pas assez fiables ou sensibles dans les bandes de fréquences requises. Aujourd'hui, les rotations peuvent être mesurées à l'aide de capteurs de mouvement constitues de liquide (Huang et al., 2013; Egorov et al., 2015), de capteurs magnéto-hydrodynamiques (Pierson et al., 2016), de gyroscopes à laser en anneau (McLeod et al., 1998; Pancha et al., 2000; Schreiber et al., 2009), des capteurs mécaniques (Brokešová and Málek, 2013) et plus récemment, en utilisant des gyroscopes à fibre optique (Kurzych et al., 2014; Lindner et al., 2016; Bernauer et al., 2018). De même, les déformations peuvent être mesurées à l'aide de extenssomètres laser (Berger and Lovberg, 1970; Goulty et al., 1974), de la Distributed Acousting System (DAS) (Willis et al., 2016) et de la Distributed Vibration Sensing (DVS) (Dean et al., 2017). Ces instruments permettent aujourd'hui d'obtenir des données plus fiables peuvent être exploitées.

Le Problème Inverse

En sismologie, le problème inverse, comme le montre le schéma III, consiste à estimer le modèle $\mathbf{m}$ à partir des observables $\mathbf{d_{obs}}$:

$$\mathbf{m} = \mathrm{G}^{-1}(\mathbf{d_{obs}}). \tag{II}$$

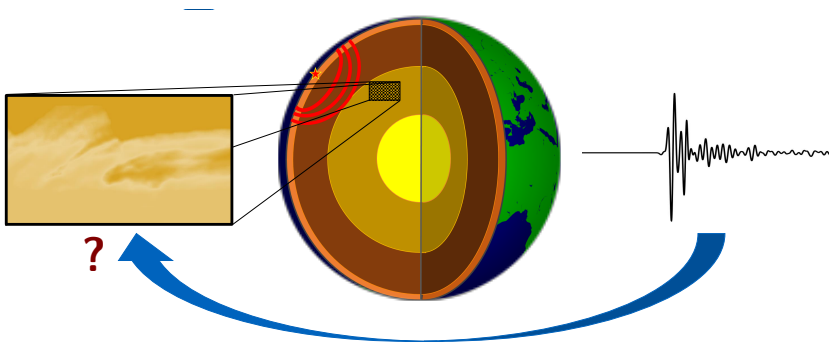

Fig. III.: Le problème inverse. [3]

Les mesures simultanées des mouvements peuvent être très utiles en sismologie car elles nous permettent de retrouver la lenteur instantanée sans utiliser les temps de parcours (Mikumo and Aki, 1964; Igel et al., 2005, 2007; Fichtner and Igel, 2009; Bernauer et al., 2012; Edme and Yuan, 2016; Wassermann et al., 2016), de limiter les propriétés des sources sismiques (Takeo and Ito, 1997; Bernauer et al., 2014; Reinwald et al., 2016; Donner et al., 2016, 2017) et d'estimer des paramètres comme la direction de propagation (Cochard et al., 2006; Igel et al., 2007) et l'historique des ruptures (Takeo and Ito, 1997). D'autres applications des mesures simultanées ont été étudiées, par exemple, par Schmelzbach et al. (2018), Li and van der Baan (2017), Igel et al. (2015) et Zhan (2019).

Les gradients de champ d'onde eux-mêmes sont importants pour déduire les contraintes causées par les ondes sismiques (Spudich et al., 1995) et pour permettre l'interprétation des ondes S (Sollberger et al., 2016).

[3] Modifié de `https://mediatum.ub.tum.de/node?id=1232040`; Dernier accès le 29 septembre 2020

Motivation et déclaration de problème

Le champ d'onde et ses gradients fournissent ensemble beaucoup d'informations sismiques. Par conséquent, les trois mouvements devrait être étudiés, ce qui n'etait pas de cas jusqu'à récemment.

Bien que des efforts considérables aient été déployés pour concevoir des instruments plus robustes et portables ces derniers temps, peu d'attention a été accordée à un autre problème concernant les gradients du champ d'onde. En effet, il a été démontré que les hétérogénéités locales à petite échelle, telles que les cavités et les discontinuités, les topographies et les hétérogénéités géologiques affectent fortement la déformation (Berger and Beaumont, 1976; Sato and Harrison, 1989; Gomberg and Agnew, 1996) et la rotation (King and Bilham, 1973; Harrison, 1976; Baker, 1980; Kohl and Levine, 1995; van Driel et al., 2012). Cet effet des hétérogénéités sur le gradient du champ d'onde est mesurable avec nos capteurs actuels et entraîne un certain nombre de problèmes: 1) le désaccord entre les données de gradient de champ d'onde et les données synthétiques calculées dans un modèle tomographique, 2) la dissimilitude entre les gradients de champ d'onde mesurés en un point et les gradients de champ d'onde estimés à ce même point à point à l'aide d'un réseau, et 3) la discordance entre les données observées par des instruments rapprochés. De telles conséquences peuvent conduire à une interprétation erronée des données. Ce point est critique car nous ignorons les détails de la croûte terrestre à l'echelle de la structure géologique, et encore plus à celle de la structure atomique. [4]

L'objectif de ce travail est triple. Premièrement, nous étudions pourquoi les gradients de champ d'onde sont affectés par des hétérogénéités locales à petite échelle. Cela nous aidera à comprendre comment un champ d'onde et ses observables interagissent réellement avec les hétérogénéités à toutes les échelles, afin de mieux interpreter les données sismiques. Ensuite, nous cherchons à savoir s'il est possible de corriger les gradients du champ d'onde pour cet effet, dans le but d'assurer une meilleure concordance entre les données de gradients de champ d'onde et les synthétiques qui ont été corrigées. Cela permettra également d'aligner les gradients de champ d'onde mesurés en un point et les gradients de champ d'onde estimés à ce même point à l'aide

[4] Et qui peut dire que la structure atomique est là où tout s'arrête ? Consultez le modèle standard à `https://home.cern/science/physics/standard-model`; Dernier accès le 29 septembre 2020

d'un réseau. Enfin, nous examinons si les gradients de champ d'onde aident améliorer les inversions complètes de la forme d'onde (FWI) en termes de précision et de résolution, et si l'effet des hétérogénéités à petite échelle a un impact sur celles-ci.

I Homogénéisation

La théorie de l'homogénéisation a pour but d'obtenir d'équations macroscopiques, ou homogénéisées ou effectives pour des systèmes ayant des structures microscopiques. En sismologie, un milieu microscopique est caractérisé par des variations de propriétés élastiques à des échelles beaucoup plus petites que la longueur d'onde minimale du milieu. En utilisant l'homogénéisation, toutes ces structures microscopiques sont lissées, c'est-à-dire que le milieu dont les structures varient rapidement peut être remplacé par un autre où les structures ne varient que lentement.

Par conséquent, l'homogénéisation est utilisée à la fois dans le problème direct pour étudier la propagation des ondes dans un milieu à couches fines (Backus, 1962), pour permettre un maillage plus espacé afin de gagner en vitesse de calcul (Capdeville et al., 2010b; Guillot et al., 2010; Cupillard and Capdeville, 2018) [voir Figure IV] mais aussi que dans le problème inverse pour aider à interpréter les résultats de l'inversion complète de la forme d'onde (Capdeville and Métivier, 2018).

Dans ce résumé, nous donnons un bref aperçu de la théorie de l'homogénéisation pour le cas 2D. Capdeville et al. (2010a), Capdeville et al. (2010b) et Guillot et al. (2010), Cupillard and Capdeville (2018) sont proposent une description plus complète pour les cas 1D, 2D et 3D respectivement.

Dans l'homogénéisation, la limite entre les variables macroscopiques et microscopiques est décrite par $\varepsilon = \frac{\lambda_0}{\lambda_m}$, où λ_0 est le longueur en dessous de laquelle les échelles sont considérées comme microscopiques et λ_m est la longueur d'onde minimale du le milieu. Pour séparer explicitement les variables microscopiques et macroscopiques, une nouvelle variable spatiale $\mathbf{y} = \frac{\mathbf{x}}{\varepsilon}$ est introduite où $\mathbf{x}$ prendre en compte toutes les variations macroscopiques et $\mathbf{y}$ toutes les variations microscopiques. Nous supposons que $\mathbf{x}$ et $\mathbf{y}$ peuvent

[5] Modifié de Capdeville et al. (2015)

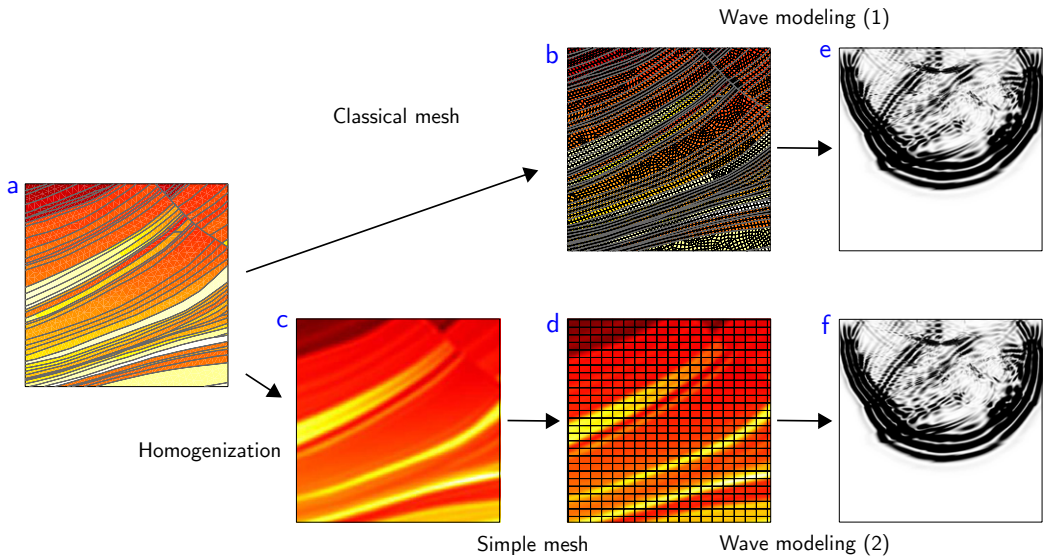

Fig. IV.: Le concept d'homogénéisation illustré sur une partie du modèle Marmousi2
5

être traités comme des variables indépendantes. Par conséquent, toutes les dérivées partielles par rapport à x sont redéfinies comme

$$\nabla_{\mathbf{x}} \rightarrow \nabla_{\mathbf{x}} + \frac{1}{\varepsilon}\nabla_{\mathbf{y}}. \tag{III}$$

Dans l'homogénéisation, le déplacement $\mathbf{u}(\mathbf{x},t)$ et la contrainte $\boldsymbol{\sigma}(\mathbf{x},t)$ sont supposés être des développement asymptotiques à deux échelles dans ε:

$$\begin{aligned}\mathbf{u}^{\varepsilon}(\mathbf{x},t) &= \sum_{i=0}^{\infty} \varepsilon^i \mathbf{u}^i(\mathbf{x},\mathbf{y},t),\\ \boldsymbol{\sigma}^{\varepsilon}(\mathbf{x},t) &= \sum_{i=-1}^{\infty} \varepsilon^i \boldsymbol{\sigma}^i(\mathbf{x},\mathbf{y},t),\end{aligned} \tag{IV}$$

où les exposants i sont des puissances pour les ε mais sont des indices d'expansion pour $\mathbf{u}$ et $\boldsymbol{\sigma}$. En introduisant les Équations (III) et (IV) dans l'équation d'onde, nous obtenons une série d'équations qui peuvent être résolues pour chaque i. Pour $i = 0$, il ressort que $\mathbf{u}^0$ ne dépend pas de la variable microscopique $\mathbf{y}$, c'est-à-dire à l'ordre 0,

$$\mathbf{u}^{\varepsilon}(\mathbf{x},\mathbf{y},t) = \mathbf{u}^0(\mathbf{x},t). \tag{V}$$

Contrairement à $i = 0$, les termes d'ordre supérieur dans la série (IV) dépendent de $\mathbf{y}$, par exemple,

$$\mathbf{u}^1(\mathbf{x}, \mathbf{y}, t) = \boldsymbol{\chi}^1(\mathbf{x}, \mathbf{y}, t) : \ \boldsymbol{\epsilon}_{\mathbf{x}}(\mathbf{u}^0(\mathbf{x}, t)) + \langle \mathbf{u}^1(\mathbf{x}, t) \rangle, \tag{VI}$$

où $\boldsymbol{\chi}^1$, le correcteur du premier ordre, est un tenseur du rank 3. En allant plus loin, nous obtenons également l'équation du problème de cellule :

$$\nabla_{\mathbf{y}}(\mathbf{c}^{\varepsilon}.(\mathbf{I} + \nabla_{\mathbf{y}}\boldsymbol{\chi}^1)) = 0, \tag{VII}$$

où $\mathbf{c}$ est le tenseur élastique.

De ce fait, $\mathbf{u}^0$, le déplacement effectif d'ordre zéro, est une solution de l'équation classique de l'onde

$$\rho^* \ddot{\mathbf{u}}^0 - \nabla.\mathbf{c}^* : \nabla \mathbf{u}^0 = \mathbf{f}^*, \tag{VIII}$$

où le modèle effectif $(\rho^*, \mathbf{c}^*)$ peut être obtenu en résolvant le problème de cellule (Capdeville et al., 2010b).

II Effets des hétérogénéités à petite échelle sur les gradients du champ d'onde

L'effet des structures à petite échelle sur les gradients du champ d'onde peut être mieux décrit par un exemple numérique.

Nous considérons un cas élastique 2D où les domaines de calcul sont deux carrés de 20×20 km^2. Ces carrés, à l'exception d'une petite hétérogénéité variant dans l'espace au centre du second carré, sont sinon homogènes. Les vitesses P et S dans la zone homogène des carrés sont respectivement de 5 kms^{-1} et 3.2 kms^{-1}. L'extension spatiale de l'hétérogénéité au centre du deuxième carré est de 200×200 m^2. Sa géométrie reste simple afin de faciliter à la fois le maillage et la modélisation de la forme d'onde. Les vitesses dans chaque élément de l'hétérogénéité diffèrent de ±50% par rapport à celle des alentours. Ce contraste de vitesse est fort mais réaliste pour une telle gamme d'échelles. Par exemple, le contraste de vitesse entre le granit et les

sédiments non consolidés est généralement encore plus prononcé. Toutes les frontières sont absorbantes.

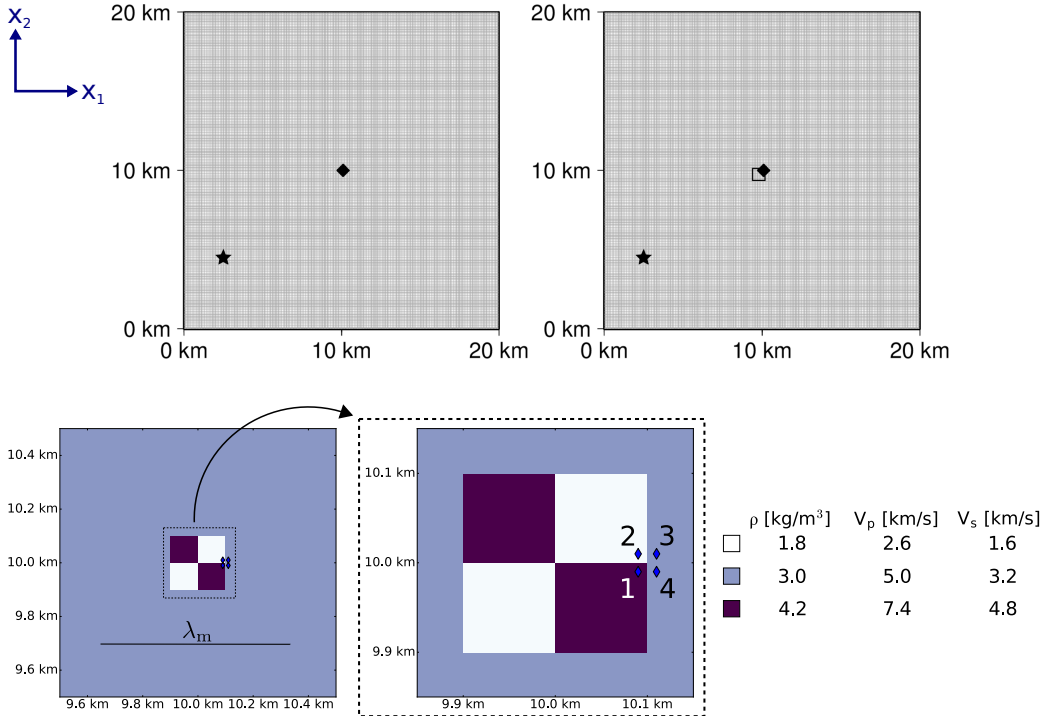

Fig. V.: Haut : domaines 2D utilisés dans la Section II. Les deux domaines font 20×20 km^2. Toutes les limites sont absorbantes. L'étoile indique l'emplacement de la source et les diamants indiquent l'emplacement de quatre récepteurs. À gauche : milieu entièrement homogène. À droite : Une hétérogénéité de 200×200 m^2, placée au centre, est indiquée par le carré (pas à l'échelle).
En bas : V_p, V_s et ρ à l'hétérogénéité. La longueur de la longueur d'onde minimale pour la simulation est indiquée dans le panneau le plus à gauche.

Nous plaçons quatre récepteurs dans les deux carrés de sorte que pour le carré hétérogène, deux récepteurs se trouvent juste à l'intérieur de l'hétérogénéité et les deux autres juste à l'extérieur, comme le montre la Figure V. La distance entre les récepteurs est d'environ 15 m.

Dans les deux cas, nous calculons le champ d'onde induit par un double-couple horizontal. La fonction source-temps est une ondelette de Ricker (deuxième dérivée d'une ondelette gaussienne). Avec une fréquence centrale de la source de 1.5 Hz (fréquence maximale de 4.1 Hz), la longueur d'onde minimale λ_m est d'environ 700 m. Il faut noter que la dimension de l'hétérogénéité est environ 3 fois inferieure à λ_m. En utilisant le programme d'Éléments Spectraux, les déplacements, vitesses, accélérations, le cisaillement et rotation mesurées par les quatre récepteurs des deux modèles sont

calculées[6]. Ceux-ci sont présentés sur la Figure VI. Comme le maillage utilisé pour le calcul respecte les interfaces de l'hétérogénéité, les solutions ainsi obtenues sont considérées comme précises.

Il ressort de la Figure VI que si les quatre récepteurs mesurent presque le même déplacement, la même vitesse et la même accélération dans les deux modèles, ce n'est pas le cas pour la rotation et la déformation. Les quatre récepteurs mesurent une rotation et une déformation très similaires dans le cas homogène, mais en présence d'une hétérogénéité, bien que beaucoup plus petite que la longueur d'onde minimale, les mesures sont sensiblement différentes. La différence peut être observée à la fois dans les amplitudes et les phases, et elle dépend de l'emplacement relatif du récepteur par rapport à l'hétérogénéité.

Il est important de noter que les résultats des exemples numériques ne sont pas spécifiques aux seules quantités indiquées. La conclusion serait la même pour toute mesure du champ d'onde (et ses dérivées temporelles, telles que le déplacement, la vitesse et l'accélération) et pour toute mesure du gradient du champ d'onde (et ses dérivées temporelles, telles que la déformation, la vitesse de déformation, la rotation et la vitesse de rotation).

L'homogénéisation pour expliquer l'effet

Dans cette section, nous examinons cet effet de manière théorique en utilisant la théorie de l'homogénéisation [voir Section I].

Dans le cadre de la théorie de l'homogénéisation, la séparation des échelles en petites échelles $\mathbf{y}$ et grandes échelles $\mathbf{x}$ fait que tous les gradients par rapport à $\mathbf{x}$ sont redéfinis comme

$$\nabla_{\mathbf{x}} \to \nabla_{\mathbf{x}} + \frac{1}{\varepsilon}\nabla_{\mathbf{y}}, \tag{IX}$$

où $\nabla_{\mathbf{x}} = {}^t(\partial_{x1}, \partial_{x2})$ et $\nabla_{\mathbf{y}} = {}^t(\partial_{y1}, \partial_{y2})$.

[6]Le programme Élément Spectral est basé sur la méthode des éléments spectraux (SEM). Dans la SEM, les déplacements sont approximés à l'aide de polynômes de Lagrange à Gauss-Lobatto-Legendre (GLL) points. Leurs dérivés, qui nous permettent de calculer les contraintes et les rotations, peuvent être déterminés en prenant les dérivés des polynômes de Lagrange.

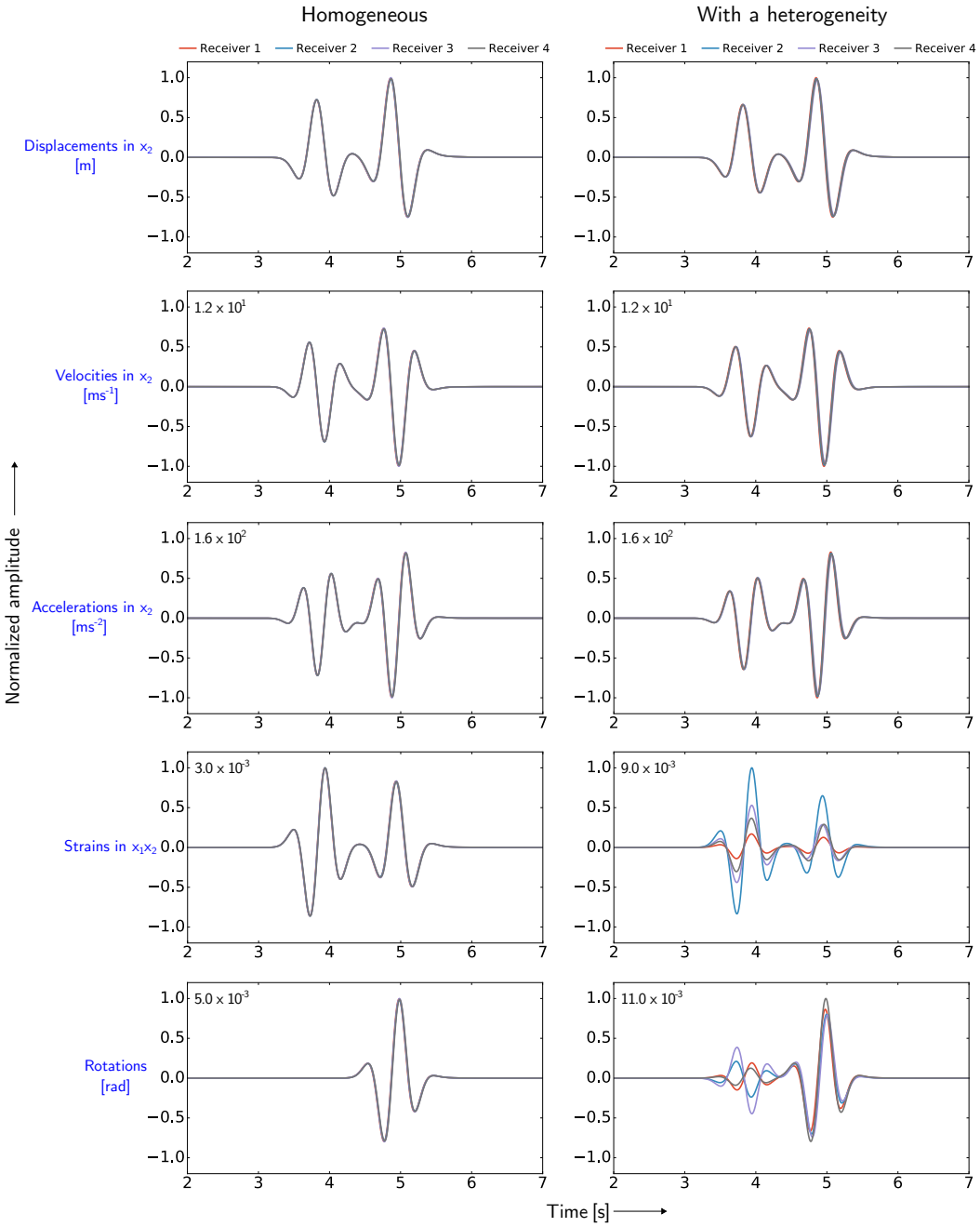

Fig. VI.: A gauche : Mesures dans le milieu homogène. A droite : Mesures dans le milieu hétérogène. Les deux milieux sont représentés sur la Figure V.
En partant du haut, les déplacements verticaux, les vitesses verticales, les accélérations verticales, les cisaillements et les rotations sont indiqués. Les facteurs d'échelle pour chaque panneau sont indiqués en haut à gauche.

L'objectif de l'homogénéisation est de trouver des solutions aux équations d'onde sous la forme d'un développement asymptotique en ε. Ainsi, les équations pour le déplacement réel $\mathbf{u}^\varepsilon$ et le gradient réel $(\nabla\mathbf{u})^\varepsilon$ prennent la forme

$$\begin{aligned}\mathbf{u}^\varepsilon(\mathbf{x},\mathbf{y},t) &= \mathbf{u}^0(\mathbf{x},\mathbf{y},t) + \varepsilon\mathbf{u}^1(\mathbf{x},\mathbf{y},t) + \varepsilon^2\mathbf{u}^2(\mathbf{x},\mathbf{y},t) + ... \\ (\nabla\mathbf{u})^\varepsilon(\mathbf{x},\mathbf{y},t) &= (\nabla\mathbf{u})^0(\mathbf{x},\mathbf{y},t) + \varepsilon(\nabla\mathbf{u})^1(\mathbf{x},\mathbf{y},t) + \varepsilon^2(\nabla\mathbf{u})^2(\mathbf{x},\mathbf{y},t) + ... \quad \text{(X)}\end{aligned}$$

Dans (X), les exposants i sont des puissances pour les ε mais sont des indices d'expansion pour $\mathbf{u}$ et $(\nabla\mathbf{u})$.

En rappelant les Équations (V) et (VI), nous avons,

$$\begin{aligned}\mathbf{u}^0(\mathbf{x},\mathbf{y},t) &= \mathbf{u}^0(\mathbf{x},t), \\ \mathbf{u}^1(\mathbf{x},\mathbf{y},t) &= \boldsymbol{\chi}(\mathbf{y}) : \boldsymbol{\epsilon}(\mathbf{u}^0(\mathbf{x},t)). \quad \text{(XI)}\end{aligned}$$

Dans la deuxième Équation de (XI), $\boldsymbol{\epsilon}$ désigne la déformation ($[\epsilon(\mathbf{u}^0)]_{ij} = \frac{1}{2}(\partial_i u_j^0 + \partial_j u_i^0)$) et ne doit pas être confondu avec le paramètre d'homogénéisation ε de la Section I. $\boldsymbol{\chi}$, le correcteur du premier ordre, est un tenseur du rank 3. C'est une solution du la problème de cellule [voir Section I]. Notez que $\boldsymbol{\chi}$ ne dépend pas du temps ou des sources.

Par conséquent, à l'ordre 0, le déplacement réel $\mathbf{u}^\varepsilon$ devient

$$\mathbf{u}^\varepsilon(\mathbf{x},\mathbf{y},t) = \mathbf{u}^0(\mathbf{x},t). \quad \text{(XII)}$$

En utilisant les Équations (IX) et l'expansion de $\mathbf{u}^\varepsilon(\mathbf{x},\mathbf{y},t)$ dans (X), le gradient réél $(\nabla\mathbf{u})^\varepsilon$ est alors

$$\begin{aligned}(\nabla\mathbf{u})^\varepsilon(\mathbf{x},\mathbf{y},t) &= \left(\nabla_\mathbf{x} + \frac{1}{\varepsilon}\nabla_\mathbf{y}\right)(\mathbf{u}^0(\mathbf{x},\mathbf{y},t) + \varepsilon\mathbf{u}^1(\mathbf{x},\mathbf{y},t) + \varepsilon^2\mathbf{u}^2(\mathbf{x},\mathbf{y},t) + ...), \\ (\nabla\mathbf{u})^\varepsilon(\mathbf{x},\mathbf{y},t) &= \nabla_\mathbf{x}\left(\mathbf{u}^0(\mathbf{x},\mathbf{y},t) + \varepsilon\mathbf{u}^1(\mathbf{x},\mathbf{y},t) + \varepsilon^2\mathbf{u}^2(\mathbf{x},\mathbf{y},t) + ...\right) + \\ &\quad \frac{1}{\varepsilon}\nabla_\mathbf{y}\left(\mathbf{u}^0(\mathbf{x},\mathbf{y},t) + \varepsilon\mathbf{u}^1(\mathbf{x},\mathbf{y},t) + \varepsilon^2\mathbf{u}^2(\mathbf{x},\mathbf{y},t) + ...\right).\end{aligned}$$

En utilisant (XI), le gradient réel $(\nabla\mathbf{u})^\varepsilon$ à l'ordre 0 est donc

$$(\nabla\mathbf{u})^\varepsilon(\mathbf{x},\mathbf{y},t) = (\nabla_\mathbf{x}\mathbf{u}^0)(\mathbf{x},t) + \nabla_\mathbf{y}\boldsymbol{\chi}(\mathbf{y}) : \boldsymbol{\epsilon}(\mathbf{u}^0(\mathbf{x},t)). \quad \text{(XIII)}$$

Notez que les termes à droite de cette équation constituent le premier terme de l'expansion de $(\nabla \mathbf{u})^{\varepsilon}(\mathbf{x}, \mathbf{y}, t)$ dans (X).

Cela implique que pour la rotation en 2D, qui est un scalaire,

$$\begin{aligned} \omega^{\varepsilon} &= \theta_{ij}\ (\partial_i u_j)^0 \\ &= \omega^0 + J_{ij} : \epsilon_{ij}(u^0), \end{aligned} \tag{XIV}$$

où $J_{ij} = \theta_{mn}\partial_{y_m}\chi_{ijn}$ et θ représente le symbole de Levi-Civita 2D . De même, pour la rotation en 3D,

$$\begin{aligned} \omega_i^{\varepsilon} &= \theta_{ijk}\ (\partial_j u_k)^0 \\ &= \omega_i^0 + J_{ijk} : \epsilon_{jk}(u^0), \end{aligned} \tag{XV}$$

où $J_{ijk} = \theta_{imn}\partial_{y_m}\chi_{njk}$ et θ représente le symbole de Levi-Civita 3D. Et pour un récepteur rotationnel sur la surface d'un domaine 3D dans des conditions de surface libre,

$$\omega_i^{\varepsilon} = \omega_i^0 + \bar{J}_{ijk} : \sigma_{jk}, \tag{XVI}$$

où $\bar{J}_{ijk} = J_{imn}\ v_{mnjk}$, $\boldsymbol{\sigma}$ est le tenseur de contrainte et $\mathbf{v}$ est l'inverse du tenseur élastique $\mathbf{c}$.

De même, pour les vitesses de rotation en 3D, nous obtenons

$$\dot{\omega_i}^{\varepsilon} = \dot{\omega_i}^0 + J_{ijk} : \dot{\epsilon_{jk}}(u^0),$$

où $J_{ijk} = \theta_{imn}\partial_{y_m}\chi_{njk}$ et θ représente le symbole 3D de Levi-Civita.

Dans (X), $\mathbf{u}^{\varepsilon}$ est le déplacement réel et $\mathbf{u}^0$ est le déplacement effectif d'ordre zéro. De même, $(\nabla \mathbf{u})^{\varepsilon}$ représente le gradient réél du déplacement et $(\nabla \mathbf{u})^0$ représente le gradient effectif du déplacement d'ordre zéro. Les quantités réelles correspondent aux données réelles qui peuvent être collectées sur le terrain. En théorie, il est possible de les modéliser à l'aide d'équations d'onde mais comme elles dépendent de toutes les échelles possibles, elles nécessitent une connaissance à l'échelle infinie des propriétés élastiques de la Terre. Cela n'est pas réalisable dans la pratique. D'autre part, pour une bande de fréquence donnée, les quantités effectives peuvent être modélisées en utilisant les mêmes équations mais en utilisant des propriétés élastiques homogénéisées qui ne contiennent aucune petite échelle. Ainsi, les quantités effectives peuvent être décrites avec un ensemble fini de paramètres. Ce

sont ces paramètres qui sont récupérés dans l'inversion complète de la forme d'onde et l'imagerie tomographique (Capdeville and Métivier, 2018). La plupart des modèles tomographiques qui existent sont donc en réalité une approximation de la Terre homogénéisée.

En comparant les termes dans (XII), nous constatons que les termes de droite ne dépendent que de $\mathbf{x}$, c'est-à-dire de grandes échelles. Cela signifie que le déplacement effectif peut être utilisé comme une bonne approximation du déplacement réel sans se soucier des petites échelles. C'est un résultat bien connu de Backus (1962) et Chapman (2004, p. 277). Une conséquence de ce résultat est que l'accord entre les données réelles et les synthétiques est raisonnablement bon pour le déplacement, la vitesse et l'accélération. Ceci est également cohérent avec les résultats obtenus dans la Section II et avec de nombreux exemples concernant des données réelles. Par exemple, les ondes de surface de très longue période peuvent être modélisées à l'aide de PREM (Dziewoński and Anderson, 1981) avec une bonne précision, même si la croûte est très hétérogène. La grande amplitude et l'hétérogénéité à petite échelle de la croûte ne sont pas visibles dans le champ de déplacement, et il n'est pas nécessaire de disposer d'informations complètes sur la croûte pour sa modélisation. C'est également la raison pour laquelle nos modèles terrestres unidimensionnels sont si performants (Dziewoński and Anderson, 1981; Kennett et al., 1995).

Cependant, cela n'est pas vrai pour tout gradient de déplacement. Les termes utilisés dans (XIII) dépendent à la fois de $\mathbf{x}$ et de $\mathbf{y}$, c'est-à-dire à la fois des grandes et des petites échelles. En raison des petites échelles, le gradient réél de déplacement est couplé avec la déformation du déplacement effectif. Ce couplage est dû au correcteur du premier ordre $\boldsymbol{\chi}$, c'est pourquoi nous l'appelons "correction". De même, nous appelons $\mathbf{J}$ le tenseur de couplage.

L'apparition de la correction dans (XIII) implique que la mise en place d'un problème d'inversion avec le gradient de champ d'onde est complexe car les observations reposent sur toutes les échelles. Chaque détail, à toutes les échelles, serait nécessaire pour mettre en place le problème d'inversion. Dans le cas du déplacement, de la vitesse ou de l'accélération, où les quantités effectives sont une bonne approximation des quantités réelles, il n'est pas nécessaire de prendre en compte les hétérogénéités de petit échelle est la mise en place problème d'inversion n'est pas un problème. Pour les gradients de champ d'onde, cependant, la correction doit être prise en compte.

III Correction des gradients de champ d'onde pour les effets des structures à petite échelle

Nous savons grâce à (XIV), (XV) et (XVI) que le gradient réel du champ d'onde est couplé à la déformation du déplacement effectif à travers le tenseur **J**. De plus, **J** ne dépend ni du temps ni de la source. Il dépend uniquement de l'emplacement du récepteur. Si les propriétés élastiques au niveau du récepteur sont suffisamment bien connues, **J** peut être calculé en résolvant le problème de cellule (Capdeville et al., 2010b; Guillot et al., 2010). Ce n'est pas le cas en pratique. Néanmoins, nous pouvons calculer **J** par inversion à condition de disposer d'un modèle effectif qui correspond raisonnablement bien aux données de déplacement (ou de vitesse ou d'accélération). Le choix évident pour ce modèle effectif est le modèle homogénéisé car c'est ce que les ondes peuvent observer (Capdeville and Métivier, 2018). Ce modèle effectif n'est généralement pas connu, mais tout modèle tomographique peut être une bonne approximation comme nous le verrons après. Pour les données réelles, nous pouvons utiliser n'importe quel modèle terrestre qui correspond raisonnablement bien aux données de déplacement (ou de vitesse ou d'accélération). Ceci est similaire à l'inversion du tenseur de moment d'un tremblement de terre, où un modèle de la Terre est nécessaire pour calculer les fonctions de Green.

Parce que tous les exemples ici sont réalisés pour la rotation, nous partons de l'Équation XIII :

$$\omega^{\varepsilon}(\mathbf{x}_r, t; \mathbf{x}_s) = \omega^{0}(\mathbf{x}_r, t; \mathbf{x}_s) + \mathbf{J}(\mathbf{y}_r) : \boldsymbol{\epsilon}^{0}(\mathbf{x}_r, t; \mathbf{x}_s), \tag{XVII}$$

où ω^{ε} sont les données de rotation, ω^{0} et $\boldsymbol{\epsilon}^{0}$ sont la rotation et la déformation calculées dans le modèle effectif et **J** est l'inconnu. $\mathbf{x}_s$ indique l'emplacement de la source et $\mathbf{y}_r = \frac{\mathbf{x}_r}{\varepsilon}$ indique l'emplacement du récepteur. Nous calculons **J** par inversion en résolvant le problème linéaire surdéterminé au sens des moindres carrés (Tarantola and Valette, 1982). Nous cherchons de minimiser l'inadéquation de L^2 entre les synthétiques et les données par

$$\mathbf{J} \sim ({}^{t}\mathbf{F}\ \mathbf{F})^{-1}\ \mathbf{F}\ \delta d, \tag{XVIII}$$

où $\delta d = \omega^{\varepsilon} - \omega^{0}$ et $\mathbf{F}$ est la matrice où toutes les déformations du déplacement effectif sont prises en compte.

Le processus d'inversion pour $\mathbf{J}$ est simple : nous n'avons besoin que d'une simulation par source pour déduire $\mathbf{F}$. Ensuite, nous appliquons l'Équation (XVIII) sans aucune modification car l'inversion est stable et aucun amortissement n'est nécessaire. Nous inversons pour 3 paramètres en 2D et pour 18 paramètres, pour les 3 composantes de la rotation, en 3D. Comme la réponse de l'instrument, le correcteur peut être utilisé pour séparer les effets de site non désirés des données.

Une fois que nous avons calculé $\mathbf{J}$ par inversion, nous devons évaluer la qualité de nos résultats d'inversion. Une façon de le faire serait de comparer le $\mathbf{J}$ calculé par inversion à celui obtenu en résolvant la série d'équations d'homogénéisation [voir le problème de cellule dans la Section I]. Cependant, cette solution n'est disponible que lorsque toutes les échelles fines sont parfaitement connues, c'est-à-dire uniquement pour les tests synthétiques. Par conséquent, pour tous nos exemples, nous commençons par séparer les données en deux groupes : l'ensemble des données d'inversion et l'ensemble des données de validation. Nous utilisons l'ensemble de données d'inversion pour effectuer l'inversion et l'ensemble de données de validation pour évaluer la précision de $\mathbf{J}$. Dans tous les exemples qui suivent, nous utilisons le $\mathbf{J}$ pour corriger les rotations synthétiques. Par conséquent, une meilleure concordance entre les données observées et les rotations synthétiques corrigées, en particulier pour les événements non utilisés dans l'inversion, implique que $\mathbf{J}$ est une bonne mesure du couplage en raison des petites échelles au niveau du récepteur.

Exemple synthétique en 2D

Le modèle est un domaine 2D dont les vitesses P et S sont respectivement de 5 kms^{-1} et 3.2 kms^{-1}. La taille du domaine est de 20×20 km^2. Une hétérogénéité de taille 200×200 m^2 est au centre du domaine et les vitesses P et S dans chaque élément de l'hétérogénéité sont $\pm$ 50% par rapport au domaine environnant. La configuration géométrique du modèle est illustrée dans la Figure VII.

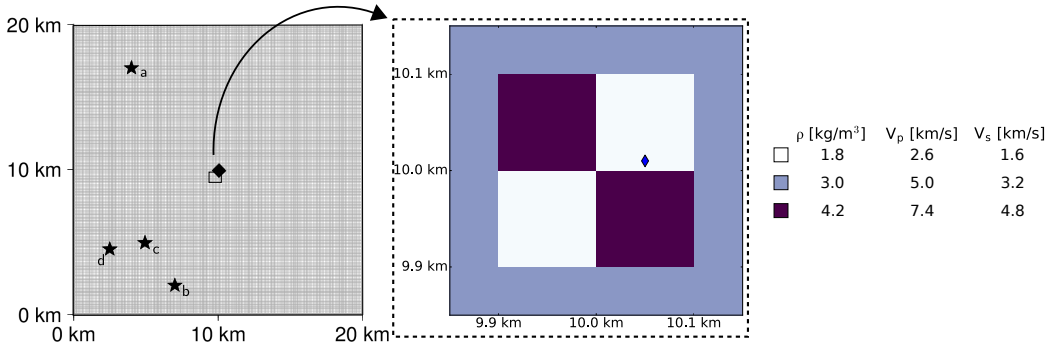

Fig. VII.: A gauche : domaine 2D utilisé dans la Section III. Le domaine est de 20×20 km^2 et l'hétérogénéité au centre, pas à l'échelle, est de 200×200 m^2. Les étoiles indiquent l'emplacement des sources et le diamant celui du récepteur. Toutes les limites sont absorbantes. Au centre : Zoom sur l'hétérogénéité. A droite : V_p, V_s et ρ dans le domaine. Les vitesses P et S dans le domaine extérieur sont de 5 kms^{-1} et 3.2 kms^{-1}, et les vitesses de chaque élément à l'intérieur de l'hétérogénéité sont de $\pm$50% par rapport au domaine environnant.

Nous plaçons le récepteur de rotation dans l'hétérogénéité de sorte que nous nous attendons à ce que l'hétérogénéité affecte les mesures de rotation. Nous calculons donc le tenseur de couplage **J** par inversion. Pour cela, nous effectuons d'abord trois simulations dans ce milieu avec des sources aux positions indiquées par les étoiles a, b et c respectivement dans la Figure VII pour générer les données [Figures VIII et IX ; lignes noires]. Ces rotations constituent le terme de gauche dans l'Équation XVII. La fréquence centrale des trois sources est de 1.5 Hz (fréquence maximale 4.1 Hz). Deux de ces sources considérées sont des double-couples, tandis qu'une est une force. Bien que l'hétérogénéité soit beaucoup plus petite que λ_m, le maillage des éléments spectraux pour la simulation respecte toutes les interfaces de l'hétérogénéité. Les rotations calculées sont donc considérées comme précises.

Ensuite, nous devons choisir un modèle effectif pour l'inversion. Ici, nous calculons **J** par inversion contre deux modèles effectifs différents. Le premier modèle effectif est la version homogénéisée du milieu original avec $\varepsilon = 0.5$. Le second modèle effectif est un modèle entièrement homogène avec l'hypothèse sous-jacente que la zone hétérogène a un effet négligeable sur le modèle effectif [voir Appendix C]. Dans ce second cas, nous rapprochons des situations réalistes où les modèles tomographiques sont loin d'être parfaits.

Nous utilisons les trois mêmes sources qu'auparavant dans les deux milieux effectifs pour calculer les rotations et les déformations au niveau du récepteur. Ce sont les deux quantités connues sur la droite dans l'Équation XVII. Les

rotations mesurées dans le modèle homogénéisé sont indiquées dans la Figure VIII (lignes vertes) et celles calculées dans le modèle homogène sont présentées dans la Figure IX (lignes vertes). La comparaison des rotations mesurées dans les cas hétérogène et homogénéisé/homogène de la figure révèle une différence significative dans les quatre panneaux. Il apparaît clairement que la différence est due à la présence de l'hétérogénéité et qu'elle dépend du chemin que prend la forme d'onde à travers l'hétérogénéité.

Nous utilisons les données et les synthétiques ainsi obtenues pour calculer **J** par inversion. Le fait que nous utilisions le SEM à la fois pour générer des données et pour calculer **J** par inversion n'est pas ici un crime d'inversion. Ce serait un crime d'inversion si les données étaient générées en utilisant la théorie de l'homogénéisation et si l'inversion était effectuée avec le même maillage. Ici, nous générons les données en utilisant un maillage fin avec une taille d'élément de 100 m, c'est-à-dire sans la théorie de l'homogénéisation, mais nous effectuons l'inversion sur un maillage clairsemé avec une taille d'élément de 200 m.

Une fois que nous obtenons **J**, il est utilisé pour corriger les synthétiques, c'est-à-dire que nous ajoutons le dernier terme de l'Équation XVII aux rotations mesurées en milieu homogénéisé/homogène. Celles-ci sont illustrées dans les Figures VIII et IX (lignes rouges). Nous pouvons voir que les rotations synthétiques corrigées s'adaptent beaucoup mieux aux rotations hétérogènes, mais cela n'est pas surprenant car ces données ont été utilisées pour l'inversion. Par conséquent, pour rendre réellement compte de sa précision, nous utilisons ce **J** à un nouvel ensemble de données qui n'a pas été utilisé pour l'inversion [Figures VIII et IX ; Panneau d] comme validation ; la nouvelle source positionnée à l'endroit indiqué par l'étoile d dans la Figure VII. Cette nouvelle source est une force verticale. Comme nous l'attendions, nous pouvouns voir que **J** nous permet de retrouver la rotation dans le milieu hétérogène.

La différence d'amplitude entre les rotations homogénéisées et homogènes (lignes vertes) dans les Figures VIII et IX respectivement est présente dans tous les panneaux. Cette différence est très subtile et confirme notre hypothèse selon laquelle la zone hétérogène a un effet négligeable sur le modèle effectif.

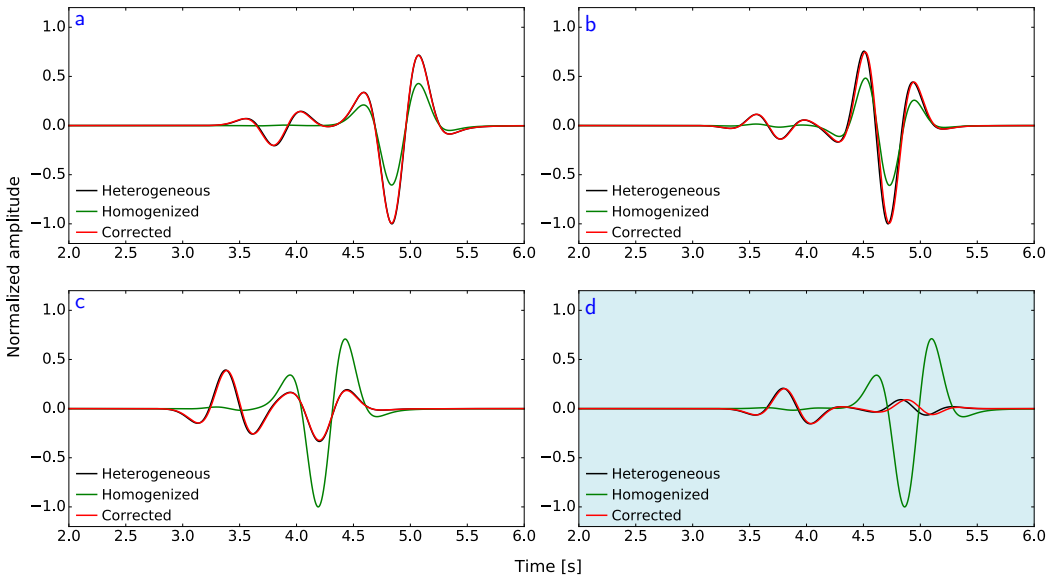

Fig. VIII.: Rotations. Panneaux a, b, c : Les trois événements utilisés pour l'inversion du correcteur. Panneau d : L'événement utilisé comme validation en applicant ce correcteur. Il est représenté sur fond bleu pour indiquer qu'il n'a pas été utilisé pour l'inversion.
Les rotations hétérogènes et homogénéisées sont indiquées en noir et en vert respectivement. Les rotations qui ont été corrigées à l'aide du tenseur de couplage **J** sont indiquées en rouge.

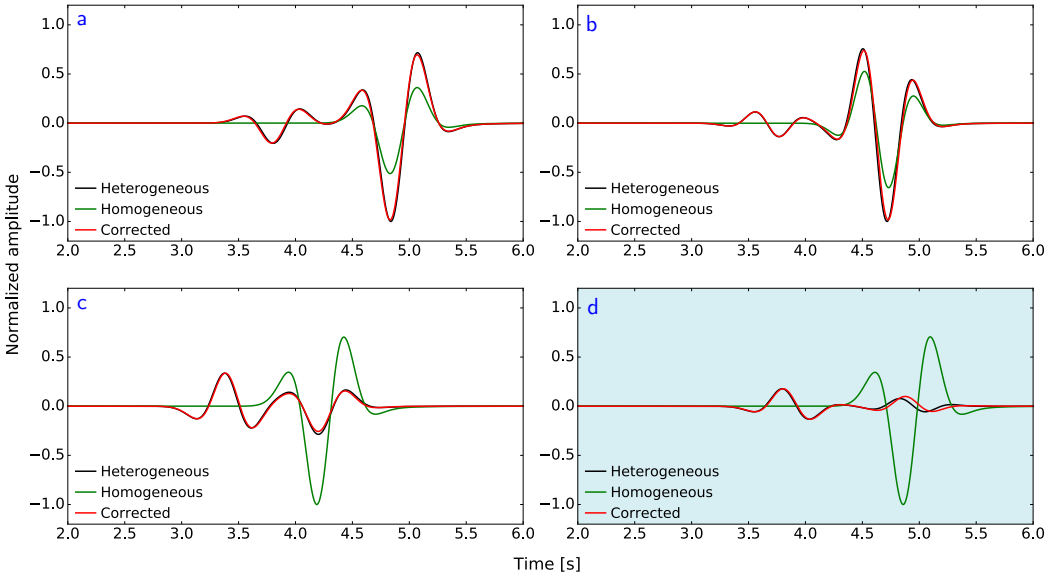

Fig. IX.: Rotations. Panneaux a, b, c : Les trois événements utilisés pour l'inversion du correcteur. Panneau d : L'événement utilisé comme validation en applicant ce correcteur. Il est représenté sur fond bleu pour indiquer qu'il n'a pas été utilisé pour l'inversion.
Les rotations hétérogènes et homogènes sont indiquées en noir et en vert respectivement. Les rotations qui ont été corrigées à l'aide du tenseur de couplage **J** sont indiquées en rouge.

G Ring Laser, Wettzell

Depuis son fonctionnement en 2001, le laser G Ring de Wettzell, à 150 km au nord-est de Munich, enregistre avec succès la composante verticale des vitesses de rotation générées par les sources sismiques (Igel et al., 2005; Suryanto et al., 2006; Igel et al., 2007). En utilisant deux faisceaux opposés de longueur d'onde 633 nm pour générer une fréquence de battement, il mesure des vitesses de rotation jusqu'à 10^{-10}rads^{-1}Hz$^{-1/2}$ (Schreiber et al., 2003).

Dans cette section, le tenseur de couplage **J** est calculé par inversion pour le laser G Ring pour les événements télésismiques de longue période. Nous utilisons la définition de la norme L^2 définie ci-dessous pour quantifier l'inadéquation entre les vitesses de rotation observés et synthétiques.

$$\xi := \frac{\sqrt{\int_0^{t_{max}} (\dot{\omega} - \dot{\omega}^{data})^2(t)\ dt}}{\sqrt{(\dot{\omega}^{data})^2(t)\ dt}}; \tag{XIX}$$

où $\dot{\omega}$ est le vitesse de rotation verticale synthétique et $\dot{\omega}^{data}$ est la vitesse de rotation verticale observée. Notez que cette inadéquation prend en compte toutes les parties du sismogramme.

Nous utilisons Obspy (Krischer et al., 2015) pour obtenir les vitesses de rotation enregistrées par le laser et les vitesses enregistrées par le sismomètre WET situé au même endroit pour tous les événements survenus entre janvier 2007 et juin 2018 et dans les limites de M_w 7.0 et 9.0. Après le téléchargement, toutes les données sont corrigées en fonction de la réponse instrumentale. Nous calculons ensuite les vitesses synthétiques et les vitesses de rotation en utilisant un programme de sommation en mode normal pour résoudre l'équation de l'onde dans un PREM prenant en compte l'océan et l'anisotropie. Pour cela, le tenseurs des moments du catalogue du GCMT (Ekström et al., 2012) sont utilisées avec une fonction d'étape comme fonction source-temps.

Nous comparons les vitesses observées et synthétiques afin d'éliminer les données observées sans signal sismique visible. En dehors de cela, aucune sélection préalable des événements n'est effectuée.

En comparant l'inadéquation entre les vitesses observées et synthétiques à l'ajustement entre les vitesses de rotation observées et synthétiques pour tous les événements dans les fréquences de 0.002 à 0.009 Hz, nous constatons que les vitesses de rotation sont en moins bon accord que les vitesses [voir Appendix C]. Dans la plupart des cas, les défauts d'ajustement tels que définis dans (XIX) sont d'environ 0.3 entre les vitesses mais sont supérieurs à 0.7 entre les vitesses de rotation. Nous pensons que cela est dû à des hétérogénéités à petite échelle au niveau du laser et donc, calculons **J** par inversion en utilisant 32 événements. Une figure montrant la distribution source-récepteur dans Appendix D. Le **J** ainsi obtenu est à son tour utilisé pour corriger les vitesses de rotation synthétiques. L'un de ces événements est illustré dans la Figure X (panneau supérieur). Un ensemble de données de validation est ensuite mis en place pour faciliter l'accès à la qualité de nos résultats. Il comprend 32 événements non utilisés dans l'inversion. Deux des événements de cet ensemble de données de validation sont illustrés dans la Figure X (panneaux inférieur). Dans tous les panneaux, nous voyons des arrivées distinctes d'onde de Love directes et d'onde de Love indirectes. Nous voyons également que les vitesses de rotation corrigées (lignes rouges) correspondent mieux aux vitesses de rotation observées (lignes noires) que les vitesses de rotation synthétiques (lignes vertes). Les inadéquations pour environ 72% des événements de l'ensemble des données de validation s'améliorent après l'introduction de **J**, ce qui prouve qu'en effet, **J** est une bonne indication du couplage. Par exemple, l'inadéquation pour l'événement indiqué dans le panneau central de la Figure X est passé de 0.86 à 0.63.

IV Inversions synthétiques de la forme d'onde complète avec gradients de champ d'onde

Dans cette section, nous voulons déterminer si la réalisation de FWI avec des gradients de champ d'onde est avantageuse en termes de précision et de résolution. Nous nous concentrons sur l'inversion avec rotations. Les inversions avec les déformation sont indiquées en Appendix H.

Notre modèle cible est un domaine 2D dont les vitesses P et S sont respectivement de 5 kms^{-1} et 2.8 kms^{-1}. La taille du domaine est de 40×40 km^2 et

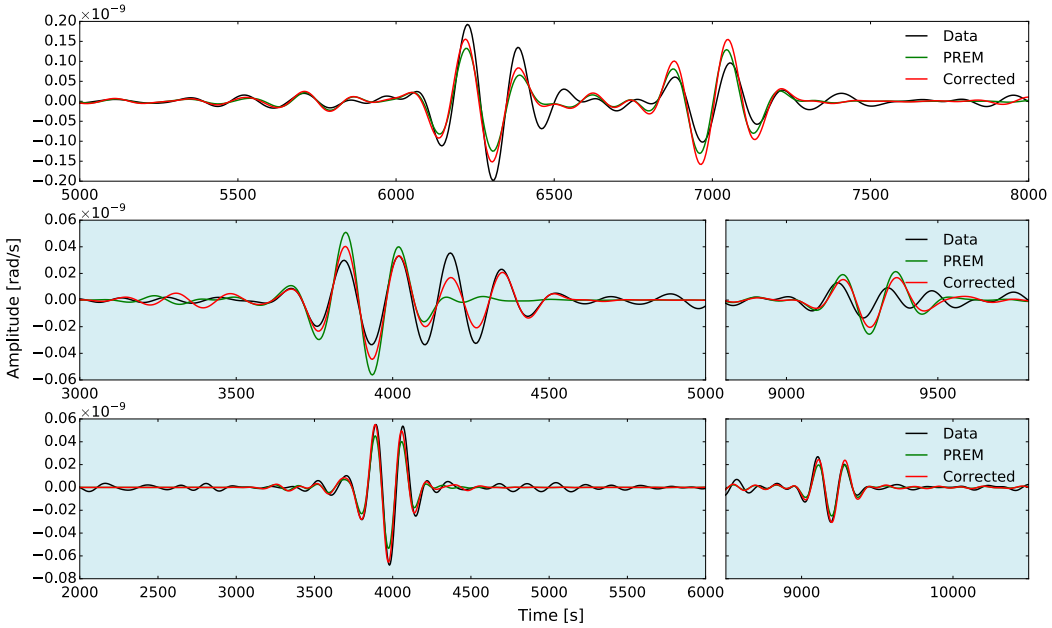

Fig. X.: Vitesses de rotation de l'axe vertical. Haut : 201611131102A Île du Sud, Nouvelle-Zélande. Un des 32 événements qui servent au calcul du tenseur de couplage **J** par inversion. Milieu : 201210280304A Îles de la Reine-Charlotte. Un événement de l'ensemble des données de validation. En bas : 201006121926A Îles Nicobar. Également un événement de l'ensemble des données de validation. Les événements de l'ensemble des données de validation sont représentés sur fond bleu pour indiquer que ces événements n'ont pas été utilisés pour l'inversion.
Les données, les vitesses de rotation synthétiques et corrigées sont indiquées en noir, vert et rouge respectivement.

la taille de chaque élément est de 400×400 m^2. Une hétérogénéité de taille 16×16 km^2 est au centre du domaine et les vitesses P et S dans chaque élément de l'hétérogénéité sont de $\pm$ 40% par rapport au domaine environnant. Cela implique qu'il y a 1600 valeurs individuelles et non corrélées de V_p, V_s et ρ. La configuration géométrique du modèle est illustrée dans la Figure XI.

Toutes les frontières sont absorbantes.

Nous plaçons 8 sources sismiques espacées régulièrement autour de l'hétérogénéité. Leur fonction source-temps est une ondelette de Ricker. Avec une fréquence centrale de la source de 0.45 Hz (fréquence maximale 1.2 Hz), la longueur d'onde minimale λ_m dans le domaine est d'environ 2260 m. Il faut noter que chaque élément de l'hétérogénéité est d'environ 0.18 fois λ_m.

Nous définissons une fonction d'inadéquation qui prend en compte toutes les parties du sismogramme, puis nous mettons en œuvre le schéma itératif de Gauss-Newton pour minimiser la fonction d'inadéquation.

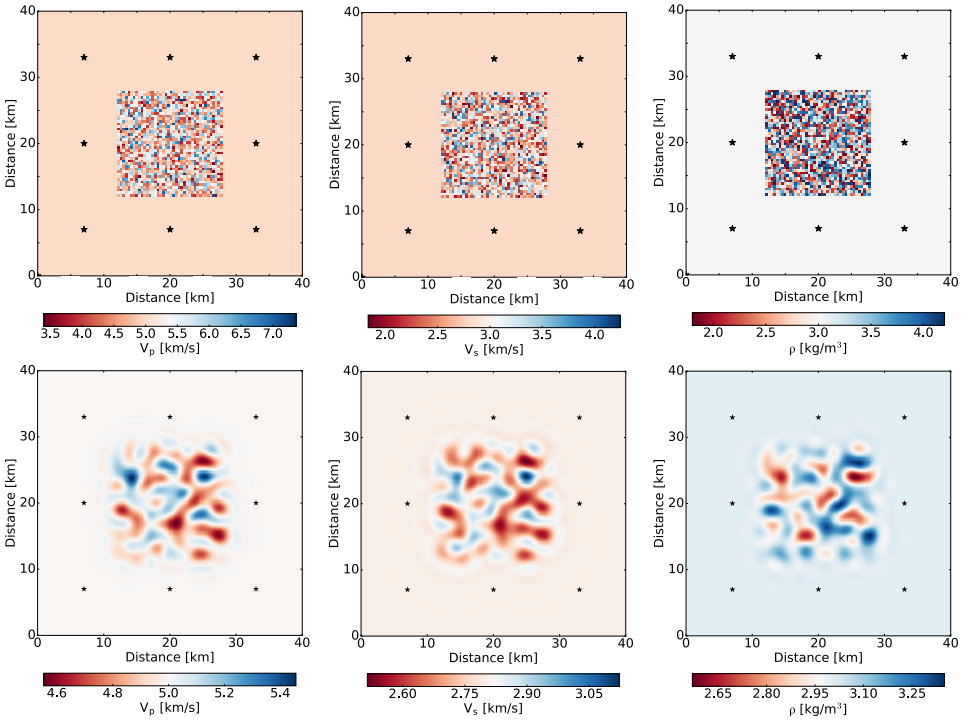

Fig. XI.: En haut : modèle cible brut, en bas : modèle cible homogénéisé avec $\varepsilon = 2$. Le domaine est 40×40 km^2 et l'hétérogénéité au centre est 16×16 km^2. Les étoiles indiquent l'emplacement des sources. Toutes les limites sont absorbantes. A gauche : V_p, au centre : V_s et à droite : ρ dans le domaine. Les vitesses P et S dans le domaine extérieur sont de 5 kms^{-1} et de 3.2 kms^{-1}, et les vitesses pour chaque élément à l'intérieur de l'hétérogénéité sont de $\pm$40% par rapport au domaine environnant.

Nous effectuons deux tests. Pour le premier test, nous plaçons les récepteurs loin de l'hétérogénéité pour comparer l'inversion avec les déplacements à inversion avec les rotations. Pour le second test, nous plaçons les récepteurs près de l'hétérogénéité de sorte que les données de rotation soient affectées par l'hétérogénéité. Pour chaque test, nous commençons notre inversion à partir d'un modèle entièrement homogène dont V_p, V_s et ρ sont respectivement de 5 kms^{-1}, 2.8 kms^{-1} et 3.0 kgm^{-3}. La zone d'inversion est de 18×18 km^2 et s'étend légèrement au-delà de l'hétérogénéité. Elle est divisée en 36×36 éléments, et pour chaque élément, le tenseur élastique $\mathbf{c}$ et la densité ρ sont inversés. Pour le problème direct, nous utilisons un nombre de points GLL de 4 alors que pour l'inversion, nous un seul point GLL. Cela permet de s'assurer que les erreurs de discrétisation sont différentes. En outre, le maillage choisi pour l'inversion ne peut pas représenter avec précision la structure à petite échelle (la taille des éléments pour l'inversion est de $\sim$0.22 λ_m, tandis que la taille de l'hétérogénéité individuelle est de $\sim$0.18 λ_m) et cela garantit que nous n'injectons pas d'informations préalables à travers notre maillage. Par conséquent, nous évitons tout crime d'inversion.

Après convergence, le modèle final est homogénéisé selon la méthode décrite dans la Section I, et on choisit ε=2 pour se concentrer sur les résultats sur les grandes longueurs d'onde ($2\lambda_m$). D'après Capdeville and Métivier (2018), nous comparons la version homogénéisée de nos modèles récupérés avec la version homogénéisée du modèle cible. Nous projetons le tenseur anisotrope $\mathbf{c}$ au tenseur isotrope $\mathbf{c}^{\text{iso}}$ le plus proche suivant Browaeys and Chevrot (2004). Par la suite, V_p, V_s et l'anisotropie totale sont définis comme suit :

$$
\begin{aligned}
V_p &= \sqrt{\frac{c^{\text{iso}}_{1111}}{\rho}}, \\
V_s &= \sqrt{\frac{c^{\text{iso}}_{1212}}{\rho}}, \\
\text{anisotropy} &= \sqrt{\frac{\sum_{ijkl}(c^{\text{iso}}_{ijkl} - c_{ijkl})^2}{\sum_{ijkl}(c^{\text{iso}}_{ijkl})^2}}.
\end{aligned}
$$

Pour valider les résultats de notre inversion, nous montrons des exemples de données d'ajustement au déplacement et de rotation pour les cas où elles n'ont pas été utilisées dans l'inversion. Un bon ajustement entre les données indépendantes du modèle cible et les modèles récupérés implique que nos inversions sont fiables. Pour cela, nous plaçons un récepteur dans le modèle cible à un nouvel endroit, et nous calculons les déplacements et les rotations. Ensuite, nous plaçons le récepteur au même endroit dans les modèles récupérés et nous calculons à nouveau les mesures. Les validations sont effectuées à ε=0.5 pour se concentrer sur la limite de résolution ($\frac{\lambda_m}{2}$).

Notez qu'en 2D, le nombre de composantes de déplacement est deux fois plus élevé que le nombre de composantes de rotation.

Des récepteurs loin de l'hétérogénéité

Le modèle de départ est présenté sur la Figure XII avec les emplacements des récepteurs. Le domaine d'inversion est donné par le carré intérieur noir.

Pour les deux inversions, l'amélioration de la réduction de l'inadéquation est de 99%. Les résultats sont présentés dans la Figure XIV pour V_p, V_s, ρ et l'anisotropie. Ces valeurs sont également représentées dans les modèles sur deux sections transversales. Les valeurs sur la section verticale sont indiquées

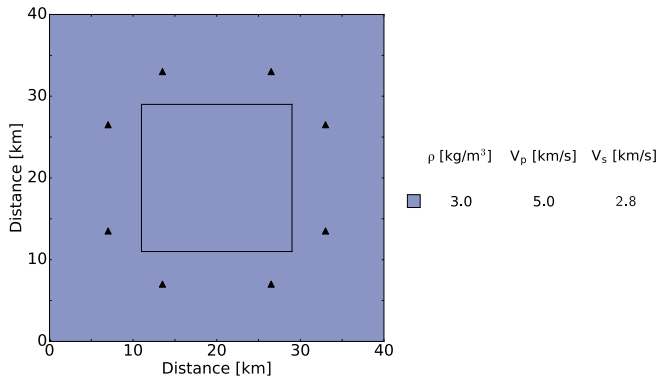

Fig. XII.: Modèle de départ utilisé dans l'inversion de la Section IV. Les triangles indique l'emplacement des récepteurs. Toutes les limites sont absorbantes. Le carré intérieur montre la zone d'inversion.

à droite (lignes rouges) et les valeurs sur la section horizontale sont indiquées sous chaque panneau (lignes rouges). Les valeurs respectives dans le modèle cible homogénéisé sont également indiquées (lignes vertes).

Les coupes transversales de la Figure XIV montrent que l'inversion des déplacements est en accord avec le modèle cible. Cela est moins vrai pour l'inversion avec rotation, où de légères divergences existent. Celles-ci sont plus évidentes dans la section verticale de V_p et V_s. Nous associons cela au nombre de mesures, car si nous doublons le nombre de recepteurs (de sorte que le nombre de mesures de rotation soit égal au nombre de mesures de déplacement), cela améliore les résultats de l'inversion.

Maintenant, les modèles récupérés doivent être validés. Les positions du nouveau récepteur et de la source sont indiquées par le triangle et l'étoile respectivement sur le panneau gauche de la Figure XIV et les mesures sont indiquées sur le panneau droit. Les mesures dans le modèle cible sont indiquées en noir, celles dans le modèle récupéré par déplacement sont indiquées en vert, et celles dans le modèle récupéré par rotation sont indiquées en rouge. Les amplitudes ont été normalisées.

Dans le panneau de droite de XIV, nous pouvons voir que les deux modèles récupérés sont capables de décrire les mesures du modèle cible, ce qui signifie que les deux inversions sont fiables.

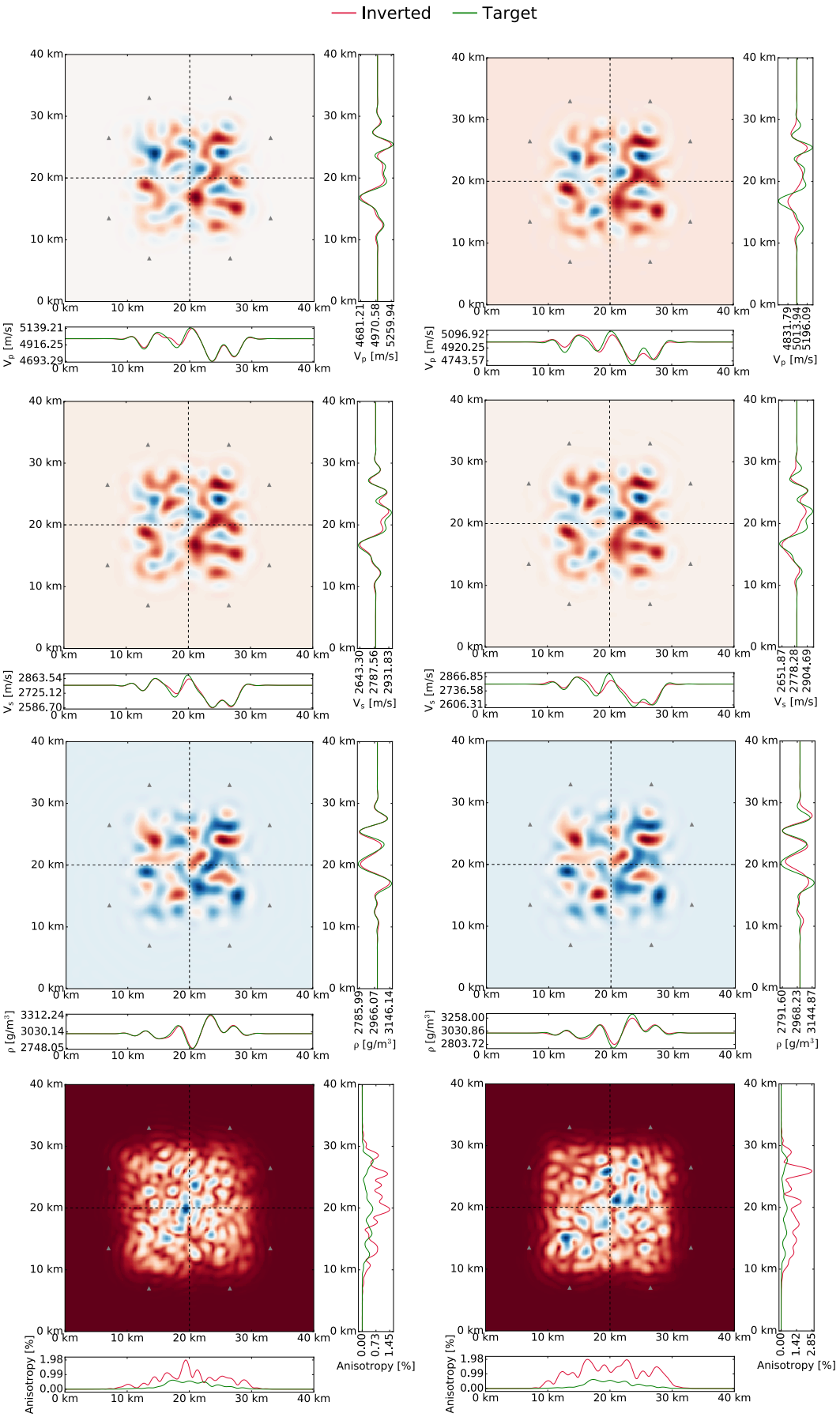

Fig. XIII.: Résultats du premier test. A gauche : inversion avec seulement des déplacements, à droite : inversion avec seulement des rotations. En partant du haut, V_p, V_s, ρ et anisotropie sont affichés. Pour chaque résultat, la coupe transversale le long de la ligne pointillée horizontale est indiquée en dessous et la coupe transversale le long de la ligne pointillée verticale est indiquée à droite. Les coupes transversales respectives le long du modèle cible sont également indiquées en vert.

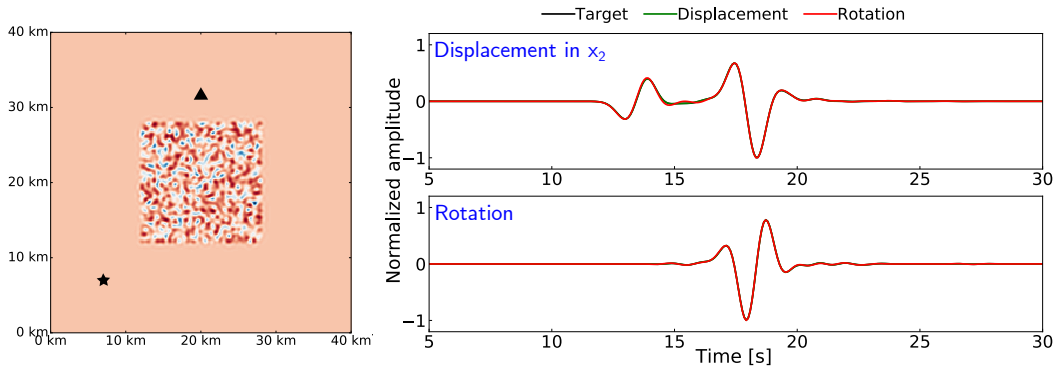

Fig. XIV.: Validation des modèles récupérés. A gauche : Configuration source-récepteur. L'emplacement de la source est donné par l'étoile et l'emplacement du récepteur est donné par le triangle. A droite : Déplacements verticaux (en haut) et rotations (en bas). Les mesures dans le modèle cible sont indiquées en noir, celles dans le modèle récupéré à partir des déplacements sont indiquées en vert, celles dans le modèle récupéré à partir des rotations sont indiquées en rouge.

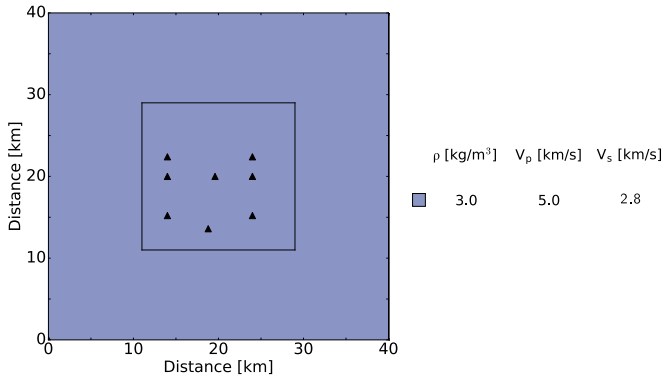

Fig. XV.: Modèle de départ utilisé dans l'inversion de la section IV. Les triangles indique l'emplacement des récepteurs. Toutes les limites sont absorbantes. Le carré intérieur montre la zone d'inversion.

Des récepteurs proches de l'hétérogénéité

Le modèle de départ est présenté sur la Figure XV avec les emplacements des récepteurs. Le domaine d'inversion est donné par le carré intérieur noir.

Une fois de plus, pour les deux inversions, l'amélioration de la réduction de l'inadéquation est de 99%. Les résultats sont présentés dans la Figure XIV pour V_p, V_s, ρ et l'anisotropie. Ces valeurs sont également représentées dans les modèles sur deux sections transversales. Les valeurs sur la section verticale sont indiquées à droite (lignes rouges) et les valeurs sur la section horizontale sont indiquées sous chaque panneau (lignes rouges). Les valeurs respectives dans le modèle cible homogénéisé sont également indiquées (lignes vertes).

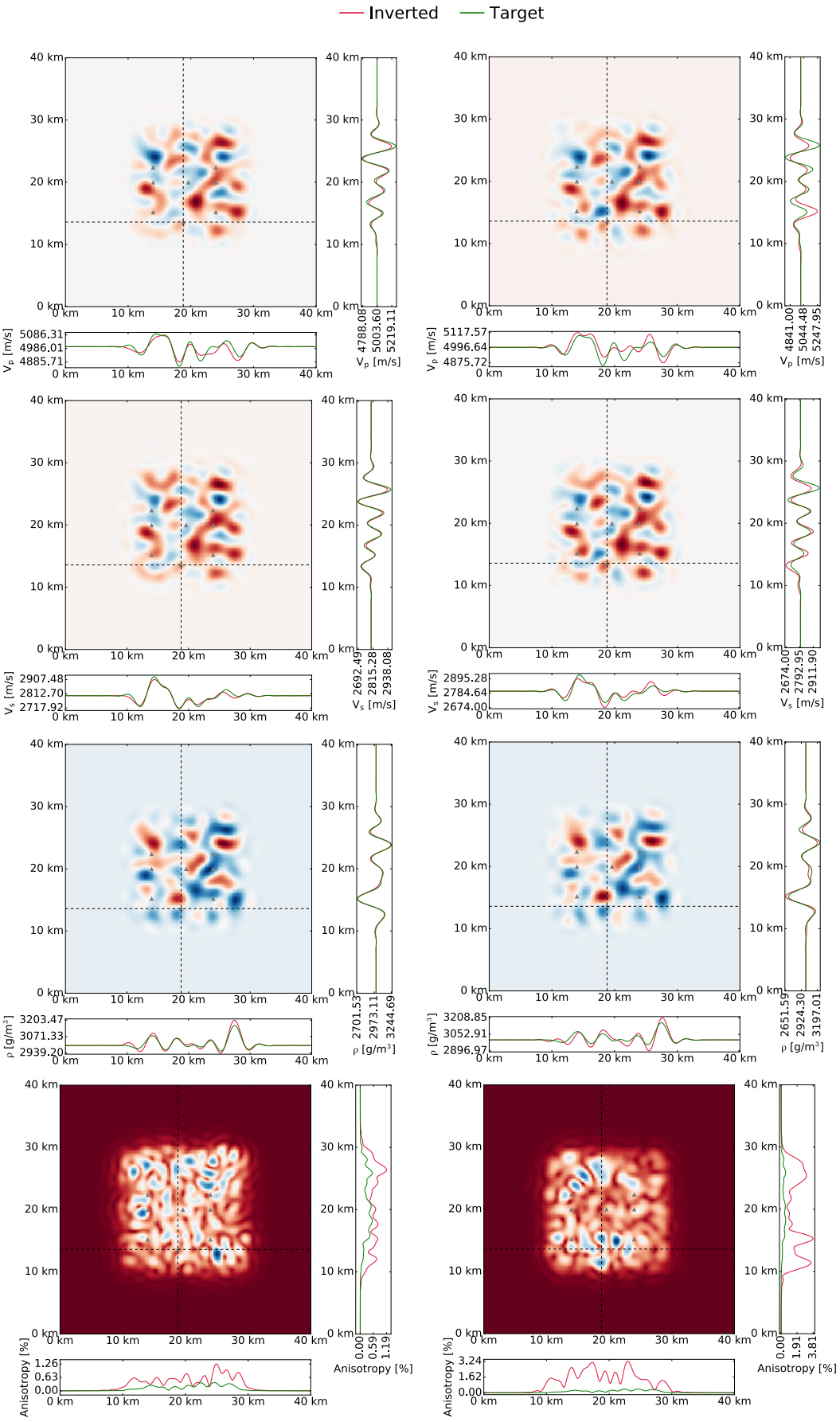

Fig. XVI.: Résultats du premier test. A gauche : inversion avec seulement des déplacements, à droite : inversion avec seulement des rotations. En partant du haut, V_p, V_s, ρ et anisotropie sont affichés. Pour chaque résultat, la coupe transversale le long de la ligne pointillée horizontale est indiquée en dessous et la coupe transversale le long de la ligne pointillée verticale est indiquée à droite. Les coupes transversales respectives le long du modèle cible sont également indiquées en vert.

Une fois de plus, on peut constater que l'inversion des déplacements est en meilleur accord avec le modèle cible par rapport à l'inversion des rotations. Cela est particulièrement évident dans les sections transversales de V_p et V_s. Bien que cela provienne en partie d'une couverture insuffisante, l'augmentation du nombre de récepteurs n'aide pas. Nous attribuons cela à l'effet des structures à petite échelle.

Maintenant, les modèles récupérés doivent être validés. Les positions du nouveau récepteur et de la source sont indiquées par le triangle et l'étoile respectivement sur le panneau gauche de la Figure XVII et les mesures sont indiquées sur le panneau droit. Les mesures dans le modèle cible sont indiquées en noir, celles dans le modèle récupéré par déplacement sont indiquées en vert, et celles dans le modèle récupéré par rotation sont indiquées en rouge. Les amplitudes ont été normalisées.

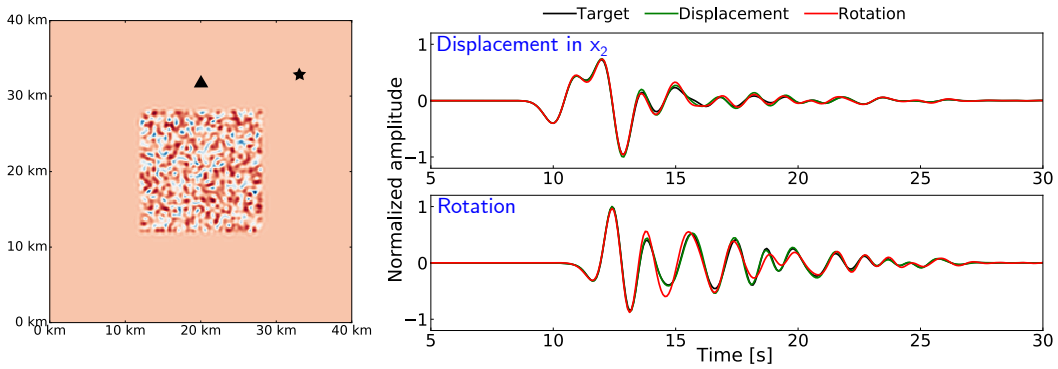

Fig. XVII.: Validation des modèles récupérés. A gauche : Configuration source-récepteur. L'emplacement de la source est donné par l'étoile et l'emplacement du récepteur est donné par le triangle. A droite : Déplacements verticaux (en haut) et rotations (en bas). Les mesures dans le modèle cible sont indiquées en noir, celles dans le modèle récupéré à partir des déplacements sont indiquées en vert, et celles dans le modèle récupéré à partir des rotations sont indiquées en rouge.

Dans le panneau de droite de XVII, nous pouvons voir que le modèle dérivé de la rotation ne représente pas les mesures dans le modèle cible. Par conséquent, le modèle récupéré à partir de la rotation n'est pas fiable.

V Conclusions

Dans ce travail, nous étudions l'effet des structures à petite échelle sur les gradients de champ d'ondes dans le contexte du problème direct et

de l'inversion. Dans le contexte du problème direct, nous montrons que les structures à petite échelle affectent les mesures de gradients de champ d'onde, mais comme l'effet ne dépend pas de la source et du temps, nous pouvons l'expliquer. Dans le contexte du problème inverse, nous montrons que lorsque les récepteurs sont placés à proximité des structures à petite échelle, c'est-à-dire lorsque leurs mesures sont affectées par les structures, le modèle qui est récupéré n'est pas correct. Nous étudions actuellement si l'ajout de correcteurs pendant l'inversion aide à récupérer le modèle correct. Avec ce travail, nous espérons faire progresser la sismologie vers l'utilisation des trois mouvements.

1 Seismology 101

It is a tranquil Sunday morning. What sounds can your ears pick up? Perhaps your favourite music playing from across the room, the chirping of birds and rustling of wind outside, or the ringing of distant church bells.

Seismology is basically listening to what happens inside planets. Seismometers placed on the surface of planetary bodies are like ears that record waves generated by seismic sources. These measurements help in understanding earthquake processes, seismic cycles and crustal deformations of the planet; analysing disasters such as landslides and volcanic eruptions; and ultimately quantifying seismic hazards. Modelling of this aspect is referred to as the forward problem in seismology. And in a manner akin to how the sound recorded by the ears is used to locate its source and direction, those seismic measurements can be used to constrain the location of the seismic source; image the structure of the interior of the planet; and explore for hydrocarbon reserves. This aspect is referred to as the inverse problem in seismology.

A brief description of each aspect follows below.

1.1 The Forward Problem

The forward problem can be summarized by the cartoon 1.1, or by the equation

$$\mathbf{d} = \mathbf{G}\mathbf{m}. \tag{1.1}$$

Through it, we try to determine the data or seismic observables $\mathbf{d}$ for any given model $\mathbf{m}$ via a relationship G. In seismology, the relationship is usually the elastic wave equation. Here, we follow Lay and Wallace (1995) and Shearer (2019) to derive this elastic wave equation. We adopt a Cartesian co-ordinate system and the Lagrangian description of motion, where we follow the motion of a particle as a function of space and time.

We start with describing how forces can be applied to any solid body. Forces can either be applied to the boundary of the body, or in its interior. Some

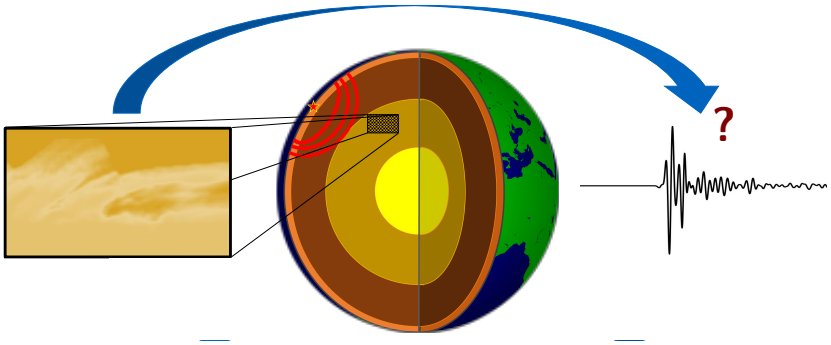

Fig. 1.1.: The forward problem. [1]

examples of the former are contact forces, fluid pressures and some examples of the latter are gravitational forces. Traction is the term used to describe the force acting on any surface (real or imaginary) per unit area of the body.

At any arbitrary point in the body, there can be an infinite number of planes passing through it and therefore, it can have an infinite number of tractions associated to it. Fortunately, a complete description of the forces at any arbitrary point in the body requires only knowing the tractions at three perpendicular planes passing the point. This can be achieved by using the stress tensor $\boldsymbol{\sigma}$ where for instance, the ij component of the stress tensor $\boldsymbol{\sigma}$ represents the traction in the direction j on a plane with normal in the direction $\mathbf{e}_i$.

Because the sum of forces acting on a solid body in static equilibrium must be 0, $\frac{\partial \sigma_{ij}}{\partial x_i} = 0$. Similarly, since it cannot have any net moment, the stress tensor is symmetric, i.e. contains only six independent elements.

$$\boldsymbol{\sigma} = \begin{bmatrix} \sigma_{ii} & \sigma_{ij} & \sigma_{ik} \\ \sigma_{ij} & \sigma_{jj} & \sigma_{jk} \\ \sigma_{ik} & \sigma_{jk} & \sigma_{kk} \end{bmatrix}. \tag{1.2}$$

Next, we need to define absolute changes in positions within the body. Let us consider that a reference point P in the body has been displaced by the displacement $\mathbf{u}(x_0; t)$ to a position P'. And that another point Q has also been displaced to its new position Q' via its displacement $\mathbf{u}(x; t)$ [see Cartoon 1.2].

[1] Modified from `https://mediatum.ub.tum.de/node?id=1232040`; Last Accessed on September 29, 2020

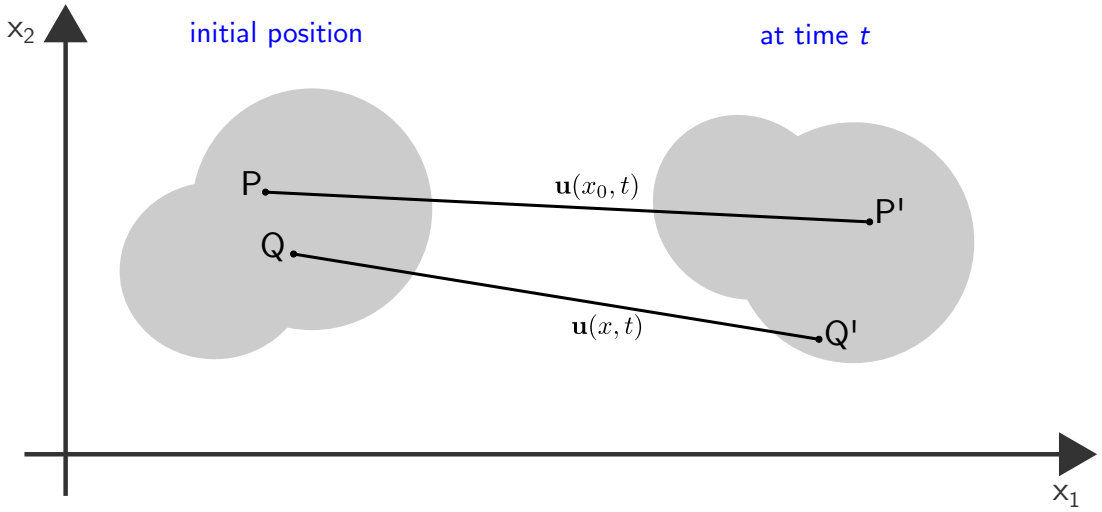

Fig. 1.2.: Left: initial position of a particle within the body. Right: its position at a time t.

Assuming that the distance $\mathbf{s}$ between the two points is small, the displacement $\mathbf{u}(x;t)$ can be related to the displacement $\mathbf{u}(x_0;t)$ using Taylor series.

$$\begin{aligned}\mathbf{u}(\mathbf{x};t) =& \mathbf{u}(\mathbf{x_0};t) + \begin{bmatrix} \frac{\partial u_i}{\partial x_i} & \frac{\partial u_i}{\partial x_j} & \frac{\partial u_i}{\partial x_k} \\ \frac{\partial u_j}{\partial x_i} & \frac{\partial u_j}{\partial x_j} & \frac{\partial u_j}{\partial x_k} \\ \frac{\partial u_k}{\partial x_i} & \frac{\partial u_k}{\partial x_j} & \frac{\partial u_k}{\partial x_k} \end{bmatrix} \begin{bmatrix} s_{x_i} \\ s_{x_j} \\ s_{x_k} \end{bmatrix} \\ =& \mathbf{u}(\mathbf{x_0};t) + \mathbf{E}\mathbf{s}\end{aligned}$$

Note that higher-order terms in the expansion have been ignored following the assumption that the partial derivatives are small enough for their products to be ignored. This approximation is valid in seismology since we are always dealing with very small deformations, i.e. in the order of 10^{-6} in far-field.

The second-order tensor $\mathbf{E}$ can be decomposed into a symmetric part $\boldsymbol{\epsilon}$ and an antisymmetric part $\boldsymbol{\Omega}$, with

$$\boldsymbol{\epsilon} = \begin{bmatrix} \frac{\partial u_i}{\partial x_i} & \frac{1}{2}\left(\frac{\partial u_i}{\partial x_j} + \frac{\partial u_j}{\partial x_i}\right) & \frac{1}{2}\left(\frac{\partial u_i}{\partial x_k} + \frac{\partial u_k}{\partial x_i}\right) \\ \frac{1}{2}\left(\frac{\partial u_j}{\partial x_i} + \frac{\partial u_i}{\partial x_j}\right) & \frac{\partial u_j}{\partial x_j} & \frac{1}{2}\left(\frac{\partial u_j}{\partial x_k} + \frac{\partial u_k}{\partial x_j}\right) \\ \frac{1}{2}\left(\frac{\partial u_k}{\partial x_i} + \frac{\partial u_i}{\partial x_k}\right) & \frac{1}{2}\left(\frac{\partial u_k}{\partial x_j} + \frac{\partial u_j}{\partial x_k}\right) & \frac{\partial u_k}{\partial x_k} \end{bmatrix},$$

$$\boldsymbol{\Omega} = \begin{bmatrix} 0 & \frac{1}{2}\left(\frac{\partial u_i}{\partial x_j} - \frac{\partial u_j}{\partial x_i}\right) & \frac{1}{2}\left(\frac{\partial u_i}{\partial x_k} - \frac{\partial u_k}{\partial x_i}\right) \\ \frac{1}{2}\left(\frac{\partial u_j}{\partial x_i} - \frac{\partial u_i}{\partial x_j}\right) & 0 & \frac{1}{2}\left(\frac{\partial u_j}{\partial x_k} - \frac{\partial u_k}{\partial x_j}\right) \\ \frac{1}{2}\left(\frac{\partial u_k}{\partial x_i} - \frac{\partial u_i}{\partial x_k}\right) & \frac{1}{2}\left(\frac{\partial u_k}{\partial x_j} - \frac{\partial u_j}{\partial x_k}\right) & 0 \end{bmatrix}.$$

$\boldsymbol{\epsilon}$ is the strain tensor that contains six independent elements while $\boldsymbol{\Omega}$ is the rotation tensor that contains three independent elements.

The relationship between stress and strain for any elastic medium is given by the constitutive relation or the generalized Hooke's law, which is

$$\sigma_{ij} = c_{ijkl}\epsilon_{kl}. \tag{1.3}$$

This relationship assumes perfect elasticity, i.e. no energy loss during the deformation, which is not valid for example, near earthquake sources where fracturing has happened and deformation is permanent. Here, c_{ijkl} is called the elastic tensor. It is a fourth-order tensor with 81 independent elements. However, because the stress and strain tensors are symmetric, the number of independent elements is reduced to 21. To first-order, most of the Earth's interior can be approximated as isotropic. Under the assumption of isotropy, the number of independent elements further reduces to 2.

$$c_{ijkl} = \lambda\delta_{ij}\delta_{kl} + \mu(\delta_{il}\delta_{jk} + \delta_{ik}\delta_{jl}), \tag{1.4}$$

where λ and μ are the independent elements of the elastic tensor and are called Lamé parameters, and δ is the Kronecker delta function.

Finally, we consider the force balance of the body that is undergoing internal motion. We use the Newton's second law of motion to get the equation of motion.

$$\rho\ddot{u}_i = f_i + \frac{\partial\sigma_{ij}}{\partial x_j}. \tag{1.5}$$

Here, ρ is the density of the body, and f is the body force per unit volume acting on it. In cases where body forces can be neglected, for example, for high frequency cases when gravity can be neglected, we get the homogeneous equation of motion,

$$\rho\ddot{u}_i = \frac{\partial\sigma_{ij}}{\partial x_j}. \tag{1.6}$$

Now, using (1.3) and (1.4) in (1.6) along with some vector simplifications, we get,

$$\rho\ddot{\mathbf{u}} = \nabla\lambda(\nabla.\mathbf{u}) + \nabla\mu.[\nabla\mathbf{u} +^t (\nabla\mathbf{u})] + (\lambda + 2\mu)\nabla\nabla.\mathbf{u} - \mu\nabla\times\nabla\times\mathbf{u}. \tag{1.7}$$

If the gradient terms are ignored, which is often done in ray-based methods in seismology, we arrive at the momentum equation for the homogeneous media.

$$\rho\ddot{\mathbf{u}} = (\lambda + 2\mu)\nabla\nabla.\mathbf{u} - \mu\nabla\times\nabla\times\mathbf{u}. \tag{1.8}$$

This is the seismic wave equation, but we emphasize once again that this equation has its approximations of homogeneity, linearity and isotropy.

From source to the ears (Seismic Observables)

The seismic wave equation allows us to study how waves travel from the seismic source and how they can be measured at the receivers. According to Aki and Richards (1980, 2002), we can measure the following motions at the receivers.

1. Translations define changes where every point in the body moves by the same vector.

$$u_i$$

2. Strains define motions due to the symmetric portion of the strain tensor.

$$\epsilon_{ij} = \frac{1}{2}(\partial_i u_j + \partial_j u_i)$$

3. Rotations define motions due to the skew-symmetric portion of the strain tensor.

$$\omega_{ij} = \frac{1}{2}(\partial_i u_j - \partial_j u_i)$$

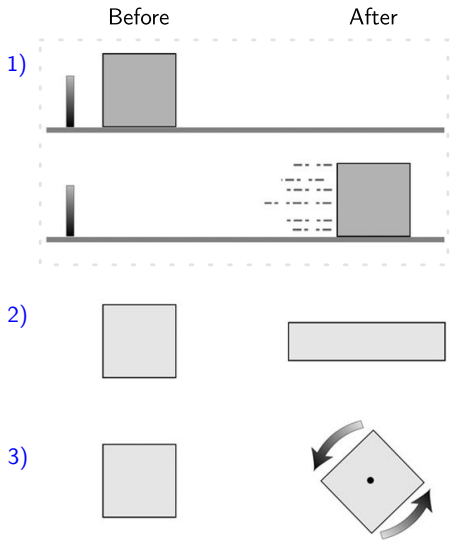

Fig. 1.3.: The seismic observables. 1) Translation, 2) Strain, and 3) Rotation. [2]

Rigid translations are absolute measures of position changes. Strains and rigid rotations are relative measures of the position changes, hence they are assembled from displacement gradients. In this work, I choose to use the term 'wavefield gradients' for both strains and rotations.

To assess any ground motion completely, the six components of strain and the three components of rotation are as important as the three components of translation (Aki and Richards, 2002). Concurrent measurements of all three kinds of motions also help us remove the coupling that one motion

[2] Modified from `https://www.slideserve.com/aric/general-geology-crustal-deformation`; Last Accessed on September 29, 2020

introduces on the other, for example, horizontal rotations on translation (Aki and Richards, 2002, p. 604) and vertical rotation on translation (Trifunac and Todorovska, 2001; Graizer, 2009). Similarly, wavefield gradients are necessary in earthquake engineering to assess seismic hazards (Trifunac, 1982; Abdel-Ghaffar and Rubin, 1984; Castellani and Boffi, 1989; Basu et al., 2015).

While instruments to measure translations evolved from simple pendulum instruments (Milne, 1888) to ocean-bottom seismometers (Sutton and Duennebier, 1987; Lázaro et al., 2012), geophones (McCarter, 1956; Lawton and Bertram, 1990), and broadband seismometers (Owens et al., 1993; Wielandt and Steim, 1986); strains and rotations were were primarily estimated using dense arrays (Spudich et al., 1995; Bodin et al., 1997; Huang, 2003) because seismic instruments to measure them were either not reliable enough or sensitive enough in the required frequency bands. Nowadays, rotations can be measured using liquid-based motion sensors (Huang et al., 2013; Egorov et al., 2015), magneto-hydrodynamic sensors (Pierson et al., 2016), ring laser gyroscopes (McLeod et al., 1998; Pancha et al., 2000; Schreiber et al., 2009), mechanical sensors (Brokešová and Málek, 2013) and more recently, using fiber-optic gyroscopes (Kurzych et al., 2014; Lindner et al., 2016; Bernauer et al., 2018). Similarly, strains can be measured using laser strainmeters (Berger and Lovberg, 1970; Goulty et al., 1974), Distributed Acoustic Sensing (DAS) (Willis et al., 2016) and Distributed Vibration Sensing (DVS) (Dean et al., 2017). These instruments now make it possible to obtain more reliable data that can be exploited.

1.2 The Inverse Problem

In seismology, the inverse problem as shown by cartoon 1.4 deals with estimating the model $\mathbf{m}$ from the observed data $\mathbf{d_{obs}}$:

$$\mathbf{m} = \mathrm{G}^{-1}(\mathbf{d_{obs}}). \tag{1.9}$$

In rare cases, it is straight forward to calculate $\mathbf{m}$, for example, when the Herglotz-Wiechert formula is used to invert the travel times (Herglotz, 1907; Wiechert, 1907). As far as we are concerned, our forward problem is non-

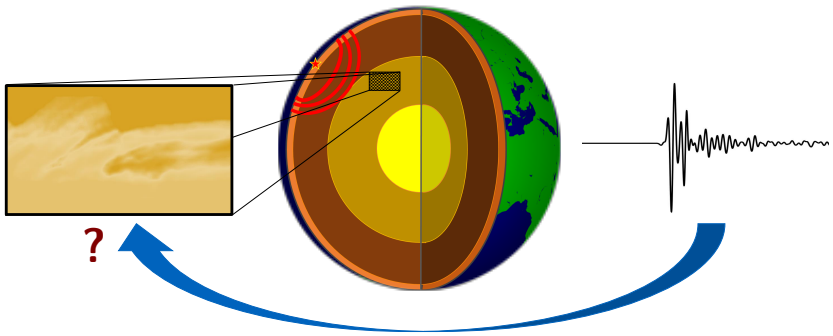

Fig. 1.4.: The inverse problem. [3]

linear, our theory is incomplete and our measurements are often inconsistent, meaning we cannot compute G^{-1}. This forces us to construct a workaround: we wish for a model $\mathbf{m}$ that produces the synthetic data $\mathbf{d}$ that is as close to the $\mathbf{d_{obs}}$ as possible when the wave operator G is applied to it. As such, we could simply define a misfit functional that quantifies the difference between the synthetic data $\mathbf{d}$ and the observed data $\mathbf{d_{obs}}$. In other words, our goal is to minimize the misfit functional

$$\phi(\mathbf{m}) = \|\mathbf{d} - \mathbf{d_{obs}}\|_{\mathrm{L2}} + \alpha\|\mathbf{m} - \mathbf{m_0}\|_{\mathrm{L2}}. \tag{1.10}$$

The first term on the right hand side of (1.10) denotes the data misfit, while the second term introduces the apriori knowledge we have on our model through $\mathbf{m_0}$. α is a regularization term that allows us to favour certain terms over the other, depending on our apiori knowledge.

Ideally, the entire misfit space should be explored to determine where in the space the misfits low are (convergence rate), how many number of minima there are (global vs local minima), and how large their widths are (error estimation). This can be discouraging in seismology because the forward problem is computationally expensive and the number of parameters is large. Despite this, probabilistic approaches have shown promise (Resovsky and Trampert, 2003; Bodin and Sambridge, 2009; Mosca et al., 2012; Käufl et al., 2013).

When exploring the entire misfit space is not possible, one could take advantage of the misfit function and its gradient to find out the direction in which the misfit function decreases, thereby updating the model successively until a certain acceptance criteria is reached. The underlying assumption

[3] Modified from `https://mediatum.ub.tum.de/node?id=1232040`; Last Accessed on September 29,2020

in deterministic inversions such as these is that this minimum is indeed the global minimum.

Expanding the misfit function in a Taylor series, we get,

$$\phi(\mathbf{m} + \delta\mathbf{m}) = \phi(\mathbf{m}) + \delta\mathbf{m}\nabla_m\phi(\mathbf{m}) + \frac{1}{2}\,{}^t\delta\mathbf{m}\;\mathbf{H}\;\delta\mathbf{m}, \tag{1.11}$$

where $\mathbf{H}$ is the second-derivative matrix. A minimum with respect to $\delta\mathbf{m}$ happens when its gradient is 0, therefore at

$$\delta\mathbf{m} = -\mathbf{H}^{-1}\nabla_m\phi. \tag{1.12}$$

This is the basis for Newton's method, which converges quadratically. Although this is feasible in theory, the computation of the full Hessian matrix is in practice expensive due to its size. Fortunately, we can substitute the Hessian with an approximate Hessian. The simplest strategy is employed in the steepest-descent method, where the Hessian is approximated as an identity matrix. The model updates are thus in the direction of the steepest descent. Other methods employed are the Gauss-Newton Method, where the Hessian in the Newton method is substituted with the approximate Hessian; or the conjugate gradient, where the use an optimal step length for the descent ensures that the convergence is reached within a finite number of iterations, which is the dimension of the model space.

From ears to the source and medium properties (Inversion with wavefield gradients)

Collocated measurements of motions can be of great benefit for seismology because they allow us to retrieve instantaneous slowness without using travel times (Mikumo and Aki, 1964; Igel et al., 2005, 2007; Fichtner and Igel, 2009; Bernauer et al., 2012; Edme and Yuan, 2016; Wassermann et al., 2016), to constrain seismic source properties (Takeo and Ito, 1997; Bernauer et al., 2014; Reinwald et al., 2016; Donner et al., 2016, 2017) and to estimate parameters like propagation direction (Cochard et al., 2006; Igel et al., 2007) and rupture history (Takeo and Ito, 1997). Further applications of collocated measurements have been discussed for example, in Schmelzbach et al. (2018), Li and van der Baan (2017), Igel et al. (2015) and Zhan (2019).

Wavefield gradients themselves are important to deduce the stresses caused by seismic waves (Spudich et al., 1995) and to enable S wave interpretation (Sollberger et al., 2016).

1.3 Motivation and Problem Statement

The wavefield and its gradients together provide a plethora of seismic information. Hence, all three motions should be studied in seismology but this was not the case up until recently.

Although considerable effort has been put into devising more robust and portable instruments lately, little attention has been paid to yet another issue concerning wavefield gradients. It has been shown that local small-scale heterogeneities, such as cavities and discontinuities, topographies as well as geological heterogeneities strongly affect strain (Berger and Beaumont, 1976; Sato and Harrison, 1989; Gomberg and Agnew, 1996) and rotation (King and Bilham, 1973; Harrison, 1976; Baker, 1980; Kohl and Levine, 1995; van Driel et al., 2012). This effect of heterogeneities on wavefield gradient is measurable with our current sensors and leads to a number of consequences, such as 1) disagreement between wavefield gradient data and synthetics computed in a tomographic model, 2) dissimilarity between wavefield gradients measured at a point and wavefield gradients estimated at the point using an array, and 3) discrepancy between data observed among closely-spaced instruments. Such consequences may lead to an erroneous interpretation of the data. This is critical because we are ignorant of details on the crust down to the geologic structure, let alone the atomic one. [4]

The purpose of this work is threefold. First, we study why wavefield gradients are affected by local small-scale heterogeneities. This will help us understand how a wavefield and its observables really interact with heterogeneities on all scales, which will eventually help us in better interpreting seismic data. Second, we investigate if it is possible to correct wavefield gradients for this effect. This will ensure a better agreement between wavefield gradient data and the synthetics that have been corrected. This will also help align the wavefield gradients measured at a point and wavefield gradients estimated

[4] And who is to say that atomic structure is where it all ends? Check out the Standard Model at `https://home.cern/science/physics/standard-model`; Last Accessed on September 29, 2020

at the point using an array. Finally, we examine if wavefield gradients help improve Full Waveform Inversions (FWI) in terms of accuracy and resolution, and whether the effect of small-scale heterogeneities impact these.

1.4 Thesis Structure

Chapter 2 describes the basic theoretical foundations of homogenization, which deals with recovering effective results for systems that have also small-scale structures. This is necessary to understand and compare the effect of small-scale structures on wavefield and on wavefield gradients.

Chapter 3 introduces the effect of sub-wavelength structures on wavefield gradients in more detail. The brief numerical examples presented in this chapter are intended as a showcase of the effect of sub-wavelength structures on wavelength gradients.

Chapter 4 applies a method to correct for the effect using the theory of homogenization. With the help of numerical examples and real data measured at the G-Ring laser, I show that the effect of sub-wavelength structures on wavefield gradients can be accounted for.

Chapter 5 harnesses the effect on wavefield gradients to map the small-scale structures. Using a dense array of wavefield gradients, I show that it is possible to locate geological boundaries.

Chapter 6 investigates if there is an improvement on accuracy and resolution when FWI are performed with wavefield gradients instead of the conventional displacements. Through synthetic examples, we compare inversions for cases when the receivers are placed far away and in the proximity of small-scale structures.

Chapter 7 provides a synthesis of all that has been done in this thesis and includes an outlook on potential future research works that can be carried out.

A modified form of Chapters 3 and 4 has been published in the Geophysical Journal International in 2019. A publication for the contents of Chapter 6 is in preparation. f

2 Homogenization

The theory of homogenization deals with obtaining macroscopic, or homogenized or effective equations for systems with microscopic structures. In seismology, a microscopic medium is characterized by variations in elastic properties at scales much smaller than the minimum wavelength in the medium. By using homogenization, all these microscopic structures are smoothened out, i.e. the medium with rapidly-varying structures can be substituted with another where the structures are only slowly-varying.

Therefore, homogenization is used both in the forward problem to study wave propagation in a fine-layered media (Backus, 1962), to allow sparser meshing to gain computational speed (Capdeville et al., 2010b; Guillot et al., 2010; Cupillard and Capdeville, 2018) as well as in the inverse problem to help interpret the results of full waveform inversion (Capdeville and Métivier, 2018).

We begin the chapter with the applications of homogenization in the framework of forward and inverse problems in Sections 2.1 and 2.2. Then, we move on to a concise mathematical derivation of the two-scale homogenization problem in Sections 2.3, 2.4 and 2.5. We conclude the chapter with an overview on other possible homogenization methods.

2.1 Homogenization in context of the forward problem

When solving the wave equation from Section 1.1 numerically, the approach is usually meshing the medium and then solving the wave equation using a solver. When the medium that we want to be modelled is complex, i.e. contains structures at scales much smaller than the minimum wavelength, two problems may arise. Since all discontinuities must be honoured by a mesh for accuracy reasons, it may be impossible to design the mesh. In cases when mesh generation is not a problem, structures with small-scales and thus,

smaller mesh size induces a higher numerical cost because of the Courant criteria (Courant et al., 1928) that needs to be met:

$$\Delta t \leq \mathrm{C}\left[\frac{\Delta x}{\mathrm{V_p}}\right]_{min},$$

where Δt denotes the time step of the computation, C is a constant which depends on the method used to solve the wave equation, Δx is the mesh size and $\mathrm{V_p}$ is the P wave velocity in the medium. This implies that everywhere, where the mesh size is not the smallest, is oversampled.

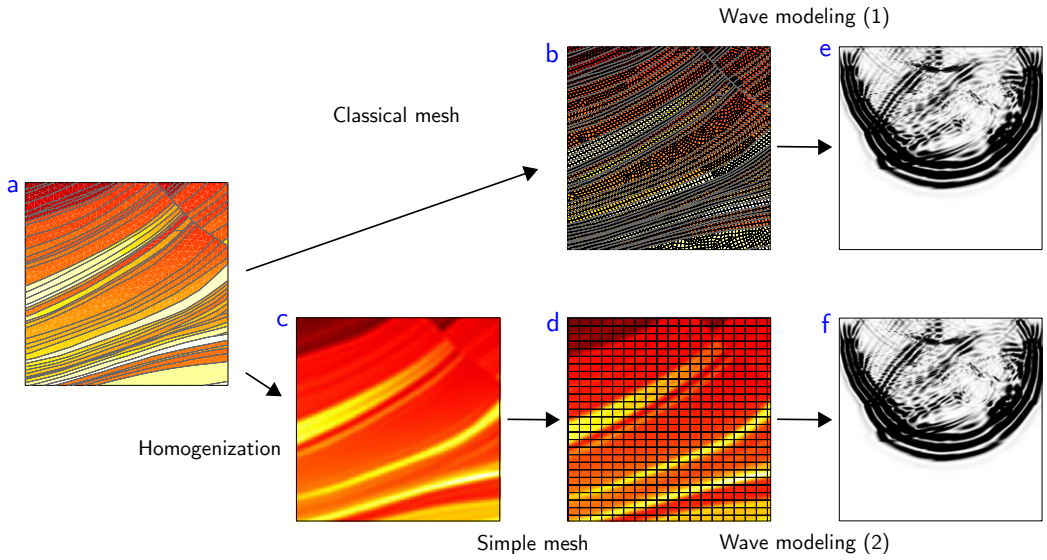

Fig. 2.1.: The concept of homogenization illustrated on a part of the Marmousi2 model [1]

Homogenization can be used as a preprocessing step in the approach. The concept has been demonstrated in Figure 2.1. When all the small-scale structures are smoothened out, the meshing becomes simpler because a regular mesh suffices. This also allows for lower computational costs while producing the same waveform as in the original medium up to a desired accuracy. This has been shown by Capdeville et al. (2010a) for 1D case, Capdeville et al. (2010b) and Guillot et al. (2010) for 2D P-SV and SH case respectively and Cupillard and Capdeville (2018) for the 3D case. For instance, Capdeville et al. (2010b) showed that solving the wave equation numerically for a part of the Marmousi2 model (Martin, 2004; Martin et al., 2006) which would ordinarily take seven days could be done within an hour with homogenization. Similarly, in Cupillard et al. (2019), the wave propagation in the

[1] Modified from Capdeville et al. (2015)

SAGE-EAGE overthrust structure that takes ∼13 days to compute could be done in over an hour in the homogenized case. Homogenization thus helps in the macroscopic analysis of the media with small-scale structures.

Burgos et al. (2016) used homogenization to study how sources close to small-scale structures interact with them. They showed that the moment tensor of an explosion type source may have a deviatoric contribution due to its interaction with surrounding heterogeneities. This generates phases that are not expected from an explosion but have been cited (Press and Archambeau, 1962; Vavryčuk and Kim, 2014). Furthermore, through moment tensor inversions using low frequencies, it is not the true moment tensor but the effective moment tensor that is accessible.

Boundaries and topographies have also been treated in Capdeville et al. (2010a) and Capdeville and Marigo (2012) respectively.

2.2 Homogenization in context of the inverse problem

It was accepted early on that seismic anisotropy can also be induced when heterogeneous isotropic media are sampled by waves whose wavelengths are much larger than the scale at which the heterogeneity varies (Backus, 1962; Babuška and Cara, 1991; Maupin and Park, 2007; Fichtner and Igel, 2008). Therefore, whether a medium is heterogeneous or anisotropic depends on the scale at which its properties are analysed. This is relevant for the Earth because crustal structures have been shown to produce apparent anisotropy in the mantle (Bozdağ and Trampert, 2008; Ferreira et al., 2010). This apparent anisotropy is indistinguishable from the intrinsic anisotropy emanating from for example, Lattice Preferred Orientation (LPO), also known as Crystallographic Preferred Orientation (CPO)(Levshin and Ratnikova, 1984). It follows that any interpretation of anisotropy in terms of LPO must be proceeded with caution.

Following these, Fichtner et al. (2013a) used homogenization to analyse if this apparent anisotropy can be separated from the intrinsic one but concluded that current seismic observables only provide weak constraints on their distinction. Additional data from geodynamics, topography, gravity and/or

scattered waves are required to be able to interpret anisotropy in terms of LPO. Similarly, Alder et al. (2017) investigated the relation between the amplitude of the heterogeneities and the extent of induced radial anisotropy. They showed that the anisotropy increases with the square of the amplitude of the heterogeneities. As a consequence, the apparent anisotropy in seismic tomography can be substantial. Similar studies on anisotropy have been carried out by Wang et al. (2013); Bodin et al. (2015); Faccenda et al. (2019).

Similar to anisotropy, structures that cannot be mapped by seismic wavelengths emerge as attenuation at second order (Ricard et al., 2014).

Since tomographic models differ in their parametrizations, regularizations and data set used, and each model inherits an imprint of this, it is not straightforward to merge the models in order to achieve global convergence across all models and scales. Afanasiev et al. (2015) discussed the advantage of homogenization in assimilating these models. Likewise, Afanasiev et al. (2016) formulated seismic inversion as a constrained optimization problem, such that properties of the model at low frequencies are preserved when updates are made at the higher frequencies. Fichtner et al. (2013b) developed a full waveform inversion method that incorporates seismic data on a wide range of scales by breaking up a multiscale Earth model into various single-scale models using homogenization. Advantages include ability to resolve structures at various scales simultaneously while still employing information from the entire seismogram within reasonable computational bounds.

Considering that out true models depend on all scales but our inversions are usually performed in a limited frequency band[2] and are therefore, accompanied by a certain resolution, it is obvious one cannot access the true multiscale model with inversion. This also makes our inverse problem non-unique. Provided that our data is not suffering from noise or poor coverage, Capdeville and Métivier (2018) and Capdeville et al. (2013) show that the result obtained from inversion is the homogenized version of the true model. Otherwise, the result is a degraded version of the homogenized model. Fur-

[2]Even the term "full-waveform inversion" can be misleading because in fact, we can never use the full waveform for inversion. Our receivers are not capable of recording seismic waves in the full frequency band. Even if, we perform full-waveform inversion in selected windows such that our measurements exceed the noise level and our effort is sensible. Furthermore, we do not invert for the full viscoelastic wave equation, but only for a small subset of parameters as mentioned in Section 1.1.

thermore, inverting for the homogenized model instead of the true model renders the inversion problem unique. Despite this, the model derived from inversion is poorly suited to interpretation. Interpretation is better when left for a stage called dehomogenization or downscaling that comes after inversion and tries to find a set of all possible models with small-scale structures using some apriori information (Hedjazian et al., 2020).

2.3 Homogenization for the 2D periodic media

Here, we give an intuitive construction of the homogenization problem using the method of two-scale expansion. For simplicity, we consider an infinite 2D periodic media (to avoid the treatment of boundary conditions here but handling of boundary conditions have been discussed in Capdeville and Marigo (2007) and Capdeville and Marigo (2008)) where the properties repeat after a certain grid interval $\mathbf{Y}$.

The wave equation is defined as

$$\begin{aligned} \rho\partial_{tt}\mathbf{u} - \nabla.\boldsymbol{\sigma} &= \mathbf{f}, \\ \boldsymbol{\sigma} &= \mathbf{c} : \boldsymbol{\epsilon}(\mathbf{u}), \end{aligned} \tag{2.1}$$

and its initial and boundary conditions. Here, $\mathbf{u}$ is the displacement; $\mathbf{f}$ is the external source; ρ and $\mathbf{c}$ the density and elastic tensor in the medium; and $\boldsymbol{\sigma}$ and $\boldsymbol{\epsilon}(\mathbf{u}) = \frac{1}{2}(\nabla\mathbf{u} +^t \nabla\mathbf{u})$ are the stress and the strain tensors. Note that this is a more general form of (1.8) because isotropy has not been assumed.

We begin the problem by first mathematically distinguishing between small-scales and large-scales. Since most geophysical media have no clear scale separation, we do this by manually assigning a scale-separation λ. All spatial variations of the wavefield below λ are considered small-scales whereas all those above λ are considered large-scales. Accordingly, we introduce the parameter ε,

$$\varepsilon = \frac{\lambda}{\lambda_m}, \tag{2.2}$$

where λ_m denotes the minimum spatial wavelength of the wavefield $\mathbf{u}$. [3]

To separate large scales from small scales explicitly, we introduce a new space variable $\mathbf{y}$,

$$\mathbf{y} = \frac{\mathbf{x}}{\varepsilon}. \tag{2.3}$$

$\mathbf{y}$ represents all the small-scales and $\mathbf{x}$ represents all the large-scales. The relationship between λ, λ_m, $\mathbf{x}$ and $\mathbf{y}$ is demonstrated in the Cartoon 2.2. An example of separation of large-scale variations and small-scale variations for a function in Figure 2.3 is shown in Figure 2.4. A word of caution for this separation: this simple example illustrates a linear filtering. For homogenization, the filtering is non-linear and thus, not this simple.

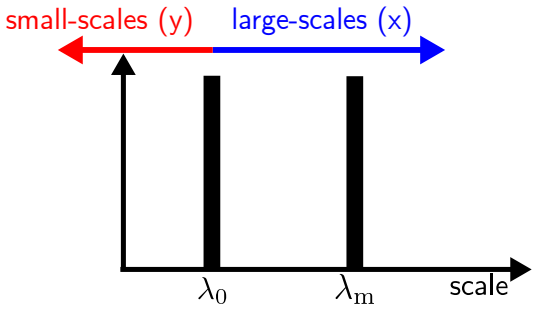

Fig. 2.2.: Cartoon showing the relation between λ, λ_m, $\mathbf{x}$ and $\mathbf{y}$.

Since any change in $\mathbf{y}$ induces only a very small change in $\mathbf{x}$, it is assumed that $\mathbf{x}$ and $\mathbf{y}$ can be treated as independent variables. This two-scale assumption can be mathematically justified by demonstrating its convergence towards the solution of a one-scale variable (Allaire, 1992; Dal Maso, 1993). Consequently, all gradients with respect to $\mathbf{x}$ are redefined as

$$\nabla_{\mathbf{x}} = \nabla_{\mathbf{x}} + \frac{1}{\varepsilon}\nabla_{\mathbf{y}}, \tag{2.4}$$

where $\nabla_{\mathbf{x}} = {}^t(\partial x_1, \partial x_2)$ and $\nabla_{\mathbf{y}} = {}^t(\partial y_1, \partial y_2)$.

Using this, we can also define the cell average for a function $h(\mathbf{x}, \mathbf{y})$ which is λ_m periodic over the grid interval $\mathbf{Y}$ is defined as

$$\langle h \rangle(\mathbf{x}) = \frac{1}{|\mathbf{Y}|}\int_{\mathbf{Y}} h(\mathbf{x}, \mathbf{y}) d\mathbf{y}. \tag{2.5}$$

[3] That is, if the minimum wavelength for the medium exits. For oscillators such as Helmholtz resonators, there exists no minimum wavelength and therefore, homogenization is not possible.

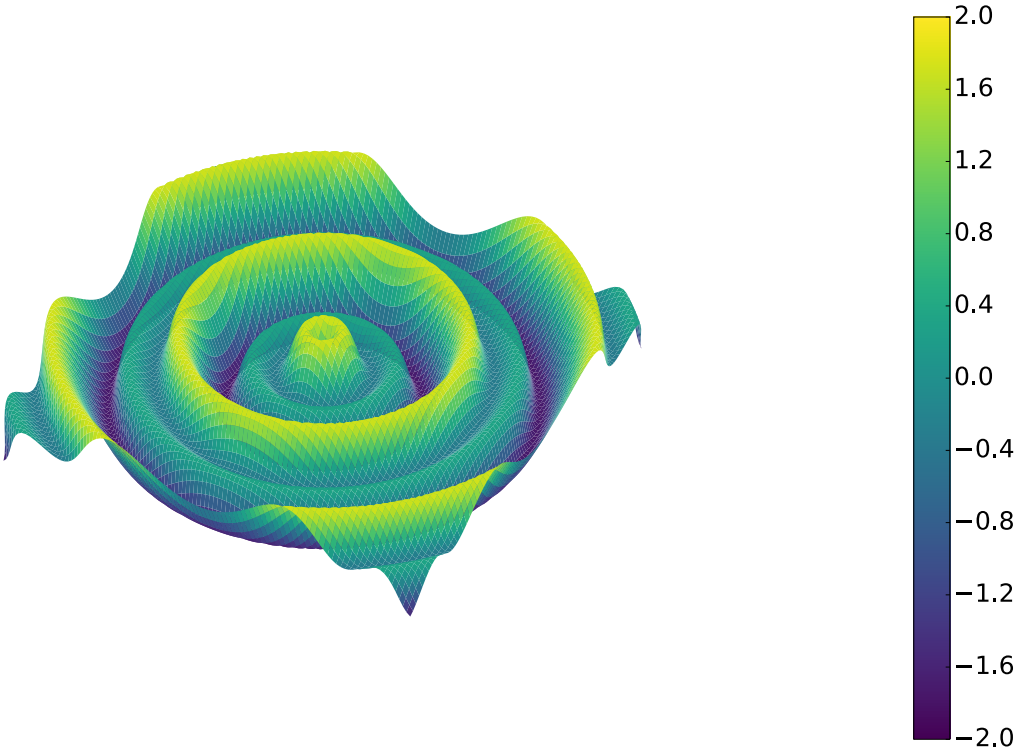

Fig. 2.3.: All scales.

Here, the characteristic of the function $h(\mathbf{x}, \mathbf{y})$ is that $\mathbf{x}$ contains variations that are only large-scales whereas $\mathbf{y}$ contains variations that are only small-scales.

This also allows us to redefine ρ and $\mathbf{c}$ as $\rho^{\varepsilon}(\varepsilon\mathbf{y})$ and $\mathbf{c}^{\varepsilon}(\varepsilon\mathbf{y})$, such that they are functions of $\mathbf{y}$ and repeat over the grid interval $\mathbf{Y}$. Simply put, the medium is now seen as containing only small-scale variations that repeat over $\mathbf{Y}$.

The aim of homogenization is to find solutions to the wave equations as an asymptotic expansion in ε. As such, the equations for true displacement $\mathbf{u}^{\varepsilon}$ and true stress $\boldsymbol{\sigma}^{\varepsilon}$ are postulated to be two-scale asymptotic expansions in ε:

$$\begin{aligned} \mathbf{u}^{\varepsilon}(\mathbf{x}, t) &= \sum_{i=0}^{\infty} \varepsilon^{i} \mathbf{u}^{i}(\mathbf{x}, \mathbf{y}, t), \\ \boldsymbol{\sigma}^{\varepsilon}(\mathbf{x}, t) &= \sum_{i=-1}^{\infty} \varepsilon^{i} \boldsymbol{\sigma}^{i}(\mathbf{x}, \mathbf{y}, t), \end{aligned} \tag{2.6}$$

where the i are powers in ε but are expansion indexes in $\mathbf{u}$ and $\boldsymbol{\sigma}$. It is necessary to begin the expansions for $\boldsymbol{\sigma}$ at $i = -1$ because the relation between stress and displacement also involves Equation 2.4. Introducing

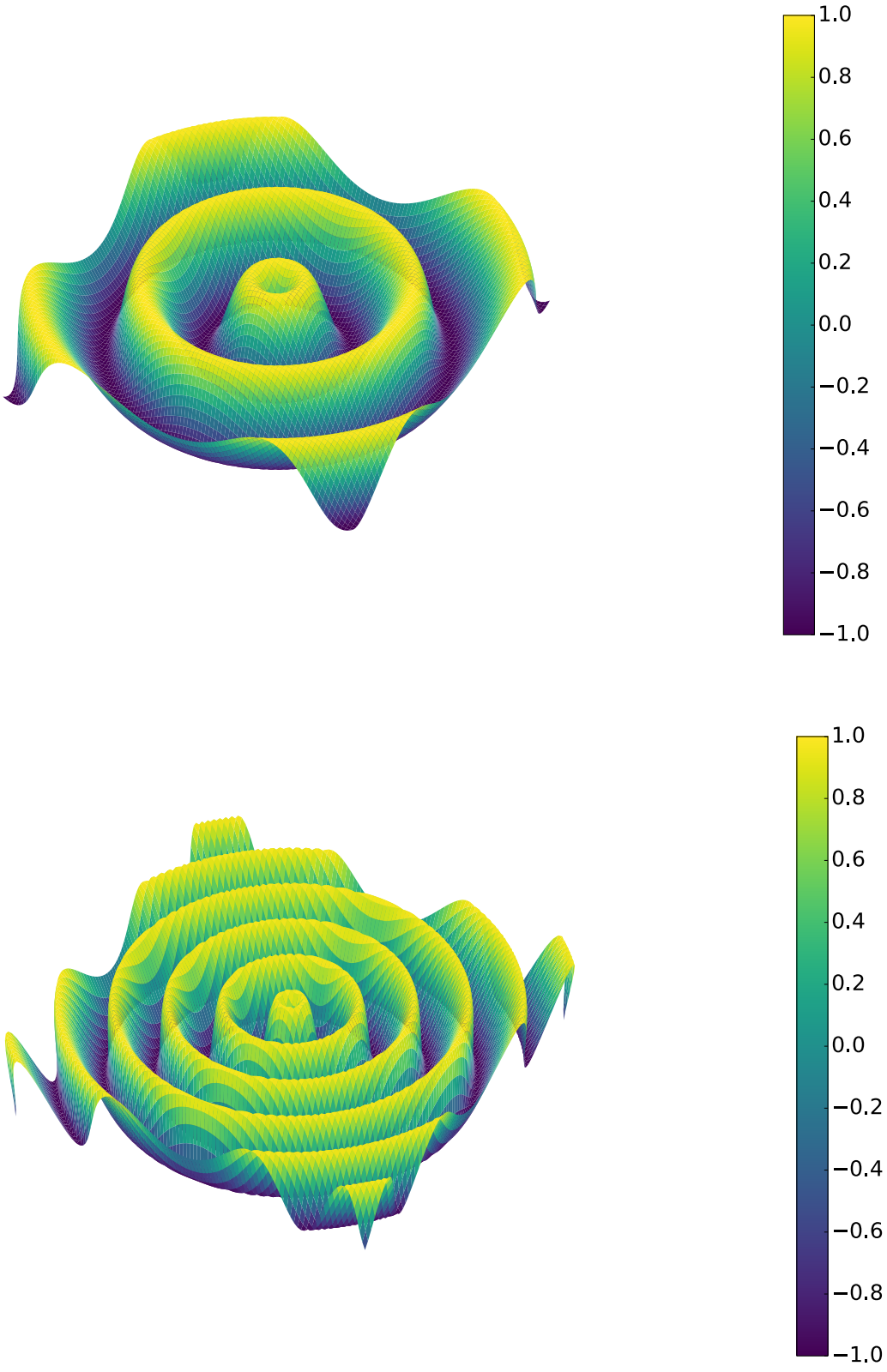

Fig. 2.4.: Separation into large-scales (top) and small-scales (bottom).

these expansions in the wave equation, and assuming the source to be independent of ε (this is not always true and sources should be treated in the manner shown by Capdeville et al. (2010a) and Capdeville et al. (2010b)), we get

$$\begin{aligned} \rho^{\varepsilon}\partial_{tt}\mathbf{u}^{i} - \nabla_{\mathbf{x}}.\boldsymbol{\sigma}^{i} - \nabla_{\mathbf{y}}.\boldsymbol{\sigma}^{i+1} &= \mathbf{f}, \\ \boldsymbol{\sigma}^{i} = \mathbf{c}^{\varepsilon} : (\boldsymbol{\epsilon}_{\mathbf{x}}(\mathbf{u}^{i}) + \boldsymbol{\epsilon}_{\mathbf{y}}(\mathbf{u}^{i+1})). \end{aligned} \tag{2.7}$$

These equations can be solved for each i.

Results

In the interest of brevity, we summarize the main results of the 2D periodic homogenization here.

Plugging in $i = -2$ and $i = -1$ for the first and second equations in (2.7), we can show that

$$\mathbf{u}^{0}(\mathbf{x}, \mathbf{y}) = \mathbf{u}^{0}(\mathbf{x}). \tag{2.8}$$

Note the remarkable result here: the right-hand side does not depend on small-scales $\mathbf{y}$, i.e., to order 0, displacement is not affected by small-scale structures. Consequently, $\boldsymbol{\sigma}^{-1} = 0$.

Next, substituting $i = -1$ and $i = 0$ in the first and second equations in (2.7), we can establish

$$\mathbf{u}^{1}(\mathbf{x}, \mathbf{y}) = \boldsymbol{\chi}(\mathbf{x}, \mathbf{y}) : \ \boldsymbol{\epsilon}_{\mathbf{x}}(\mathbf{u}^{0}(\mathbf{x})) + \left\langle \mathbf{u}^{1}(\mathbf{x}) \right\rangle. \tag{2.9}$$

For examples in this work, $\langle \mathbf{u}^{1}(\mathbf{x}) \rangle$ is assumed to be 0. $\boldsymbol{\chi}$, called the first-order corrector, is a third-order tensor which accounts for the heterogeneities at the receiver through its dependence on $\mathbf{y}$. Furthermore, it depends neither on time nor on sources. It is the solution of the cell problem defined as:

$$\nabla_{\mathbf{y}}.\left[\mathbf{c}^{\varepsilon} : \left[\mathbf{I} + \frac{1}{2}(\nabla_{\mathbf{y}}\boldsymbol{\chi} + {}^{t}\nabla_{\mathbf{y}}\boldsymbol{\chi})\right]\right] = 0, \tag{2.10}$$

where $\mathbf{I}$ is the third-order identity-tensor.

Meanwhile, we can also find the relation

$$\langle \boldsymbol{\sigma}^0 \rangle = \mathbf{c}^* : \boldsymbol{\epsilon}_{\mathbf{x}}(\mathbf{u}^0) \tag{2.11}$$

and introduce the effective elastic tensor as $\mathbf{c}^* = \langle \mathbf{c}^\varepsilon (\mathbf{I} + \frac{1}{2}(\nabla_{\mathbf{y}} \boldsymbol{\chi} +^t \nabla_{\mathbf{y}} \boldsymbol{\chi}) \rangle$.

Replacing $i = 0$ in the first equation in (2.7) and taking the cell average, we end up with

$$\rho^* \partial_{tt} \mathbf{u}^0 - \nabla . \langle \boldsymbol{\sigma}^0 \rangle = \mathbf{f}. \tag{2.12}$$

Combining this with (2.11), we get

$$\begin{aligned} \rho^* \partial_{tt} \mathbf{u}^0 - \nabla . \langle \boldsymbol{\sigma}^0 \rangle &= \mathbf{f}, \\ \langle \boldsymbol{\sigma}^0 \rangle &= \mathbf{c}^* : \boldsymbol{\epsilon}_{\mathbf{x}}(\mathbf{u}^0). \end{aligned} \tag{2.13}$$

This equation is the effective wave equation at order 0, for the effective elastic model $(\rho^*, \mathbf{c}^*)$. It differs from the classical wave equation only through the effective quantities. We repeat the effective elastic quantities again: $\rho^* = \langle \rho^\varepsilon \rangle$ and $\mathbf{c}^* = \langle \mathbf{c}^\varepsilon (\mathbf{I} + \frac{1}{2}(\nabla_{\mathbf{y}} \boldsymbol{\chi} +^t \nabla_{\mathbf{y}} \boldsymbol{\chi}) \rangle$.

2.4 Homogenization for 2D non-periodic media

Unlike the periodic case, establishing the boundary between small-scales and large-scales is not straightforward for non-periodic cases. However, non-periodic cases are more realistic because most geological media are not a repeating amalgamation of small-scale structures.

Therefore, a set of functions $f(\mathbf{x}, \mathbf{y}) : \mathbb{R}^2 \to \mathbb{R}$ is denoted by Ψ such that $\mathbf{x}$ includes only the large-scale variations while $\mathbf{y}$ includes only small-scale variations. The equations for true displacement $\mathbf{u}^\varepsilon$ and true stress $\boldsymbol{\sigma}^\varepsilon$ are postulated to be two-scale asymptotic expansions, but with the condition that they must belong to Ψ. Also unlike the periodic case, ρ and $\mathbf{c}$ cannot be redefined to ρ^ε and $\mathbf{c}^\varepsilon$ as functions of $\mathbf{y}$ but need to forged using a low-pass filter $\mathcal{F}^\varepsilon$, which for any function $h(\mathbf{x}, \mathbf{y})$ is given by

$$\mathcal{F}^\varepsilon \{h(\mathbf{x}, \mathbf{y})\} = \int h(\mathbf{x}, \mathbf{y}') w_m(\mathbf{y} - \mathbf{y}') d\mathbf{y}',$$

where the wavelet w_m in its spectral domain $\hat{w_m}$ is ideally

$$\hat{w_m}(\mathbf{k}) = \begin{cases} 1 & k \leq \frac{2\pi}{\lambda}, \\ 0 & \text{otherwise.} \end{cases}$$

This filter thus removes all scales smaller than λ.

Assuming that this forging is possible, the effective wave equation to the order 0 is similar to one in the periodic case and is given by

$$\begin{aligned} \rho^* \partial_{tt} \mathbf{u}^0 - \nabla . \langle \boldsymbol{\sigma}^0 \rangle &= \mathbf{f}, \\ \langle \boldsymbol{\sigma}^0 \rangle &= \mathbf{c}^* : \boldsymbol{\epsilon}_{\mathbf{x}}(\mathbf{u}^0), \end{aligned} \tag{2.14}$$

where $\rho^* = \langle \rho^\varepsilon \rangle$ and $\mathbf{c}^* = \langle \mathbf{c}^\varepsilon (\mathbf{I} + \frac{1}{2}(\nabla_{\mathbf{y}} \boldsymbol{\chi} +^t \nabla_{\mathbf{y}} \boldsymbol{\chi}) \rangle$; where $\mathbf{I}$ is the third-order identity-tensor.

ρ^ε is forged as

$$\rho^\varepsilon = \mathcal{F}^\varepsilon\{\rho\}(\mathbf{x}) + [\rho - \mathcal{F}^\varepsilon\{\rho\}(\mathbf{y})], \tag{2.15}$$

implying that the quantity ρ^* in (2.14) is simply $\mathcal{F}^\varepsilon\{\rho\}$. Unlike ρ, $\mathbf{c}^\varepsilon$ is not easy to forge. Nevertheless, we introduce two tensors $\mathbf{G}(\mathbf{x}, \mathbf{y})$ and $\mathbf{H}(\mathbf{x}, \mathbf{y})$:

$$\begin{aligned} \mathbf{G} &= \mathbf{I} + \frac{1}{2}(\nabla_{\mathbf{y}} \boldsymbol{\chi} +^t \nabla_{\mathbf{y}} \boldsymbol{\chi}), \\ \mathbf{H} &= \mathbf{c}^\varepsilon : \mathbf{G} \end{aligned} \tag{2.16}$$

The definitions (2.16) imply that $\mathbf{G}$ and $\mathbf{H}$ are the stress and strain associated with the first-order corrector $\boldsymbol{\chi}$. Using the low-pass filter $\mathcal{F}^\varepsilon$, $\mathbf{G}^\varepsilon$ and $\mathbf{H}^\varepsilon$ can be built, and $\mathbf{c}^\varepsilon$ is finally given by.

$$\mathbf{c}^\varepsilon = \mathcal{F}^\varepsilon\{\mathbf{H}_s\}(\mathbf{x}) : [\mathcal{F}^\varepsilon\{\mathbf{G}_s\}(\mathbf{x})]^{-1}; \tag{2.17}$$

where $\mathbf{H}_s$ and $\mathbf{G}_s$ are the solutions built from the starting corrector $\boldsymbol{\chi}_s$, which is the solution of the cell problem [See (2.10)] when it is solved for the entire domain, i.e. when all scales of the elastic tensor are considered to be small. More details are found in Capdeville et al. (2010b); Guillot et al. (2010) and Cupillard and Capdeville (2018).

Finally, in the non-periodic case, it is not possible go up to higher orders other than the leading order of the expansion and that of the first-order corrector.

2.5 Homogenization for 1D and 3D media

For the 1D case, $\langle u^1 \rangle$ is always equal to 0. Furthermore, an analytical solution to the cell problem is possible and a direct solution can be found. For the non-periodic case, the zeroth order effective properties can be computed by simply filtering the density and the inverse of the elastic tensor.

Homogenization for 3D media closely follows the 2D media.

2.6 Other homogenization techniques

Backus (1962) used a weighting function and moving averages to homogenize finely layered media. He showed that the effective media for a finely layered isotropic medium is orthotropic, thus providing an elegant solution to the problem addressed by Bruggeman (1937). His work is still extensively used in exploration seismology (Helbig, 1984; Schoenberg and Muir, 1989; Tiwary et al., 2009) and upper mantle polarization anisotropy investigations (Gee and Jordan, 1988; Wang et al., 2013). Further improvements/generalisations on his work were made by Gold et al. (2000) and Grechka (2003). The order 0 homogenization method described above falls back to Backus (1962)'s solution.

Homogenization based on scale expansions for vibrations can be traced back to Sanchez-Palencia (1980). But it was only developed for the periodic case.

The Fast Fourier homogenization developed from Moulinec and Suquet (1998) by Capdeville et al. (2015) is an alternative method (compared to the usually used Finite Element method (FEM)) to solve the cell problem [Equation 2.10] described above using Fast Fourier Transforms (FFT). Advantages include efficiency, accuracy and speed, however, care must be taken to alleviate Gibbs phenomena introduced in discontinuous media.

Jordan (2015) relied on the Born approximation to express elastic parameters in a media with small-scale heterogeneities. Results, which are explicitly derived for transversely isotropic medium, reduce to the second-order equations derived by Backus (1962).

The wavelet-based expansion by Engquist and Runborg (2002) works on the discretized version of the wave equation. The homogenization method introduced by Fichtner and Hanasoge (2017) is also applied to the uniformly discretized wave equation in the wavenumber domain. It involves decomposing the Fourier transform matrix in the discrete wave equation such that only quantities for only low wavenumbers are retained. The advantages are that it is simple and easy to implement, on the other hand, the use of Fourier transform limits equidistant discretizations.

3 Effect of small-scale structures on gradients

For several decades now, it has been observed that local small-scale structures affect wavefield gradients.

In this chapter, I begin by giving a summary of all previous accounts of this observation in Section 3.1. Then, I make my own observations regarding these studies through simple numerical examples in Section 3.2 and examine the effect theoretically using the theory of homogenization in Section 3.3.

3.1 Previous Work

Although Wood and King (1977) and Wyatt et al. (1988) had already showed the correlation between tilt measurements and soil conditions, i.e, weathering due to rainfall, it was King and Bilham (1973) who, perhaps for the fist time, suggested that the poor agreement between theoretical and observed tidal tilts reported by Baker and Lennon (1973) maybe because of strain-rotation coupling due to inhomogeneities in underlying rocks. Harrison (1976) then expanded on this idea and used Finite Element Method (FEM) to investigate the effect of cavities, topographies and geological heterogeneities on strains. Through his synthetic studies, he showed that due to these structures, strains and tilts can be greatly modified. Similarly, Berger and Beaumont (1976) used FEM to investigate the substantial discrepancies that occurred between their observations and theoretical predictions of tidal strain observations at several sites in the United States. They concluded the effect due to small-scale structures can be significant and its correction therefore, necessary.

Kohl and Levine (1995) ruled out instrumental and environmental effects in favour of site effects as the cause of differences of up to about 50% in tidal measurements of closely-spaced tiltmeters at the Piñon Flat Observatory.

Gomberg and Agnew (1996) evaluated the accuracy of dynamic strain estimated from seismic data at Piñon Flat Observatory by comparing them to

theoretical array-derived strains and showed that due to local heterogeneities, the strain field could be distorted by as much as about 20%. Likewise, van Driel et al. (2012) showed that point-measured and array-derived rotations may have intrinsic differences for example, in volcanic environments, in the far field or in low frequency spectrum due to local small-scale structures.

More recently, Wassermann et al. (2020) measured rotational ground motions at the Kīlauea volcano shortly after its eruption and concluded that they are largely affected by near-receiver heterogeneities due to the strain-rotation coupling and/or detailed source effects.

3.2 Numerical examples

We consider a 2D elastic case where the computational domains are two 20×20 km^2 squares. These squares, except for a spatially varying small-scale heterogeneity at the center of the second square, are otherwise homogeneous. The P and S velocities in the homogeneous area of the squares are 5 kms^{-1} and 3.2 kms^{-1} respectively. The spatial extension of the heterogeneity at the center of the second square is 200×200 m^2. Its geometry is kept simple in order to make both meshing and waveform modelling easier. The velocities in each element of the heterogeneity differ by $\pm50\%$ from the surroundings. This velocity contrast is strong but realistic for such a scale range. For example, the velocity contrast between granite and unconsolidated sediments is usually even larger. All boundaries are absorbing.

Here, we show the results of two numerical simulations. All simulations are performed using a 2D Spectral Element program (Komatitsch and Vilotte, 1998).

3.2.1 Numerical example 1

The aim of this numerical example is to compare the effect of a sub-wavelength heterogeneity on displacements with its gradients. For this, four receivers are placed in both squares such that for the heterogeneous square, two receivers lie just inside the heterogeneity and the other two just outside as shown in Figure 3.1. The distance between the receivers is around 15 m.

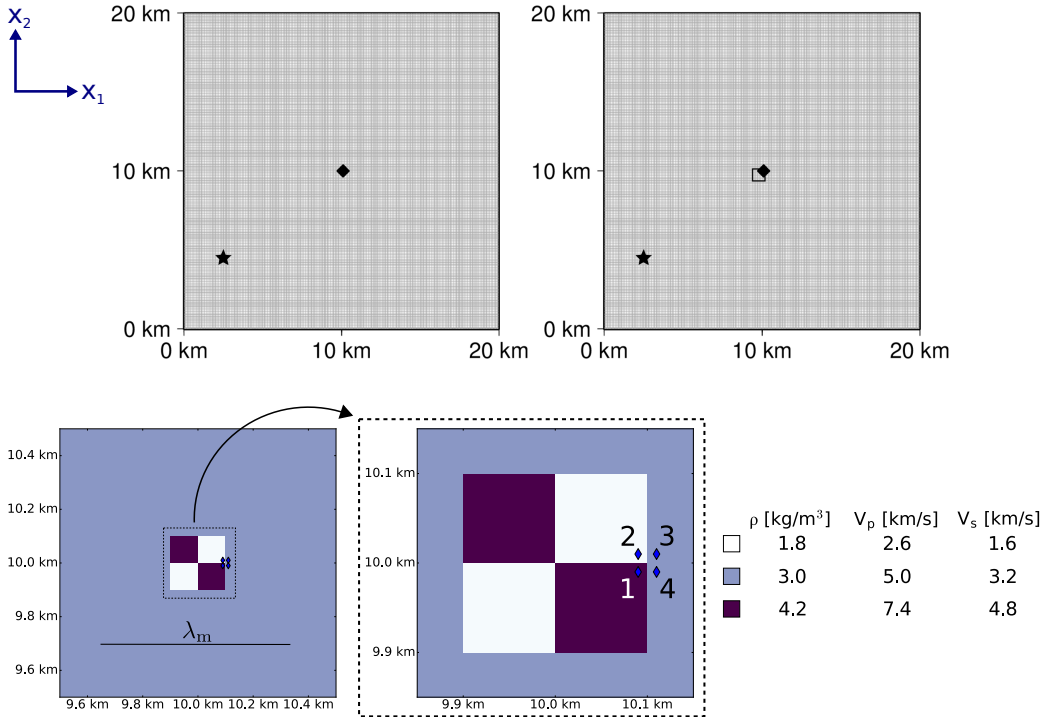

Fig. 3.1.: Top: 2D domains used in Section 3.2.1. Both domains are 20×20 km^2. All boundaries are absorbing. The star shows the location of the source and the diamonds show the locations of four receivers. Left: Entirely homogeneous medium. Right: A heterogeneity of 200×200 m^2, placed at the centre, is shown by the square (not to scale).
Bottom: V_p, V_s and ρ at the heterogeneity. The length of the minimum wavelength for the simulation is shown in the leftmost panel.

In both cases, we compute the wavefield induced by a horizontal double-couple source. The source-time function is a Ricker wavelet (second derivative of a Gaussian). With a source central frequency of 1.5 Hz (maximum frequency of 4.1 Hz), the minimum wavelength λ_m is around 700 m. It should be noted that the dimension of the heterogeneity is around 3 times smaller than λ_m. Using the Spectral Element program, displacements, velocities, accelerations, shear strain and rotation measured by the four receivers in the two models are computed[1]. These are shown in Figure 3.2. Because the mesh used for the computation honors the interfaces of the heterogeneity, the solutions thus obtained are considered to be accurate.

It follows from Figure 3.2 that while all four receivers measure almost the same displacement, velocity and acceleration in both models, this is not true

[1]The Spectal Element program is based on the Spectral Element Method (SEM). In the SEM, displacements are approximated using Lagrange polynomials at Gauss-Lobatto-Legendre (GLL) points. Their derivatives, which allow us to compute strains and rotations, can be determined by taking derivatives of the Lagrange polynomials.

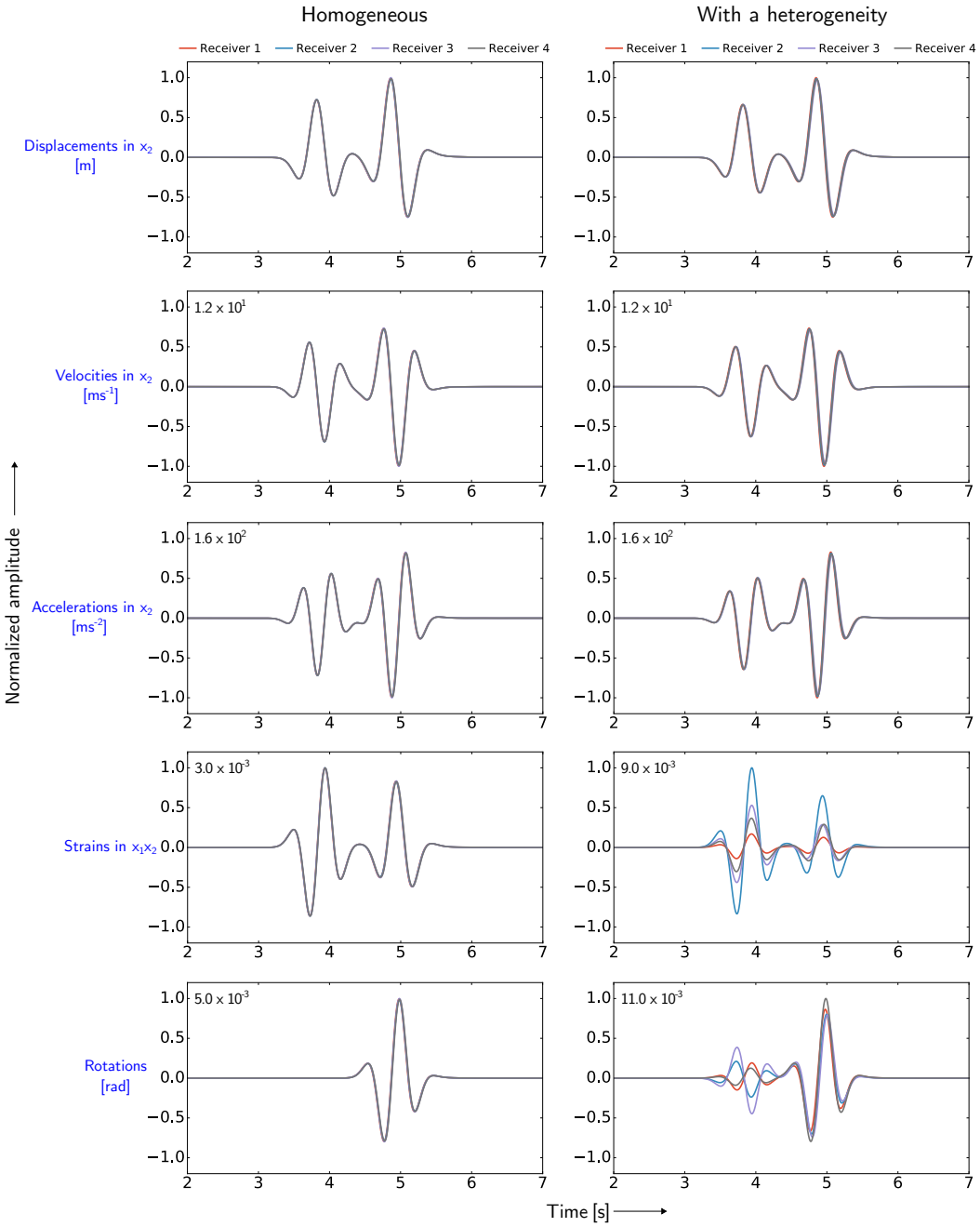

Fig. 3.2.: Left: Measurements in the homogeneous medium. Right: Measurements in the medium with the heterogeneity. The two media are shown in Figure 3.1. Starting from top, vertical displacements, vertical velocities, vertical accelerations, shear strains and rotations are shown. The scaling factors for each panel are shown on the top left.

for rotation and strain. The four receivers measure a very similar rotation and strain in the homogeneous case, but in the presence of a heterogeneity, though much smaller than the minimum wavelength, the measurements are substantially different (this is the third effect mentioned in Section 1.3, i.e. discrepancy between data observed between closely spaced instruments). The difference can be observed in both amplitudes and phases, and it depends on the relative location of the receiver to the heterogeneity.

When we look at the bottom panels in 3.2 that show the rotations, it may seem that the converted P to S waves (at approximately 4 s) are more affected than the S waves (at approximately 5 s). We emphasize here that this is particular only to this example and some other examples (not shown) result in contrasting situations. Therefore, this observation is not to be generalised.

3.2.2 Numerical example 2

The purpose of this numerical example is to show how, in the presence of a heterogeneity, array-derived gradients differ from point-estimated gradients. To that end, three receivers are placed in both squares such that all three receivers lie in the heterogeneity [Figure 3.3]. The distance between the receivers is around 100 m.

In both cases, we compute the wavefield induced by a horizontal double-couple source. The source-time function is a Ricker wavelet. With a source central frequency of 0.5 Hz (maximum frequency of 1.4 Hz), the minimum wavelength λ_m is around 2370 m. It should be noted that the dimension of the heterogeneity is around 12 times smaller than λ_m and that the distance between the receivers is around 23 times smaller.

Using the Spectral Element program, displacements measured by the three receivers in the two models are computed. The three displacements are used to compare the array-derived rotation rates at Receiver 2 [see Appendix A]. These are shown in Figure 3.4. Also shown is the rotation measured at Receiver 2. Because the mesh used for the computation honours the interfaces of the heterogeneity, the displacement and rotation solutions thus obtained are considered to be accurate.

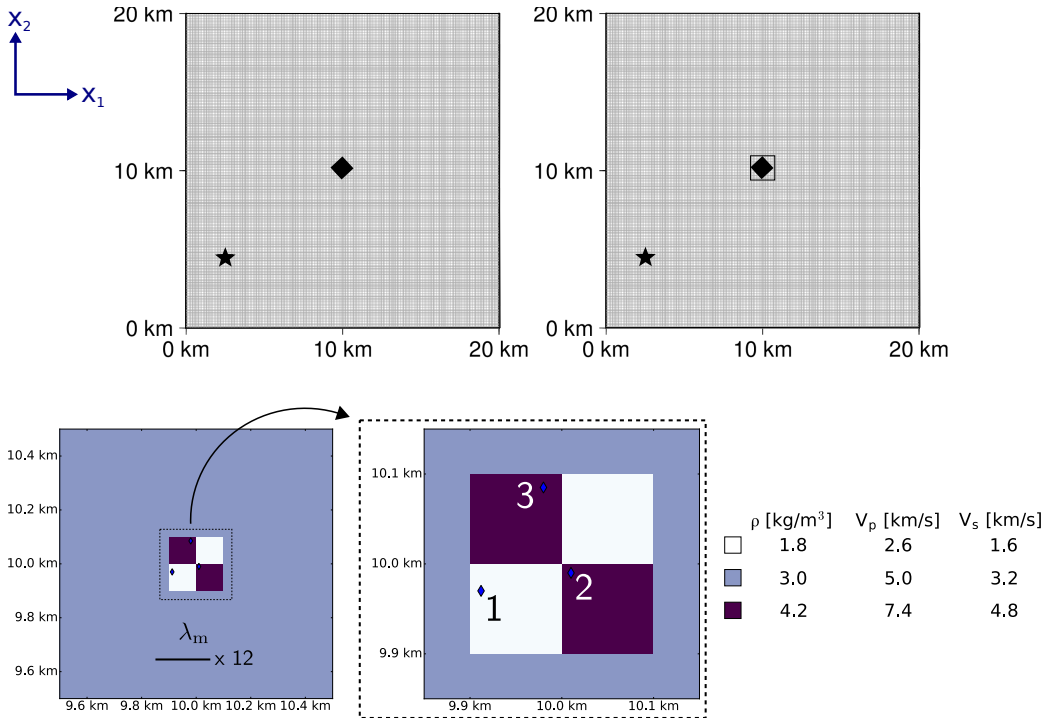

Fig. 3.3.: Top: 2D domains used in Section 3.2.2. Both domains are 20×20 km^2. All boundaries are absorbing. The star shows the location of the source and the diamonds show the locations of three receivers. Left: Entirely homogeneous medium. Right: A heterogeneity of 200×200 m^2, placed at the centre, is shown by the square (not to scale).
Bottom: V_p, V_s and ρ at the heterogeneity. The length of the minimum wavelength for the simulation is shown in the leftmost panel.

It follows from Figure 3.4 that while all three receivers measure almost the same displacement, velocity and acceleration in both models, the point-measured and array-derived strains and rotations are not the same in both. The point-measured and array-derived strains and rotations are similar in the homogeneous case, but in the presence of a heterogeneity, though much smaller than the minimum wavelength, the measurements are substantially different (this is the second effect mentioned in Section 1.3, i.e. dissimilarity between wavefield gradients measured at a point and wavefield gradients estimated at the point using an array. The difference can be observed in both amplitudes and arrival times, and from the example before, one can assume that the difference varies with the relative location of the receiver to the heterogeneity.

Because our current sensors are sensitive enough to measure differences as subtle as those shown in Figures 3.2 and 3.4, interpretations derived from the wavefield gradients would be incoherent. For example, if the four receivers

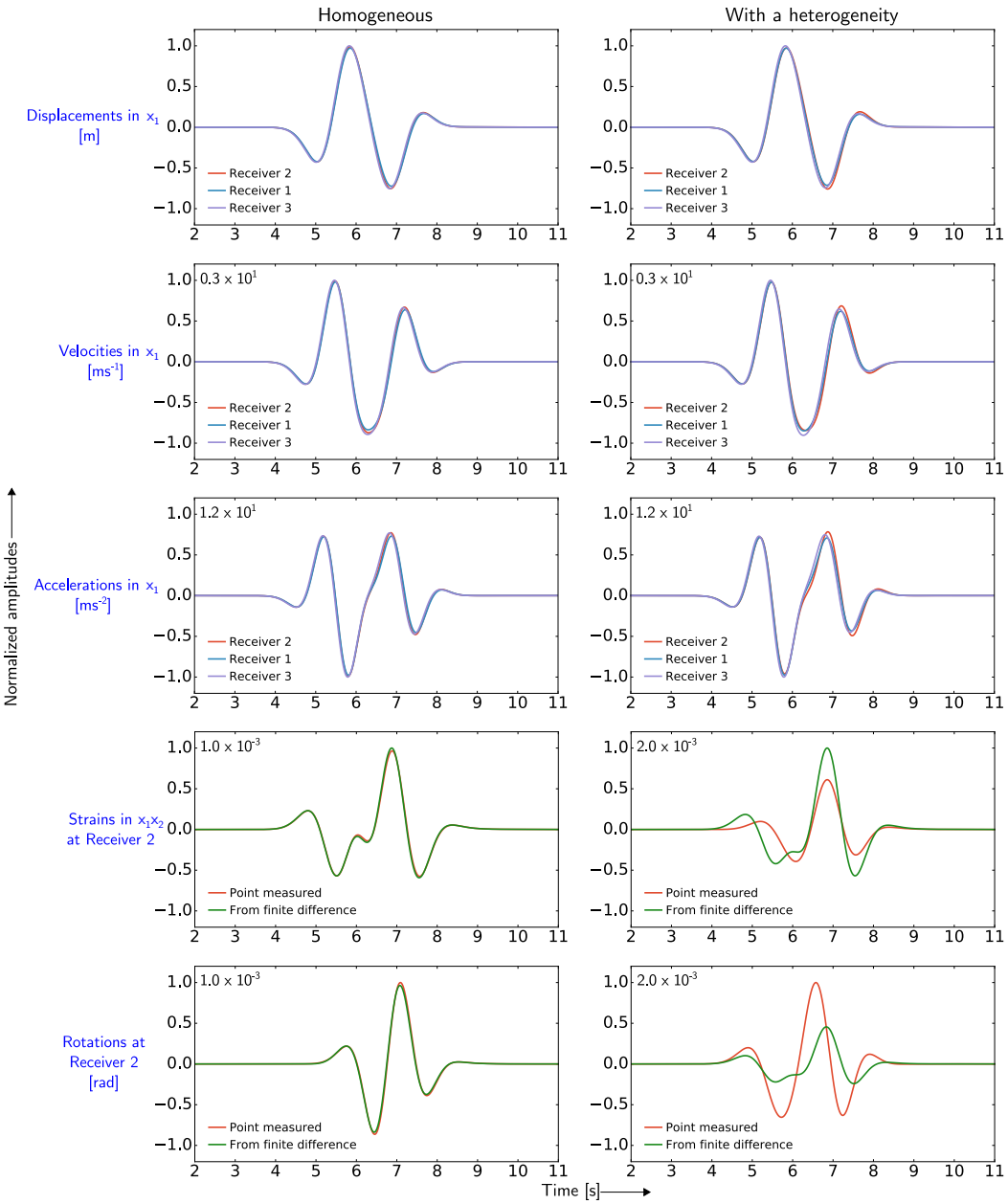

Fig. 3.4.: Left: Measurements in the homogeneous medium. Right: Measurements in the medium with the heterogeneity. The two media are shown in Figure 3.3. Starting from top, horizontal displacements, horizontal velocities, horizontal accelerations, shear strains at Receiver 2 and rotations at Receiver 2 are shown. The scaling factors for each panel are shown on the top left.

from Figure 3.1 rotations were to be used to determine instantaneous slowness, one would arrive at four different values of slowness. It is worth noting that acceleration is insensitive to the heterogeneity while rotation rate is. Because rotation rates are related to local phase velocities through transverse accelerations (Igel et al., 2005; Cochard et al., 2006; Igel et al., 2007), this might seem inexplicable. However, the relation is only valid in the absence of heterogeneities, and as Figures 3.2 and 3.4 show, it no longer holds when the receiver is placed at a heterogeneity. Similarly, Brokešová and Málek (2015a) and Brokešová and Málek (2015b) have shown that under certain conditions, velocities might be as important as accelerations for relating rotations to translations. However, as Figure 3.2 and 3.4 show, the effect on rotations does not originate from velocities either.

Note that the results of the numerical examples are not specific to just the quantities shown. The conclusion would be the same for any measurements of wavefield (and its time derivatives, such as displacement, velocity and acceleration) and for any measurements of wavefield gradient (and its time derivatives, such as strain, strain rate, rotation and rotation rate).

3.3 Homogenization to explain the effect

From the two simple numerical examples in Section 3.2, it can be concluded that small-scale heterogeneities have almost no effect on wavefield measurements but have a much stronger effect on wavefield gradient measurements. This observation is an issue for any wavefield gradient based instrument as the measurements can be tainted by nearby heterogeneities. A more intensive set of experiments would have shown that the amplitude of this effect depends mainly on the velocity contrast and not the heterogeneity's spatial extent with respect to the wavelength. In this section, we examine this effect theoretically using the theory of homogenization [see Chapter 2].

In homogenization, the separation of scales into small-scales $\mathbf{y}$ and large-scales $\mathbf{x}$ causes all gradients with respect to $\mathbf{x}$ are redefined as

$$\nabla_{\mathbf{x}} \to \nabla_{\mathbf{x}} + \frac{1}{\varepsilon}\nabla_{\mathbf{y}}, \tag{3.1}$$

where $\nabla_{\mathbf{x}} = {}^t(\partial_{x1}, \partial_{x2})$ and $\nabla_{\mathbf{y}} = {}^t(\partial_{y1}, \partial_{y2})$.

The aim of homogenization is to find solutions to the wave equations as an asymptotic expansion in ε. As such, the equations for true displacement $\mathbf{u}^\varepsilon$ and true gradient $(\nabla\mathbf{u})^\varepsilon$ take the form

$$\begin{aligned}\mathbf{u}^\varepsilon(\mathbf{x},\mathbf{y},t) &= \mathbf{u}^0(\mathbf{x},\mathbf{y},t) + \varepsilon\mathbf{u}^1(\mathbf{x},\mathbf{y},t) + \varepsilon^2\mathbf{u}^2(\mathbf{x},\mathbf{y},t) + ...\\ (\nabla\mathbf{u})^\varepsilon(\mathbf{x},\mathbf{y},t) &= (\nabla\mathbf{u})^0(\mathbf{x},\mathbf{y},t) + \varepsilon(\nabla\mathbf{u})^1(\mathbf{x},\mathbf{y},t) + \varepsilon^2(\nabla\mathbf{u})^2(\mathbf{x},\mathbf{y},t) + ...\end{aligned} \tag{3.2}$$

In (3.2), the superscripts are powers in ε but are expansion indexes in the $\mathbf{u}$ and $(\nabla\mathbf{u})$.

Recalling Equations (2.8) and (2.9), we have,

$$\begin{aligned}\mathbf{u}^0(\mathbf{x},\mathbf{y},t) &= \mathbf{u}^0(\mathbf{x},t),\\ \mathbf{u}^1(\mathbf{x},\mathbf{y},t) &= \boldsymbol{\chi}(\mathbf{y}) : \boldsymbol{\epsilon}(\mathbf{u}^0(\mathbf{x},t)).\end{aligned}$$

In the second equation here, $\boldsymbol{\epsilon}$ denotes the strain ($[\epsilon(\mathbf{u}^0)]_{ij} = \frac{1}{2}(\partial_i u_j^0 + \partial_j u_i^0)$) and is not to be confused with the homogenization parameter ε from (2.2). $\boldsymbol{\chi}$, the first-order corrector, is a third-order tensor. It is a solution of the cell equation [see Chapter 2]. Note that $\boldsymbol{\chi}$ does not depend on time or sources.

Therefore, to leading order, the true displacement $\mathbf{u}^\varepsilon$ can be rewritten as

$$\mathbf{u}^\varepsilon(\mathbf{x},\mathbf{y},t) = \mathbf{u}^0(\mathbf{x},t). \tag{3.3}$$

Using (3.1) and the expansion of $\mathbf{u}^\varepsilon(\mathbf{x},\mathbf{y},t)$ in (3.2), the true gradient $(\nabla\mathbf{u})^\varepsilon$ is then

$$\begin{aligned}(\nabla\mathbf{u})^\varepsilon(\mathbf{x},\mathbf{y},t) &= \left(\nabla_\mathbf{x} + \frac{1}{\varepsilon}\nabla_\mathbf{y}\right)(\mathbf{u}^0(\mathbf{x},\mathbf{y},t) + \varepsilon\mathbf{u}^1(\mathbf{x},\mathbf{y},t) + \varepsilon^2\mathbf{u}^2(\mathbf{x},\mathbf{y},t) + ...),\\ (\nabla\mathbf{u})^\varepsilon(\mathbf{x},\mathbf{y},t) &= \nabla_\mathbf{x}\left(\mathbf{u}^0(\mathbf{x},\mathbf{y},t) + \varepsilon\mathbf{u}^1(\mathbf{x},\mathbf{y},t) + \varepsilon^2\mathbf{u}^2(\mathbf{x},\mathbf{y},t) + ...\right) +\\ &\qquad \frac{1}{\varepsilon}\nabla_\mathbf{y}\left(\mathbf{u}^0(\mathbf{x},\mathbf{y},t) + \varepsilon\mathbf{u}^1(\mathbf{x},\mathbf{y},t) + \varepsilon^2\mathbf{u}^2(\mathbf{x},\mathbf{y},t) + ...\right).\end{aligned}$$

Using (**??**), the true gradient $(\nabla\mathbf{u})^\varepsilon$ to the leading order therefore is

$$(\nabla\mathbf{u})^\varepsilon(\mathbf{x},\mathbf{y},t) = (\nabla_\mathbf{x}\mathbf{u}^0)(\mathbf{x},t) + \nabla_\mathbf{y}\chi(\mathbf{y}) : \boldsymbol{\epsilon}(\mathbf{u}^0(\mathbf{x},t)). \tag{3.4}$$

Note that the terms on the right of this equation make up the first term in the expansion of $(\nabla \mathbf{u})^{\varepsilon}(\mathbf{x}, \mathbf{y}, t)$ in (3.2).

This implies that for rotation in 2D, which is a scalar,

$$\begin{aligned} \omega^{\varepsilon} &= \theta_{ij}\ (\partial_i u_j)^0 \\ &= \omega^0 + J_{ij} : \epsilon_{ij}(u^0), \end{aligned} \tag{3.5}$$

where $J_{ij} = \theta_{mn}\partial_{y_m}\chi_{ijn}$ and θ represents the 2D Levi-Civita symbol. Similarly, for rotation in 3D,

$$\begin{aligned} \omega_i^{\varepsilon} &= \theta_{ijk}\ (\partial_j u_k)^0 \\ &= \omega_i^0 + J_{ijk} : \epsilon_{jk}(u^0), \end{aligned} \tag{3.6}$$

where $J_{ijk} = \theta_{imn}\partial_{y_m}\chi_{njk}$ and θ represents the 3D Levi-Civita symbol. And for a rotational receiver on the surface of a 3D domain under free surface conditions,

$$\omega_i^{\varepsilon} = \omega_i^0 + \bar{J}_{ijk} : \sigma_{jk}, \tag{3.7}$$

where $\bar{J}_{ijk} = J_{imn}\ v_{mnjk}$, $\boldsymbol{\sigma}$ is the stress tensor and $\mathbf{v}$ is the inverse of the elastic tensor $\mathbf{c}$.

Likewise, for rotation rates in 3D, we have

$$\dot{\omega_i}^{\varepsilon} = \dot{\omega_i}^0 + J_{ijk} : \dot{\epsilon_{jk}}(u^0), \tag{3.8}$$

where $J_{ijk} = \theta_{imn}\partial_{y_m}\chi_{njk}$ and θ represents the 3D Levi-Civita symbol.

In (3.2), $\mathbf{u}^{\varepsilon}$ is the true displacement and $\mathbf{u}^0$ is the zeroth order effective displacement. Similarly, $(\nabla \mathbf{u})^{\varepsilon}$ represents the true gradient of displacement and $(\nabla \mathbf{u})^0$ represents the zeroth order effective gradient of displacement. True quantities correspond to real data that can be collected in the field. In theory, it is possible to model them using wave equations but because they depend on all possible scales, they require an infinite scale knowledge of the elastic properties of the Earth. This is not feasible in practice. On the other hand, for a given frequency band, effective quantities can be modeled using the same equations but using homogenized elastic properties which do not contain any small scales. Thus, effective quantities can be described with a finite set of parameters. Retrieving these parameters is what is actually done in full waveform inversion and tomography imaging (Capdeville and

Métivier, 2018). Most of the tomographic models that exist are therefore actually an approximation to the homogenized Earth.

Comparing the terms in (3.3), we note that the terms on the right depends only on $\mathbf{x}$, i.e. large-scales. This means that effective displacement can be used as good approximation for true displacement without worrying about small-scales. This is a well known result from Backus (1962) and Chapman (2004, p. 277). One consequence of this result is that the agreement between data and synthetics is reasonably good for displacement, velocity and acceleration. This is also consistent with the results obtained from Section 3.2 and with many examples concerning real data. For instance, very long period surface waves can be modelled using PREM (Dziewoński and Anderson, 1981) with good accuracy even though the crust is highly heterogeneous. The large amplitude and small-scale heterogeneity of the crust is inconspicuous to the displacement field, and one does not need complete information on the crust for its modelling. This is also why our one dimensional Earth models are so successful (Dziewoński and Anderson, 1981; Kennett et al., 1995).

On the contrary, this is not true for any gradient of displacement. The terms in (3.4) depend on both $\mathbf{x}$ and $\mathbf{y}$, i.e. both large-scales and small-scales. Due to small-scales, the true gradient of displacement now couples with strain of effective displacement. The coupling is due to the first-order corrector χ, therefore, we refer to this coupling as 'correction'. Similarly, we refer to $\mathbf{J}$ as the coupling tensor.

The appearance of correction in (3.4) implies that setting up an inversion problem with wavefield gradient is difficult because observations rely on all scales. Every detail in all scales would be necessary to set up the inversion problem. For the case of displacement, velocity or acceleration where effective quantities are a good approximation to the true quantities, this is not the case and setting up an inversion problem is not an issue. For the wavefield gradients, however, correction needs to be accounted for and this is the purpose of the next chapter.

3.4 Discussion and Conclusion

In this study, through simple examples, we showed that local small-scale heterogeneities have little or almost no effect on the wavefield (displacement, velocity and acceleration) but a strong effect on its gradients (strain, strain rate, rotation and rotation rate). This stands in line with previous studies conducted by Kohl and Levine (1995) and Gomberg and Agnew (1996). Local small-scale heterogeneities can cause phases, amplitudes and arrival times of the waveform to alter, thus causing a disagreement between the observed data and synthetics (and point-measured and array-derived values). Consequently, these effects are obstacles in direct applications of the measurements, for example, when rotations are used to determine phase velocities (Igel et al., 2005, 2007) or strains are used to deduce stresses generated by earthquakes (Spudich et al., 1995). Such differences have also been mentioned to cause non-zero surface strains (Harrison, 1976; Gomberg and Agnew, 1996). This could also be the reason for small inconsistencies in rotations observed by Stedman et al. (1995), McLeod et al. (1998) and Pancha et al. (2000).

4 Correcting wavefield gradients for the effects of small-scale structures

On grounds of their theory of homogenization (Capdeville et al., 2010b; Guillot et al., 2010), in Chapter 3, we made the case that wavefield (displacements, velocities or accelerations) is sensitive to sub-wavelength structures only in an effective manner. This assumption, however, breaks down, when wavefield gradients (strains or rotations) are considered.

As instruments for strain and rotation measurements are becoming increasingly popular and interest in extracting information from strain and rotation is growing, this issue is becoming more and more important. Therefore, this chapter is dedicated to correcting for this effect.

4.1 Previous Work

Harrison (1976) used the coupling coefficients as defined by Eshelby and Peierls (1957) to quantify the effects of cavity, topography and geological heterogeneities on strain and tilt. Using Finite Element Method (FEM) simulations, he showed that due to geological boundary between sedimentary rocks of the plains and the basement rocks of the mountains, the strain coefficient, defined as the ratio of actual strain to the strain which would be measured if the medium were homogeneous, at an idealized cross-section of the Rocky mountains varied from 1.7 to 0.37. The coefficients approached 1 only far away from the boundary. Wielandt and Forbriger (1999) also calculated the coupling constants J_{ij} (defined as the ratio of actual rotations around j axis to the strain component i) for tilts for near-source region at Stromboli volcano, and found those to be in the order of 0.3. van Driel et al. (2012) calculated those coupling constants due to topography for the G Ring laser in Wettzell, Germany. They showed for an area 100 m around the Wettzell, the average of the coupling constants J_{xz}, J_{yz} and J_{sz} are

-0.016±0.012, 0.021±0.010 and 0.02±0.04 respectively and that the ring laser is located at the local minima of absolute values of all three constants.

Berger and Beaumont (1976) used transformation matrices to compute the perturbations in strain field due to topography, cavity and geology. Using FEM, he showed that the T_{11} component of the transformation matrix due to topography is greater than 0.80 at all six sites evaluated, meaning that at all those sites, the applied horizontal strain ϵ_{11} is modified by at least 80%. Similarly, the T_{22} component of the matrix is greater than 0.90, meaning that the applied horizontal strain ϵ_{22} is modified by at least 90%.

Lambotte et al. (2006) calculated the coupling constants by decomposing observations of tides on a basis of synthetic signals for three stations GNI in Armenia, BFO in Germany and MAJO in Japan. Although these coefficients are difficult to interpret in terms of small-scale structures, they can be used to remove the effects of small-scale structures from the data.

Corrections were also attempted by Meertens and Wahr (1986) and Sato and Harrison (1989).

4.2 Correction

We know from (3.5), (3.6) and (3.7) that the true wavefield gradient is coupled with strain of the effective displacement through the tensor **J**. Moreover, **J** depends neither on time nor on source. It depends only on the location of the receiver. If the elastic properties at the receiver are known well enough, **J** can be computed by solving the cell problem (Capdeville et al., 2010b; Guillot et al., 2010). This is not the case in practice. Nevertheless, we can invert for **J** provided that we have an effective model that fits the displacement (or velocity or acceleration) data reasonably well. The obvious choice for this effective model is the homogenized model because this is what the waves can see (Capdeville and Métivier, 2018). This effective model is usually not known, but any tomographic model can be a good approximation as we shall see from the synthetic examples in Section 4.3. For real data, any Earth model which fits the displacement (or velocity or acceleration) data reasonably well can be used. This is similar to an earthquake moment tensor inversion where an Earth model is necessary to compute Green's functions.

Because all examples here are carried out for rotation, we start from Equation 3.4:

$$\omega^{\varepsilon}(\mathbf{x}_r, t; \mathbf{x}_s) = \omega^0(\mathbf{x}_r, t; \mathbf{x}_s) + \mathbf{J}(\mathbf{y}_r) : \boldsymbol{\epsilon}^0(\mathbf{x}_r, t; \mathbf{x}_s), \tag{4.1}$$

where ω^{ε} is the rotation data, ω^0 and $\boldsymbol{\epsilon}^0$ are the rotation and the strain computed in the effective model and $\mathbf{J}$ is the unknown. $\mathbf{x}_s$ denotes the location of the source and $\mathbf{y}_r = \frac{\mathbf{x}_r}{\varepsilon}$ denotes the location of the receiver. We invert for $\mathbf{J}$ by solving the over-determined linear problem in the least-squares sense (Tarantola and Valette, 1982). We seek to minimise the L^2 misfit between the synthetics and the data through

$$\mathbf{J} \sim ({}^t\mathbf{F}\,\mathbf{F})^{-1}\,\mathbf{F}\,\delta d, \tag{4.2}$$

where $\delta d = \omega^{\varepsilon} - \omega^0$ and $\mathbf{F}$ is the matrix where all strains of the effective displacement are stacked.

The process of inverting for $\mathbf{J}$ is straight-forward: we need only one simulation per source to assemble $\mathbf{F}$. Then, we apply either Equation (4.2) [or Equation (B.4); See Appendix B] with absolutely no modification as the inversion is stable and no damping is necessary. We invert for 3 parameters in 2D and for 18 parameters for the 3 components of rotation in 3D. Like the instrument response, the corrector can be used to separate unwanted site effects from data.

Once we invert for $\mathbf{J}$, we need to evaluate the quality of our inversion results. One way to do so would be to compare the $\mathbf{J}$ computed through inversion to the one obtained by solving the series of homogenization equations [see the cell problem in Chapter 2]. However, this solution is only available when all fine-scales are perfectly known, i.e only for synthetic tests. Therefore, for all our examples, we start by dividing the data into two pools: the inversion data set and the validation data set. We use the inversion data set to perform the inversion and the validation data set to assess the accuracy of $\mathbf{J}$. In all examples that follow, we use the $\mathbf{J}$ to correct the synthetic rotations. Therefore, a better fit between observed data and corrected synthetics, especially for events not used in the inversion, implies that $\mathbf{J}$ is a good measure of the coupling due to small-scales at the receiver.

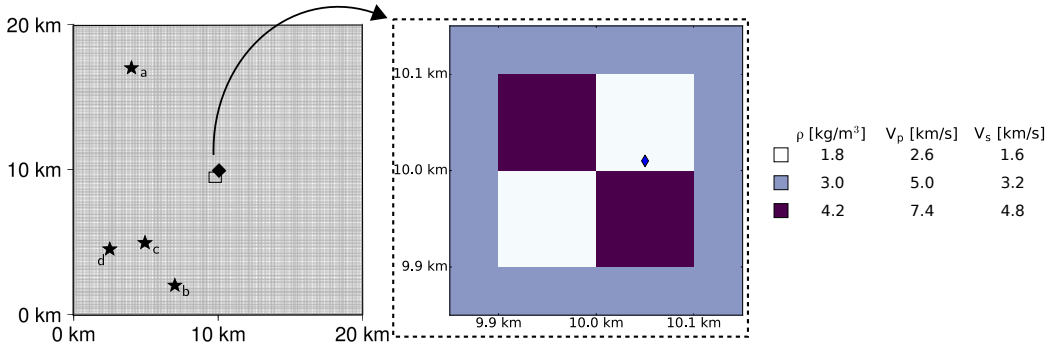

Fig. 4.1.: Left: 2D domain used in Section 4.3.1. The domain is 20×20 km^2 and the heterogeneity at the centre, not to scale, is 200×200 m^2. The stars show the location of the sources and the diamond shows the location of the receiver. All boundaries are absorbing. Middle: Zoom in into the heterogeneity. Right: V_p, V_s and ρ in the domain. The P and S velocities in the outer domain are 5 kms^{-1} and 3.2 kms^{-1}, and velocities for each element inside the heterogeneity are $\pm$50% of the surrounding domain.

4.3 Synthetic Tests

To test inversion of the coupling tensor **J**, we first conduct synthetic tests. In Section 4.3.1, we invert for **J** for a rotational receiver in 2D. This will be followed in Section 4.3.2 where we invert for **J** for a rotational receiver placed on the free surface of a 3D domain. The set up that has been considered in both cases is quite simple in the sense that it does not take into account factors like attenuation and source uncertainties. All simulations are conducted using the Spectral Element Method (SEM) that solves the elastic wave equation.

In both cases, the sources are either forces or moment tensors but we always choose the Ricker wavelet (second derivative of a Gaussian) as the source-time function.

4.3.1 Inversion of **J** for a receiver in a 2D volume

Our first model is a 2D domain whose P and S velocities are 5 kms^{-1} and 3.2 kms^{-1} respectively. The size of the domain is 20×20 km^2. A heterogeneity of size 200×200 m^2 is at the center of the domain and the P and S velocities in each element in the heterogeneity are $\pm$ 50% of the surrounding domain. The geometric configuration of the model is shown in Figure 4.1.

We place the rotational receiver in the heterogeneity so we expect the heterogeneity to affect rotation measurements. We therefore invert for the coupling tensor **J**. To this end, we first perform three simulations in this medium with sources at positions shown by the stars a, b and c respectively in Figure 4.1 to generate the data [Figures 4.2 and 4.3; black lines]. These rotations make up the term on the left in Equation 4.1. The central frequency of all three sources is 1.5 Hz (maximum frequency 4.1 Hz). Two of the sources considered are double-couple, while one is a force. Although the heterogeneity is much smaller than λ_m, the spectral element mesh for the simulation honours all interfaces of the heterogeneity. The rotations computed are therefore considered accurate.

Next, we need to choose an effective model for the inversion. Here, we invert for **J** against two different effective models. The first effective model is the homogenized version of the original medium with $\varepsilon = 0.5$. The second effective model is an entirely homogeneous model with an underlying assumption that the heterogeneous area has negligible effect on the effective model [see Appendix C]. Moreover, this situation is closer to realistic situations where tomographic models are far from perfect.

We use the same three sources as before in the two effective media to compute the rotations and strains at the receiver. These are the two known quantities on the right in Equation 4.1. The rotations measured in the homogenized model are shown in Figure 4.2 (green lines) and those computed in the homogeneous model are shown in Figure 4.3 (green lines). Comparison of the rotations measured in the heterogeneous and homogenized/homogeneous case in the figure reveals a significant difference in all four panels. Clearly, the difference is due to the presence of the heterogeneity and it depends on the path that the waveform takes through the heterogeneity (this is the first effect mentioned in Section 1.3, i.e. disagreement between wavefield gradient data and synthetics computed in a tomographic model).

We use the data and synthetics thus obtained to invert for **J**. The fact that we use SEM to both generate data and to invert for **J** is not an inversion crime here. It would be an inversion crime if the data were generated using the theory of homogenization and if the inversion were performed with the same mesh. Here, we generate the data using a fine mesh with an element size of 100 m, i.e. without the theory of homogenization, but carry out the inversion on a sparse mesh with an element size of 200 m.

Once we obtain **J**, we use it to correct the synthetics, i.e. we add the last term in Equation 4.1 to the rotations measured in homogenized/homogeneous medium. These are shown in Figures 4.2 and 4.3 (red lines). It can be seen that the corrected synthetic rotations are a much better fit to the heterogeneous rotations, but this is unsurprising because these data have been used for the inversion. Therefore, to truly render its accuracy, we use this **J** to a new set of data which has not been used for the inversion [Figures 4.2 and 4.3; Panel d] as validation; the new source positioned at the location shown by the star d in Figure 4.1. The new source is a vertical force. As expected, it can be seen that **J** is able to recover the rotation in the heterogeneous medium.

Difference in amplitudes between the homogenized and the homogeneous rotations (green lines) in Figures 4.2 and 4.3 respectively is present in all panels. This difference is very subtle and further endorses our assumption that the heterogeneous area has negligible effect on the effective model.

4.3.2 Inversion of **J** for a receiver on a 3D surface

Our second model is a 3D domain whose P and S velocities are 5 kms^{-1} and 3.2 kms^{-1} respectively. The domain size is $40\times40\times10$ km^3. A heterogeneity is placed at the center of the surface, with P and S velocities for each element in the heterogeneity chosen randomly and independently but within 25% of the surrounding domain. The spatial extent of the heterogeneity is $1334\times1334\times222$ m^3. The geometric configuration of the model is shown in Figure 4.4.

Because the rotational receiver here is surrounded by the heterogeneity, the rotation measurements are most likely affected by the heterogeneity. We therefore seek for the coupling tensor **J** for this receiver. Here, we only invert for **J** for one component of the rotation, i.e. rotation around the vertical-axis. This allows us to invert for just 6 parameters instead of 18. Note that in this case - where the receiver has been placed at the surface - the free surface condition also allows us to further reduce the number of scalars to be inverted for to 3 [Equation 3.7]. To this end, we perform simulations for three different sources at locations shown by the stars a, b and c in Figure 4.4 in the original medium to generate data [Figures 4.5 and 4.6; black lines]. These rotations form the term on the left in Equation 4.1. All sources have a

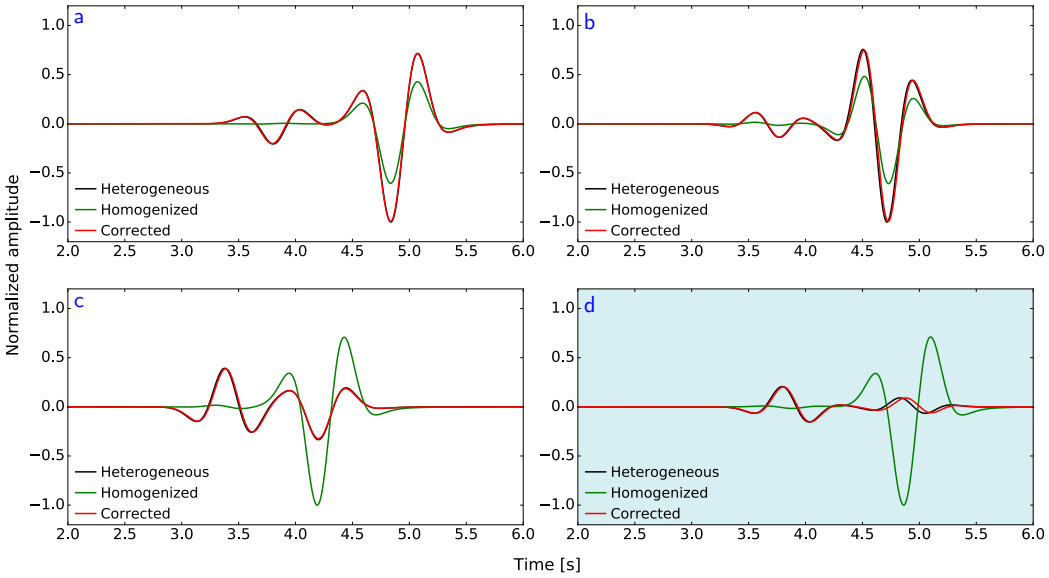

Fig. 4.2.: Rotations. Panels a, b, c: Three events used for inversion of the corrector. Panel d: The event used as validation using this corrector. It is shown on blue to indicate that it has not been used for the inversion.
Heterogeneous and homogenized rotations are shown in black and green respectively. Rotations that have been corrected using the coupling tensor **J** are shown in red.

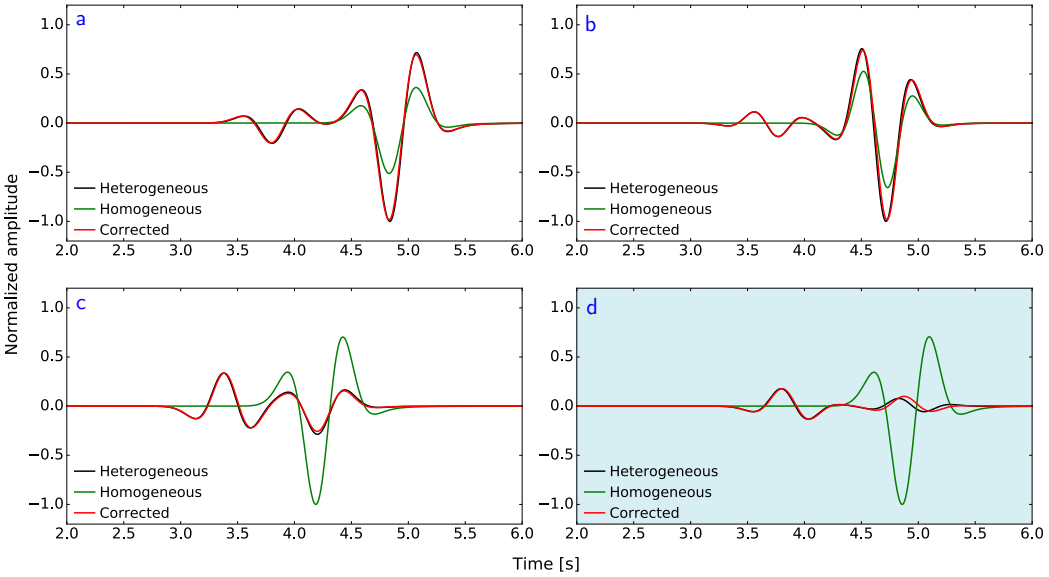

Fig. 4.3.: Rotations. Panels a, b, c: Three events used for inversion of the corrector. Panel d: The event used as validation using this corrector. It is shown on blue to indicate that it has not been used for the inversion.
Heterogeneous and homogeneous rotations are shown in black and green respectively. Rotations that have been corrected using the coupling tensor **J** are shown in red.

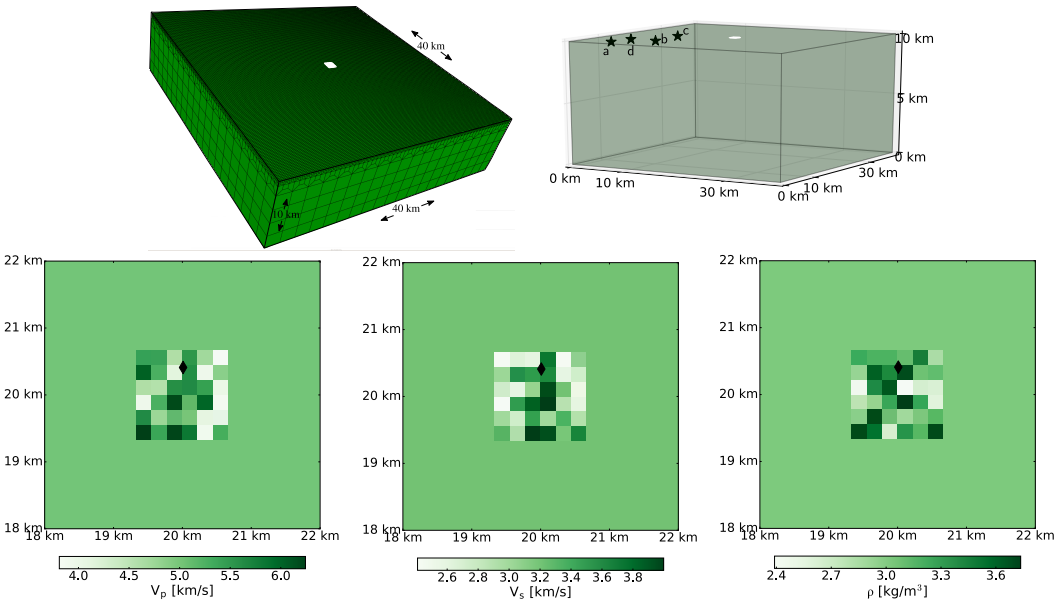

Fig. 4.4.: Top: 3D domain used in Section 4.3.2. The domain is $40\times40\times10$ km^3, and the heterogeneity at the centre, not to scale, is $1334\times1334\times222$ m^3. The stars show the location of the sources and the diamond shows the location of the receiver. All but top boundary are absorbing.
Bottom: Zoom in into the heterogeneity from the top showing the V_p, V_s and ρ in the domain. The P and S velocities in the outer domain are 5 kms^{-1} and 3.2 kms^{-1}, and velocities for each element inside the heterogeneity are chosen randomly and independently, but within 25% of the surrounding domain.

central frequency of 0.5 Hz (maximum frequency 1.4 Hz). Two of the sources are forces, while the third one is a moment tensor. Once again, the mesh honors all boundaries and therefore, the solutions obtained are considered accurate.

Similar to Section 4.3.1, we carry out the inversion using two different effective media: the first one being the homogenized version of the original medium with $\varepsilon = 0.25$ and the second one being the homogeneous medium as an approximation for the effective one [see Appendix C]. We use the same three sources in both media to generate rotations and strains. These are the two known quantities on the right in Equation 4.1. The rotations in these tomographic media are shown in Figures 4.5 and 4.6 (green lines). Comparing the rotations in the heterogeneous and the homogenized/homogeneous media, we see that the waveform is altered in all four cases owing to the heterogeneity (this is the first effect mentioned in Section 1.3, i.e. disagreement between wavefield gradient data and synthetics computed in a tomographic model).

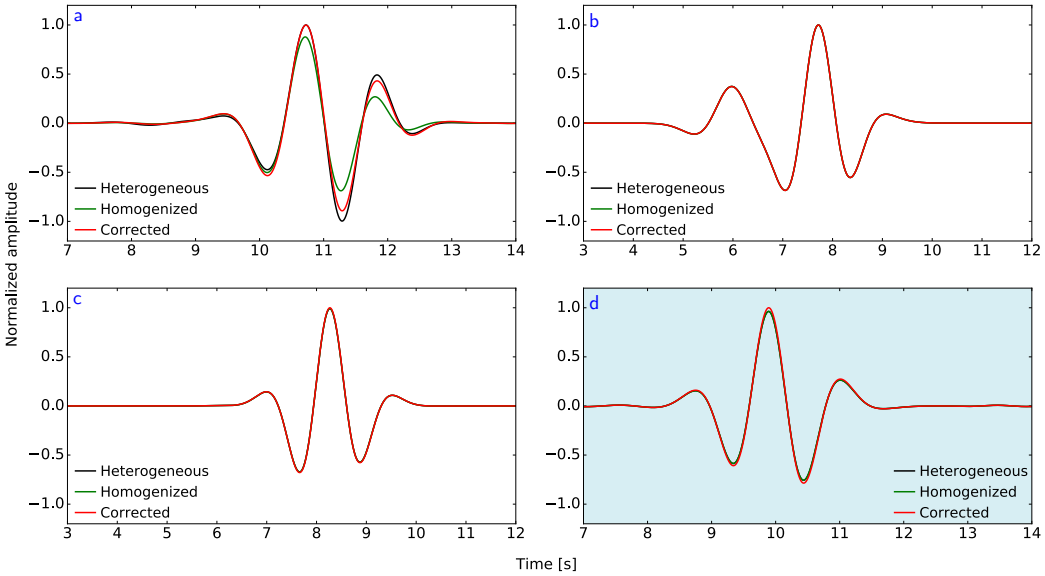

Fig. 4.5.: Rotations around the vertical axis. Panels a, b, c: Three events used for inversion of the corrector. Panel d: The event used as validation using this corrector. It is shown on blue to indicate that it has not been used for the inversion. Heterogeneous and homogenized rotations are shown in black and green respectively. Rotations that have been corrected using the coupling tensor **J** are shown in red.

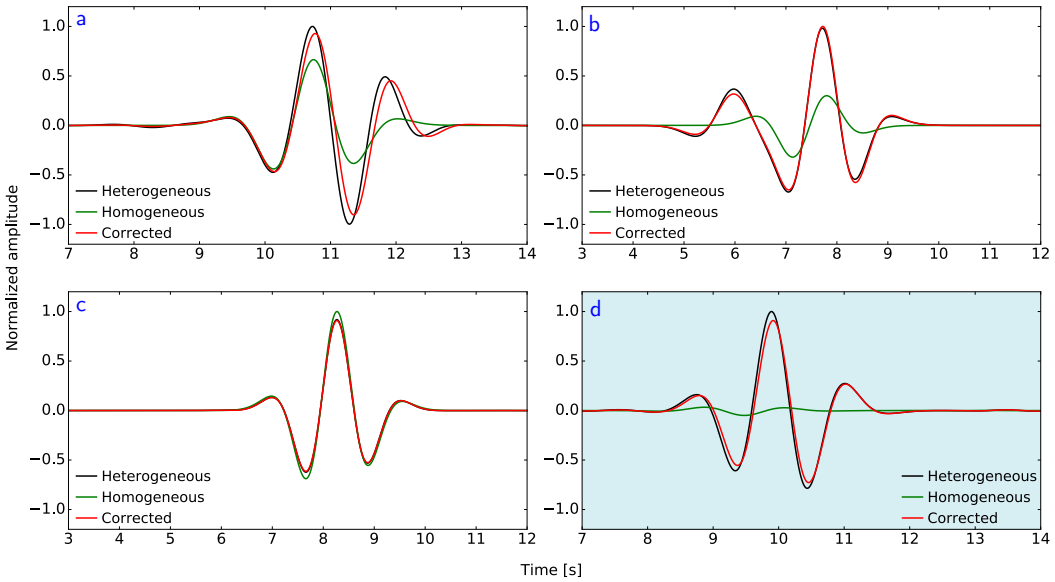

Fig. 4.6.: Rotations around the vertical axis. Panels a, b, c: Three events used for inversion of the corrector. Panel d: The event used as validation using this corrector. It is shown on blue to indicate that it has not been used for the inversion. Heterogeneous and homogeneous rotations are shown in black and green respectively. Rotations that have been corrected using the coupling tensor **J** are shown in red.

We use the data and synthetics thus derived from these simulations to invert for the coupling tensor **J** which is in turn used to correct the synthetic rotations (Figures 4.5 and 4.6; red lines). The corrected synthetic rotations are a much better fit to the heterogeneous rotations, which is expected because these data have been used for the inversion. Finally, we perform one last simulation with the source, which is a moment tensor, at location shown by the star d in Figure 4.4 to validate the coupling on a new set of data [Figures 4.5 and 4.6; Panel d], one that has not been used previously for the inversion. Doing this allows us to estimate the accuracy of **J**. Unsurprisingly, the recovery of the heterogeneous rotation is achievable through **J**.

Unlike Section 4.3.1, the homogenized and the homogeneous rotations (green lines) in Figures 4.5 and 4.6 respectively do not present a subtle difference. The homogenized rotations are much closer to the rotations in the heterogeneous media.

It is important to note that the correction is not always perfect, i. e. the corrected rotations do not always overlap the heterogeneous rotations. This is especially evident in Panels d in Figures 4.2 and 4.3; and a and d in Figure 4.6. The reasons for this are 1) the homogeneous models used here are not a perfect approximation to the homogenized or effective model and 2) the method, being asymptotic, implies some errors.

4.4 Real World Scenario

Ever since it's operation in 2001, the G Ring laser in Wettzell, 150 km north-east of Munich (Figure 4.8; the seismometer WET and the G Ring laser are collocated), has been successfully recording the vertical component of rotation rates that are generated by seismic sources (Igel et al., 2005; Suryanto et al., 2006; Igel et al., 2007). Using two counter propagating beams of wavelength 633 nm to generate a beat frequency, it measures rotation rates as small as $10^{-10}\text{rads}^{-1}\text{Hz}^{-1/2}$ (Schreiber et al., 2003).

Here, we invert for the coupling tensor **J** at this ring laser for long period teleseismic events. In Section 4.4.1, we use the normal mode summation program to compute velocities and rotation rates in PREM (Dziewoński and Anderson, 1981). We show that the agreement between the rotation rates measured at the ring laser and the rotation rates computed in PREM is

less compared to the one between velocities. We invert for the coupling tensor **J** and correct the rotation rates computed in PREM to improve the agreement. In Section 4.4.2, we show that due to small-scale heterogeneities at the receiver, observations of rotation rates and array-derived estimations of rotation rates at the ring laser are not the same. We invert for the coupling tensor **J** and correct the array-derived rotation rates such that they are in better agreement to the observed rotation rates.

We use the definition of L^2 norm defined below to quantify the misfit between the observed and synthetic rotation rates.

$$\xi := \frac{\sqrt{\int_0^{t_{max}} (\dot{\omega} - \dot{\omega}^{data})^2(t)\ dt}}{\sqrt{(\dot{\omega}^{data})^2(t)\ dt}}; \tag{4.3}$$

where $\dot{\omega}$ is the synthetic vertical rotation rate and $\dot{\omega}^{data}$ is the observed vertical rotation rate. Note that this misfit takes into account all parts of the seismogram.

4.4.1 Inversion for **J** at the Ring laser, Wettzell using PREM

We use Obspy (Krischer et al., 2015) to get rotation rates recorded by the ring laser and velocities recorded by the collocated seismometer WET for all events between January 2007 and June 2018 and within Mw 7.0 and 9.0. After download, all data are corrected for instrument response. Next, we compute synthetic velocities and rotation rates by using a normal mode summation program to solve the wave equation in a PREM with ocean and anisotropy. For this, centroid-moment tensor solutions from the GCMT catalog (Ekström et al., 2012) are used with a step function as the source-time function.

We compare the observed and synthetic velocities in order to remove observed data with no visible earthquake signal. Apart from that, no prior selection of events is done.

Comparing the fit between observed and synthetic velocities to the fit between observed and synthetic rotation rates for all events within frequencies 0.002-0.009 Hz, we find that the rotation rates are less in agreement compared to the velocities [see Appendix C]. Often, the misfits as defined in (4.3) are about

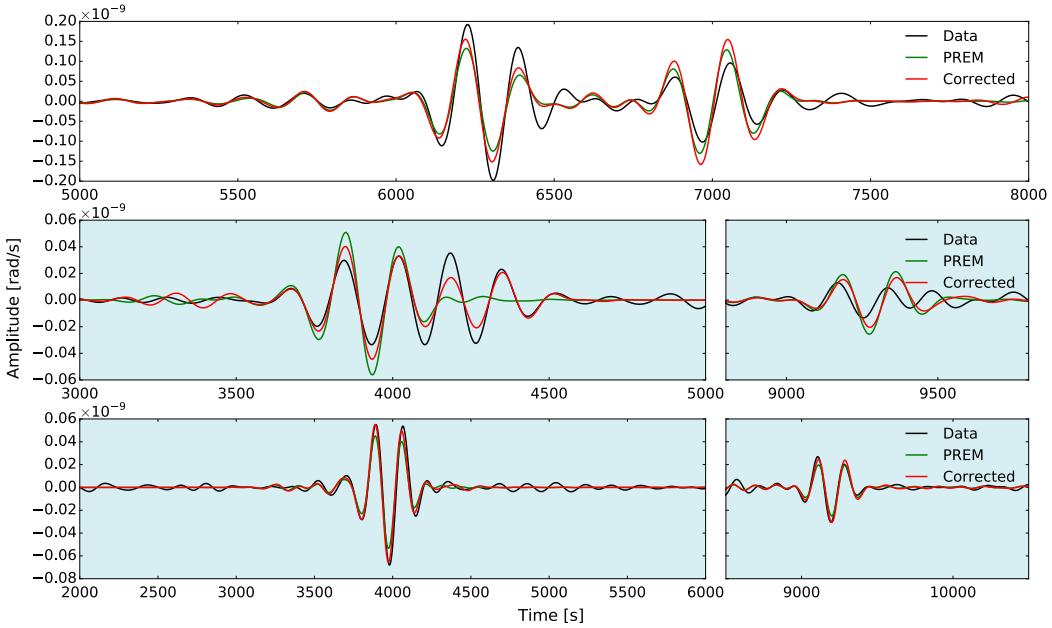

Fig. 4.7.: Rotation rates around the vertical axis. Top: 201611131102A South Island, New Zealand. One of the 32 events from the inversion data set that are used to invert for the coupling tensor **J**. Middle: 201210280304A Queen Charlotte Islands. An event from the validation data set. Bottom: 201006121926A Nicobar Islands. Also an event from the validation data set. The events from the validation data set are shown on blue to indicate that these events have not been used for the inversion.
Data, synthetic and corrected rotation rates are given in black, green and red respectively.

0.3 between the velocities but are greater than 0.7 between the rotation rates (this is the first effect mentioned in Section 1.3, i.e. disagreement between wavefield gradient data and synthetics computed in a tomographic model). We suspect this to be due to small-scale heterogeneities at the ring laser and therefore, invert for **J** using 32 events. A figure showing the source-receiver distribution in shown in Appendix D. The **J** thus obtained is in turn used to correct the synthetic rotation rates. One of such events is shown in Figure 4.7 (top panel). A validation data set is then set up to help access the quality of our results. It includes 32 events not used in the inversion. Two of the events from this validation data set are shown in Figure 4.7 (bottom panels). In all panels, we see distinct arrivals of direct Love waves and indirect Love waves. We also see that the corrected rotation rates (red lines) are a better fit to the observed rotation rates (black lines) than the synthetic rotation rates (green lines). Misfits for about 72% of the events in the validation data set improve after the introduction of **J**, proving that indeed, **J** is a good indication of the coupling. For example, the misfit for the event shown in the middle panel of Figure 4.7 reduced from 0.86 to 0.63.

4.4.2 Inversion for **J** at the Ring laser, Wettzell using array-derived estimates

In the absence of small-scale heterogeneities, wavefield gradients estimated at a point using the finite-difference of array data are the same as wavefield gradients measured at the point. In practice, this is not the case. Wavefield gradients estimated from an array have their coupling tensor although it appears in a slightly different form [see Appendix B] than that of wavefield gradients measured at a point. In the case of rotation, the two coupling tensors are related through the following equations:

$$\omega(\mathbf{x},\mathbf{y},t) = \omega^0(\mathbf{x}) + \mathbf{J}(\mathbf{y}) : \boldsymbol{\epsilon}(\mathbf{u}^0(\mathbf{x},t)),$$
$$\omega^{\text{AD}}(\mathbf{x},\mathbf{y},t) = \omega^0(\mathbf{x}) + \mathbf{J}^{\text{AD}}(\mathbf{y}) : \boldsymbol{\epsilon}(\mathbf{u}^0(\mathbf{x},t)),$$

where ω^0 is the rotation in an effective model. ω is the rotation measured at a point and $\mathbf{J}$ is its coupling tensor. Similarly, ω^{AD} is the rotation estimated at a point using array derived measurements and $\mathbf{J}^{\text{AD}}$ is its coupling tensor. These equations lead to

$$\omega(\mathbf{x},\mathbf{y},t) = \omega^{\text{AD}}(\mathbf{x},\mathbf{y},t) + \mathbf{J}^{\dagger}(\mathbf{y}) : \boldsymbol{\epsilon}(\mathbf{u}^0(\mathbf{x},t)), \tag{4.4}$$

where $\mathbf{J}^{\dagger}(\mathbf{y}) = \mathbf{J}(\mathbf{y}) - \mathbf{J}^{\text{AD}}(\mathbf{y})$.

If we consider a similar equation for array-derived strains, we have,

$$\boldsymbol{\epsilon}^{\text{AD}}(\mathbf{x},\mathbf{y},t) = \boldsymbol{\epsilon}(\mathbf{u}^0(\mathbf{x},t)) + \mathbf{K}^{\text{AD}}(\mathbf{y}) : \boldsymbol{\epsilon}(\mathbf{u}^0(\mathbf{x},t)),$$
$$\boldsymbol{\epsilon}^{\text{AD}}(\mathbf{x},\mathbf{y},t) = \mathbf{G}(\mathbf{y}) : \boldsymbol{\epsilon}(\mathbf{u}^0(\mathbf{x},t)),$$

where $\boldsymbol{\epsilon}(\mathbf{u}^0(\mathbf{x},t))$ is the strain in the effective medium, $\boldsymbol{\epsilon}^{\text{AD}}$ is the array-derived strain and $\mathbf{K}^{\text{AD}}$ is its corrector, similar to the $\mathbf{J}^{\text{AD}}$ for rotations. $\mathbf{G} = \mathbf{I} + \mathbf{K}^{\text{AD}}$. These equations lead to

$$\boldsymbol{\epsilon}(\mathbf{u}^0(\mathbf{x},t)) = \mathbf{G}^{-1}(\mathbf{y})\ \boldsymbol{\epsilon}^{\text{AD}}(\mathbf{x},\mathbf{y},t) \tag{4.5}$$

Substituting $\boldsymbol{\epsilon}(\mathbf{u}^0(\mathbf{x},t))$ in Equation 4.4 by Equation 4.5, we get

$$\omega(\mathbf{x},\mathbf{y},t) = \omega^{\text{AD}}(\mathbf{x},\mathbf{y},t) + \mathbf{J}^{\dagger}(\mathbf{y})\mathbf{G}^{-1} : \boldsymbol{\epsilon}^{\text{AD}}(\mathbf{x},\mathbf{y},t). \tag{4.6}$$

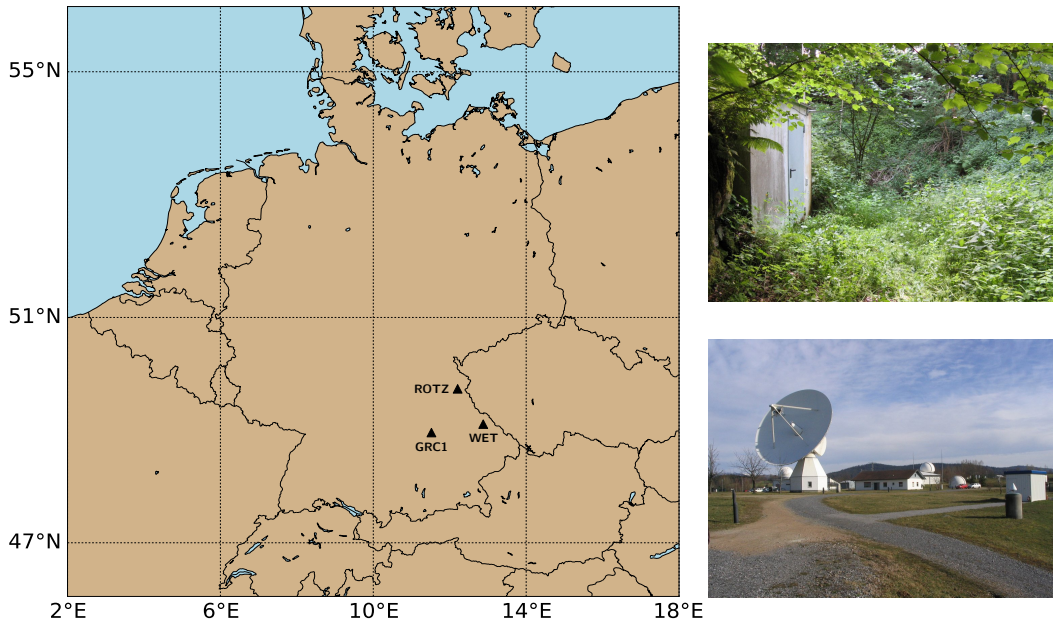

Fig. 4.8.: Left: location of the receivers used for the finite difference. Right: Location of the seismometer ROTZ (top) and WET (bottom).

Note that through Equation 4.6, we eliminate the need of an effective medium. But unlike the sections before, we invert not only for coupling tensor for rotation $\mathbf{J}$ but the product of the coupling tensor for rotation and the inverse of coupling tensor for strain, i.e $\mathbf{J}^{\dagger}(\mathbf{y})\mathbf{G}^{-1}(\mathbf{y})$.

For our purpose, we use velocities recorded at stations WET, ROTZ and GRC1 (Figure 4.8) [see Appendix A] to estimate array-derived rotation rates at the ring laser. Each station is a broadband STS-2 seismometer that measures velocity with a sampling rate of 20 Hz. The distance between each station is in the order of 100 km. Assuming an average phase velocity of 3 kms^{-1}, we look at all events between January 2007 and June 2018 for frequencies between 0.0005 and 0.003 Hz following Poppeliers and Evans (2015) and Langston (2007b).

We select only 7 events due to their good signal to noise ratio. A figure showing the source-receiver distribution in shown in Appendix D. Comparing the array-derived rotation rates to those observed at the ring laser, we find that the misfits are always above 0.75 even though the velocities from three seismometers are always in agreement (this is the second effect mentioned in Section 1.3, i.e. dissimilarity between wavefield gradients measured at a point and wavefield gradients estimated at the point using an array). Therefore,

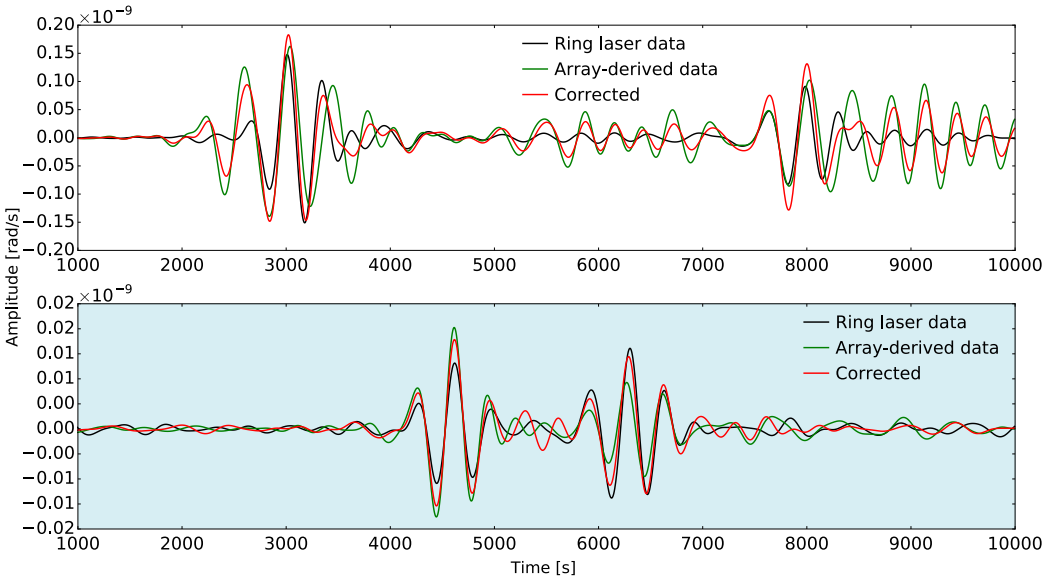

Fig. 4.9.: Rotation rates around the vertical axis. Top: 201103110546A Near East Coast of Honsh. One of the 6 events from the inversion data set that are used to invert for the coupling tensor $\mathbf{J}^{\dagger}\mathbf{G}$. Bottom: 200909291748A Samoa Islands Region. An event from the validation data set. It is shown on blue to indicate that this event has not been used for the inversion.
Observed, array-derived and corrected rotation rates are given in black, green and red respectively.

we follow the same procedure as in Section 4.4.1 and use 6 events for the inversion of $\mathbf{J}^{\dagger}\mathbf{G}$. We then use $\mathbf{J}^{\dagger}\mathbf{G}$ to correct the array-derived rotation rates. One of these events is shown in Figure 4.9 (top panel). The validation data set in this case consists of 1 event that has not been used for the inversion. This event is shown in Figure 4.9 (bottom panel). For both events, we see distinct arrivals of direct Love waves and indirect Love waves phases. Furthermore, we see that the corrected rotation rates (red lines) are in better agreement to the observed rotation rates (black lines) than the array-derived rotation rates (green lines). In this case, the misfit for the validation data set was 0.66 originally. After the introduction of the coupling tensor however, the misfit improved to 0.45.

Note that usually, when estimating array-derived rotations, the effect of small-scale structures is often ignored. In that case, many stations are needed to average out the effect and minimize the coupling tensor $\mathbf{J}$. Here, we explicitly account for the effect and therefore, it is futile to increase the number of stations.

4.5 Discussion and Conclusion

Through the theory of homogenization, we introduced the coupling tensor **J** and showed that at any receiver measuring wavefield gradient, small-scale heterogeneities cause the wavefield gradient to couple with the strain of effective displacement through J. Although we focused on the coupling tensor for rotations, it turns out that the coupling tensor for strains is the transformation matrix **T** introduced in Berger and Beaumont (1976).

Therefore, a knowledge of **J** is needed to correct for this coupling. One option to determine **J** would be through direct computation, but this is only feasible if all fine-scales at the receiver are well-known. The second option is to determine **J** through linear inversion and unlike the speculation made by King and Bilham (1973), it is easy to correct for the coupling. It is indeed possible to perform this inversion because **J** does not depend on source or time. It is a characteristic of the receiver location. One necessary condition for this inversion however is that an effective model that fits displacement data well is needed. This is not an issue for most synthetic cases where either the homogenous or homogenized equivalent of the medium can be used as an effective model, and for low frequency data where PREM can be used as the effective model.

We then inverted for **J** for rotational receivers in two synthetic cases, one in 2D and one in 3D. In both these examples, we used the **J** to correct synthetic rotations and saw that the corrected synthetic rotations were a better match to the synthetic data as compared to synthetic rotations. This was also true for rotations that were not used for inversion. We conclude that although the effect of small-scale heterogeneities can be substantially large, it can be corrected for. The setting for our synthetic examples was one where the sources are either forces or moment tensors; however, further tests in different settings reveal the same conclusion.

Next, we introduced **J** to rotation rates measured by the G Ring laser in Germany. It is important to note that data are unavoidably affected by factors such as topography, instrument errors, background noise and so on. Furthermore, the bedrock at Wettzell consists mostly of igneous and metamorphic rocks, thus suggesting a very small correction. Nevertheless, we saw that the misfit was better between the observed and the corrected rotation rates

as compared to the one between observed and synthetic rotation rates. According to van Driel et al. (2012), the G Ring laser is situated at the local minima of the coupling tensor due to topography. This can be verified also for geological heterogeneities if other rotational sensors are installed nearby.

One other consequence of small-scale heterogeneities is that wavefield gradients measured at a point do not coincide with wavefield gradients estimated at the point using an array. However, we showed that the coupling tensor $\mathbf{J}$ for one can be related to coupling tensor $\mathbf{J}$ of another. This was confirmed in the last section where we see a disagreement between the rotation rates estimated at the G Ring laser using an array and the rotation rates measured by it. We corrected for the array-derived rotation rates and the agreement between corrected rotation rates and the rotation rates measured by the ring laser improved significantly. Our corresponding values to the three coupling constants given by van Driel et al. (2012) are 0.43, 0.19 and 0.12. These are large compared to their values, but we compute the array-derived rotation areas over a greater area. Furthermore, our coupling tensor does not take into account only the effects of topography, but also the effects due to geological heterogeneities.

Although all examples here are based on rotation and rotation rates, the results can be extended to any other wavefield gradient with no modifications.

Acknowledgements

We would like to thank Michael Afanasiev, Johana Brokešová and Martin van Driel whose comments have really improved the clarity of the work.

This work was funded by the French National Research Agency (ANR-16-CE31-0022). We also thank the support through the European Research Council (Advanced Grant: ROMY, number: 339991). Numerical simulations were performed at CCIPL and we thank the people who work endlessly to maintain the system. Obspy was acquired from `https://github.com/obspy/obspy/wiki`[1] and all event data were acquired from the global CMT catalog, i.e. `https://www.globalcmt.org/`[7] (Ekström et al., 2012).

[1]Last Accessed on September 29, 2020

Mapping discontinuities 5

In Chapter 3, we demonstrated that wavefield gradients (strains and rotations) are affected by small-scale structures close to the receiver, such as discontinuities or geological heterogeneities. Therefore, using a dense array of receivers that measure strains or rotations, one could take advantage of this property to explore and map small-scale structures.

I begin the chapter with a brief account of previous works that have been done so far. This is followed by two sections where I introduce two ways in which the property can be harnessed to map discontinuities. Each section begins with a numerical example as a proof of concept before moving on to real data.

5.1 Previous Work

Studies such as Harrison (1976); Kohl and Levine (1995); Langston (2007b,a) suggested that since tilts and strains are affected by small-scale structures, they could be used to infer geological heterogeneities.

Takeo and Ito (1997) showed that analysis of rotations from an array near a fracture site can help in the location of fault lines. Similarly, Meertens et al. (1989) used the discrepancies between tiltmeter measurements recorded and tiltmeter predictions obtained from Finite Element Method (FEM) at five sites in the Yellowstone National Park to locate sharp contrasts in the region. They used the axially symmetric model from Harrison (1978) to generate a 3D model of the region but their model was inconsistent with those derived from other seismic, refraction and gravity data.

5.2 Mapping discontinuities through the wavefield

In Chapter 3, we showed that wavefield gradients obtained using a dense array are affected by structures smaller than the dimension of the array. Here, we benefit from this property to map these structures. In other words, an imprint of the small-scale structures such as discontinuities will show up on wavefield gradients but will be missed by translations. At this point, we simply try to see if small-scale discontinuities are visible on the wavefield gradient. We do not make any link between wavefield gradients and small-scale structures in the medium, but we reserve this for the next section instead.

In all examples that follow[1], we simply look at displacement gradient instead of wavefield gradient. This allows us to make use of real data where only one component of translation is recorded.

5.2.1 Numerical Example

Our model for the numerical example is a 3D domain whose P and S velocities are 5 kms^{-1} and 3.2 kms^{-1} respectively. The domain size is $40\times40\times10$ km^3. A heterogeneity is placed at the center of the surface, with P and S velocities for each element in the heterogeneity chosen randomly and independently but within 25% of the surrounding domain. This particular value has no special intention; but it is still meaningful because even larger velocity contrasts can be found in nature. The spatial extent of the heterogeneity is $1334\times1334\times222$ m^3, extending over 6×6 elements. The geometric configuration of the model is shown in Figure 5.1.

This heterogeneity chosen exhibits a flat power spectrum (within the range of wavenumber chosen). This is unlike for the Earth where the mantle exhibits a spectrum of $\frac{1}{k}$ (Batchelor, 1959; Olson et al., 1984; Mancinelli et al., 2016) and where the crust exhibits a spectrum of $\frac{1}{k^2}$; where k is the wavenumber of the heterogeneities (Wu et al., 1994; Meschede and Romanowicz, 2014). For

[1] All examples in this section are accompanied by a movie. Links are provided, but not all web browsers seem to support them. Using Google Chrome is a surefire way to enjoy the movies.

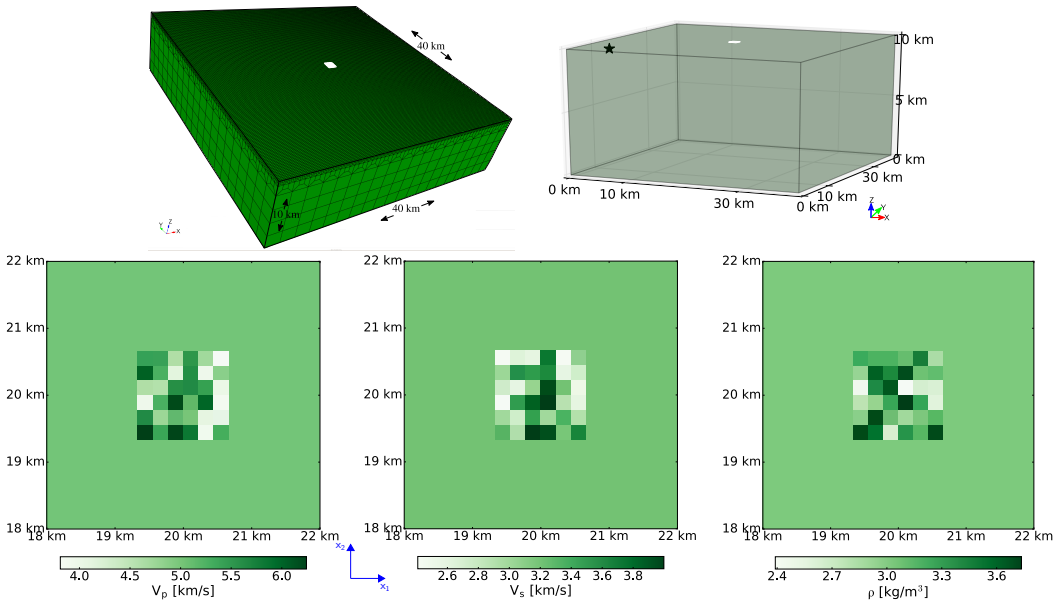

Fig. 5.1.: Top: 3D domain used in Section 5.2.1. The domain is $40\times40\times10$ km^3, and the heterogeneity at the centre, not to scale, is $1334\times1334\times222$ m^3. The star shows the location of the source. The location of the receivers is shown in Figure 5.2. All but top boundary are absorbing.
Bottom: Zoom in into the heterogeneity from the top showing the V_p, V_s and ρ in the domain. The P and S velocities in the outer domain are 5 kms^{-1} and 3.2 kms^{-1}, and velocities for each element inside the heterogeneity are chosen randomly and independently, but within 25% of the surrounding domain.

this numerical example, we could have chosen a heterogeneity spectrum that is closer to the Earth, but we prefer a simpler one to validate our concept. Furthermore, for the numerical example, the variation of both large-scales and small-scales is such that there is a possibility to sample the medium smoothly enough, i.e. with the help of a close receiver configuration. In that case, there is no (spatial) aliasing introduced. This is not the case for the Earth. The small-scales are multi-scale: they have no lower limit. This implies that no receiver configuration will be dense enough to avoid (spatial) aliasing.

We start by placing a source with central frequency 0.5 Hz (maximum frequency 1.4 Hz) at a location shown by the star in Figure 5.1. The source is a moment tensor and its source-time function is a Ricker wavelet (second derivative of a Gaussian). Then, we lay out 1225 receivers at the top right corner of the heterogeneity such that they are spaced 20 m apart on a square grid. The location of the receivers is shown in Figure 5.2.

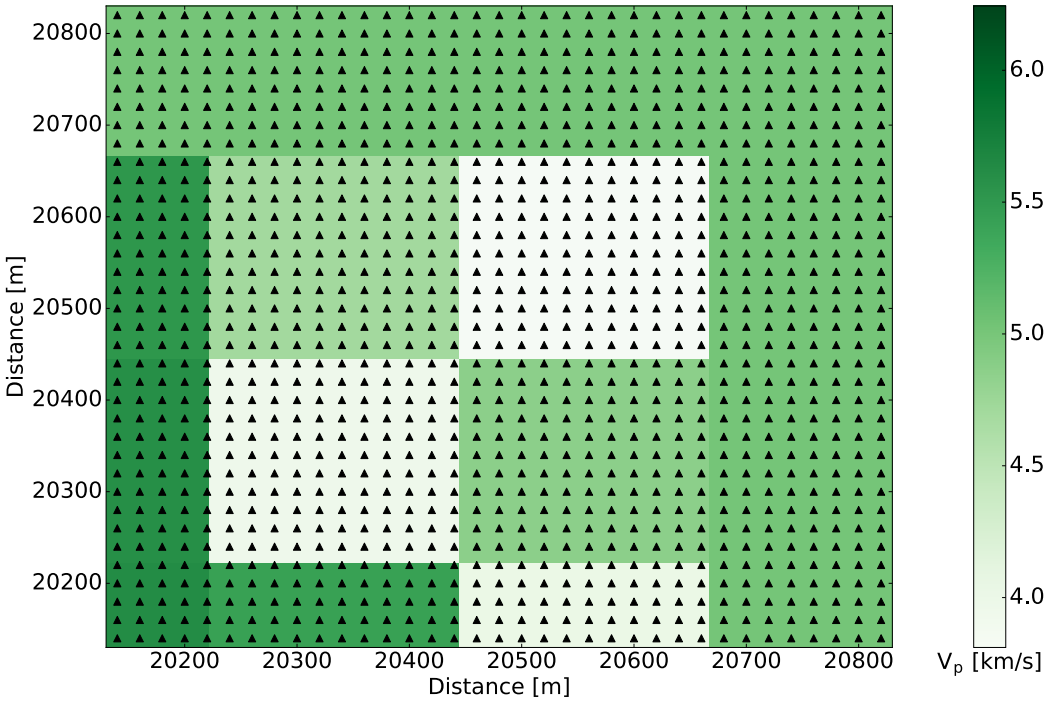

Fig. 5.2.: Zoom in on the surface of the 3D domain shown in Figure 5.1. The receiver locations are shown by the triangles. Background color shows the P-wave velocity.

We use the Spectral Element Method (SEM) to obtain the displacements recorded by the 1225 receivers. Then, we use the horizontal displacements $\mathrm{u}_{x_2}(x_1, x_2)$ to get the spatial displacements through the array. A forward scheme in the x_1-direction is employed, i.e. at each receiver location, $\partial x \mathrm{u}'_{x_2}(x_1, x_2) = \mathrm{u}_{x_2}(x_1 + \partial x, x_2) - \mathrm{u}_{x_2}(x_1, x_2)$; where $\mathrm{u}'_{x_2}(x_1, x_2)$ is the spatial gradient of the horizontal displacement $\mathrm{u}_{x_2}(x_1, x_2)$, $\mathrm{u}_{x_2}(x_1 + \partial x, x_2)$ and $\mathrm{u}_{x_2}(x_1, x_2)$ are the vertical displacements measured at locations $(x_1 + \partial x, x_2)$ and (x_1, x_2) respectively and $\partial x = 20$ m. Finally, we render the displacement $\mathrm{u}_{x_1}(x_1, x_2)$ and spatial gradient $\mathrm{u}'_{x_2}(x_1, x_2)$ data across the array and render them into movies, found here.[2] A snapshot of the movie is shown in Figure 5.3.

In the movies, we can see the arrival of P waves at approximately 8.2 s, the arrival of S waves at approximately 10.7 s, and the arrival of Rayleigh waves after. As each wave passes by, we notice that the displacement does not carry any imprint of the small-scale structures, but its gradient carries imprints of the heterogeneity boundaries.

[2] https://lpg-umr6112.fr/lpg/fichiers/singh-s/syn.mp4; Last Accessed on September 29, 2020

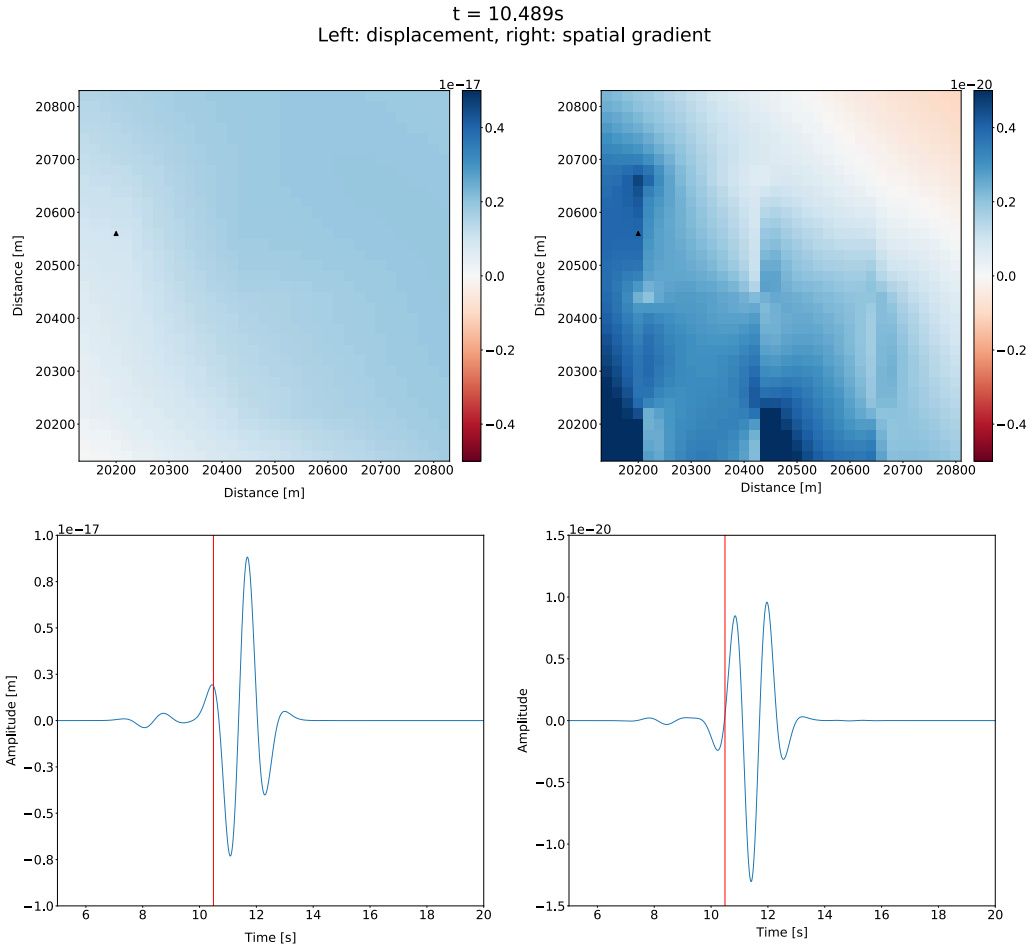

Fig. 5.3.: Snapshot of the movie for the numerical example. Horizontal displacement $u_{x_1}(x_1, x_2)$ is shown on the left and the spatial gradient $u'_{x_2}(x_1, x_2)$ is shown on the right. The two panels below show the displacement and spatial gradient recorded at a receiver, which is marked in the upper panels by the black triangle.

5.2.2 Real Data

Here, we mimic the synthetic example with real data. We emphasize once again that we are only trying to observe structural discontinuities on the wavefield gradient.

Our requirement is a dense network that has records of earthquakes at far-field. We start therefore with the Transportable Array in the western United States, then the Sage Brush Nodal Flats Array in California and then the Sweetwater Array in Texas. We use Obspy (Krischer et al., 2015) to get all data. Assuming an average phase velocity of 3 kms^{-1}, the frequency range chosen for all arrays are between those suggested by Langston (2007b) and

Poppeliers and Evans (2015). For each example, the full seismogram for a given receiver is shown in Appendix E.

We also drift from the (x_1, x_2) coordinate system used in the numerical example to (E,N), where E and N stand for the east and the north directions respectively.

Transportable Array

The Transportable Array (Meltzer et al., 1999; Liang and Langston, 2009; Kerr, 2013) is a part of the USArray, a brad-band network in the United States with more than 400 stations and a spacing of 70 km. The initial deployment was in the west coast in August 2007; the stations were then gradually rolled to the east coast for a span of 10 years. At present, it is being deployed at Alaska and north-western Canada. A long term Reference Network is an additional network of $\sim$100 sites with a spacing of 300 km that serves as its reference frame.

The seismometers are the Guralp CMG3T braodband sensors with a flat velocity response down to a period of 120 s and a sampling rate of 40 Hz. Here, we use the displacements recorded at 216 receivers of the array due to the Mw7.7 Sea of Okhotsk event which occurred on July 5, 2008 (GCMT catalog; Ekström et al. (2012)). The latitude, longitude and depth of the source according to the catalog are 54.12° N, 153.37° E and 610.8 km respectively. At that time, the array was stationed at the west coast. The distance between the source and the array is around 6500 km. A figure showing the source and subsequent receiver locations are shown in Figure 5.4.

We get vertical displacements recorded by 216 receivers for the event. After download, all data are corrected for instrument response and filtered between 0.001 and 0.008 Hz (between 125 and 1000 s) using a band-pass filter. We then use these displacements to obtain the spatial gradients through the array. A forward difference scheme in the east direction is employed, i.e. at each receiver location, the spatial gradient is computed via $\partial \mathrm{E} u'_{\mathrm{Z}}(\mathrm{E}, \mathrm{N}) = u_{\mathrm{Z}}(\mathrm{E} + \partial \mathrm{E}, \mathrm{N}) - u_{\mathrm{Z}}(\mathrm{N}, \mathrm{E})$; where $u'_{\mathrm{Z}}(\mathrm{N}, \mathrm{E})$ is the spatial gradient of vertical displacement, $u_{\mathrm{Z}}(\mathrm{E} + \partial \mathrm{E}, \mathrm{N})$ and $u_{\mathrm{Z}}(\mathrm{E}, \mathrm{N})$ are the vertical displacements measured at locations $(\mathrm{E} + \partial \mathrm{E}, \mathrm{N})$ and (E, N) respectively and $\partial \mathrm{E} = 70$

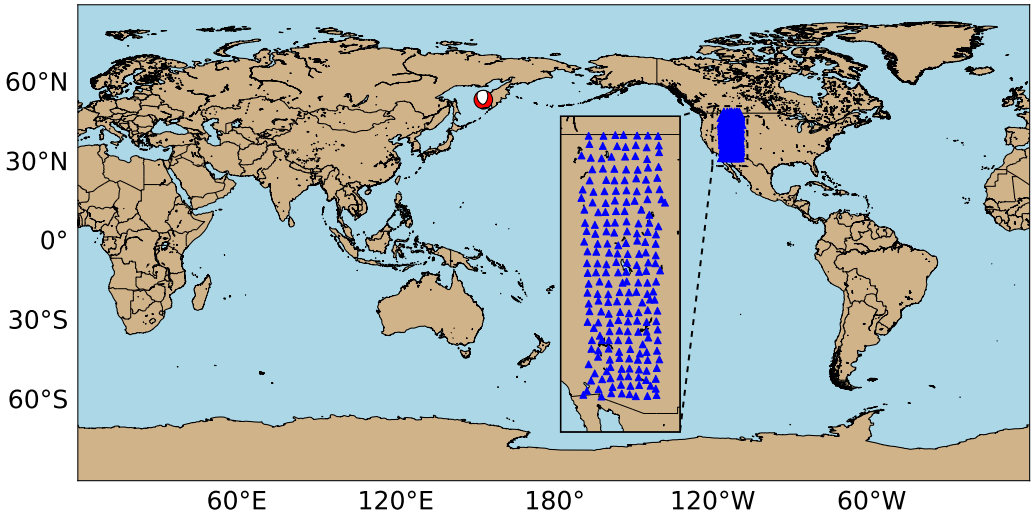

Fig. 5.4.: Receivers of the US Transportable Array used in Section 5.2.2. The inset zooms in on the relative location of the receivers. The source location is shown by the beachball.

km. Although all the receivers chosen do not lie exactly on a regular grid [see Figure 5.4], we assume that the error due to this is negligible, and do not attempt to correct for this.

Finally, we render the displacement and the spatial gradient data across the array and bundle them into movies, found here.[3] A snapshot of the movie is shown in Figure 5.5. Vertical displacement is shown on the left and its spatial gradient is shown on the right. The two panels below show the displacement and spatial gradient recorded by the receiver L15A, which is marked in the movies by the black triangle.

From the movie, we can see the arrival of P waves at approximately 500 s and the S waves at approximately 905 s. At 620 s, we can see a PP wave in the movie for displacement. Note that some of the receivers are noisy [See for example, the receiver marked 'N' in the left panel in Figure 5.5] and that this noise propagates into the spatial gradient [See for example, the two receivers marked 'N' in the right panel in Figure 5.5]. As a result, it is difficult to see an imprint of any small-scale structures.

[3] `https://lpg-umr6112.fr/lpg/fichiers/singh-s/us.mp4`; Last Accessed on September 29, 2020

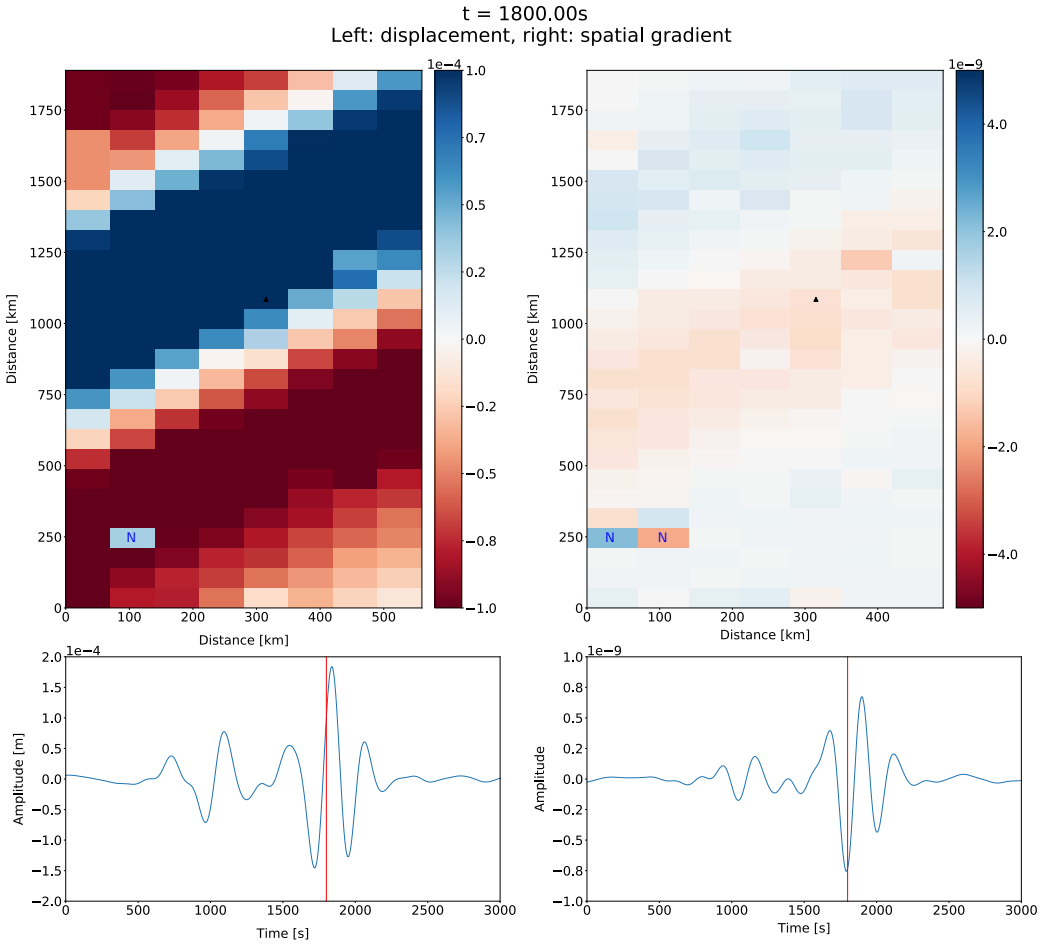

Fig. 5.5.: Snapshot of the movie for the US Transportable Array. Vertical displacement $u_Z(E, N)$ is shown on the left and its spatial gradient $u'_Z(E, N)$ is shown on the right. The two panels below show the displacement and spatial gradient recorded at the receiver L15A, which is marked in the upper panels by the black triangle.

This is also true when one decides to get rid of the noisiest receivers by looking at only a part of the network, as shown by the movie here[4] and the snapshot in Figure 5.6. Although the last five rows of receivers have been removed, some other receivers are noisier than others [See for example, the receiver marked 'N' in the left panel in Figure 5.6] and this dominates in the spatial gradient [See for example, the two receivers marked 'N' in the right panel in Figure 5.6].

[4] `https://lpg-umr6112.fr/lpg/fichiers/singh-s/half_us.mp4`; Last Accessed on September 29, 2020

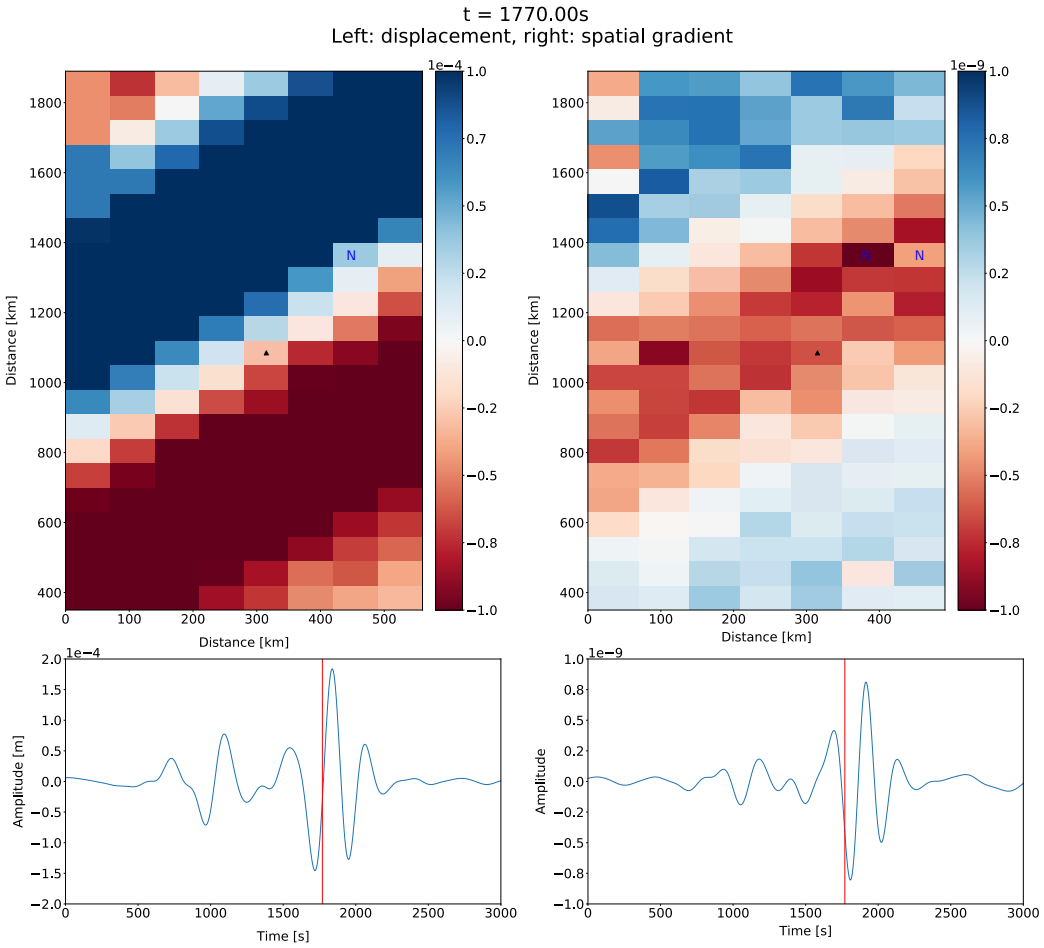

Fig. 5.6.: Snapshot of the movie for the part of US Transportable Array. Vertical displacement $u_Z(E, N)$ is shown on the left and its spatial gradient $u'_Z(E, N)$ is shown on the right. The two panels below show the displacement and spatial gradient recorded at the receiver L15A, which is marked in the upper panels by the black triangle.

Sage Brush Nodal Flats Experiment

The Sage Brush Nodal Flats Experiment is an array of 1108 vertical geophones straddling on the Clark branch of the San Jacinto Fault Zone at the Sage Brush site southeast of Anza, California (Ben-Zion et al., 2015; Meng and Ben-Zion, 2017; Gradon et al., 2019) from 7 May, 2014 to 13 June, 2014. 20 rows perpendicular to the fault line with each row of 50 sensors were deployed and the remaining 108 sensors were developed as extensions to some rows such that the entire array occupied an area of 600 $\times$ 600 m^2. The distance between each row was 30 m and each column was 10 m.

The geophones had a corner frequency of 10 Hz and a sampling rate of 500 Hz. During their deployment, they recorded the vertical component of earthquakes, noise and other controlled source signals. Here, we look at the MW4.2 Southern California event that occurred on June 2, 2014 (IRIS Event Page). The latitude, longitude and depth of the event are 34.09° N, 118.50° W and 9.7 km respectively. The distance between the source and the array is around 190 km.

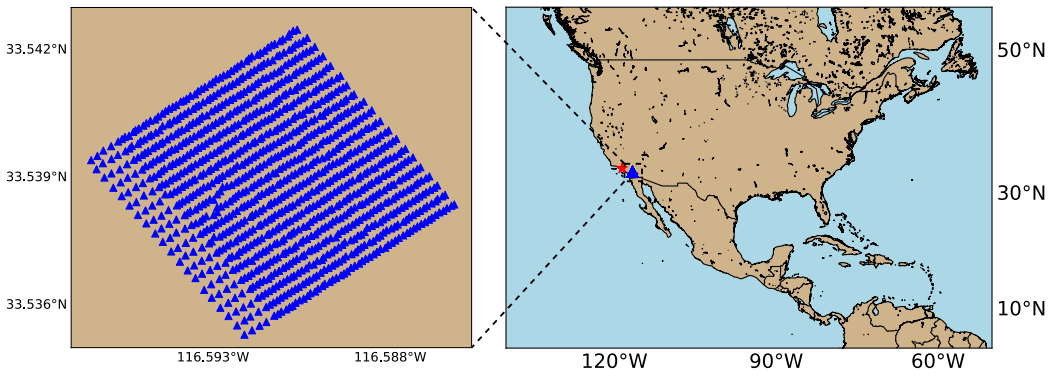

Fig. 5.7.: Right: Receivers of the Sage Brush Nodal Flats Experiment used in Section 5.2.2. The source location is shown by the red star. Left: Zoom in showing the relative location of the receivers.

We get vertical displacements recorded by 1080 geophones for this event. The location of the source and the receivers used are shown in Figure 5.7. After download, all data are corrected for instrument response and filtered between 2 and 24 Hz (between 0.42 and 0.5 s) using a bandpass filter. The receivers with no data are substituted with their immediate neighbours to the west.

We use the vertical displacements to obtain spatial gradients through the array. A forward difference scheme in the north direction is deployed, i.e. at each receiver location, the spatial gradient is computed via $\partial \mathrm{N} u'_{\mathrm{N}}(\mathrm{E}, \mathrm{N}) = u_{\mathrm{Z}}(\mathrm{E}, \mathrm{N} + \partial \mathrm{N}) - u_{\mathrm{Z}}(\mathrm{E}, \mathrm{N})$; where $u'_{\mathrm{Z}}(\mathrm{E}, \mathrm{N})$ is the spatial gradient of displacement, $u_{\mathrm{Z}}(\mathrm{E}, \mathrm{N} + \partial \mathrm{N})$ and $u_{\mathrm{Z}}(\mathrm{E}, \mathrm{N})$ are the vertical displacements measured at locations $(\mathrm{E}, \mathrm{N} + \partial \mathrm{N})$ and (E, N) respectively and $\partial \mathrm{N} = 30$ m. Finally, we render the displacement and the spatial gradient data and bundle them into movies, found here.[5] A snapshot of the movie is shown in Figure 5.8. Vertical displacement is shown on the left and its spatial gradient is shown on the right. The two panels below show the displacement and spatial gradient

[5] `https://lpg-umr6112.fr/lpg/fichiers/singh-s/zg.mp4`; Last Accessed on September 29, 2020

recorded by the receiver R2010, which is marked in the movies by the black triangle.

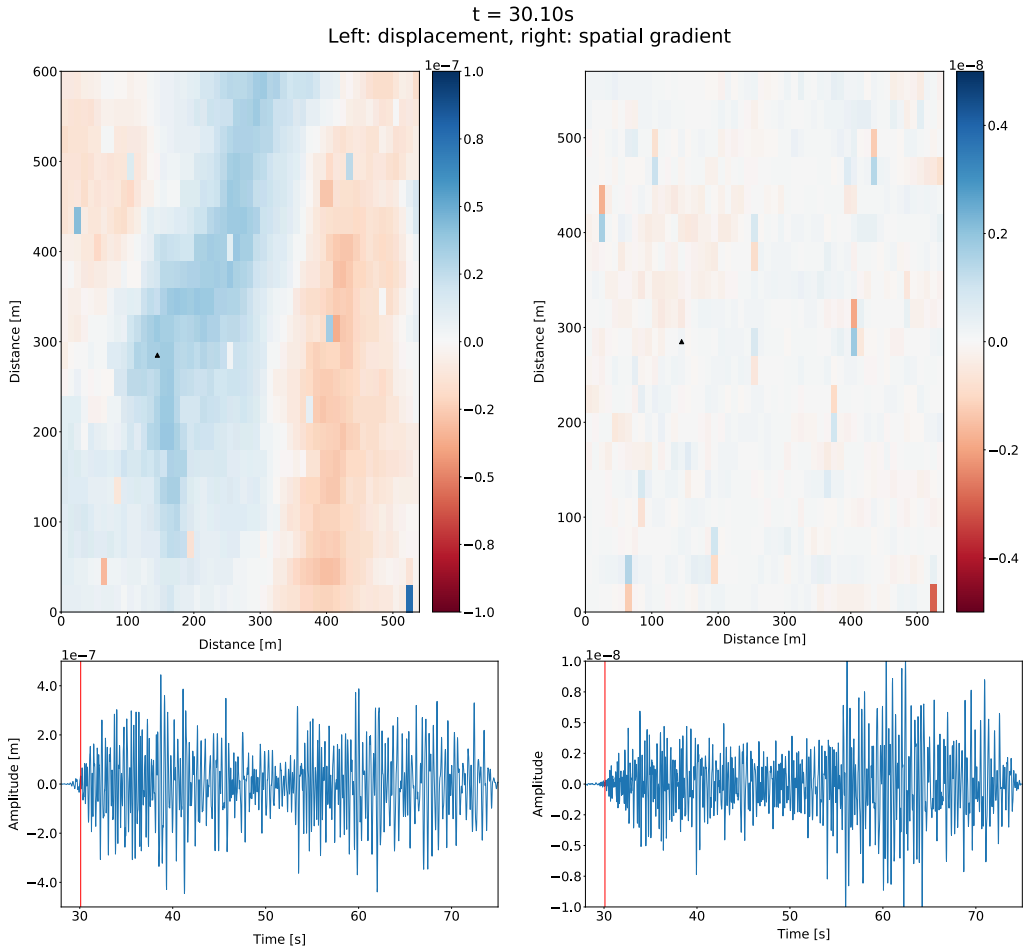

Fig. 5.8.: Snapshot of the movie for the Sage Brush Nodal Flats Experiment. Vertical displacement $u_Z(E, N)$ is shown on the left and its spatial gradient $u'_Z(E, N)$ is shown on the right. The two panels below show the displacement and spatial gradient recorded at the receiver R2010, which is marked in the upper panels by the black triangle.

From the movie, we can notice the P wave and the S wave at 29 s and 48 s respectively. Between those are PP, pP and SP phases arrivals. The movie and Figure 5.8 also helps reiterate our observations from the Transportable Array, i.e. presence of a few noisy receivers is inevitable; but the error is carried over to the spatial gradient.

Sweetwater Array, Texas

The Sweetwater Array (Sumy et al., 2015) is an array of geophones complemented by broadband sensors deployed near Sweetwater, Texas in 2014. The tight configuration the core grid consists of 74 rows, and a few of their extensions, with a spacing of 100 m and 24 columns, and a few of their extensions, with a spacing of 200 m. The array design maximized recording of horizontal-travelling seismic energy for surface wave analysis.

The geophones were the GS-30CT with a corner frequency of 10Hz and a sampling rate of 500 Hz. They detected various local and teleseismic earthquakes and here, we choose the mb4.5 Oklahoma event that occurred on March 30, 2014 (IRIS Event Page). The latitude, longitude and depth of the event are 36.16° N, 97.62° W and 10.0 km respectively. The distance between the source and the array is around 460 km.

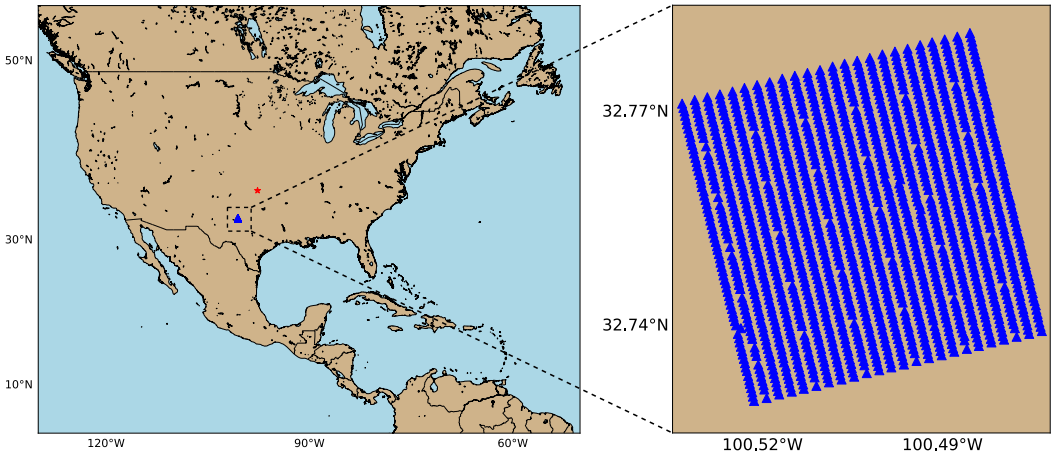

Fig. 5.9.: Left: Receivers of the Sweetwater Array used in Section 5.2.2. The source is shown by the red star. Right: Zoom in on the relative location of the receivers.

We get vertical displacements recorded by 1728 geophones for this event. The location of the receivers used are shown in Figure 5.9. After download, all data are corrected for instrument response and filtered between 1 and 3 Hz (between 0.33 and 1 s). The receivers with no data are substituted with their immediate neighbours to the west.

Using the vertical displacements, we compute spatial gradients through the array. A forward difference scheme in the north direction is deployed, i.e. at each receiver location, the spatial gradient is computed via $\partial \mathrm{Nu}'_{\mathrm{Z}}(\mathrm{E}, \mathrm{N}) =$

$u_Z(E, N + \partial N) - u_Z(E, N)$; where $u'_Z(E, N)$ is the spatial gradient of displacement, $u_Z(E, N + \partial N)$ and $u_Z(E, N)$ are the vertical displacements measured at locations $(E, N + \partial N)$ and (E, N) respectively and $\partial N = 100$ m. Finally, we render the displacement and the spatial gradient data and bundle them into movies, found here.[6] A snapshot of the movie is shown in Figure 5.10. Vertical displacement is shown on the left and its spatial gradient is shown on the right. The two panels below show the displacement and spatial gradient recorded by the receiver 6B446, which is marked in the movies by the black triangle.

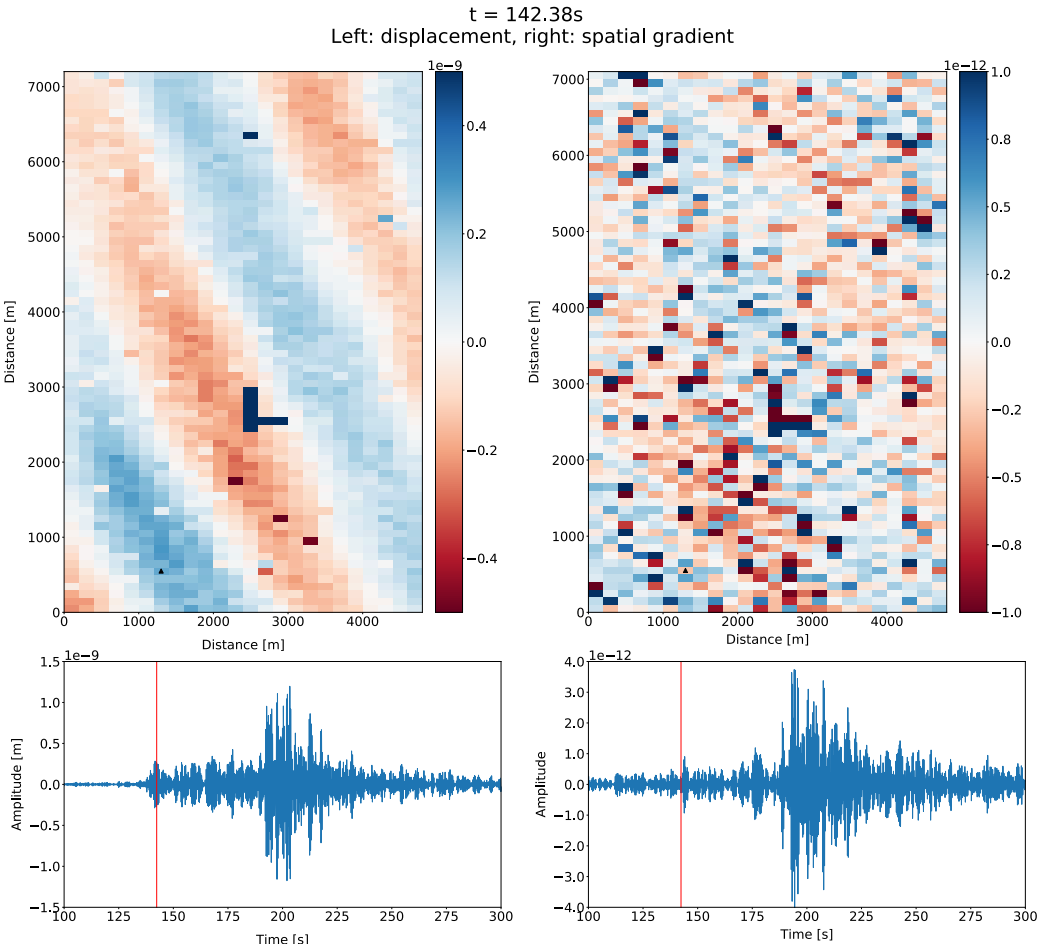

Fig. 5.10.: Snapshot of the movie for the Sweetwater Array. Vertical displacement $u_Z(E, N)$ is shown on the left and the spatial gradient $\partial N u'_Z(E, N)$ is shown on the right. The two panels below show the displacement and spatial gradient recorded at the receiver 6B446, which is marked in the upper panels by the black triangle.

Here, the P wave arrivals are at around 60 s (not shown). At around 109 s, one can notice the arrivals of S wave phases and other wave trains after.

[6] https://lpg-umr6112.fr/lpg/fichiers/singh-s/xb_small.mp4; Last Accessed on September 29, 2020

For this array, the waves can be seen passing by also on the spatial gradient but unfortunately, they are all too inconspicuous to decipher any small-scale heterogeneities.

Analysis of the US Transportable Array, Sage Brush Nodal Flats Experiment and Sweetwater Array tells us that at present, we are incapable of extending the synthetic example in Section 5.2.1 to real data. This is because some receivers are not well configured, i.e. either their amplitude responses are not well-calibrated, or their housing is not well isolated, or they are in the proximity of artificial noise sources, or they are located on basins whose geology enhance noise. One can also argue in favour of lack of sufficient theory that explains noise due to ocean, wind and human activities. Furthermore, the spectrum of the heterogeneity of the Earth's crust makes aliasing unavoidable, no matter how dense the receiver configuration.

Other less successful attempts of mapping discontinuities are shown in Appendix F.

5.3 Mapping discontinuities using correctors

According to the Equation 3.3 in Chapter 3, repeated below for convenience, wavefield gradients couple with strain of effective displacement due to small-scale structures.

$$(\nabla \mathbf{u})^{\varepsilon}(\mathbf{x}, \mathbf{y}, t) = (\nabla_{\mathbf{x}} \mathbf{u}^0)(\mathbf{x}, t) + \mathbf{J}(\mathbf{y}) : \epsilon(\mathbf{u}^0(\mathbf{x}, t)). \tag{5.1}$$

Here, $\epsilon(\mathbf{u}^0(\mathbf{x}, t))$ is the strain of effective displacement and $\mathbf{J}$ is the coupling tensor. Similarly, $(\nabla \mathbf{u})^{\varepsilon}$ represents the true wavefield gradient and $(\nabla_{\mathbf{x}} \mathbf{u}^0)$ represents the zeroth order effective wavefield gradient. True wavefield gradients correspond to real data that can be collected in the field. Effective wavefield gradients can be modeled using the same equations as true wavefield gradients but using homogenized elastic properties which do not contain any small scales [see Section 3.3].

Note that the strain of effective displacement and the zeroth order wavefield gradient themselves do not depend on small-scales; the effect of small-scales

is captured by the coupling tensor **J**, which is independent of source and time. Provided that an effective model that fits displacement data well can be found, **J** can be determined through linear inversion [see Section 4.2]. Consequently, a map of **J** helps us locate the small-scale structures.

5.3.1 Numerical Example

Here, we use the same 3D domain as in Section 5.2.1. The P and S velocities are 5 kms^{-1} and 3.2 kms^{-1} respectively. The domain size is $40\times40\times10$ km^3. A heterogeneity is placed at the center of the surface, with P and S velocities for each element in the heterogeneity chosen randomly and independently but within 25% of the surrounding domain. The spatial extent of the heterogeneity is $1334\times1334\times222$ m^3, extending over 6×6 elements. The geometric configuration of the model is shown in Figure 5.11.

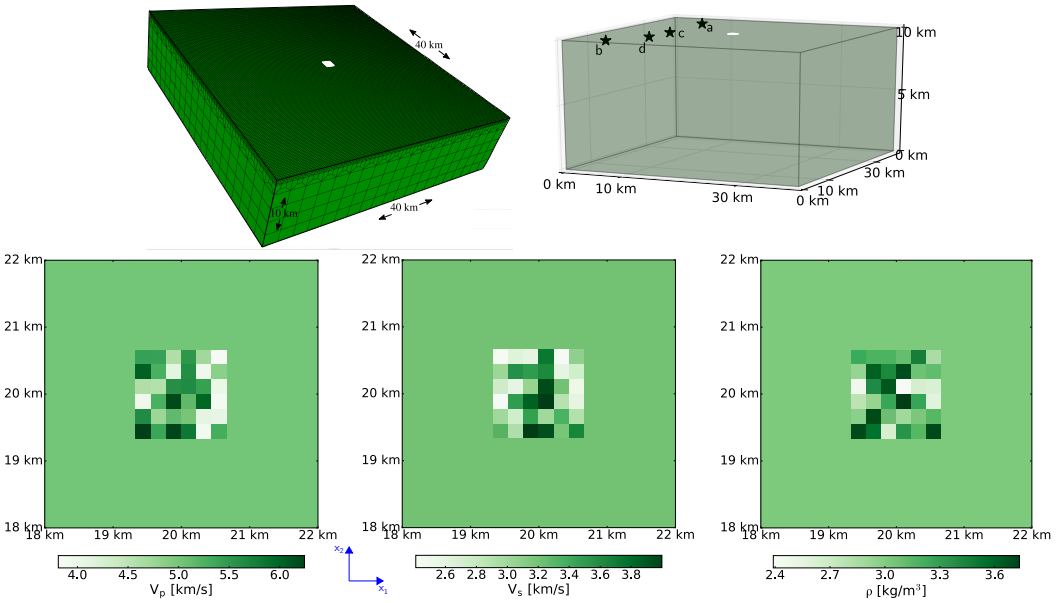

Fig. 5.11.: Top: 3D domain used in Section 5.3.1. The domain is $40\times40\times10$ km^3, and the heterogeneity at the centre, not to scale, is $1334\times1334\times222$ m^3. The stars show the location of the sources. The location of the receivers is shown in Figure 5.12. All but top boundary are absorbing.
Bottom: Zoom in into the heterogeneity from the top showing the V_p, V_s and ρ in the domain. The P and S velocities in the outer domain are 5 kms^{-1} and 3.2 kms^{-1}, and velocities for each element inside the heterogeneity are chosen randomly and independently, but within 25% of the surrounding domain.

We have the 1225 receivers from Section 5.2.1 lying at the top right corner of the heterogeneity such that they are spaced 20 m apart on a square grid.

The relative location of the receivers to the heterogeneity is also shown in Figure 5.12.

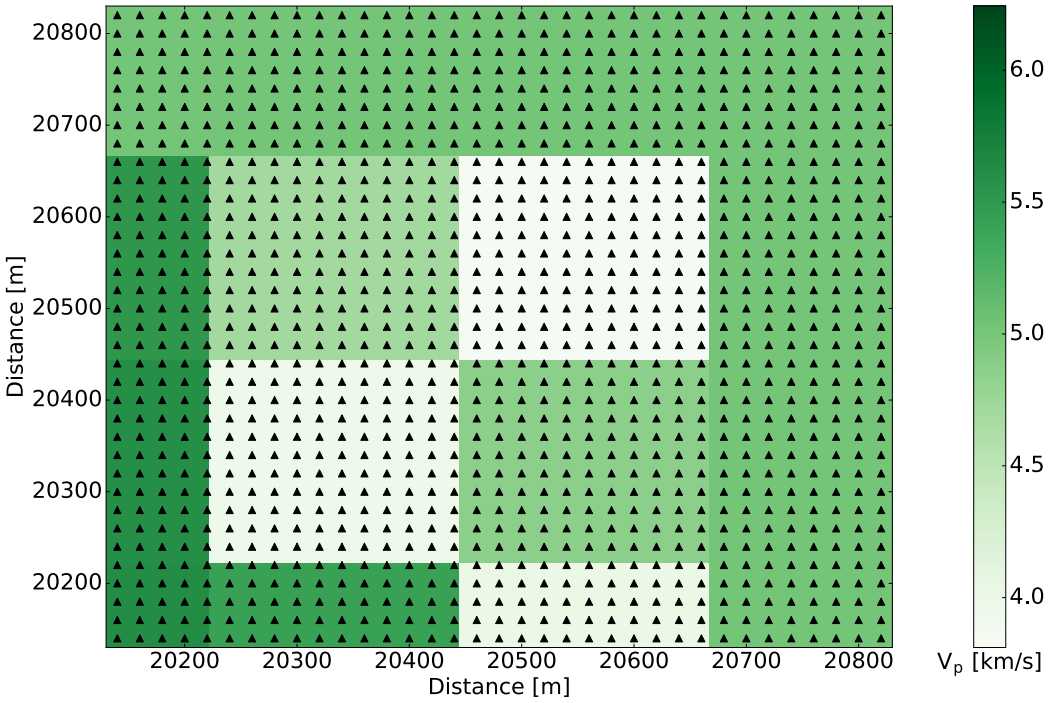

Fig. 5.12.: Zoom in on the surface of the 3D domain shown in Figure 5.11. The receiver locations are shown by the diamonds. Background color shows the P-wave velocity.

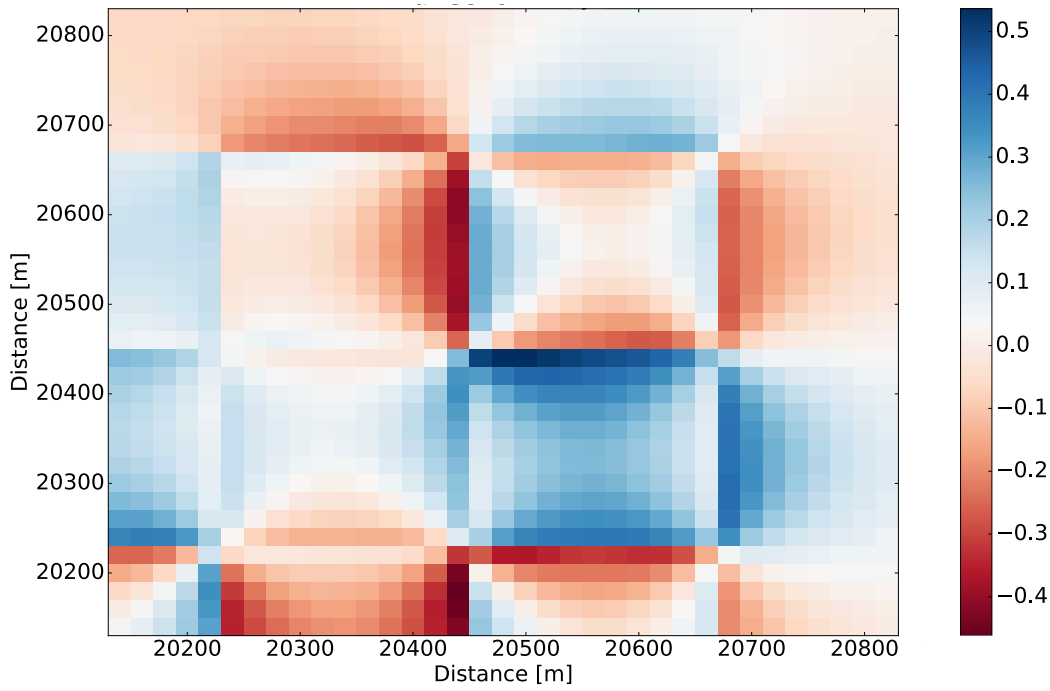

Fig. 5.13.: One of the components of the coupling tensor **J** for the 1225 receivers.

Here, we seek for the coupling tensor **J** for all 1225 receivers. Like in Section 4.3.2, we only invert for **J** for one component of the rotation, i.e. rotation around the vertical axis. This allows us to invert for just 6 parameters instead of 18. And in this case - where the receiver has been placed at the surface - the free surface condition also allows us to further reduce the number of scalars to be inverted for to 3 [Equation 3.7]. To this end, we perform simulations for three different sources at locations shown by the stars a, b and c in Figure 5.11 to generate data. These rotations form the term on the left in Equation 5.1. All sources have a central frequency of 0.5 Hz (maximum frequency 1.4 Hz) and the source-time function for all is a Ricker wavelet.

Here, we carry out the inversion against the homogeneous medium as an approximation for the effective one. We use the same three sources in the homogeneous media generate rotations and strains. These are the two known quantities on the right in Equation 5.1. Using these, we invert for the coupling tensor **J**. A map of one of the components of **J** is shown in Figure 5.13.

From Figure 5.13, we can see that the corrector clearly outlines the heterogeneity boundaries. The correctors at the outermost boundary seem smoother because they have enough space to decay.

5.3.2 Real Data

Apart from the constraint mentioned in Section 5.2.2, one additional constraint needed to compute the correctors is that the network has to de deployed for a long period of time so that sufficient number of events are recorded. However, most dense networks are deployed only for a temporary period of time.

Considering the outcomes of real data in Section 5.2.2, no attempts to compute correctors for an array were made.

5.4 Discussion and Conclusion

Here, we showed that since wavefield gradients are affected by small-scale structures, they can be used to infer geological heterogeneities. This echoes the sentiments of Harrison (1976); Kohl and Levine (1995); Langston

(2007b,a). Through numerical examples, we introduced the two ways in which this is possible. One was through directly observing the wavefield, and one was through the corrector **J**.

In geophysics, detection and characterization of tunnels, mines, karsts and other voids is an important task. But it is also very difficult task since there is no single method that works for all. The geophysical method has to be chosen depending on the geological context and the depth and geometry of the cavity. For example, the penetration depth of Ground Penetrating Radar is reduced in the presence of sediments like clays. Similarly, the noise and 3D effects caused by cellars and basements renders the applicability of microgravimetric method uncertain (Valensi et al., 2015). Keeping this in mind, our method could be an alternative to treat the wide spectrum of cavity imaging problems thus resulting in an improvement in the resolution of seismic images in the lithosphere.

Unfortunately, we could not extend the numerical examples to real cases. This was mostly because we did not find a dense array that has been deployed for a long period of time. For arrays that are dense enough, some receivers are not well configured. This could either come from their amplitude response being not well calibrated, or their housing not well isolated, or their placement on basins that intensify noise. Furthermore, natural media is complex and the spectrum of heterogeneity on the surface of the Earth is not in favour of mapping discontinuities. All these are further augmented by noise due to ocean, wind and human activities. Had these issues not been present, we could have attempted to link the correctors to the geology of the subsurface medium. Nevertheless, we remain hopeful. For example, with sufficient theory on noise processes, we will be able understand our seismograms better. Similarly, with the advent of more accurate and sensitive instruments, the issue of calibration can be averted. Already, instruments such as Distributed Acoustic Sensing (DAS) systems (Willis et al., 2016) and portbale blueSeis-3A (iXblue) (Bernauer et al., 2018) are advantageous since they have no issues of calibration. Furthermore, DAS permits continuous recordings which may help alleviate aliasing.

Although we did not find a dense array suitable for our work, we believe reduced scale experiments such as the ones conducted by (Bretaudeau et al., 2011; Valensi et al., 2015; Pageot et al., 2017) will be useful in bridging the

numerical simulations with applications to real data. Until then, we could seek for ways to configure our seismic instruments better.

Acknowledgements

We would like to thank Mickaël Bonnin, Akiko Toh and Ellen Yu for always answering my questions related to data downloading and processing. My questions were never-ending but you were always very patient.

This work was funded by the French National Research Agency (ANR-16-CE31-0022). We also thank the support through the European Research Council (Advanced Grant: ROMY, number: 339991). Obspy was acquired from `https://github.com/obspy/obspy/wiki`[7]. Event data were acquired either from the global CMT catalog, i.e. `https://www.globalcmt.org/`[7] (Ekström et al., 2012) or the IRIS Event Page, i.e. `https://ds.iris.edu/wilber3/find_event`[7].

[7]Last Accessed on September 29, 2020

6 Synthetic Full Waveform Inversion with wavefield gradients

In Chapter 3, we made the case that wavefield (displacements, velocities or accelerations) is sensitive to sub-wavelength structures only in an effective manner. This assumption, however, breaks down, when wavefield gradients (strains or rotations) are considered. One of the effects of this could be on inversions performed with wavefield gradients. In this chapter, we want to investigate the advantages and drawbacks of performing inversions with wavefield gradients compared to inversions with displacements. It will help us find out whether inversions with wavefield gradients are better in terms of accuracy and resolution. Meanwhile, we can also explore the extent to which small-scale structures impact full waveform inversions with wavefield gradients.

We start the chapter with a summary on previous inversions that have been carried out with wavefield gradients. Then, we describe our inversion strategy in Section 6.2, show our work in Sections 6.3 and 6.4, before finally concluding the chapter in Section 6.5.

6.1 Previous Work

Mikumo and Aki (1964) used the strains and displacements together to determine the local phase velocity of seismic waves for earthquakes recorded at Pasadena and the results they obtained were in good agreement with the theoretically predicted values.

Maeda et al. (2011) developed a new moment tensor inversion method that takes into account seismograms that are affected by tilt. Following Maeda et al. (2011), on the basis of numerical examples at Mt. Mepi volcano in Java, Indonesia, van Driel et al. (2015) showed that when the horizontal components of seismograms are dominate by tilt, for example at long periods,

it can have a strong effect on moment tensor inversions. This effect on moment tensor recovery is strong even if the effect is inconspicuous in the seismograms.

Fichtner and Igel (2009) showed that sensitivities of rotations are similar to the sensitivities of displacements but the sensitivities of apparent S-wave speeds are mostly focused at the receiver. Due to its specific form, sensitivities of apparent S-wave speeds can be used to recover small-scale structures at the receiver. Expanding on this work, Bernauer et al. (2009) used finite-frequency kernels for apparent S-wave speeds to invert for structure using combined measurements of translations and rotations. Through synthetic examples, they showed that tomographic images from such measurements are well-resolved. However, extension to real measurements is hindered because changes in apparent S-wave speeds due to unknown structures are difficult to spot. Similarly, Bernauer et al. (2012) showed that apparent P-wave and S-wave speeds are sensitive mainly to structures near the receiver thus, using these for tomographic inversions allows to constrain local structure without having the need to know the deeper structures within the Earth.

Bernauer et al. (2014) showed that using including rotational data increases the information gain and reduces the non-uniqueness in kinematic source inversions. This is especially true for slip amplitudes closest to the surface, rupture velocity and rise time. However, the measurement uncertainty in rotations have to be approximately similar to or smaller than the uncertainties in translations.

Donner et al. (2016, 2017, 2020) incorporated rotational motions into moment tensor inversions. They showed that the resolution of the six components of the moment tensor and depth increased remarkably when rotations were included. This is true also when only one station is used for the inversion, although it is difficult to retrieve the correct moment tensor with one station. Adding more stations increases the probability of recover the correct moment tensor, and even more so when rotations are included. Furthermore, the probability is highest when inversions employ highly accurate 3D structural models.

Similarly, Ichinose et al. (2019) used rotational Greens functions to invert for moment tensors using both translational and rotational data. They used the array-derived rotations at Piñon Flat Observatory and showed that

including these components improved the sensitivity of the moment tensor solutions by increasing the Double Couple (DC) components and reducing the Compensated Linear Vector Dipole (CLVD) and isotropic (ISO) components.

6.2 Inversion Strategy

Our work focuses on Full Waveform Inversion (FWI) and we want to investigate whether performing inversions with wavefield gradients is preferable to performing inversions with displacements in terms of accuracy and resolution. In this section, we elaborate on the numerical experiments that we have carried out. To have a proof of concept without exceeding reasonable computational time and effort, we refrain from having a model that is deliberately complex.

Model

Our target model is a 2D domain whose P and S velocities are 5 kms^{-1} and 2.8 kms^{-1} respectively. The size of the domain is 40×40 km^2 and the size of each element is 400×400 m^2. A heterogeneity of size 16×16 km^2 is at the center of the domain and the P and S velocities in each element in the heterogeneity are ± 40% of the surrounding domain. This implies that there are 1600 individual and uncorrelated values of V_p, V_s and ρ. The geometric configuration of the model is shown in Figure 6.1.

This heterogeneity chosen exhibits a flat power spectrum (within the range of wavenumber chosen). This is unlike for the Earth where the mantle exhibits a spectrum of $\frac{1}{k}$ (Batchelor, 1959; Olson et al., 1984; Mancinelli et al., 2016) and where the crust exhibits a spectrum of $\frac{1}{k^2}$; where k is the wavenumber of the heterogeneities (Wu et al., 1994; Meschede and Romanowicz, 2014).

All boundaries are absorbing.

Sources and Receivers

There are 8 seismic sources placed regularly around the heterogeneity. Their source-time function is a Ricker wavelet (second derivative of a Gaussian

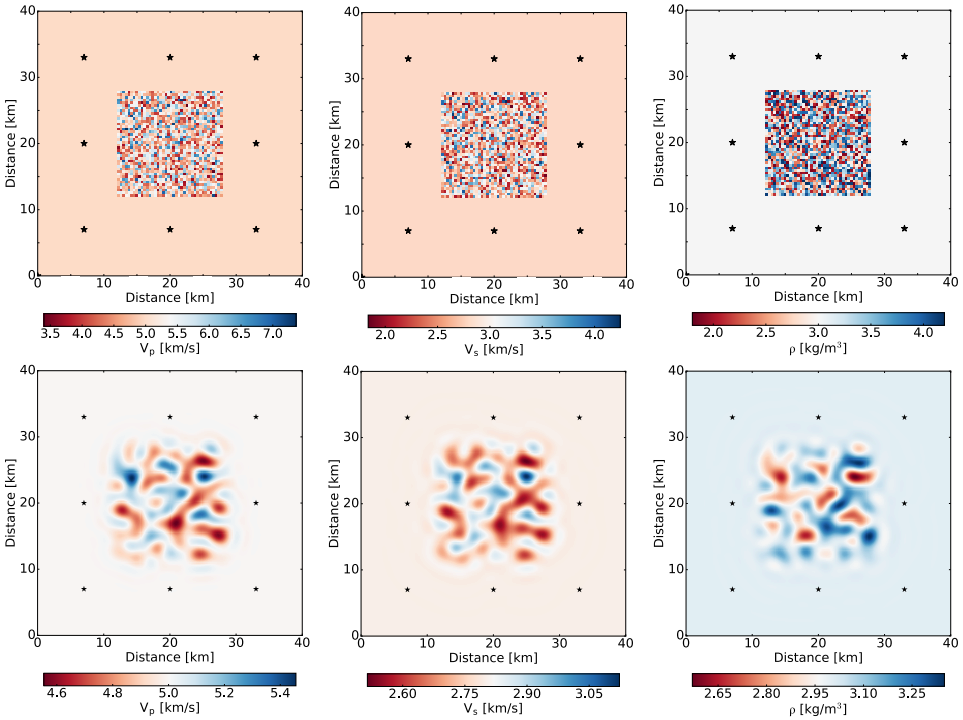

Fig. 6.1.: Top: Raw target model, bottom: homogenized target model with $\varepsilon = 2$. The domain is 40×40 km^2 and the heterogeneity at the centre is 16×16 km^2. The stars show the location of the sources. All boundaries are absorbing. Right: V_p, middle: V_s and left: ρ in the domain. The P and S velocities in the outer domain are 5 kms^{-1} and 3.2 kms^{-1}, and velocities for each element inside the heterogeneity are $\pm$40% of the surrounding domain.

wavelet). With a source central frequency of 0.45 Hz (maximum frequency 1.2 Hz), the minimum wavelength λ_m in the domain is around 2260 m. It should be noted that each element in the heterogeneity is around 0.18 times λ_m.

There are 8 receivers placed in the domain but their configuration depends on the test [details in Section 6.3]. Regardless of the test, the source-receiver configuration is chosen so that it provides sufficient coverage in each case. The seismic signals are recorded for 40 s so that all phases from all sources have the time to reach all receivers.

Seismic Waveform Inversion

Given the observations of displacements or its wavefield gradients **d** from the sources s measured at the receivers r, a 2D Spectral Element Program (Ko-

matitsch and Vilotte, 1998) is used to solve the wave equation and reproduce these data at each receiver location.

For each model $\mathbf{m}$, the misfit function is defined as:

$$\phi(\mathbf{m}) = \frac{1}{2}\sum_{\mathrm{r}}\int_0^{\mathrm{T}}[\mathbf{s}(\mathbf{x}_{\mathrm{r}},t;\mathbf{m}) - \mathbf{o}^{\mathrm{o}}(\mathbf{x}_{\mathrm{r}},t)]^2\mathrm{dt}, \tag{6.1}$$

for all sources and receivers. Note that here, $\mathbf{s}(\mathbf{x}_{\mathrm{r}},t;\mathbf{m})$ represents the synthetics for the model while the $\mathbf{o}^{\mathrm{o}}(\mathbf{x}_{\mathrm{r}},t)$ represents the observations. These could be the displacements $\mathbf{u}$, or rotations $\omega = \frac{1}{2}(\partial_j u_i - \partial_i u_j)$, or strains $\epsilon_{ij} = (\partial_j u_i + \partial_i u_j)$. This misfit function takes into account all parts of the seismogram, but is dominated by the signals with largest amplitude.

We then implement the Gauss-Newton iterative scheme to minimize the misfit function, given as

$$\mathrm{m}^{i+1} = \mathrm{m}^i + [{}^t\mathbf{F}^i\mathbf{F}^i + \lambda^i\mathbf{I}]^{-1}\ {}^t\mathbf{F}^i\ (\mathbf{d} - \mathbf{o}^{\mathrm{o}}(\mathbf{m}^i)), \tag{6.2}$$

where $\mathbf{I}$ is the second-order identity tensor. Partial derivatives $\mathbf{F}^i = [\frac{\partial \mathbf{s}}{\partial \mathbf{m}}]_{\mathbf{m}=\mathbf{m}^i}$ are evaluated using the adjoint method (Fichtner et al., 2006; Plessix, 2006; Tromp et al., 2008). The damping parameter is decreased with increasing iteration number and misfit reduction.

Frechlet derivatives

We calculate the Frechlet derivatives through the adjoint source.

The gradient of the misfit function from (6.1) is defined as:

$$\delta\phi = \sum_{\mathrm{r}}\int_0^{\mathrm{T}}[\mathbf{s}(\mathbf{x}_{\mathrm{r}},t;\mathbf{m}) - \mathbf{o}^{\mathrm{o}}(\mathbf{x}_{\mathrm{r}},t)]\ .\ \delta\mathrm{s}(\mathbf{x}_{\mathrm{r}},t;\mathbf{m})\mathrm{dt}, \tag{6.3}$$

where $\delta\mathrm{s}$ is the perturbation in the synthetic field due to a model perturbation $\delta\mathbf{m}$. We now omit the explicit dependence of the synthetics $\mathbf{s}$ on the model $\mathbf{m}$ for simplicity.

For displacements $\mathbf{u}$ measured at the receiver location $\mathbf{x}_{\mathrm{r}}$, this is given by

$$\delta\phi = \sum_{\mathrm{r}}\int_0^{\mathrm{T}}[\mathbf{u}(\mathbf{x}_{\mathrm{r}},t) - \mathbf{u}^{\mathrm{o}}(\mathbf{x}_{\mathrm{r}},t)]\ .\ \delta\mathbf{u}(\mathbf{x}_{\mathrm{r}},t)\mathrm{dt}. \tag{6.4}$$

We use the Born approximation (Hudson, 1977; Wu and Aki, 1985) to determine perturbations. The associated perturbation in displacement due to perturbations in density and elastic quantities $\{\delta\rho, \delta c_{jklm}\}$ in the background model is given by

$$\begin{aligned}\delta \mathrm{u}_i(\mathbf{x}, t) = -\int_0^t \int_V \Big[\delta\rho(\mathbf{x}') G_{ij}(\mathbf{x}, \mathbf{x}', t-t') \partial_{t'}^2 \mathrm{u}_j(\mathbf{x}', t') + \\ \delta c_{jklm}(\mathbf{x}') \partial_k' G_{ij}(\mathbf{x}, \mathbf{x}', t-t') \partial_l' \mathrm{u}_m(\mathbf{x}', t') \Big] d^3\mathbf{x}' dt',\end{aligned} \tag{6.5}$$

where V denotes the model volume and $\mathbf{x}'$ denotes the source location. Substituting this in (6.4), we get,

$$\begin{aligned}\delta\phi = -\sum_{\mathrm{r}} \int_0^{\mathrm{T}} [\mathrm{u}_i(\mathbf{x}_{\mathrm{r}}, t) - \mathrm{u}_i^{\mathrm{o}}(\mathbf{x}_{\mathrm{r}}, t)] \int_0^t \int_V \Big[\delta\rho(\mathbf{x}') G_{ij}(\mathbf{x}_{\mathrm{r}}, \mathbf{x}', t-t') \partial_{t'}^2 \mathrm{u}_j(\mathbf{x}', t') + \\ \delta c_{jklm}(\mathbf{x}') \partial_k' G_{ij}(\mathbf{x}_{\mathrm{r}}, \mathbf{x}', t-t') \partial_l' \mathrm{u}_m(\mathbf{x}', t') \Big] d^3\mathbf{x}' dt',\end{aligned} \tag{6.6}$$

Using reciprocity of the Green's function, we have

$$G_{ik}(\mathbf{x}_{\mathrm{r}}, \mathbf{x}', t-t') = G_{ki}(\mathbf{x}', \mathbf{x}_{\mathrm{r}}, t-t').$$

Using the time reversal, the adjoint source $f^\dagger$ is given by

$$\boldsymbol{f}^\dagger = \sum_{\mathrm{r}} \delta(t)\delta(\mathbf{x} - \mathbf{x}_{\mathrm{r}}) \tag{6.7}$$

The adjoint source, which is used to compute the Frechlet derivative, therefore acts as a single force.

We follow a similar procedure for the gradient of displacement. The gradient of the misfit function for the gradient of displacement $\partial_n \mathbf{u}$ measured at the receiver location and $\mathbf{x}_{\mathrm{r}}$ is given by

$$\delta\phi = \sum_{\mathrm{r}} \int_0^{\mathrm{T}} [\partial_n \mathbf{u}(\mathbf{x}_{\mathrm{r}}, t) - \partial_n \mathbf{u}^{\mathrm{o}}(\mathbf{x}_{\mathrm{r}}, t)] \,.\, \delta\partial_n \mathbf{u}(\mathbf{x}_{\mathrm{r}}, t) \mathrm{dt}. \tag{6.8}$$

Using (6.5), the associated perturbation in gradient of displacement due to perturbations $\{\delta\rho, \delta c_{jklm}\}$ in the background model is given by

$$\begin{aligned}\delta\partial_n \mathbf{u}_i(\mathbf{x},t) = -\int_0^t \int_V \Big[& \delta\rho(\mathbf{x}') G_{ij}(\mathbf{x},\mathbf{x}',t-t')\partial_{t'}^2 \partial_n \mathbf{u}_j(\mathbf{x}',t') + \\ & \delta c_{jklm}(\mathbf{x}')\partial'_k G_{ij}(\mathbf{x},\mathbf{x}',t-t')\partial'_l \partial_n \mathbf{u}_m(\mathbf{x}',t')\Big] d^3\mathbf{x}' dt',\end{aligned} \tag{6.9}$$

where V denotes the model volume and $\mathbf{x}'$ denotes the source location. Substituting this in (6.8), we get,

$$\begin{aligned}\delta\phi = -\sum_{\mathrm{r}} \int_0^{\mathrm{T}} [\partial_n \mathbf{u}_i(\mathbf{x}_{\mathrm{r}},t) - \partial_n \mathbf{u}_i^{\mathrm{o}}(\mathbf{x}_{\mathrm{r}},t)] \int_0^t \int_V \Big[& \delta\rho(\mathbf{x}') G_{ij}(\mathbf{x}_{\mathrm{r}},\mathbf{x}',t-t')\partial_{t'}^2 \partial_n \mathbf{u}_j(\mathbf{x}',t') + \\ & \delta c_{jklm}(\mathbf{x}')\partial'_k G_{ij}(\mathbf{x}_{\mathrm{r}},\mathbf{x}',t-t')\partial'_l \partial_n \mathbf{u}_m(\mathbf{x}',t')\Big] d^3\mathbf{x}' dt',\end{aligned} \tag{6.10}$$

Using reciprocity of the Green's function, we have

$$\partial'_l G_{ij}(\mathbf{x}_{\mathrm{r}},\mathbf{x}',t-t') = \partial'_l G_{ji}(\mathbf{x}',\mathbf{x}_{\mathrm{r}},t-t').$$

For rotation in 2D, which is given by $\omega = \frac{1}{2}(\partial_i u_j - \partial_j u_i)$, the adjoint source $f^\dagger$ is given by

$$\boldsymbol{f}^\dagger = \sum_{\mathrm{r}} \delta(t)\delta(\mathbf{x}-\mathbf{x}_{\mathrm{r}}) \begin{bmatrix} 0 & \frac{1}{2} \\ -\frac{1}{2} & 0 \end{bmatrix}. \tag{6.11}$$

The adjoint source, which is used to compute the Frechlet derivative, acts as an anti-symmetric moment tensor.

With the help of adjoint source and its wavefield, the Frechlet derivatives can be represented with respect to ρ and c_{jklm}. More details can be found for example in Tromp et al. (2005).

Validation

After convergence, our inversion results need to be assessed for quality. To validate our results, we show examples of fits to displacement and wavefield gradient data, for cases where they have not been used for the inversion.

Since fit to data used in the inversion is expected, a good fit between independent data in the target model and the recovered models implies that

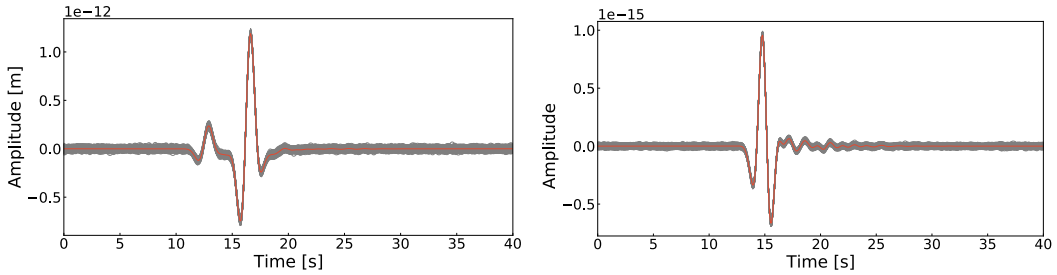

Fig. 6.2.: Left: An example of data for displacement (red line) and realisations with noise (grey lines). Right: An example of data for rotation (red line) and realisations with noise (grey lines)

our inversions are reliable and well-constrained. For this, we place some receivers at new locations the in the target model and compute displacements and wavefield gradients. Then, we place the receivers at the exact locations in the recovered models and compute the measurements once again.

Resolution Analysis

We also provide an analysis of the spatial resolution of the elastic parameters and density that arises from the combination of our data, modelling and misfit quantification. For this, we take the help of statistics. First, we perform 1000 inversions with noise on the data. For each realisation, the noise level is chosen at random but is within 10% of the maximum variance of the data. Each set of data, i.e. displacement, rotation and strain is considered separately so that the maximum amplitude for rotation and strain is not dominated by displacement data. A example showing the distribution of noise realisation is shown in Figure 6.2.

Note that here, the assumption is that the noise on displacement and wavefield gradient is the same is a strong one. This may not be true and our results may point to a different conclusion if we choose a different noise distribution. But since we do not yet know how the noise on the wavefield relates to the noise on its gradients, we stick to this assumption.

Then, we compute the resolution matrix along with the 2D distribution of correlation spread and its error. Local uncertainties in inversion can be characterized by the covariance matrix because it is closely linked to the Hessian matrix (Fichtner and Trampert, 2011; Bui-Thanh et al., 2013).

Assuming that the distribution of noise on synthetic data is Gaussian, the covariance matrix is the Hessian matrix.

To get the covariance matrix, we begin by expanding our inversion grid to a regular grid. We discretize each parameter from our inversion with 2 grid points per wavelength. This allows us to deal with the nominal size of the covariance matrix while still preserving all its spatial frequency. We then calculate the covariance between each parameter. For example, the covariance between the parameters c_{1111} and c_{1212} in each element is given by:

$$\text{cov}(c_{1111}, c_{1212}) = \frac{1}{\text{N}-1}\sum_{i=1}^{\text{N}}(c_{1111_i} - \mu_{c_{1111}})(c_{1212_i} - \mu_{c_{1212}}); \tag{6.12}$$

where $\text{N} = 1000$, c_{1111_i} and c_{1212_i} are the values of c_{1111} and c_{1212} in the element for model i; and $\mu_{c_{1111}}$ and $\mu_{c_{1212}}$ are the mean values of $\mu_{c_{1111}}$ and $\mu_{c_{1212}}$ respectively. The $\text{N}-1$ here indicates that this is an unbiased estimate.

Ideally, we want a diagonal covariance matrix because this is an indication that the model parameters can be constrained independently.

Similarly, to get the correlation matrix, we discretize each parameter from the smooth models from our inversion with 6 grid points per wavelength to have figures with better resolution. We then consider one element at the center of the area and compute its correlation with respect to all other elements in the area. For example, the correlation between the parameters c_{1111_m} and c_{1111_n} between two elements m and n is given by:

$$\text{R} = \frac{\text{cov}(c_{1111_m}, c_{1111_n})}{\sigma_{c_{1111_m}}\sigma_{c_{1111_n}}}. \tag{6.13}$$

Here, $\text{cov}(c_{1111_m}, c_{1111_n})$ represents the covariance for c_{1111} between two elements m and n [see Equation 6.12]; and $\sigma_{c_{1111_m}}$ and $\sigma_{c_{1111_n}}$ represent the standard deviations for c_{1111} at elements m and n respectively.

A correlation is a number between -1 and 1; with -1 indicating a strong negative correlation and 1 indicating a strong positive correlation. Under perfect conditions, each observed element contributes only to the corresponding element. But this is not the case in practice and each observed point will also correspond to its neighbouring elements. As a result, smearing occurs. The area of the smearing of the correlations tells us about the resolution.

Typically, the smaller the smearing of the correlations for a certain parameter, the better is the resolution for that parameter.

To get the error bars on the resolutions, we simply compute the variances at each element in the area. For example, the variance for c_{1111} at each element is the expected value of the squared deviation of c_{1111} from the mean $\mu_{c_{1111}}$ at that element.

$$\sigma^2 = \mathrm{E}[(c_{1111} - \mu_{c_{1111}})^2] \tag{6.14}$$

We want lower variances because they indicate lower errors.

6.3 Numerical Experiments

In this section, we will introduce the tests that we carry out and justify our choice of the tests. Results are shown in the succeeding section.

Regardless of the test, we always start our inversions from an entirely homogeneous model whose V_p, V_s and ρ are 5 kms^{-1}, 2.8 kms^{-1} and 3.0 kgm^{-3} respectively. The inversion area is 18×18 km^2 and extends slightly beyond the heterogeneity. It is divided into 36×36 elements, and for each element, the elastic tensor $\mathbf{c}$ and density ρ are inverted. For the forward problem, we use number of Gauss-Lobatto-Legendre (nGLL) points 4 while for the inversion, we use nGLL points 1. This ensures that the discretization errors are different. Furthermore, the mesh chosen for inversion cannot accurately represent the small-scale structure (the element size for the inversion is $\sim$0.22 λ_m, while the size of individual heterogeneity is $\sim$0.18 λ_m) and this ensures that we are not injecting prior information through our mesh. Consequently, we avoid any inversion crime.

6.3.1 Receivers far away from the heterogeneity

As our first test, we will compare FWI with displacement and FWI with wavefield gradients. To serve as a reference case where the wavefield gradients are not yet affected by any local heterogeneities, we place the receivers far away from the heterogeneity that is at the center of the domain.

The starting model is shown in Figure 6.3 along with the receiver locations. The inversion domain is given by the black inner square.

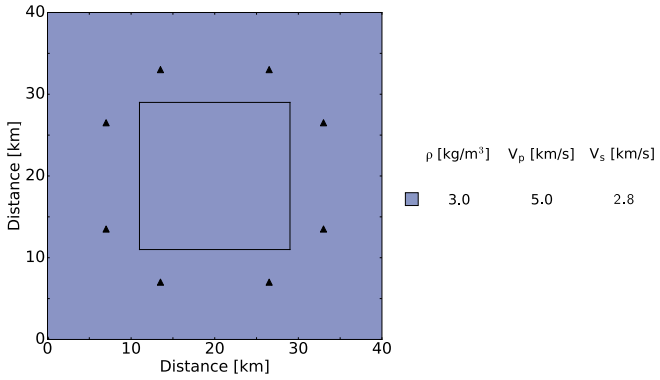

Fig. 6.3.: Starting model used in the inversion in Section 6.3.1. The triangles show the location of the receivers. All boundaries are absorbing. The inner square shows the inversion area.

6.3.2 Receivers close to the heterogeneity

In Chapter 3, we showed that local small-scale heterogeneities affect wavefield gradients measurements by causing them to change in both amplitude and phase.

While the receivers were placed far-away from the heterogeneity in the previous test, this is not very realistic. We know the Earth's crust to be very heterogeneous and varying at all scales. Therefore, in this test, we move the receivers inside the heterogeneity such that the wavefield gradient measurements, i.e. data are affected by the heterogeneity. We also choose a a slightly irregular configuration of the receivers to mimic the irregular coverage on the Earth due to logistic constraints, etc.

The starting model is shown in Figure 6.4 along with the receiver locations. The inversion domain is given by the black inner square.

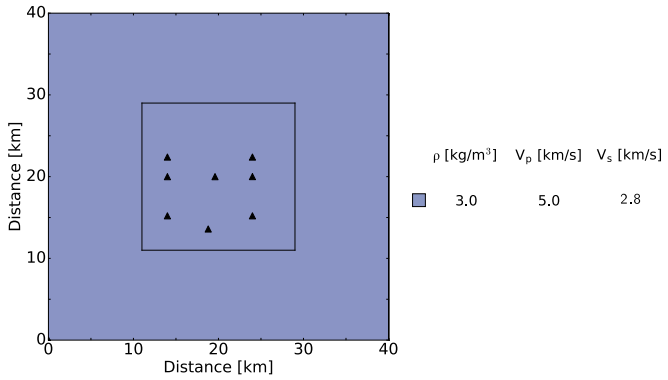

Fig. 6.4.: Starting model used in the inversion in Section 6.3.2. The triangles show the location of the receivers. All boundaries are absorbing. The inner square shows the inversion area.

6.3.3 Receivers close to the heterogeneity with correctors

In Chapter 4, we showed that we can account for the effect of local small-scale heterogeneities on wavefield gradients through the corrector **J**. Because the **J** does not depend on source and time, it can be determined in a straightforward manner through linear inversion, given that an effective medium where displacements data match exists:

$$\omega^{\varepsilon}(\mathbf{x},\mathbf{y},t) = \omega^{0}(\mathbf{x},t) + \mathbf{J}(\mathbf{y}) : \epsilon(\mathbf{u}^{0}(\mathbf{x},t)).$$

Here, $\epsilon(\mathbf{u}^0(\mathbf{x},t))$ is the strain of effective displacement and **J** is the coupling tensor. For rotation in 2D, which is a scalar, **J** has 3 components. Similarly, ω^{ε} represents the true rotation and ω^0 represents the zeroth order effective rotation. True rotations correspond to real data that can be collected in the field. Effective rotations can be modeled using the same equations as true rotations but using homogenized elastic properties which do not contain any small scales [see Section 3.3].

In this test, we use the same configuration as in Section 6.3.2 [Figure 6.4]. However, we account for the effect of heterogeneity by explicitly inverting for the corrector **J** for each receiver at each iteration. Note that the model at each iteration may not necessarily be the effective model (i.e. it may not be a model that matches the displacement of the target model), but we follow this procedure regardless.

The recipe for the inversion at each iteration is as follows.

1. Compute rotations and strains in the effective medium.

2. Use the rotations and strains from Step 1 to determine $\mathbf{J}$ for each receiver.
$$\omega^{\varepsilon}(\mathbf{x}, \mathbf{y}, t) = \omega^{0}(\mathbf{x}, t) + \mathbf{J}(\mathbf{y}) : \epsilon(\mathbf{u}^{0}(\mathbf{x}, t)).$$

3. Assemble the equation for adjoint source. The moment tensor from (6.11) is now given by:
$$\boldsymbol{f}^{\dagger} = \sum_{\mathrm{r}} \delta(t)\delta(\mathbf{x} - \mathbf{x}_{\mathrm{r}}) \left[\begin{bmatrix} 0 & \frac{1}{2} \\ -\frac{1}{2} & 0 \end{bmatrix} + \mathrm{J}_1 \begin{bmatrix} 1 & 0 \\ 0 & 0 \end{bmatrix} + \mathrm{J}_2 \begin{bmatrix} 0 & 0 \\ 0 & 1 \end{bmatrix} + \mathrm{J}_3 \begin{bmatrix} 0 & \frac{1}{2} \\ \frac{1}{2} & 0 \end{bmatrix} \right]. \tag{6.15}$$
Here, J_1 is the component of the corrector that is associated with strains ϵ_{ii}, J_2 is the component of the corrector that is associated with strains ϵ_{jj} and J_3 is the component of the corrector that is associated with strains ϵ_{ij}.

4. Run inversion.

6.4 Results

In this section, we discuss the results of all tests from Section 6.3. In the interest of brevity, we only show the results of FWI with displacements compared to FWI with rotations. Results of FWI with strains are shown in Appendix H.

After convergence, the final model is homogenized using the method described in Chapter 2, and choose $\varepsilon = 2$ to focus on long wavelength results $(2\lambda_m)$. Following Capdeville and Métivier (2018), we compare the homogenized version of each result with the homogenized version of the target model. We project the anisotropic tensor $\mathbf{c}$ to the nearest isotropic tensor $\mathbf{c}^{\mathrm{iso}}$

following Browaeys and Chevrot (2004). Subsequently, V_p, V_s and the total anisotropy are defined as follows:

$$V_p = \sqrt{\frac{c^{iso}_{1111}}{\rho}},$$
$$V_s = \sqrt{\frac{c^{iso}_{1212}}{\rho}},$$
$$\text{anisotropy} = \sqrt{\frac{\sum_{ijkl}(c^{iso}_{ijkl} - c_{ijkl})^2}{\sum_{ijkl}(c^{iso}_{ijkl})^2}}.$$

Contrary to this, the validation and resolution analysis are done at ε=0.5 to compare results at the resolution limit ($\frac{\lambda_m}{2}$).

Note also that in 2D, the number of components of displacement is twice the number of components of rotation.

6.4.1 Receivers far away from the heterogeneity

As our initial test, we want to compare the result of FWI with displacement to that with rotation when the receivers are placed far away from the heterogeneity. For both inversions, the improvement in misfit reduction is 99%. Results are shown in Figure 6.5 for V_p, V_s, ρ and anisotropy. Also shown are the respective values along two-cross sections in the model. The values along the vertical cross-section are shown on the right (red lines) and the values along the horizontal cross-section are shown just below (red lines). Also shown are the respective values in the target model (green lines), shown in Figure 6.1.

From the cross-sections in Figure 6.5, it can be seen that the inversion from displacements are in agreement with the target model. This is less true for the inversion with rotation, where slight discrepancies exist. These are most evident in the vertical cross-section of V_p and V_s. We associate this to the number of measurements, because increasing the number of receivers by twice (such that the number of rotation measurements is equal to the number of displacement measurements) improves the inversion results [see Figure 6.6].

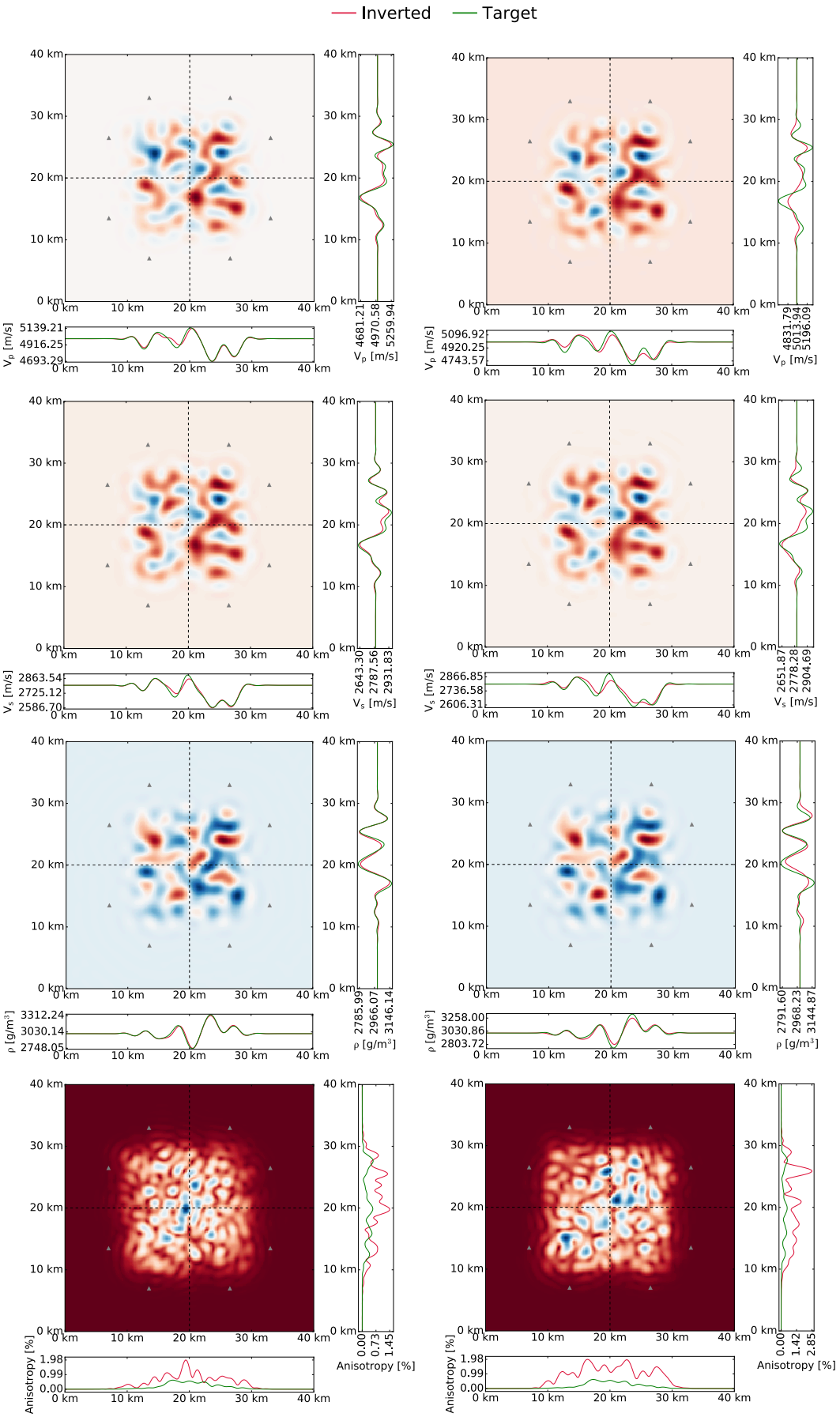

Fig. 6.5.: Results of the first test. Left: Inversion with only displacements, right: inversion with only rotations. Starting from top, V_p, V_s, ρ and anisotropy are shown. For each result, cross-section along the horizontal dotted line is shown below and cross-section along the vertical dotted line is shown to its right. Also shown in green are the respective cross-sections along the target model.

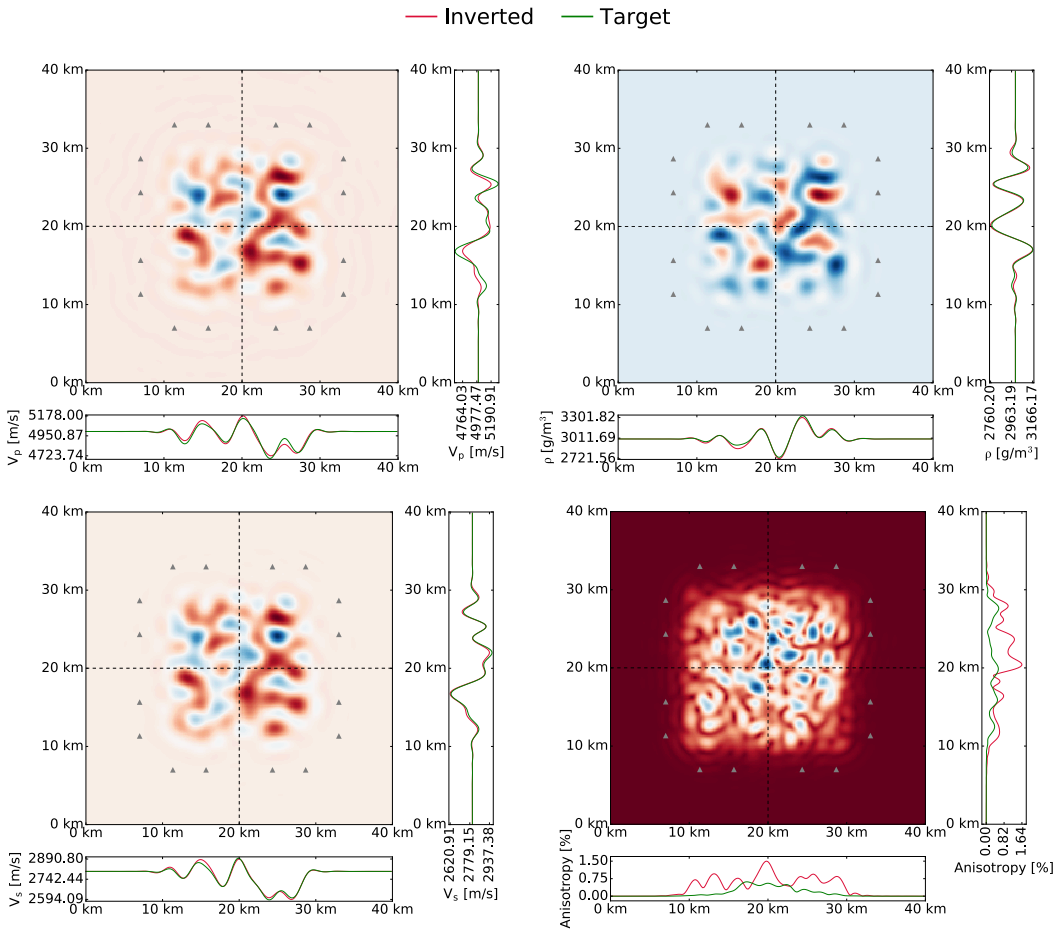

Fig. 6.6.: Results of inversion with only rotations and 16 receivers. Clockwise from top left: V_p, V_s, anisotropy and ρ. The receiver locations are shown by the grey and the starting model was entirely homogeneous. For each result, cross-section along the horizontal dotted line is shown below and cross-section along the vertical dotted line is shown to its right. Also shown in green are the respective cross-sections along the target model.

Validation

Here, we place a receiver in a new location and calculate the displacements and rotations in the recovered models to compare them to those in the target model. The receiver and source positions are shown by the triangle and the star respectively on the left panel of Figure 6.7 and the measurements are shown on the right panel. Measurements in the target model are shown in black, in the model recovered from displacement are shown in green, and in the model recovered from rotation are shown in red. The amplitudes have been normalized.

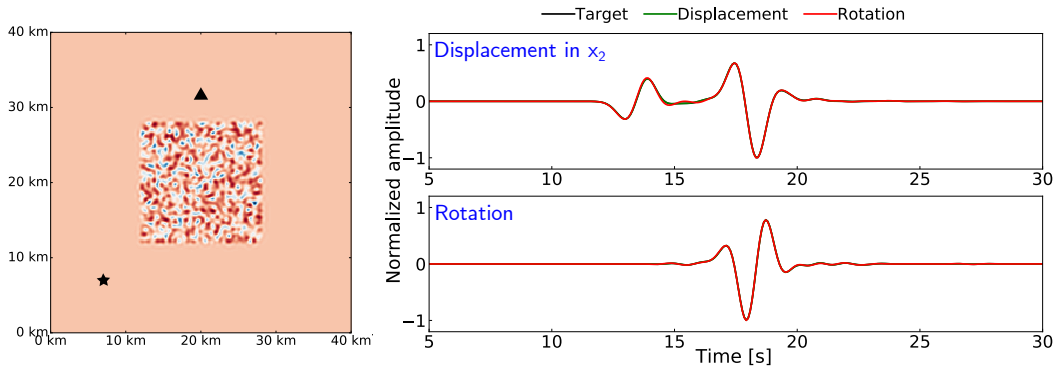

Fig. 6.7.: Validating the recovered models. Left: Source-receiver configuration. The source location is given by the star and the receiver location is given by the triangle. Right: Vertical displacements (top) and rotations (bottom). Measurements in the target model are shown in black, in the model recovered from displacements are shown in green in the model recovered from rotation are shown in red.

From the right panel in 6.7, we can see both recovered models are able to achieve the measurements in the target model, meaning that both inversions are reliable.

Resolution Analysis

The covariance matrices for the inversions are shown in Figure 6.8. The matrices are not identity matrices $\mathbf{I}$. They are dominated by the diagonal, but off-diagonal elements are present suggesting that there are inter-parameter correlations between c_{2222} and c_{1111}. The resolution is therefore not perfect and averaging and smearing arise during the inversion.

Note also that the covariances for rotation are almost twice the covariances of inversion. This arises from the fact that the number of data for rotation is half the number of data for displacement.

The resolutions are shown next in Figure 6.9. The two columns in the middle show the resolutions for inversion with displacement and inversion with rotation respectively. The column to the left of the resolution for the displacement are the corresponding variances in the resolutions. Similarly, to the right of the resolution for rotation are the corresponding variances in the resolutions. Starting from top, the figures correspond to c_{1111}, c_{1122}, c_{1112}, c_{2222}, c_{2212}, c_{1212}, and ρ respectively. For almost all parameters, the area of the correlations are the same. The only exception is c_{1122}, where the smearing for rotation is much smaller than the smearing for displacements.

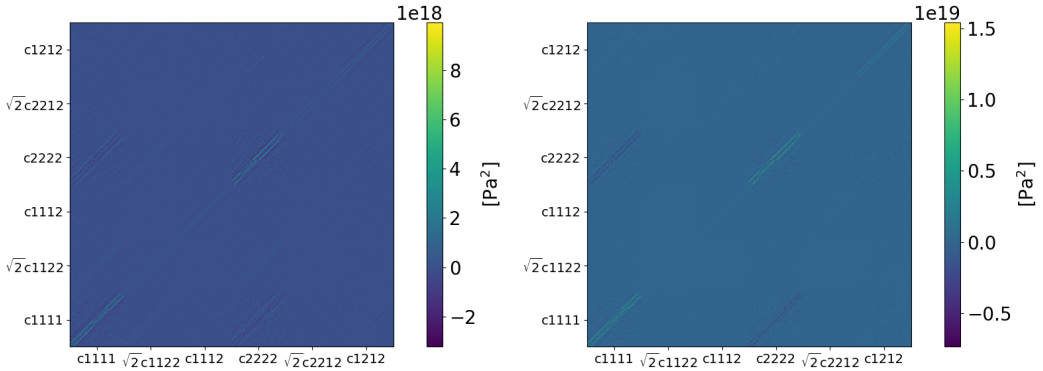

Fig. 6.8.: Covariance matrices for the first test. Left: inversion with only displacements, right: inversion with only rotations.

This reveals a much higher resolution for c_{1122} when inversion is performed with rotations. But we account this to lack of sufficient data for rotations and resolution analyses for 16 receivers instead of 8 (i.e. with sufficient data for rotation), which is currently a work in progress, may make the correlations consistent.

Taking into account the number of data for displacement and rotation to the variances, we can also see lower variances for rotations can be seen in c_{1112}, c_{2222} and c_{2212} compared to displacements, implying that there are lower errors in resolution for these parameters. But whether these are substantial remains to be studied.

6.4.2 Receivers close to the heterogeneity

As our second test, we compare the results of FWI with displacement to that with rotation when the receivers are placed close to the heterogeneity such that the rotation data are affected by the small-scale heterogeneity. Once again, the improvement in misfit reduction is 99% for both inversions. Results are shown in Figure 6.10 for V_p, V_s, ρ and anisotropy. Also shown are the respective values along two-cross sections in the model. The values along the vertical cross-section are shown on the right (red lines) and the values along the horizontal cross-section are shown just below (red lines). Also shown are the respective values in the target model (green lines), shown in Figure 6.1.

Similar to Section 6.4.1, it can be seen that the inversion from displacements are in better agreement with the target model compared to the inversion from

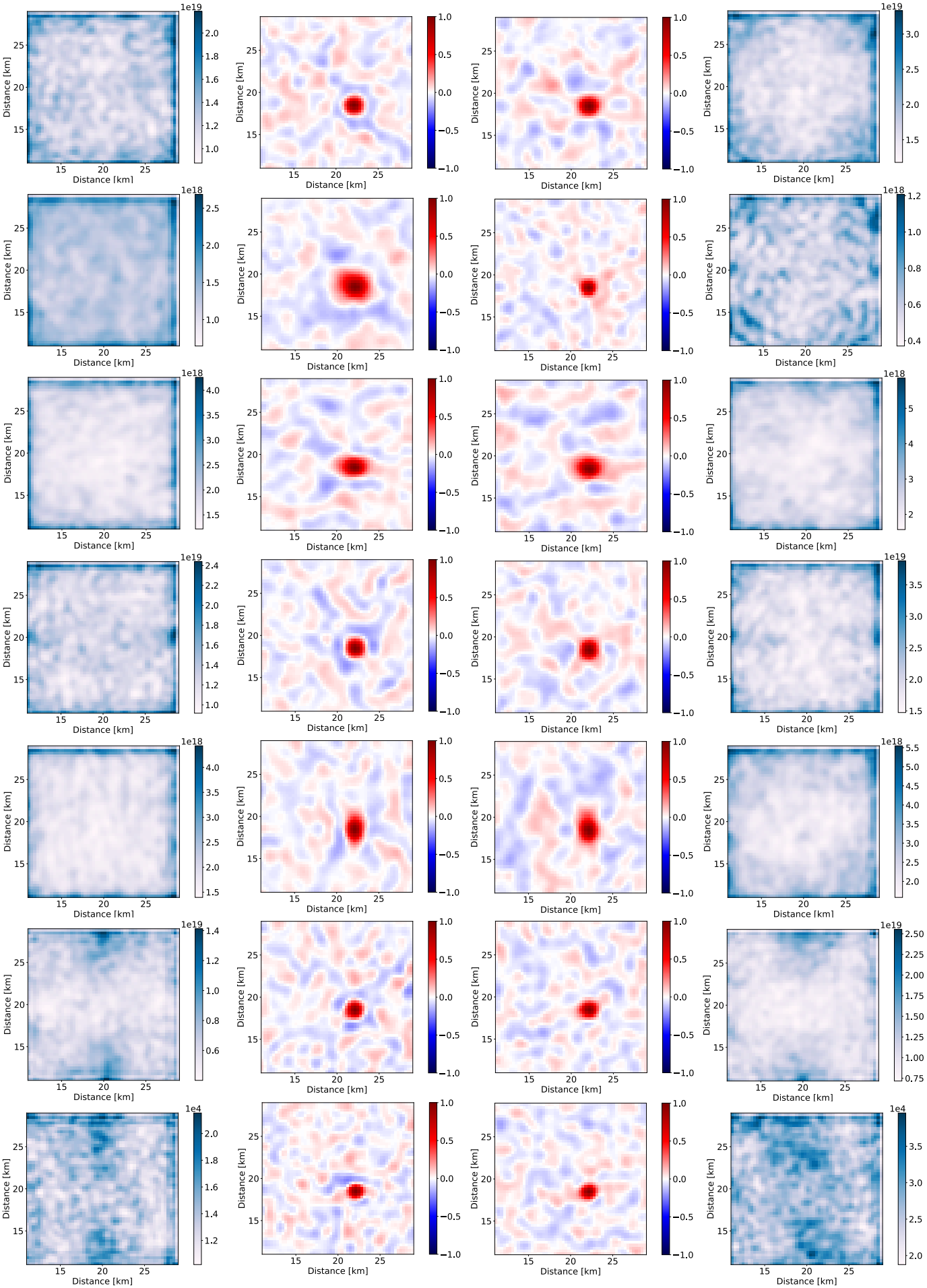

Fig. 6.9.: Resolution analysis. Starting from left, the variance in resolution for displacement, the resolution for inversion with displacement, the resolution for inversion with rotation and the variance in resolution for rotation are shown. Starting from top are the corresponding figures for c_{1111}, c_{1122}, c_{1112}, c_{2222}, c_{2212}, c_{1212}, and ρ.

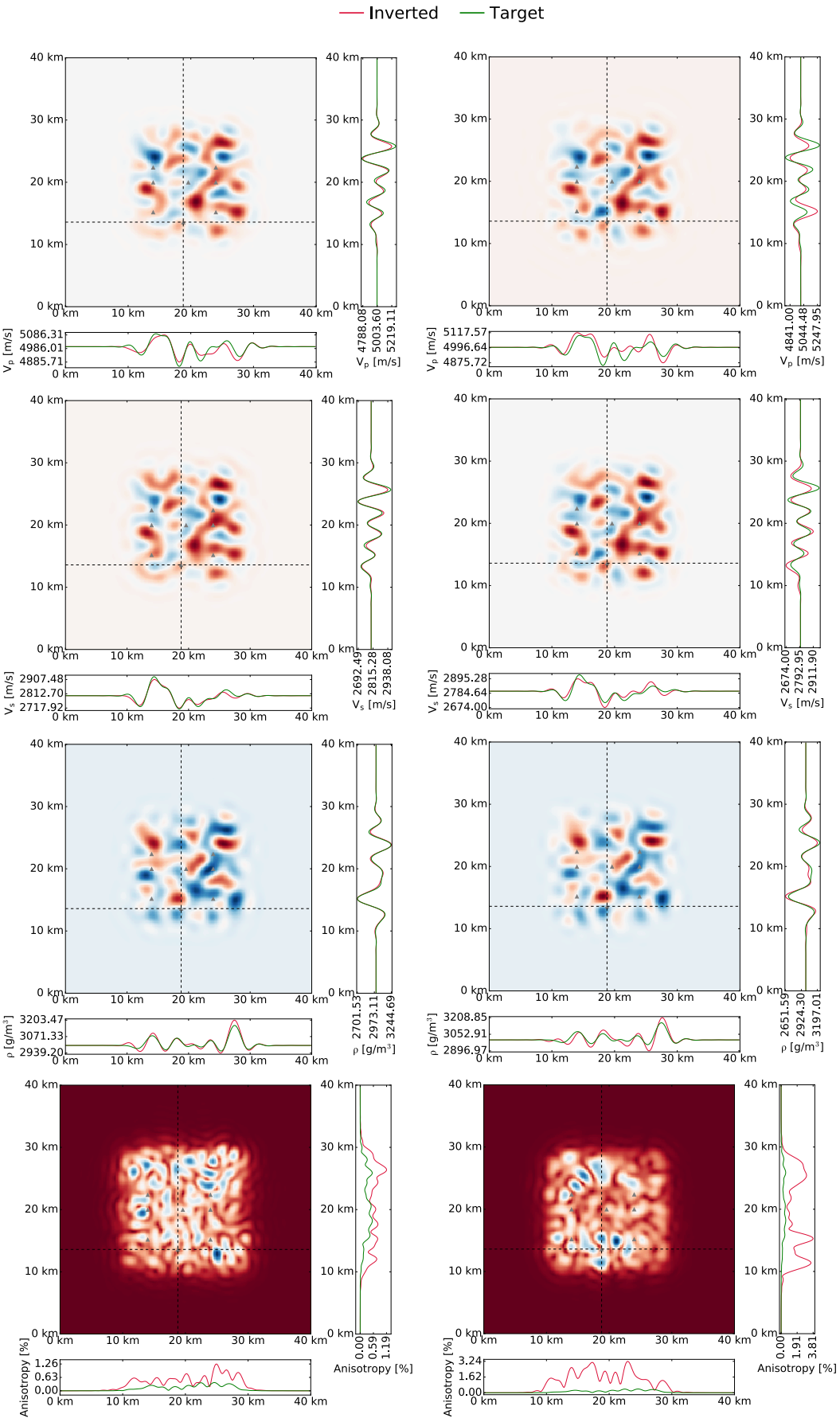

Fig. 6.10.: Results of the second test. Left: Inversion with only displacements, right: inversion with only rotations. Starting from top, V_p, V_s, ρ and anisotropy are shown. For each result, cross-section along the horizontal dotted line is shown below and cross-section along the vertical dotted line is shown to its right. Also shown in green are the respective cross-sections along the target model.

rotations. Bigger discrepancies exist for the latter. These are most evident in the cross-sections of V_p and V_s. Part of it comes from insufficient coverage as seen in Section 6.4.1. However, increasing the number of receivers does not help as shown by Figure 6.11. Slight improvements occur, for example in the vertical cross-section of V_s. The agreement is however not as good as it is for inversion with displacement and we attribute this to the effect of small-scale structures.

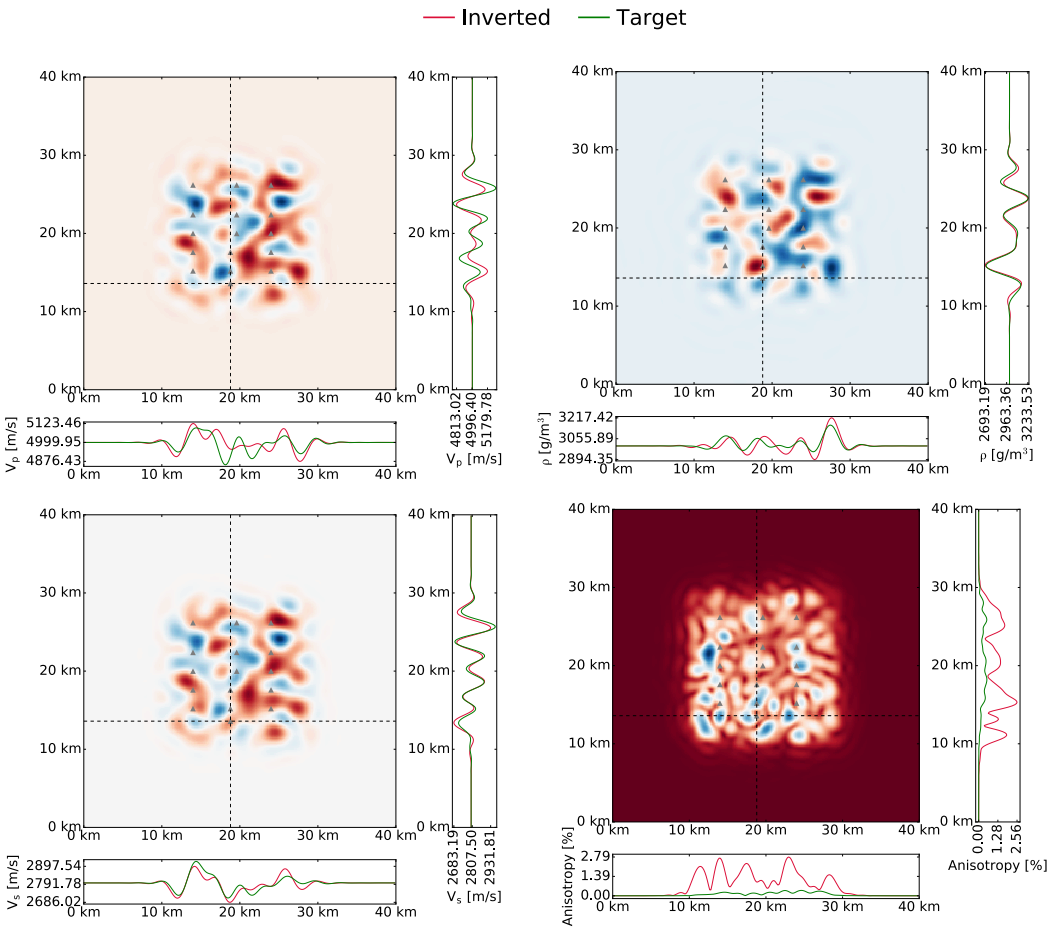

Fig. 6.11.: Results of inversion with only rotations and 16 receivers. Clockwise from top left: V_p, V_s, anisotropy and ρ. The receiver locations are shown by the grey and the starting model was entirely homogeneous. For each result, cross-section along the horizontal dotted line is shown below and cross-section along the vertical dotted line is shown to its right. Also shown in green are the respective cross-sections along the target model.

Validation

Here, we place a receiver in a new location and calculate the displacements and rotations in the recovered models to compare them to those in the target model. The receiver and source positions are shown by the triangle and the star respectively on the left panel of Figure 6.12 and the measurements are shown on the right panel. Measurements in the target model are shown in black, in the model recovered from displacement are shown in green, and in the model recovered from rotation are shown in red. The amplitudes have been normalized.

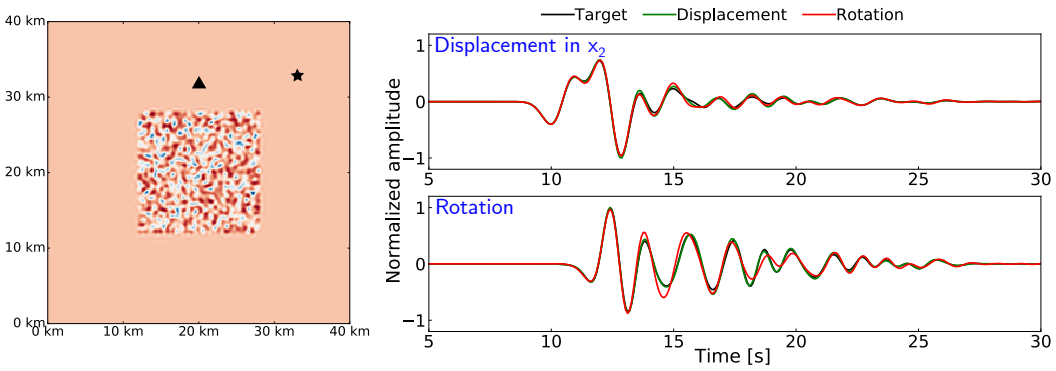

Fig. 6.12.: Validating the recovered models. Left: Source-receiver configuration. The source location is given by the star and the receiver location is given by the triangle. Right: Vertical displacements (top) and rotations (bottom). Measurements in the target model are shown in black, in the model recovered from displacements are shown in green in the model recovered from rotation are shown in red.

From the right panel in 6.12, we can see that the model derived from rotation does not achieve the measurements in the target model. Therefore, unlike the model recovered from displacement, the model recovered from rotation is not reliable.

6.4.3 Receivers close to the heterogeneity with correctors

As our third test, we compare the results of FWI with displacement to that with rotation when the receivers are placed close to the heterogeneity but when the rotation data are corrected for the effect of the small-scale heterogeneity. The improvement in misfit reduction is 96% for rotations. Results

are shown in Figure 6.13 for V_p, V_s, ρ and anisotropy on the right column. For easier comparison, the column on the left shows the inversion with displacements from Section 6.4.2. Also shown are the respective values along two-cross sections in the model. The values along the vertical cross-section are shown on the right (red lines) and the values along the horizontal cross-section are shown just below (red lines). Also shown are the respective values in the target model (green lines), shown in Figure 6.1.

Similar to the sections before, it can be seen that the inversion from displacements are still in better agreement with the target model compared to the inversion from rotations. While discrepancies exist for the latter, most evident in the cross-sections of V_p and V_s, part of it comes from insufficient coverage as seen in Section 6.4.1. Increasing the number of receivers helps as shown by Figure 6.14. The agreement is however not as good as it is for inversion with displacement.

From the right panel in 6.12, we can see that the model derived from rotation is able to achieve the measurements in the target model slightly better.

Validation

Here, we place a receiver in a new location and calculate the displacements and rotations in the recovered models to compare them to those in the target model. The receiver and source positions are shown by the triangle and the star respectively on the left panel of Figure 6.15 and the measurements are shown on the right panel. Measurements in the target model are shown in black, in the model recovered from displacement are shown in green, and in the model recovered from rotation are shown in red. The amplitudes have been normalized.

6.5 Discussion and Conclusion

The purpose of this chapter was twofold. First, we investigated the extent to which FWI can be improved when rotation data are used instead of displacement data. Second, we also assessed the impact that small-scale heterogeneities can have on the FWI with rotation when the receivers are placed near to the heterogeneity.

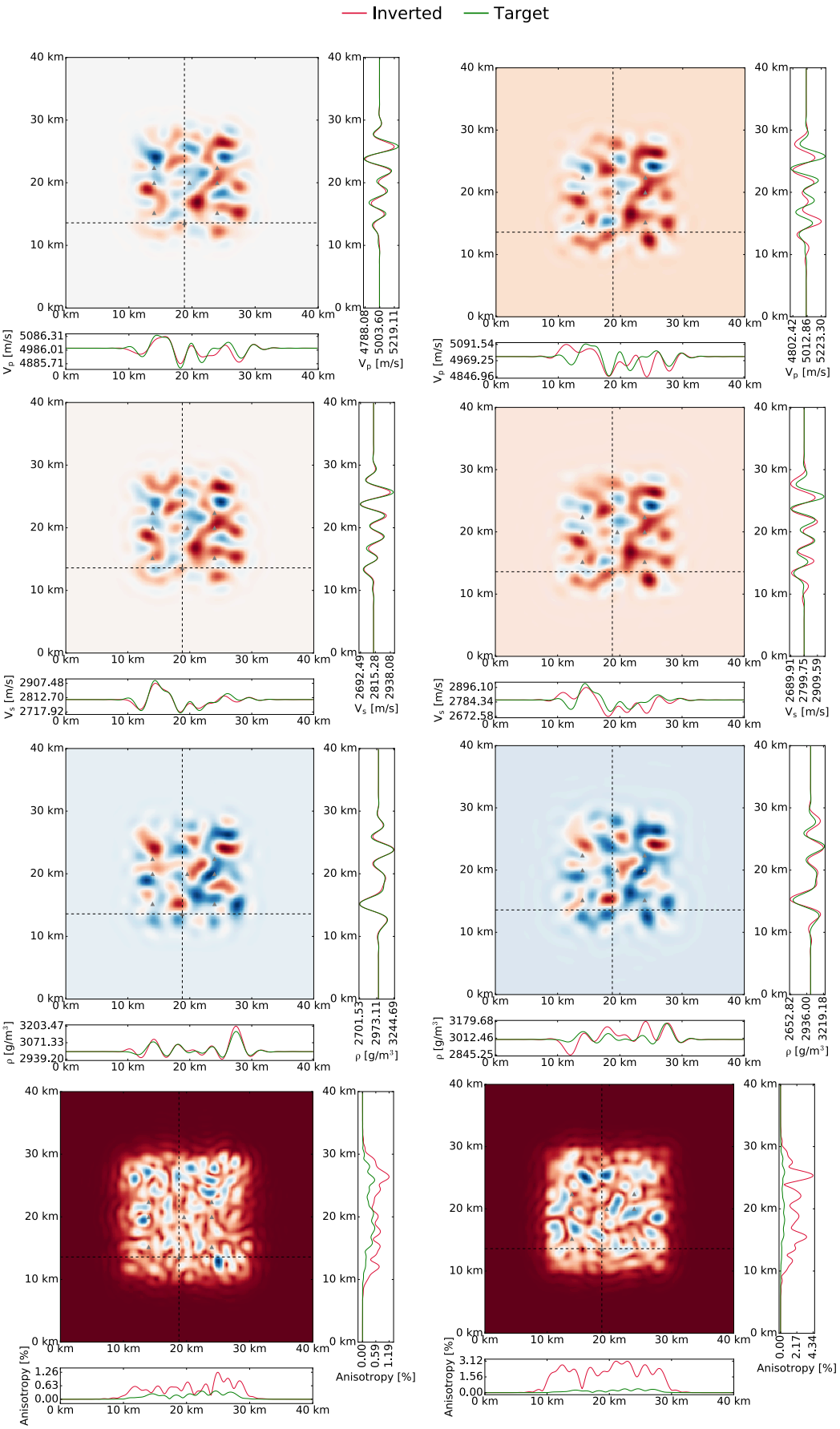

Fig. 6.13.: Results of the third test. Left: Inversion with only displacements, right: inversion with only rotations. Starting from top, V_p, V_s, ρ and anisotropy are shown. For each result, cross-section along the horizontal dotted line is shown below and cross-section along the vertical dotted line is shown to its right. Also shown in green are the respective cross-sections along the target model.

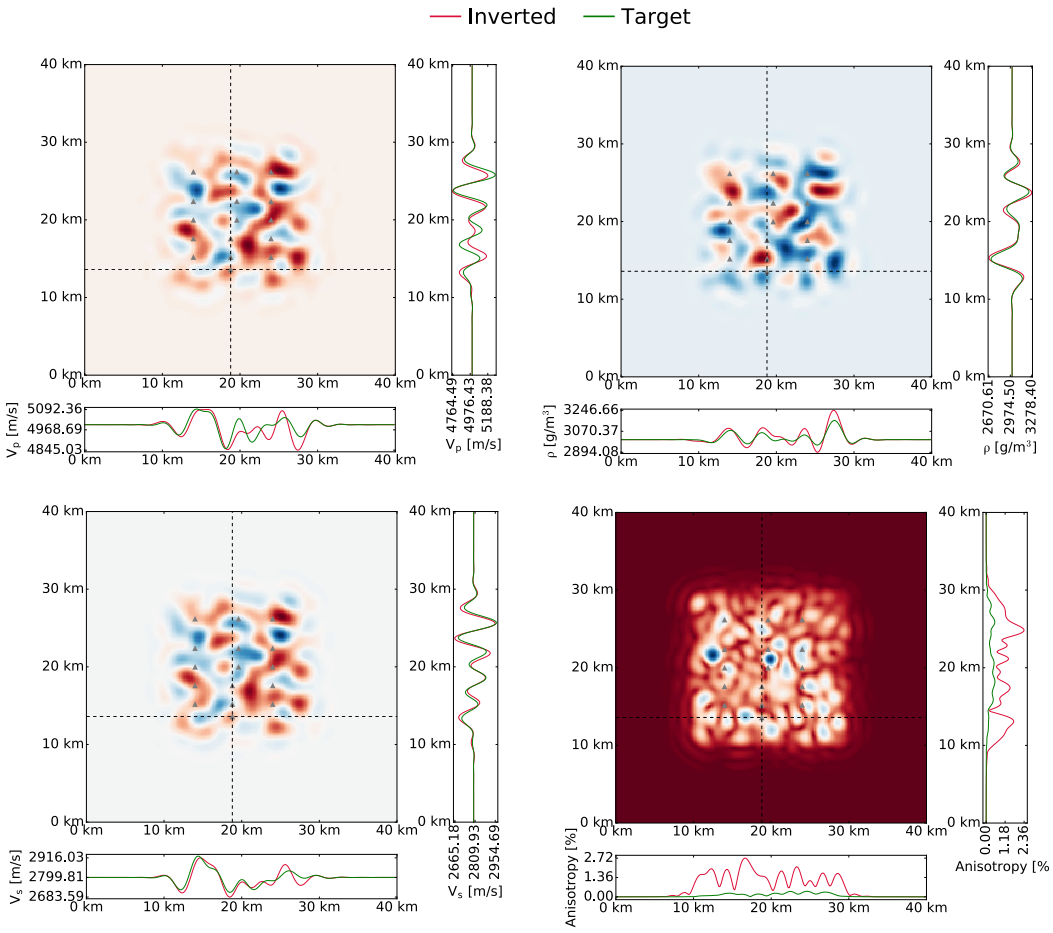

Fig. 6.14.: Results of inversion with only rotations and 16 receivers. Clockwise from top left: V_p, V_s, anisotropy and ρ. The receiver locations are shown by the grey and the starting model was entirely homogeneous. For each result, cross-section along the horizontal dotted line is shown below and cross-section along the vertical dotted line is shown to its right. Also shown in green are the respective cross-sections along the target model.

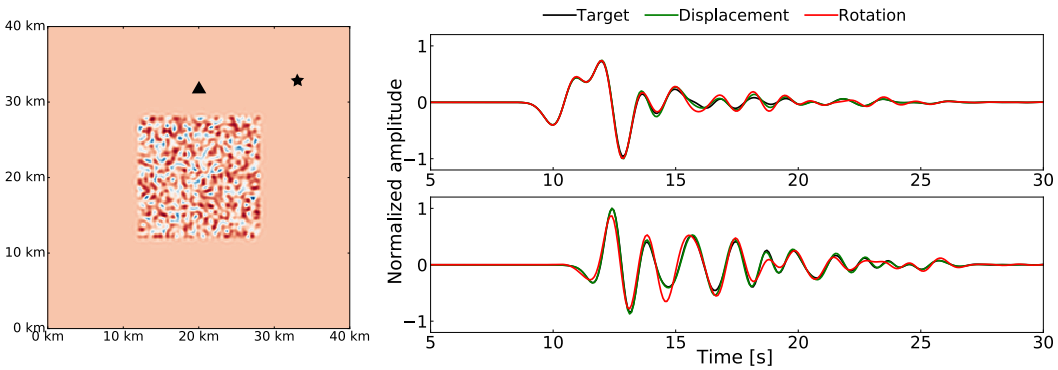

Fig. 6.15.: Validating the recovered models. Left: Source-receiver configuration. The source location is given by the star and the receiver location is given by the triangle. Right: Vertical displacements (top) and rotations (bottom). Measurements in the target model are shown in black, in the model recovered from displacements are shown in green in the model recovered from rotation are shown in red.

For the first goal, we set up a numerical example where we placed the receivers far away from the heterogeneity. This allowed us to compare the two inversions thoroughly. We showed that compared to the inversion with displacement, the inversion with rotation are less in agreement with the target model. This was only because the number of rotation data is half that of the number of rotation data. Once we doubled the number of receivers such that both had the number of data, the agreement was better.

We also showed that the inversion with rotation has a better resolution for c_{1122}. But this may stem from the insufficiency of data and may vanish if the resolution analyses are compared with enough data, i.e. 16 receivers for rotation instead of 8. This is a work in progress. Similarly, we also showed that the resolution lengths could be more accurately determined for parameters c_{1112}, c_{2222} and c_{2212} with rotation. But whether this is significant needs to be studied. Nonetheless, a better measure of resolution will come from experiments in 3D, i.e. when the number of data for displacements and rotations are the same.

Overall, we conclude that wavefield gradients do not bring any substantial improvements to full waveform inversions.

For the second goal, we moved the receivers close to the heterogeneity such that the rotation data are affected by the small-scale heterogeneity. This is the example that is relevant in practice because the Earth's crust is highly heterogeneous and varying at all scales. In this case, the inversion with displacement is less affected by the small-scale heterogeneity and the target model can be recovered. This is not the case when the inversion is performed with rotations. The target model is not recovered, and when a receiver is placed at a position not used in the inversion is used as validation, both displacements and rotations it records are not the same as those recorded in the target model. This suggests fitting of the data used in the inversion, rather than a proper inversion. Note that the small-scale structures may have a negative impact not only on FWI but all other kind of inversion because in Chapter 3, we showed that all phase, amplitude and travel times can be impacted.

Consequently, the presence of small-scale structures need to be accounted for when inversions are performed with wavefield gradients. This can be achieved with the coupling tensor **J** which was introduced in Chapter 3.

Since for any receiver, **J** is independent of source and time, it can be included in the inversion. There are several ways to achieve this: 1) The corrector can be computed for each receiver at each iteration, and it can be removed from the data. Then, the inversion would be equivalent to the conventional inversion with displacements. 2) Both the corrector and the model can be inverted for simultaneously. In this thesis, we chose the chose the first one for its simplicity.

Our numerical experiments were implemented in a simple setup that does not not take into account the effect of attenuation, background noise and uncertainties in sources and receivers. Still, our results pave the way towards inversions with wavefield gradients. We also emphasize that we assumed that the noise distribution for displacements and strains and rotations are the same, and this many not be valid.

Resolution analyses for rotations with more receivers, and inversion with receivers at the heterogeneity but with correctors are in progress.

Acknowledgements

We would like to thank Navid Hedjazian and Thomas Bodin for the helpful discussions and for consistent replies to my numerous emails that always began with 'I do not understand..' Numerical simulations were performed at CCIPL and we thank the people who work not only to endlessly maintain the system but also eagerly help the users.

This work was funded by the French National Research Agency (ANR-16-CE31-0022). We also thank the support through the European Research Council (Advanced Grant: ROMY, number: 339991).

Conclusions and Outlook

7

This PhD thesis explores the uncharted relation between wavefield gradients and small-scale structures. We began in Chapter 3 by showing that structures that are much smaller than the minimum wavelength, such as cavities, topographies and geological heterogeneities do not have a strong effect on the wavefield (displacement) but have a strong effect on their gradients (strains and its time derivatives, rotation and its time derivatives). This is true not only for wavefield gradients measured at a point by instruments such as ring lasers, portable sensors and Distributed Acoustic Systems (DAS) systems but also for wavefield gradients derived using an array. Needless to say, an interpretation of their measurements calls for a complete understanding of how they interact with small-scale structures. This is unfortunate because 1) the small-scales are multi-scale: for every given scale (on the surface of the Earth), we can always find scales that are smaller and consequently, 2) we are uninformed about a detailed small-scale structure (of the Earth).

In Chapter 4, we showed that fortunately, this effect does not depend on the small-scale structures along the entire medium in which the wave travels. It depends only on the local structures at the receiver. Using the theory of homogenization, we showed that the effect can be captured in the term **J**, which we call the corrector. Just like station response, **J** is a characteristic effect of the receiver and does not depend on time or source. Therefore, once known, it can be used to remove the effect of small-scale structures at that receiver. This **J** can be computed precisely if all the small-scale structures at the receiver are known. Since this is not feasible, we employed an alternative: we determined **J** through linear inversion. One necessary condition for this inversion however is that an effective model that fits displacement data well is needed. This is not a concern for most synthetic cases where either the homogenous or homogenized equivalent of the medium can be used as an effective model, and for low frequency data where PREM can be used as an effective model.

In Chapter 5, we explored the possibility that **J** can be used to image the small-scale structures. This is achievable if the receivers are placed dense enough to escape aliasing. While this worked very well for synthetic examples,

we encountered problems extending it to real data. The first and obvious problem is that real data are unavoidably affected by noise due to ocean, wind and human activities. Secondly, even with dense receivers, there are always a few instruments that have configuration problems. Lastly and perhaps most importantly, the heterogeneity spectrum of the Earth is such that aliasing cannot be escaped. But with better instruments that do not suffer from calibration issues, sufficient theory on noise sources to better understand our seismograms, and instruments such as DAS with continuous recordings that will help reduce effects of aliasing, we hope to be able to image small-scale structures with dense receivers someday. The next possibility would then to be establish the link between **J** and the geology of the subsurface.

In Chapter 6, we showed that full wave inversions with wavefield gradients are equivalent to that performed with displacements provided that 1) the number of data is sufficient, and 2) the receivers are placed far away from heterogeneities. They do not bring any substantial improvements to full waveform inversions in terms of accuracy and resolution. We also showed that the effect of small-scale structures on wavefield gradients impacts full waveform inversions too. Since we use the entire waveform, i. e. both phase and amplitude information for such kind of inversions, and the effect of small-scale structures is to change both phase and amplitude, the inversions that are recovered from the wavefield gradients are not reliable. An obvious extension to this work is performing resolution analyses for full waveform inversions in 3D. The synthetic examples shown in Chapter 6 were performed in 2D, where the number of displacement data is twice the number of rotation data. Doing this in 3D will help us obtain more concrete results. Furthermore, the data used in the synthetic examples are not affected by instrument errors, background noise and so on. Another extension to future research relates therefore to the challenges that will arise when inversions with actual recordings from earthquakes or geophysical exploration are considered.

Currently, instrumental developments for measuring wavefield gradients overlap with considerable improvements in applications. For example, blanketing most of seafloor by DAS systems is being envisioned. Similarly, the European Commission, through its H2020 program has approved planetary exploration with an innovative ground motion instrumentation that takes into account 6 degrees of freedom (3 component of translation and 3 component of rotation). Therefore, we believe that our work is both relevant and timely.

Bibliography

Abdel-Ghaffar, A. M. and Rubin, L. I. (1984). Torsional earthquake response of suspension bridges. *Journal of Engineering Mechanics*, 110(10):1467–1484.

Afanasiev, M., Boehm, C., May, D., and Fichtner, A. (2016). Using effective medium theory to better constrain full waveform inversion. In *78th EAGE Conference and Exhibition*.

Afanasiev, M., Peter, D., Sager, K., Simutė, S., Ermert, L., Krischer, L., and Fichtner, A. (2015). Foundations for a multiscale collaborative Earth model. *Geophysical Journal International*, 204(1):39–58.

Aki, K. and Richards, P. (2002). *Quantitative Seismology*. University Science Books.

Aki, K. and Richards, P. G. (1980). *Quantitative Seismology: theory and methods*. W. H. Freeman and Company.

Alder, C., Bodin, T., Ricard, Y., Capdeville, Y., Debayle, E., and Montagner, J. P. (2017). Quantifying seismic anisotropy induced by small-scale chemical heterogeneities. *Geophysical Journal International*, 211(3):1585–1600.

Allaire, G. (1992). Homogenization and two-scale convergence. *SIAM Journal on Mathematical Analysis*, 23(6):1482–1518.

Babuška, V. and Cara, M. (1991). *Seismic anisotropy in the Earth*. Springer Science & Business Media.

Backus, G. E. (1962). Long-wave elastic anisotropy produced by horizontal layering. *Journal of Geophysical Research*, 67(11):4427–4440.

Baker, T. F. (1980). Tidal tilt at Llanrwst, North Wales: tidal loading and Earth structure. *Geophysical Journal International*, 62(2):269–290.

Baker, T. F. and Lennon, G. (1973). Tidal tilt anomalies. *Nature*, 243:75–76.

Basu, D., Whittaker, A. S., and Constantinou, M. C. (2015). Characterizing rotational components of earthquake ground motion using a surface distribution method and response of sample structures. *Engineering Structures*, 99:685–707.

Batchelor, G. K. (1959). Small-scale variation of convected quantities like temperature in turbulent fluid part 1. General discussion and the case of small conductivity. *Journal of Fluid Mechanics*, 5(1):113–133.

Ben-Zion, Y., Vernon, F. L., Ozakin, Y., Zigone, D., Ross, Z. E., Meng, H., White, M., Reyes, J., Hollis, D., and Barklage, M. (2015). Basic data features and results from a spatially dense seismic array on the San Jacinto fault zone. *Geophysical Journal International*, 202(1):370–380.

Berger, J. and Beaumont, C. (1976). An analysis of tidal strain observations from the United States of America II. The inhomogeneous tide. *Bulletin of the Seismological Society of America*, 66(6):1821–1846.

Berger, J. and Lovberg, R. H. (1970). Earth strain measurements with a laser interferometer. *Science*, 170(3955):296–303.

Bernauer, F., Wassermann, J., Guattari, F., Frenois, A., Bigueur, A., Gaillot, A., de Toldi, E., Ponceau, D., Schreiber, K. U., and Igel, H. (2018). BlueSeis3A: Full characterization of a 3C broadband rotational seismometer. *Seismological Research Letters*, 89(2A):620–629.

Bernauer, M., Fichtner, A., and Igel, H. (2009). Inferring earth structure from combined measurements of rotational and translational ground motions. *Geophysics*, 74(6):WCD41–WCD47.

Bernauer, M., Fichtner, A., and Igel, H. (2012). Measurements of translation, rotation and strain: new approaches to seismic processing and inversion. *Journal of Seismology*, 16(4):669–681.

Bernauer, M., Fichtner, A., and Igel, H. (2014). Reducing nonuniqueness in finite source inversion using rotational ground motions. *Journal of Geophysical Research: Solid Earth*, 119(6):4860–4875.

Bodin, P., Gomberg, J., Singh, S. K., and Santoyo, M. (1997). Dynamic deformations of shallow sediments in the valley of Mexico, part I: Three-dimensional strains and rotations recorded on a seismic array. *Bulletin of the Seismological Society of America*, 87(3):528–539.

Bodin, T., Capdeville, Y., Romanowicz, B., and Montagner, J.-P. (2015). Interpreting radial anisotropy in global and regional tomographic models. In *The Earth's heterogeneous mantle*, pages 105–144. Springer.

Bodin, T. and Sambridge, M. (2009). Seismic tomography with the reversible jump algorithm. *Geophysical Journal International*, 178(3):1411–1436.

Bozdağ, E. and Trampert, J. (2008). On crustal corrections in surface wave tomography. *Geophysical Journal International*, 172(3):1066–1082.

Bretaudeau, F., Leparoux, D., Durand, O., and Abraham, O. (2011). Small-scale modeling of onshore seismic experiment: A tool to validate numerical modeling and seismic imaging methods. *Geophysics*, 76(5):T101–T112.

Brokešová, J. and Málek, J. (2015a). Six-degree-of-freedom near-source seismic motions I: rotation-to-translation relations and synthetic examples. *Journal of Seismology*, 19(2):491–509.

Brokešová, J. and Málek, J. (2015b). Six-degree-of-freedom near-source seismic motions II: examples of real seismogram analysis and S-wave velocity retrieval. *Journal of Seismology*, 19(2):511–539.

Brokešová, J. and Málek, J. (2013). Rotaphone, a self-calibrated six-degree-of-freedom seismic sensor and its strong-motion records. *Seismological Research Letters*, 84(5):737–744.

Browaeys, J. T. and Chevrot, S. (2004). Decomposition of the elastic tensor and geophysical applications. *Geophysical Journal International*, 159(2):667–678.

Bruggeman, D. A. G. (1937). Berechnung verschiedener physikalisher Konstanten von heterogenen Substanzen. III. Die elastische Konstanten der Quasiisotropen Mischkörper aus isotropen Substanzen. *Annalen der Physik*, 421:160–178.

Bui-Thanh, T., Ghattas, O., Martin, J., and Stadler, G. (2013). A computational framework for infinite-dimensional bayesian inverse problems part I: The linearized case, with application to global seismic inversion. *SIAM Journal of Scientific Computing*, 35(6):A2494–A2523.

Burgos, G., Capdeville, Y., and Guillot, L. (2016). Homogenized moment tensor and the effect of near-field heterogeneities on nonisotropic radiation in nuclear explosion. *Journal of Geophysical Research: Solid Earth*, 121(6):4366–4389.

Capdeville, Y., Guillot, L., and Marigo, J.-J. (2010a). 1-D non-periodic homogenization for the seismic wave equation. *Geophysical Journal International*, 181(2):897–910.

Capdeville, Y., Guillot, L., and Marigo, J.-J. (2010b). 2-D non-periodic homogenization to upscale elastic media for P–SV waves. *Geophysical Journal International*, 182(2):903–922.

Capdeville, Y. and Marigo, J.-J. (2007). Second order homogenization of the elastic wave equation for non-periodic layered media. *Geophysical Journal International*, 170(2):823–838.

Capdeville, Y. and Marigo, J.-J. (2008). Shallow layer correction for spectral element like methods. *Geophysical Journal International*, 172(3):1135–1150.

Capdeville, Y. and Marigo, J.-J. (2012). A non-periodic two scale asymptotic method to take account of rough topographies for 2-D elastic wave propagation. *Geophysical Journal International*, 192(1):163–189.

Capdeville, Y. and Métivier, L. (2018). Elastic full waveform inversion based on the homogenization method: Theoretical framework and 2-D numerical illustrations. *Geophysical Journal International*, 213(2):1093–1112.

Capdeville, Y., Stutzmann, É., Wang, N., and Montagner, J.-P. (2013). Residual homogenization for seismic forward and inverse problems in layered media. *Geophysical Journal International*, 194(1):470–487.

Capdeville, Y., Zhao, M., and Cupillard, P. (2015). Fast Fourier homogenization for elastic wave propagation in complex media. *Wave Motion*, 54:170–186.

Castellani, A. and Boffi, G. (1989). On the rotational components of seismic motion. *Earthquake Engineering & Structural Dynamics*, 18(6):785–797.

Chapman, C. (2004). *Fundamentals of Seismic Wave Propagation*. Cambridge University Press.

Cochard, A., Igel, H., Schuberth, B., Suryanto, W., Velikoseltsev, A., Schreiber, K. U., Wassermann, J., Scherbaum, F., and Vollmer, D. (2006). Rotational motions in seismology: theory, observation, simulation. In *Earthquake source asymmetry, structural media and rotation effects*, pages 391–411. Springer-Verlag.

Courant, R., Friedrichs, K., and Lewy, H. (1928). Über die partiellen differenzengleichungen der mathematischen physik. *Mathematische annalen*, 100(1):32–74.

Cupillard, P. and Capdeville, Y. (2018). Non-periodic homogenization of 3-D elastic media for the seismic wave equation. *Geophysical Journal International*, 213(2):983–1001.

Cupillard, P., Mulder, W. A., Irakarama, M., Mazuyer, A., and Anquez, P. (2019). Small-scale-induced anisotropy of a 3d subsurface model: quantitative analysis and numerical simulations of waves within. In *AGU Fall Meeting Abstracts, San Francisco, 9-13 December 2019, Programme & Abstracts*.

Dal Maso, G. (1993). *An introduction to* Γ*-Convergence*. Birkhäuser Basel.

Dean, T., Cuny, T., and Hartog, A. H. (2017). The effect of gauge length on axially incident P-waves measured using fibre optic distributed vibration sensing. *Geophysical Prospecting*, 65(1):184–193.

Donner, S., Bernauer, M., and Igel, H. (2016). Inversion for seismic moment tensors combining translational and rotational ground motions. *Geophysical Journal International*, 207(1):562–570.

Donner, S., Igel, H., Hadziioannou, C., and the Romy group (2017). Retrieval of the seismic moment tensor from joint measurements of translational and rotational ground motions: Sparse networks and single stations. In *Moment Tensor Solutions*, pages 263–280. Springer International Publishing.

Donner, S., Mustać, M., Hejrani, B., Tkalčić, H., and Igel, H. (2020). Seismic moment tensors from synthetic rotational and translational ground motion: Green's functions in 1-D versus 3-D. *Geophysical Journal International*, 223(1):161–179.

Dziewoński, A. M. and Anderson, D. L. (1981). Preliminary reference earth model. *Physics of the Earth and Planetary Interiors*, 25(4):297–356.

Edme, P. and Yuan, S. (2016). Local dispersion curve estimation from seismic ambient noise using spatial gradients. *Interpretation*, 4(3):SJ17–SJ27.

Egorov, E., Egorov, I., and Agafonov, V. (2015). Self-noise of the MET angular motion seismic sensors. *Journal of Sensors*, 2015:1–5.

Ekström, G., Nettles, M., and Dziewoński, A. (2012). The global CMT project 2004-2010: Centroid-moment tensors for 13,017 earthquakes. *Physics of the Earth and Planetary Interiors*, 200-201:1–9.

Engquist, B. and Runborg, O. (2002). Wavelet-based numerical homogenization with applications. In *Multiscale and multiresolution methods,Lecture Notes in*

Computational Science and Engineering, pages 97–148. Springer Verlag Berlin Heidelberg.

Eshelby, J. D. and Peierls, R. E. (1957). The determination of the elastic field of an ellipsoidal inclusion, and related problems. *Proceedings of the Royal Society of London. Series A. Mathematical and Physical Sciences*, 241(1226):376–396.

Faccenda, M., Ferreira, A. M. G., Tisato, N., Lithgow-Bertelloni, C., Stixrude, L., and Pennacchioni, G. (2019). Extrinsic elastic anisotropy in a compositionally heterogeneous Earth's mantle. *Journal of Geophysical Research: Solid Earth*, 124(2):1671–1687.

Ferreira, A. M. G., Woodhouse, J. H., Visser, K., and Trampert, J. (2010). On the robustness of global radially anisotropic surface wave tomography. *Journal of Geophysical Research*, 115(B04313).

Fichtner, A., Bunge, H.-P., and Igel, H. (2006). The adjoint method in seismology: I. theory. *Physics of the Earth and Planetary Interiors*, 157(1-2):86–104.

Fichtner, A. and Hanasoge, S. M. (2017). Discrete wave equation upscaling. *Geophysical Journal International*, 209(1):353–357.

Fichtner, A. and Igel, H. (2008). Efficient numerical surface wave propagation through the optimization of discrete crustal models—a technique based on non-linear dispersion curve matching (DCM). *Geophysical Journal International*, 173(2):519–533.

Fichtner, A. and Igel, H. (2009). Sensitivity densities for rotational ground-motion measurements. *Bulletin of the Seismological Society of America*, 99(2B):1302–1314.

Fichtner, A., Kennett, B. L., and Trampert, J. (2013a). Separating intrinsic and apparent anisotropy. *Physics of the Earth and Planetary Interiors*, 219:11–20.

Fichtner, A. and Trampert, J. (2011). Resolution analysis in full waveform inversion. *Geophysical Journal International*, 187(3):1604–1624.

Fichtner, A., Trampert, J., Cupillard, P., Saygin, E., Taymaz, T., Capdeville, Y., and Villaseñor, A. (2013b). Multiscale full waveform inversion. *Geophysical Journal International*, 194(1):534–556.

Gee, L. S. and Jordan, T. H. (1988). Polarization anisotropy and fine-scale structure of the Eurasian Upper Mantle. *Geophysical Research Letters*, 15(8):824–827.

Gold, N., Shapiro, S. A., Bojinski, S., and Müller, T. M. (2000). An approach to upscaling for seismic waves in statistically isotropic heterogeneous elastic media. *Geophysics*, 65(6):1837–1850.

Gomberg, J. and Agnew, D. (1996). The accuracy of seismic estimates of dynamic strains: An evaluation using strainmeter and seismometer data from Piñon Flat Observatory, California. *Bulletin of the Seismological Society of America*, 86(1A):212–220.

Goulty, N. R., King, G. C. P., and Wallard, A. J. (1974). Iodine Stabilized Laser Strainmeter. *Geophysical Journal International*, 39(2):269–282.

Gradon, C., Moreau, L., Roux, P., and Ben-Zion, Y. (2019). Analysis of surface and seismic sources in dense array data with match field processing and Markov chain Monte Carlo sampling. *Geophysical Journal International*, 218(2):1044–1056.

Graizer, V. (2009). The response to complex ground motions of seismometers with Galperin sensor configuration. *Bulletin of The Seismological Society of America*, 99(2B):1366–1377.

Grechka, V. (2003). Effective media: A forward modeling view. *Geophysics*, 68(6):2055–2062.

Guillot, L., Capdeville, Y., and Marigo, J.-J. (2010). 2-D non-periodic homogenization of the elastic wave equation: SH case. *Geophysical Journal International*, 182(3):1438–1454.

Harrison, J. C. (1976). Cavity and topographic effects in tilt and strain measurement. *Journal of Geophysical Research*, 81(2):319–328.

Harrison, J. C. (1978). Implications of cavity, topographic and geologic influences on tilt and strain observations. In *Applications of Geodesy to Geodynamics, an International Symposium*. Proceedings of the Ninth Geodesy/Solid Earth and Ocean Physics (GEOP), Ohio State Univesity.

Hedjazian, N., Capdeville, Y., and Bodin, T. (2020). Multiscale seismic imaging with inverse homogenization. *Geophysical Journal International*, Submitted.

Helbig, K. (1984). Transverse isotropy in exploration seismics. *Geophysical Journal of the Royal Astronomical Society*, 76(1):79–88.

Herglotz, G. (1907). Über das Benndorfsche Problem der Fortpflanzungsgeschwindigkeit der Erdbebenstrahlen. *Zeitschrift für Geophysik*, 8:145–147.

Hetényi, G., Molinari, I., Clinton, J., Bokelmann, G., Bondár, I., Crawford, W. C., Dessa, J.-X., Doubre, C., Friederich, W., Fuchs, F., Giardini, D., Gráczer, Z., Handy, M. R., Herak, M., Jia, Y., Kissling, E., Kopp, H., Korn, M., Margheriti, L., Meier, T., Mucciarelli, M., Paul, A., Pesaresi, D., Piromallo, C., Plenefisch, T., Plomerová, J., Ritter, J., Rümpker, G., Šipka, V., Spallarossa, D., Thomas, C., Tilmann, F., Wassermann, J., Weber, M., Wéber, Z., Wesztergom, V., Živčić, M., AlpArray Seismic Network Team, AlpArray OBS Cruise Crew, and AlpArray Working Group (2018). The AlpArray seismic network: A large-scale European experiment to image the Alpine Orogen. *Surveys in Geophysics*, 39(5):1009–1033.

Huang, B.-S. (2003). Ground rotational motions of the 1999 Chi-Chi, Taiwan earthquake as inferred from dense array observations. *Geophysical Research Letters*, 30(6).

Huang, H., Agafonov, V., and Yu, H. (2013). Molecular electric transducers as motion sensors: A review. *Sensors*, 13(4):4581–4597.

Hudson, J. A. (1977). Scattered waves in the coda of P. *Journal of Geophysics*, 43(1):359–374.

Hutton, K., Woessner, J., and Hauksson, E. (2010). Earthquake monitoring in Southern California for seventy-seven years (1932–2008). *Bulletin of the Seismological Society of America*, 100:423–446.

Ichinose, G., Ford, S., and Mellors, R. (2019). Regional moment tensor inversion using rotational observations. In *AGU Fall Meeting Abstracts, San Francisco, 9-13 December 2019, Programme & Abstracts*.

Igel, H., Bernauer, M., Wassermann, J., and Schreiber, K. U. (2015). Rotational seismology: Theory, instrumentation, observations, applications. In *Encyclopedia of Complexity and Systems Science*. Springer-Verlag New York.

Igel, H., Cochard, A., Wassermann, J., Flaws, A., Schreiber, K. U., Velikoseltsev, A., and Pham Dinh, N. (2007). Broad-band observations of earthquake-induced rotational ground motions. *Geophysical Journal International*, 168(1):182–196.

Igel, H., Schreiber, K. U., Flaws, A., Schuberth, B., Velikoseltsev, A., and Cochard, A. (2005). Rotational motions induced by the M8.1 Tokachi-oki earthquake, September 25, 2003. *Geophysical Research Letters*, 32(8).

Jordan, T. H. (2015). An effective medium theory for three-dimensional elastic heterogeneities. *Geophysical Journal International*, 203(2):1343–1354.

Kennett, B. L. N., Engdahl, E. R., and Buland, R. (1995). Constraints on seismic velocities in the earth from traveltimes. *Geophysical Journal International*, 122:108–124.

Kerr, R. A. (2013). Geophysical exploration linking deep earth and backyard geology. *Science*, 340(6138):1283–1285.

King, G. and Bilham, R. (1973). Tidal tilt measurement in Europe. *Nature*, 243(5402):74–75.

Kohl, M. L. and Levine, J. (1995). Measurement and interpretation of tidal tilts in a small array. *Journal of Geophysical Research*, 100(B3):3929–3941.

Komatitsch, D. and Vilotte, J. P. (1998). The spectral-element method: An efficient tool to simulate the seismic response of 2D and 3D geological structures. *Bulletin of the Seismological Society of America*, 88(2):368–392.

Krischer, L., Megies, T., Barsch, R., Beyreuther, M., Lecocq, T., Caudron, C., and Wassermann, J. (2015). Obspy : a bridge for seismology into the scientific Python ecosystem. *Computational Science & Discovery*, 8(1).

Kurzych, A., Jaroszewicz, L. R., Krajewski, Z., Teisseyre, K. P., and Kowalski, J. K. (2014). Fibre optic system for monitoring rotational seismic phenomena. *Sensors*, 14(3):5459–5469.

Käufl, P., Fichtner, A., and Igel, H. (2013). Probabilistic full waveform inversion based on tectonic regionalization—development and application to the Australian upper mantle. *Geophysical Journal International*, 193(1):437–451.

Lambotte, S., Rivera, L., and Hinderer, J. (2006). Vertical and horizontal seismometric observations of tides. *Journal of Geodynamics*, 41(1):39–58. Earth Tides and Geodynamics: Probing the Earth at Sub-Seismic Frequencies.

Langston, C. (2007a). Spatial gradient analysis for linear seismic arrays. *Bulletin of The Seismological Society of America*, 97(1B):265–280.

Langston, C. A. (2007b). Wave gradiometry in two dimensions. *Bulletin of the Seismological Society of America*, 97(2):401–416.

Lawton, D. and Bertram, M. (1990). Field test of 3-component geophones. *CREWES Research Report*, 29(2):1–17.

Lay, T. and Wallace, T. C. (1995). *Modern Global Seismology*. Elsevier.

Lázaro, A. M., Roset, X., Río, J. D., Toma, D., Carreras, N., Shariat-Panahi, S., Garcia-Benadí, A., Owen, T., and Cadena, J. (2012). Ocean bottom seismometer: Design and test of a measurement system for marine seismology. *Sensors (Basel, Switzerland)*, 12(3):3693–3719.

Levshin, A. and Ratnikova, L. (1984). Apparent ansiotropy in inhomogeneous media. *Geophysical Journal of the Royal Astronomical Society*, 76:65–69.

Li, Z., Hauksson, E., Heaton, T., Rivera, L., and Andrews, J. (2019). Monitoring data quality by comparing co-located broadband and strong-motion waveforms in Southern California Seismic Network. *Seismological Research Letters*, 90(2A):699–707.

Li, Z. and van der Baan, M. (2017). Tutorial on rotational seismology and its applications in exploration geophysics. *Geophysics*, 82(5):W17–W30.

Liang, C. and Langston, C. A. (2009). Wave gradiometry for usarray: Rayleigh waves. *Journal of Geophysical Research: Solid Earth*, 114(B2).

Lin, F.-C., Li, D., Clayton, R. W., and Hollis, D. (2013). High-resolution 3D shallow crustal structure in Long Beach, California: application of ambient noise tomography on a dense seismic array. *Geophysics*, 78(4):Q45–Q56.

Lindner, F., Wassermann, J., Schmidt-Aursch, M. C., Schreiber, K. U., and Igel, H. (2016). Seafloor ground rotation observations: Potential for improving signal-to-noise ratio on horizontal OBS components. *Seismological Research Letters*, 88(1):32–38.

Maeda, Y., Takeo, M., and Ohminato, T. (2011). A waveform inversion including tilt: method and simple tests. *Geophysical Journal International*, 184(2):907–918.

Mancinelli, N., Shearer, P., and Liu, Q. (2016). Constraints on the heterogeneity spectrum of Earth's upper mantle. *Journal of Geophysical Research: Solid Earth*, 121(5):3703–3721.

Martin, G., Wiley, R., and Marfurt, K. (2006). Marmousi2: An elastic upgrade for Marmousi. *The Leading Edge*, 25:156–166.

Martin, G. S. (2004). The Marmousi2 model: Elastic synthetic data, and an analysis of imaging and AVO in a structurally complex environment. Master's thesis, University of Houston.

Maupin, V. and Park, J. (2007). Theory and observations – wave propagation in anisotropic media. In *Treatise on Geophysics*, volume 1, pages 289–321. Elsevier.

McCarter, E. R. (1956). Testing geophone performance.

McLeod, D. P., Stedman, G. E., Webb, T. H., and Schreiber, K. U. (1998). Comparison of standard and ring laser rotational seismograms. *Bulletin of the Seismological Society of America*, 88(06):1495–1503.

Meertens, C., Levine, J., and Busby, R. (1989). Tilt observations using borehole tiltmeters: 2. Analysis of data from Yellowstone National Park. *Journal of Geophysical Research: Solid Earth*, 94(B1):587–601.

Meertens, C. M. and Wahr, J. M. (1986). Topographic effect on tilt, strain, and displacement measurements. *Journal of Geophysical Research: Solid Earth*, 91(B14):14057–14062.

Meltzer, A., Rudnick, R., Zeitler, P., Levander, A., Humphreys, G., Karlstrom, K., Ekström, G., Carlson, R., Dixon, T., Gurnis, M., Shearer, P., and Hilst, R. v. d. (1999). USArray initiative. *GSA Today*, 9:8–10.

Meng, H. and Ben-Zion, Y. (2017). Detection of small earthquakes with dense array data: example from the san jacinto fault zone, southern california. *Geophysical Journal International*, 212(1):442–457.

Meschede, M. and Romanowicz, B. (2014). Lateral heterogeneity scales in regional and global upper mantle shear velocity models. *Geophysical Journal International*, 200(2):1078–1095.

Mikumo, T. and Aki, K. (1964). Determination of local phase velocity by intercomparison of seismograms from strain and pendulum instruments. *Journal of Geophysical Research*, 69(4):721–731.

Milne, J. (1888). Pendulum seismometers. *Nature*, 37:570–571.

Mosca, I., Cobden, L., Deuss, A., Ritsema, J., and Trampert, J. (2012). Seismic and mineralogical structures of the lower mantle from probabilistic tomography. *Journal of Geophysical Research: Solid Earth*, 117(B6).

Moulinec, H. and Suquet, P. (1998). A numerical method for computing the overall response of nonlinear composites with complex microstructure. *Computer Methods in Applied Mechanics and Engineering*, 157(1):69–94.

Okada, Y., Kasahara, K., Hori, S., Obara, K., Sekiguchi, S., Fujiwara, H., and Yamamoto, A. (2004). Recent progress of seismic observation networks in japan—hi-net, f-net, k-net and kik-net. *Earth, Planets, and Space*, 56:15–28.

Olson, P., Yuen, D. A., and Balsiger, D. (1984). Mixing of passive heterogeneities by mantle convection. *Journal of Geophysical Research: Solid Earth*, 89(B1):425–436.

Oth, A., Parolai, S., and Bindi, D. (2011). Spectral Analysis of K-NET and KiK-net data in Japan, Part I: Database compilation and peculiarities. *Bulletin of the Seismological Society of America*, 101(2):652–666.

Owens, T. J., Randall, G. E., Wu, F. T., and Zeng, R. (1993). Passcal instrument performance during the Tibetan Plateau Passive Seismic Experiment. *Bulletin of the Seismological Society of America*, 83(6):1959–1970.

Pageot, D., Leparoux, D., Le Feuvre, M., Durand, O., Côte, P., and Capdeville, Y. (2017). Improving the seismic small-scale modelling by comparison with numerical methods. *Geophysical Journal International*, 211(1):637–649.

Pancha, A., Webb, T. H., Stedman, G. E., McLeod, D. P., and Schreiber, K. U. (2000). Ring laser detection of rotations from teleseismic waves. *Geophysical Research Letters*, 27(21):3553–3556.

Pierson, B., Laughlin, D., and Brune, R. (2016). Advances in rotational seismic measurements. In *SEG Technical Program Expanded Abstracts 2016*, pages 2263–2267. Society of Exploration Geophysicists.

Plessix, R.-E. (2006). A review of the adjoint-state method for computing the gradient of a functional with geophysical applications. *Geophysical Journal International*, 167(2):495–503.

Poppeliers, C. and Evans, E. V. (2015). The effects of measurement uncertainties in seismic-wave gradiometry. *Bulletin of the Seismological Society of America*, 105(6):3143–3155.

Press, F. and Archambeau, C. (1962). Release of tectonic strain by underground nuclear explosions. *Journal of Geophysical Research*, 67(1):337–343.

Reinwald, M., Bernauer, M., Igel, H., and Donner, S. (2016). Improved finite-source inversion through joint measurements of rotational and translational ground motions: a numerical study. *Solid Earth*, 7(5):1467–1477.

Resovsky, J. and Trampert, J. (2003). Using probabilistic seismic tomography to test mantle velocity–density relationships. *Earth and Planetary Science Letters*, 215(1):121–134.

Ricard, Y., Durand, S., Montagner, J.-P., and Chambat, F. (2014). Is there seismic attenuation in the mantle? *Earth and Planetary Science Letters*, 388:257–264.

Sanchez-Palencia, E. (1980). *Non-Homogeneous Media and Vibration Theory*, volume 127. Springer-Verlag Berlin Heidelberg.

Sato, T. and Harrison, J. C. (1989). Local effects on tidal strain measurements at Esashi, Japan. *Geophysical Journal International*, 102(3):513–526.

Schmandt, B. and Clayton, R. W. (2013). Analysis of teleseismic P waves with a 5200-station array in Long Beach, California: evidence for an abrupt boundary to inner borderland rifting. *Journal of Geophysical Research: Solid Earth*, 118(10):5320–5338.

Schmelzbach, C., Donner, S., Igel, H., Sollberger, D., Taufiqurrahman, T., Bernauer, F., Häusler, M., Renterghem, C. V., Wassermann, J., and Robertsson, J. (2018). Advances in 6C seismology: Applications of combined translational and rotational motion measurements in global and exploration seismology. *Geophysics*, 83(3):WC53–WC69.

Schoenberg, M. and Muir, F. (1989). A calculus for finely layered anisotropic media. *Geophysics*, 54(5):581–589.

Schreiber, K. U., Hautmann, J. N., Velikoseltsev, A., Wassermann, J., Igel, H., Otero, J., Vernon, F., and Wells, J. P. R. (2009). Ring laser measurements of ground rotations for seismology. *Bulletin of the Seismological Society of America*, 99(2B):1190–1198.

Schreiber, K. U., Velikoseltsev, A., Igel, H., Cochard, A., Flaws, A., Drewitz, W., and Müller, F. (2003). The geosensor: A new instrument for seismology. In *Geotechnologien Science Report No. 3: "Observation of the System Earth from Space", Status Seminar, Bavarian State Mapping Agency (BLVA), Munich, 12-13 June 2003, Programme & Abstracts*.

Shearer, P. M. (2019). *Introduction to Seismology*. Cambridge university press.

Sollberger, D., Schmelzbach, C., Renterghem, C. V., Robertsson, J., and Greenhalgh, S. (2016). Single-component elastic wavefield separation at the free surface using source- and receiver-side gradients. In *SEG Technical Program Expanded Abstracts 2016*, pages 2268–2273. Society of Exploration Geophysicists.

Spudich, P., Steck, L. K., Hellweg, M., Fletcher, J. B., and Baker, L. M. (1995). Transient stresses at Parkfield, California, produced by the M7.4 Landers earthquake of June 28, 1992: Observations from the UPSAR dense seismograph array. *Journal of Geophysical Research: Solid Earth*, 100(B1):675–690.

Stedman, G. E., Li, Z., and Bilger, H. R. (1995). Sideband analysis and seismic detection in a large ring laser. *Applied Optics*, 34(24):5375–5385.

Sumy, D. F., Woodward, R., Barklage, M., Hollis, D., Spriggs, N., Gridley, J. M., and Parker, T. (2015). Sweetwater, Texas large N experiment. In *AGU Fall Meeting, San Francisco, 14-18 December 2015, Programme & Abstracts*.

Suryanto, W., Igel, H., Wassermann, J., Cochard, A., Schuberth, B., Vollmer, D., Scherbaum, F., Schreiber, K. U., and Velikoseltsev, A. (2006). First comparison of array-derived rotational ground motions with direct ring laser measurements. *Bulletin of the Seismological Society of America*, 96(6):2059–2071.

Sutton, G. H. and Duennebier, F. K. (1987). Optimum design of ocean bottom seismometers. *Marine geophysical researches*, 9:47–65.

Takeo, M. and Ito, H. M. (1997). What can be learned from rotational motions excited by earthquakes? *Geophysical Journal International*, 129(2):319–329.

Tarantola, A. and Valette, B. (1982). Generalized nonlinear inverse problems solved using the least squares criterion. *Reviews of Geophysics*, 20(2):219–232.

Thorne, M. S., Takeuchi, N., and Shiomi, K. (2019). Melting at the edge of a slab in the deepest mantle. *Geophysical Research Letters*, 46(14):8000–8008.

Tiwary, D. K., Bayuk, I. O., Vikhorev, A. A., and Chesnokov, E. M. (2009). Comparison of seismic upscaling methods: From sonic to seismic. *Geophysics*, 74(2):WA3–WA14.

Trifunac, M. D. (1982). A note on rotational components of earthquake motions on ground surface for incident body waves. *International Journal of Soil Dynamics and Earthquake Engineering*, 1(1):11–19.

Trifunac, M. D. and Todorovska, M. I. (2001). A note on the useable dynamic range of accelerographs recording translation. *Soil Dynamics and Earthquake Engineering*, 21(4):275–286.

Tromp, J., Komatitsch, D., and Liu, Q. (2008). Spectral-element and adjoint methods in seismology. *Communications in Computational Physics*, 3(1):1–32.

Tromp, J., Tape, C., and Liu, Q. (2005). Seismic tomography, adjoint methods, time reversal and banana-doughnut kernels. *Geophysical Journal International*, 160(1):195–216.

Valensi, R., Leparoux, D., Durand, O., Bretaudeau, F., and Côte, P. (2015). Multi-component reduced scale seismic modelling: upgrade of the MUSC laboratory with application to polarization observations. *Geophysical Journal International*, 202(3):1993–2024.

van Driel, M., Wassermann, J., Nader, M. F., Schuberth, B. S. A., and Igel, H. (2012). Strain rotation coupling and its implications on the measurement of rotational ground motions. *Journal of Seismology*, 16(4):657–668.

van Driel, M., Wassermann, J., Pelties, C., Schiemenz, A., and Igel, H. (2015). Tilt effects on moment tensor inversion in the near field of active volcanoes. *Geophysical Journal International*, 202(3):1711–1721.

Vavryčuk, V. and Kim, S. G. (2014). Nonisotropic radiation of the 2013 North Korean nuclear explosion. *Geophysical Research Letters*, 41(20):7048–7056.

Wang, N., Montagner, J.-P., Fichtner, A., and Capdeville, Y. (2013). Intrinsic versus extrinsic seismic anisotropy: The radial anisotropy in reference Earth models. *Geophysical Research Letters*, 40:4284–4288.

Wassermann, J., Bernauer, F., Shiro, B., Johanson, I., Guattari, F., and Igel, H. (2020). Six-Axis Ground Motion Measurements of Caldera Collapse at Kīlauea Volcano, Hawai'i—More Data, More Puzzles? *Geophysical Research Letters*, 47(5).

Wassermann, J., Wietek, A., Hadziioannou, C., and Igel, H. (2016). Toward a single-station approach for microzonation: Using vertical rotation rate to estimate Love-wave dispersion curves and direction finding. *Bulletin of the Seismological Society of America*, 106(3):1316–1330.

Wiechert, E. (1907). Über Erdbebenwellen. I. Theoretisches über die Ausbreitung der Erdbebenwellen. In *Nachrichten von der königlichen Akademie der Wissenschaften zu Göttingen, Mathematischphysikalische Klasee, neue Fassung 5*, pages 415–529. Weidmannsche Buchhandlung.

Wielandt, E. and Forbriger, T. (1999). Near-field seismic displacement and tilt associated with the explosive activity of Stromboli. *Annali di Geofisica*, 42:407–416.

Wielandt, E. and Steim, J. M. (1986). A digital very-broad-band seismograph. *Annales de Geophysique Série B: terrestre et physique planétaire*, 4(3):227–232.

Willis, M. E., Barfoot, D., Ellmauthaler, A., Wu, X., Barrios, O., Erdemir, C., Shaw, S., and Quinn, D. (2016). Quantitative quality of distributed acoustic sensing vertical seismic profile data. *The Leading Edge*, 35(7):605–609.

Wood, M. D. and King, N. E. (1977). Relation between earthquakes, weather, and soil tilt. *Science*, 197(4299):154–156.

Wu, R. and Aki, K. (1985). Scattering characteristics of elastic waves by an elastic heterogeneity. *Geophysics*, 50(4):582–595.

Wu, R.-S., Xu, Z., and Li, X.-P. (1994). Heterogeneity spectrum and scale-anisotropy in the upper crust revealed by the German Continental Deep-Drilling (KTB) holes. *Geophysical Research Letters*, 21(10):911–914.

Wyatt, F. K., Morrissey, S.-T., and Agnew, D. C. (1988). Shallow borehole tilt: A reprise. *Journal of Geophysical Research: Solid Earth*, 93(B8):9197–9201.

Zhan, Z. (2019). Distributed Acoustic Sensing turns fiber-optic cables into sensitive seismic antennas. *Seismological Research Letters*, 91(1):1–15.

A

Deriving wavefield gradients from an array

It is possible to estimate wavefield gradients just from displacements. For displacements $\mathrm{u}(x_1, x_2)$,

$$\partial x_2 \, \mathrm{u}'(x_1, x_2) = \mathrm{u}(x_1, x_2 + \partial x_2) - \mathrm{u}(x_1, x_2) \tag{A.1}$$

$$\partial x_1 \, \mathrm{u}'(x_1, x_2) = \mathrm{u}(x_1, x_2) - \mathrm{u}(x_1 - \partial x_1, x_2) \tag{A.2}$$

We assume that we have three receivers in a geometry shown in Figure A.1 and we want to estimate the wavefield gradient at receiver 2.

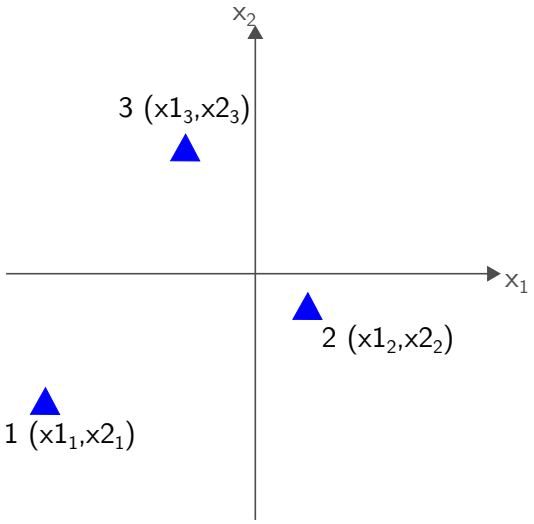

Fig. A.1.: Original receiver setup.

We can transform this geometry into a new co-ordinate system such that in the new co-ordinate system, receivers 1 and 3 are at positions (-1,0) and (0,1) respectively. The transformation leads to

$$\begin{bmatrix} \frac{\partial \bar{x_1}}{\partial x_1} & \frac{\partial \bar{x_2}}{\partial x_1} \\ \frac{\partial \bar{x_1}}{\partial x_2} & \frac{\partial \bar{x_2}}{\partial x_2} \end{bmatrix} = \begin{bmatrix} 0 & -1 \\ 1 & 0 \end{bmatrix} \begin{bmatrix} (x1_3 - x1_2) & (x1_1 - x1_2) \\ (x2_3 - x2_2) & (x2_1 - x2_2) \end{bmatrix}^{-1}$$

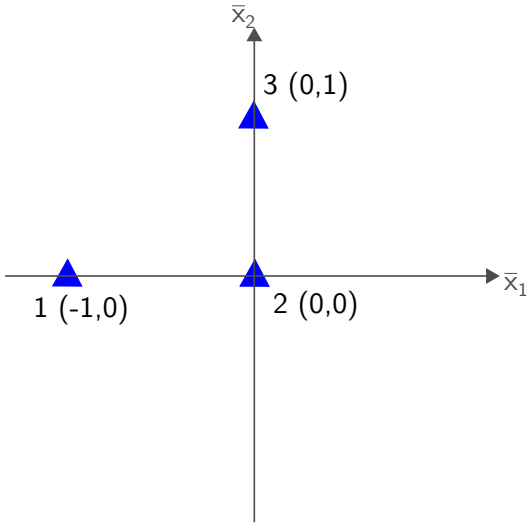

Fig. A.2.: Receiver setup after transformation.

Consequently, using chain rule,

$$\frac{\partial \mathrm{u}(x_1, x_2)}{\partial x_1} = \frac{\partial \mathrm{u}(x_1, x_2)}{\partial \bar{x_1}} \frac{\partial \bar{x_1}}{\partial x_1} + \frac{\partial \mathrm{u}(x_1)}{\partial \bar{x_2}} \frac{\partial \bar{x_2}}{\partial x_1}, \tag{A.3}$$

where $\frac{\partial \mathrm{u}(x_1,x_2)}{\partial \bar{x_1}}$ can be found through A.2 using displacements measured at receiver 1 and receiver 2. Similarly, $\frac{\partial \mathrm{u}(x_1,x_2)}{\partial \bar{x_2}}$ can be found through A.1 using displacements measured at receiver 2 and receiver 3. Note that in this particular transformation, $\partial \bar{x_1}$ and $\partial \bar{x_2}$ are equal to 1.

B

Corrector for array-derived wavefield gradient

The most straightforward procedure to estimating wavefield gradients from displacements is based on truncated Taylor series,

$$h\ \nabla_{\mathbf{j}} f(\mathbf{x}) \sim f(\mathbf{x}+h\mathbf{j}) - f(\mathbf{x}), \tag{B.1}$$

where $\mathbf{j} \in \{\hat{\mathbf{x}}_1, \hat{\mathbf{x}}_2\}$. This approximation is correct to first-order in grid spacing h and is only valid if f is smooth with respect to h. Recalling the equation for true displacement from (3.3),

$$\mathbf{u}^{\varepsilon}(\mathbf{x},\mathbf{y},t) = \mathbf{u}^{0}(\mathbf{x},t) + \varepsilon(\chi(\mathbf{y}) : \boldsymbol{\epsilon}(\mathbf{u}^{0}(\mathbf{x},t))). \tag{B.2}$$

Expanding the terms in (B.2) individually, noting that the corrector χ is not smooth with respect to $\mathbf{x}$, and using the relation $\mathbf{x} = \frac{\mathbf{y}}{\varepsilon}$, we have,

$$\mathbf{u}^{\varepsilon}(\mathbf{x}+h\mathbf{j},\mathbf{y}+\frac{h}{\varepsilon}\mathbf{j},t) = \mathbf{u}^{0}(\mathbf{x},t) + h\ \nabla_{\mathbf{j}}\mathbf{u}^{0}(\mathbf{x},t) + \varepsilon\left(\chi\left(\mathbf{y}+\frac{h}{\varepsilon}\mathbf{j}\right) : \boldsymbol{\epsilon}\left(\mathbf{u}^{0}(\mathbf{x},t)+h\ \nabla_{\mathbf{j}}\mathbf{u}^{0}(\mathbf{x},t)\right)\right). \tag{B.3}$$

Substituting (B.2) and (B.3) in (B.1), we get,

$$\begin{aligned}
\mathbf{u}^{\varepsilon}(\mathbf{x}+h\mathbf{j},\mathbf{y}+\frac{h}{\varepsilon}\mathbf{j},t) - \mathbf{u}^{\varepsilon}(\mathbf{x},\mathbf{y},t) &= h\ \nabla_{\mathbf{j}}\mathbf{u}^{0}(\mathbf{x},t) + \varepsilon\left(\chi\left(\mathbf{y}+\frac{h}{\varepsilon}\mathbf{j}\right) - \chi(\mathbf{y})\right) : \boldsymbol{\epsilon}(\mathbf{u}^{0}(\mathbf{x},t)), \\
\frac{\mathbf{u}^{\varepsilon}(\mathbf{x}+h\mathbf{j},\mathbf{y}+\frac{h}{\varepsilon}\mathbf{j},t) - \mathbf{u}^{\varepsilon}(\mathbf{x},\mathbf{y},t)}{h} &= \nabla_{\mathbf{j}}\mathbf{u}^{0}(\mathbf{x},t) + \mathbf{J}(\mathbf{y}) : \boldsymbol{\epsilon}(\mathbf{u}^{0}(\mathbf{x},t)) \\
\nabla_{\mathbf{j}}\mathbf{u}^{\varepsilon}(\mathbf{x},\mathbf{y},t) &= \nabla_{\mathbf{j}}\mathbf{u}^{0}(\mathbf{x},t) + \mathbf{J}(\mathbf{y}) : \boldsymbol{\epsilon}(\mathbf{u}^{0}(\mathbf{x},t)),
\end{aligned} \tag{B.4}$$

with $\mathbf{J}(\mathbf{y}) = \frac{\varepsilon}{h}\left(\chi(\mathbf{y}+\frac{h}{\varepsilon}\mathbf{j}) - \chi(\mathbf{y})\right)$.

C

Translations are in good agreement I

As stated in Section 4.2, the effective model needed for the inversion of J is not limited to the homogenized model. Any tomographic model that fits displacement data reasonably well can be used.

In Section 4.3.1, we used the homogeneous medium as one of our effective models and it is indeed sensible to do so because as shown by Figure C.1, the displacements in both the heterogeneous and homogenized/homogeneous media are in agreement. This reasoning was also extended to inversion in Section 4.3.2, and as can be seen in Figure C.2, it is apt.

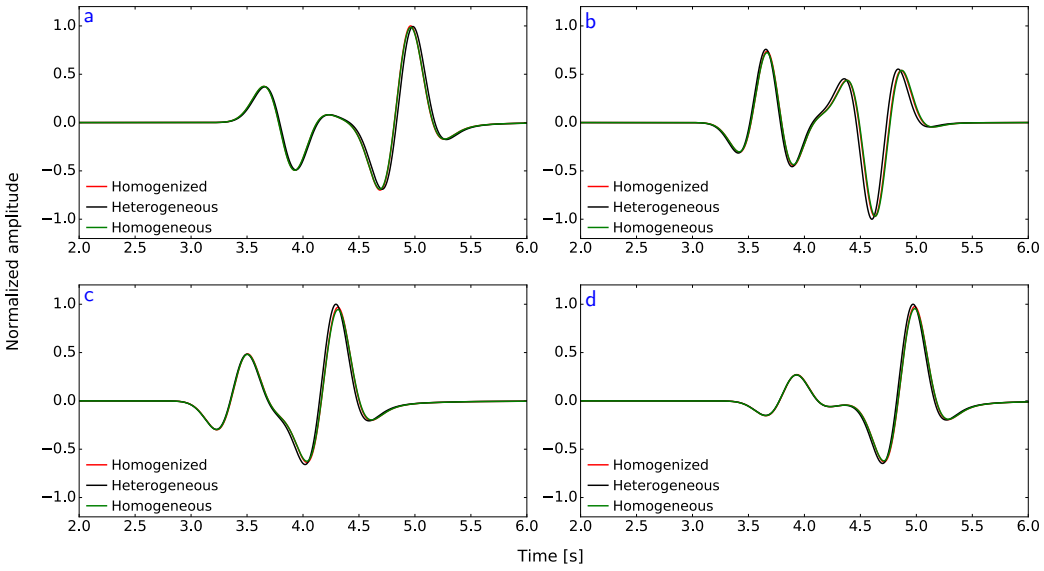

Fig. C.1.: Vertical displacements for the four events shown in Figures 4.2 and 4.3. Displacements in the heterogeneous media are shown in black, displacements in the homogeneous media are shown in green and displacements in the homogenized media are shown in red.

Similarly, in Section 4.4.1, we perform the inversion for **J** for the ring laser at Wettzell, Germany. In this case, our effective model was PREM. Figure C.3 shows that displacement data at the collocated seismometer WET and synthetics derived in this effective model are in agreement. Therefore, the

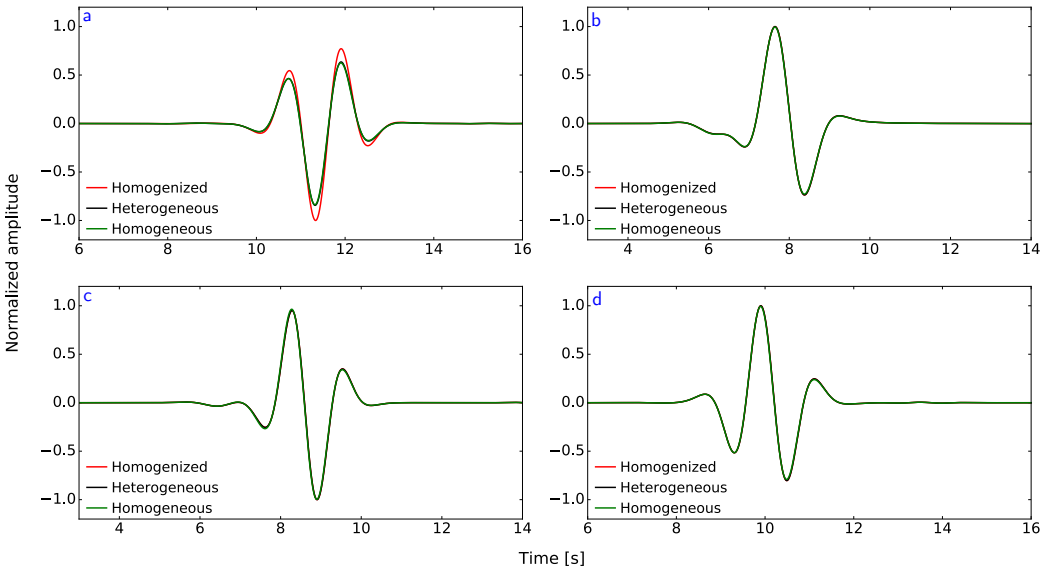

Fig. C.2.: Vertical displacements for the four events shown in Figures 4.5 and 4.6. Displacements in the heterogeneous media are shown in black, displacements in the homogeneous media are shown in green and displacements in the homogenized media are shown in red.

use of PREM here is justifiable. Note that the time axis are different than in Figure 4.7 to adjust the Rayleigh wave arrivals.

In Section 4.4.2, we estimated array derived rotation rates at the ring laser. From Figure C.4, we see that the velocities at three stations are in agreement. The distance between the stations is around 100 km.

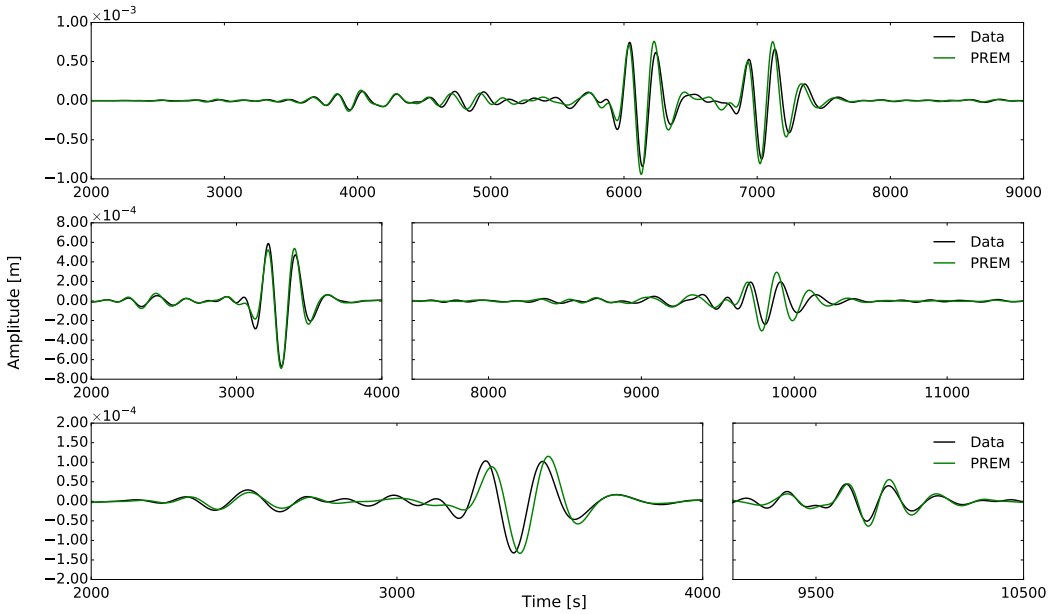

Fig. C.3.: Vertical displacements measured at WET for the three events shown in Figure 4.7. Observed displacements are shown in black and displacements computed in PREM are shown in green.
Top: 201611131102A South Island, New Zealand. Middle: 201210280304A Queen Charlotte Islands. Bottom: 201006121926A Nicobar Islands.

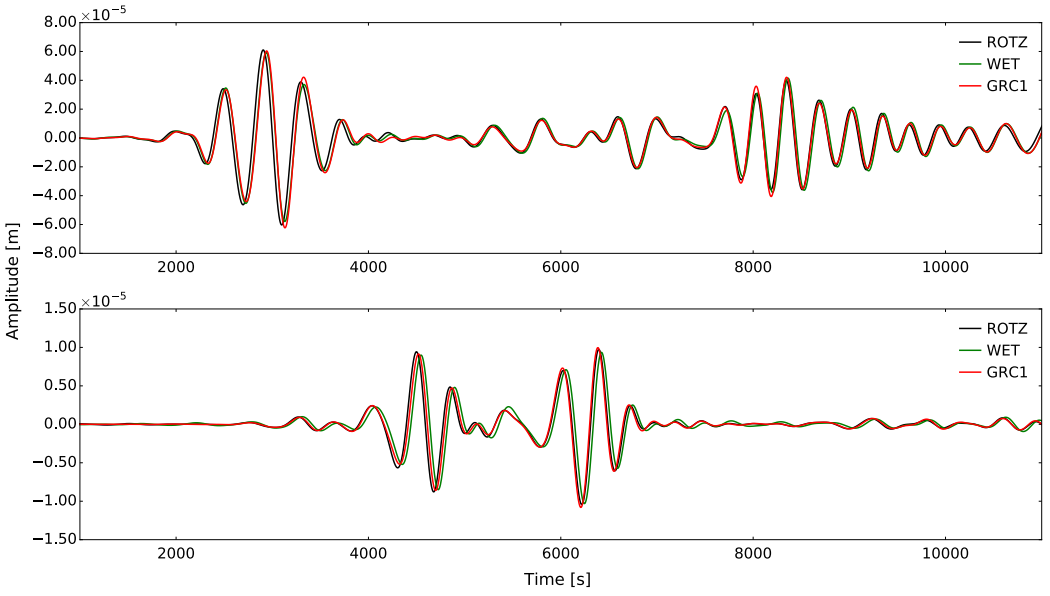

Fig. C.4.: Velocities along the East component for the two events shown in Figure 4.9. Observed velocities at stations ROTZ, WET and GRC1 are shown in black, green and red respectively.
Top: 201103110546A Near East Coast of Honsh. Bottom: 200909291748A Samoa Islands Region.

D

Source-receiver distribution

Here, we show the map of the earthquakes and station data set used in 4.4. Figure D.1 shows the source-receiver distribution for the inversion in 4.4.1, while Figure D.2 shows the source-receiver distribution for the inversion in 4.4.2.

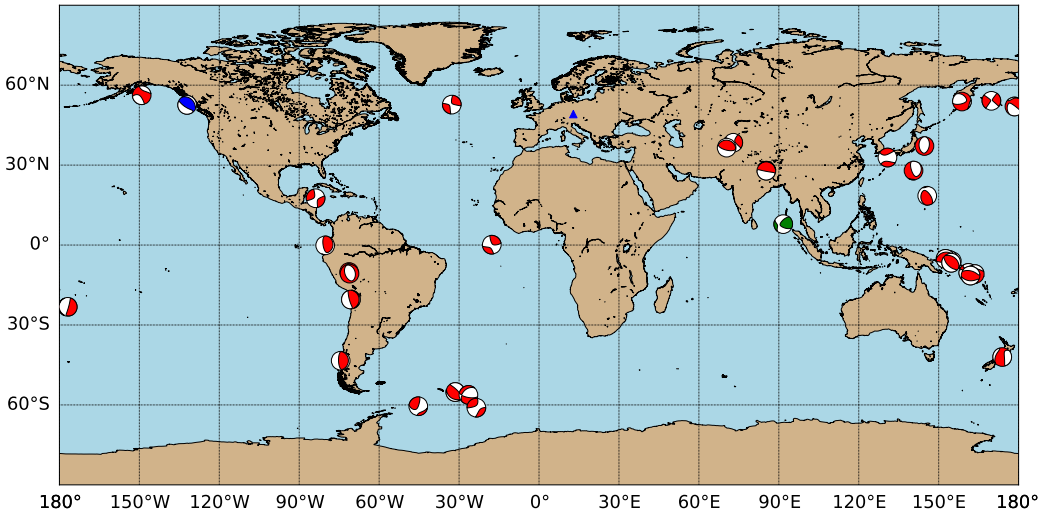

Fig. D.1.: The source receiver geometry for the events in Section 4.4.1. The 32 events used for the inversion are shown in red, while the events that were used for validation are shown in blue and green. The event in blue is the 201210280304A Queen Charlotte Islands while the event shown in green is the 201006121926A Nicobar Islands. The blue triangle shows the location of the receiver.

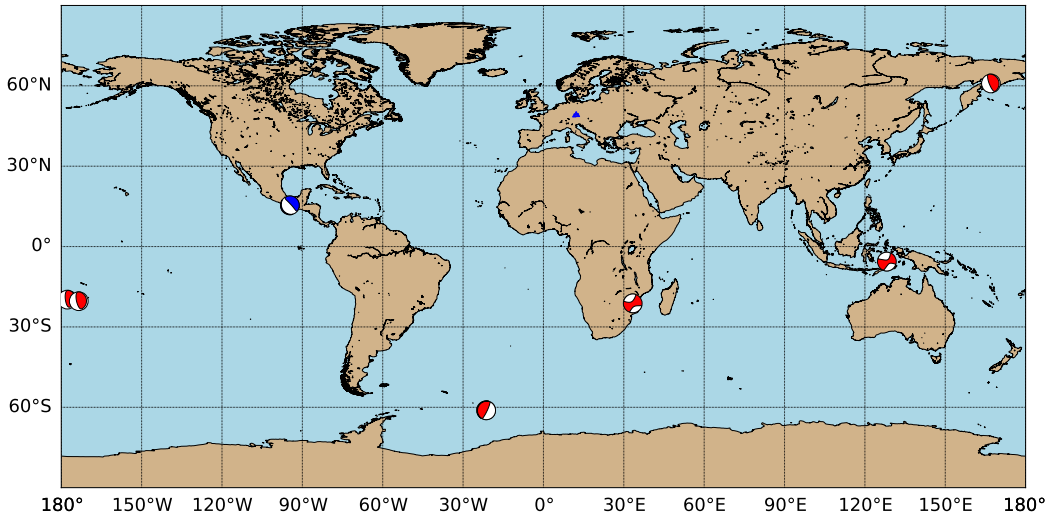

Fig. D.2.: The source receiver geometry for the events in Section 4.4.2. The 6 events used for the inversion are shown in red, while the event that was used for validation is shown in blue. The blue triangles show the location of the three receivers.

Full Seismograms

E

Here, we show the complete seismograms for all event-station pairs in Section 5.2.2.

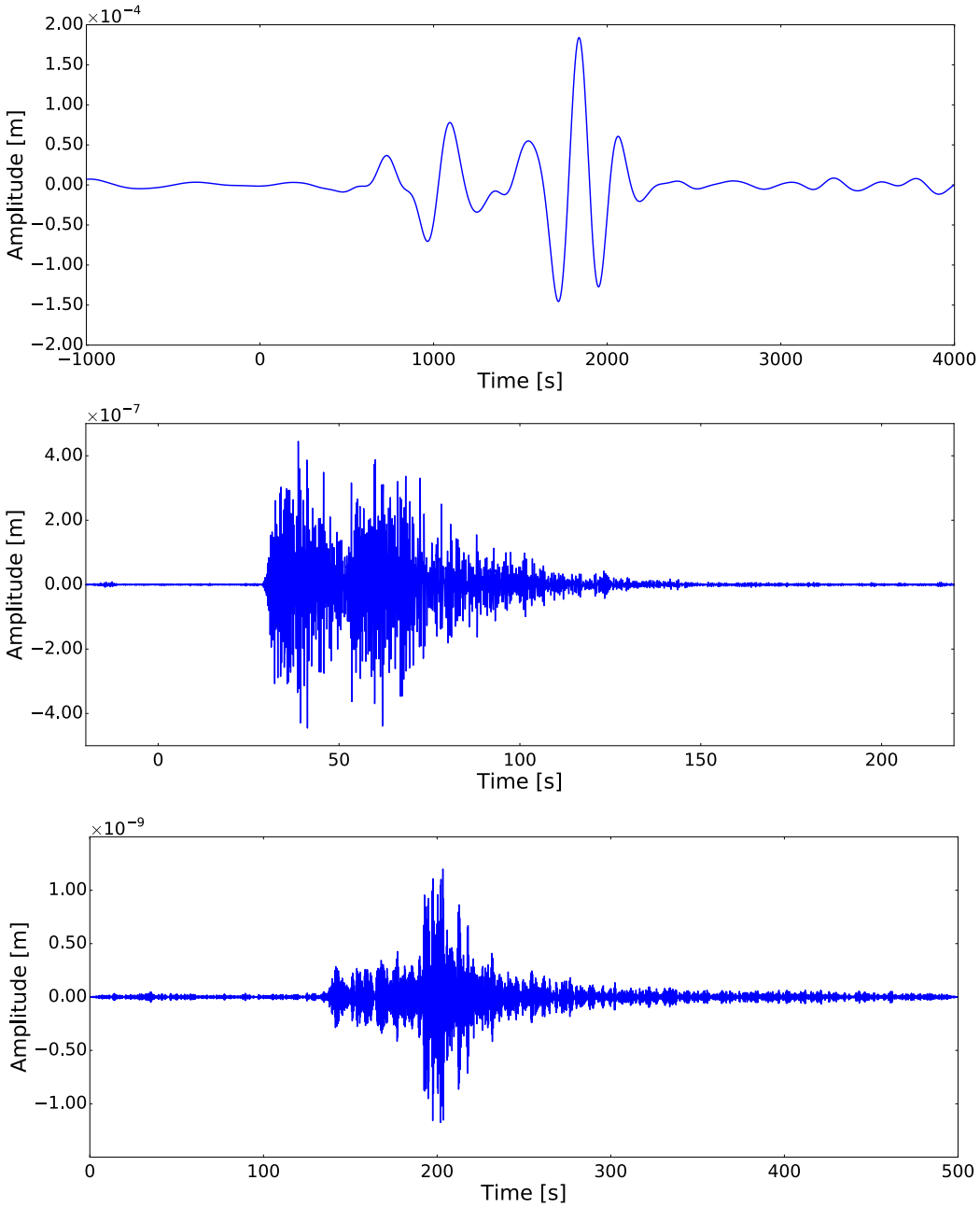

Fig. E.1.: Top: Displacement measured by the receiver L15A of the Transportable Array due to the Mw7.7 Sea of Okhotsk event. Middle: Displacement measured at the receiver R2010 of the Sage Brush Nodal Flats Experiment due to the MW4.2 Southern California event. Bottom: Displacement measured by the receiver 6B446 of the Sweetwater Array due to the mb4.5 Oklahoma event.

Other Networks

F

Apart from these networks, we also tried the Japanese seismic observation system and the Southern California Seismic Network [see Figures F.1 and F.2].

The Japanese array (Okada et al., 2004) is made up of three networks, namely K-NET/KiK-net, Hi-net,and F-Net. The F-Net is a network of broadband sensors, the K-NET/KiK-net is a network for observing strong-motion and the Hi-net a high-sensitivity network. Due to the distinction of their objectives, the three networks have a different frequency range and cannot be collectively used to look at one event. We looked at data from K-NET/KiK-net and Hi-net instead (the density of F-Net is too low to suit our goal). Both networks lie on a mesh of ∼20 km. However, data from teleseismic events are not available for the networks.

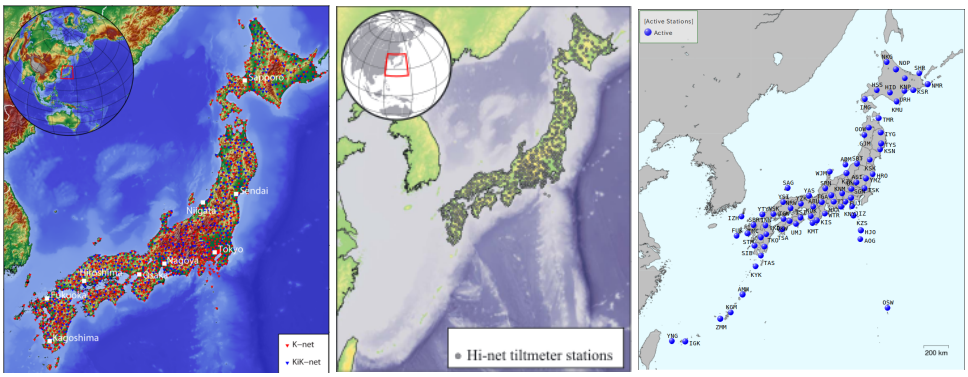

Fig. F.1.: Left: the K-NET/KiK-net. Middle: Hi-net. Right: F-net. [1]

The Southern California Seismic Network together with California Strong Motion Instrumentation Program (Hutton et al., 2010) is another one of the dense networks in the United States that has been monitoring ground motion in Southern California. We tried to look at the waveform recorded by the network for the Mw7.1 Ridgecrest Earthquake in California on July 6, 2019 but out of the desired 120 stations, were unable to locate data from one-third of the stations.

[1] Left: From Oth et al. (2011), middle: Modified from Thorne et al. (2019), and right: From `https://www.fnet.bosai.go.jp/st_info/station_map.php?LANG=en`; Last Accessed September 29, 2020

[2] From Li et al. (2019)

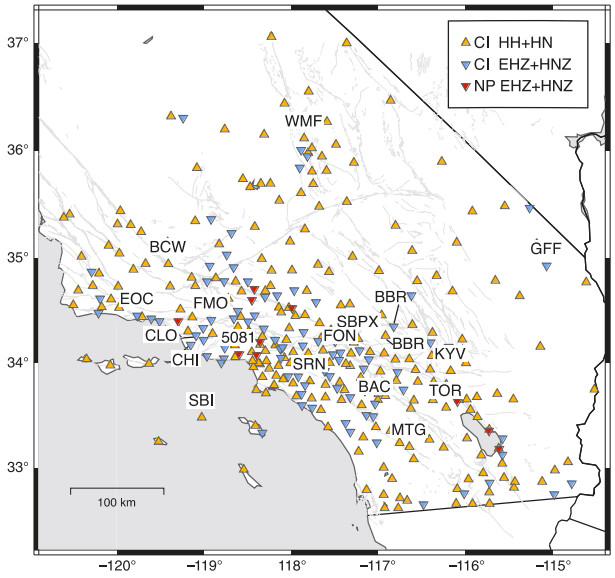

Fig. F.2.: The Southern California Seismic Network. [2]

As station density and distribution evolve along with technology, instrumentation, and data processing methods, we hope more seismic networks will be available for the work. For now, the AlpArray (Hetényi et al., 2018) and the Longbeach Array (Lin et al., 2013; Schmandt and Clayton, 2013) are interesting candidates [see Figure F.3].

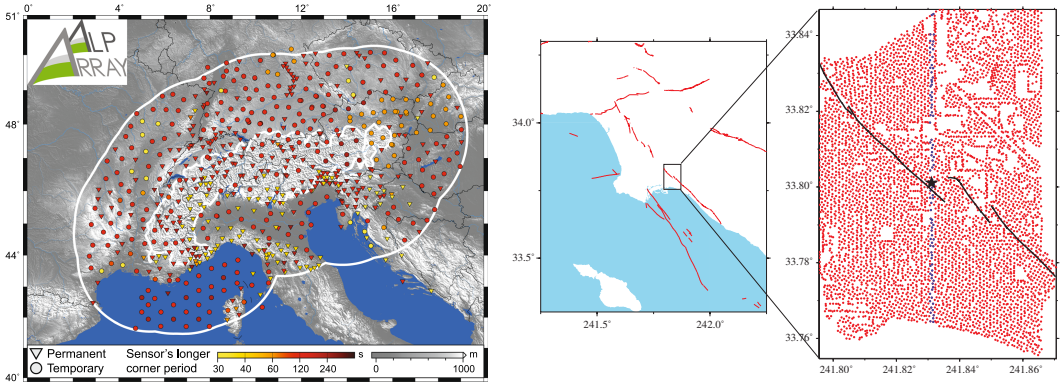

Fig. F.3.: Left: the AlpArray, right: the Long Beach Array. [3]

[3] From Hetényi et al. (2018) and Lin et al. (2013) respectively

G

Translations are in good agreement II

As stated in Section 4.2, the effective model needed for the inversion of J is not limited to the homogenized model. Any tomographic model that fits displacement data reasonably well can be used.

In Section 5.3.1, we computed the corrector for the 1225 receivers. The receiver arrangement is shown in Figure G.1 once again.

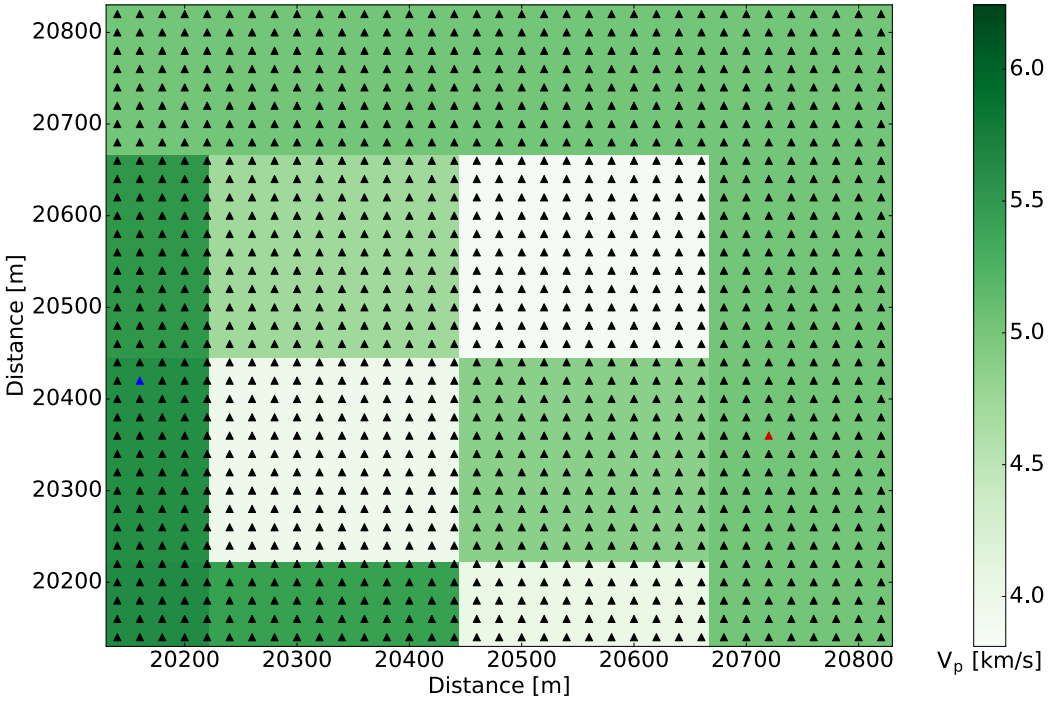

Fig. G.1.: Zoom in on the surface of the 3D domain shown in Figure 5.11. The receiver locations are shown by the diamonds. Background color shows the P-wave velocity.

For computing the correctors, we used the homogeneous medium as our effective model and it is indeed sensible to do so because as shown by Figures G.2 and G.3, the displacements in both the heterogeneous and homogeneous media are in agreement.

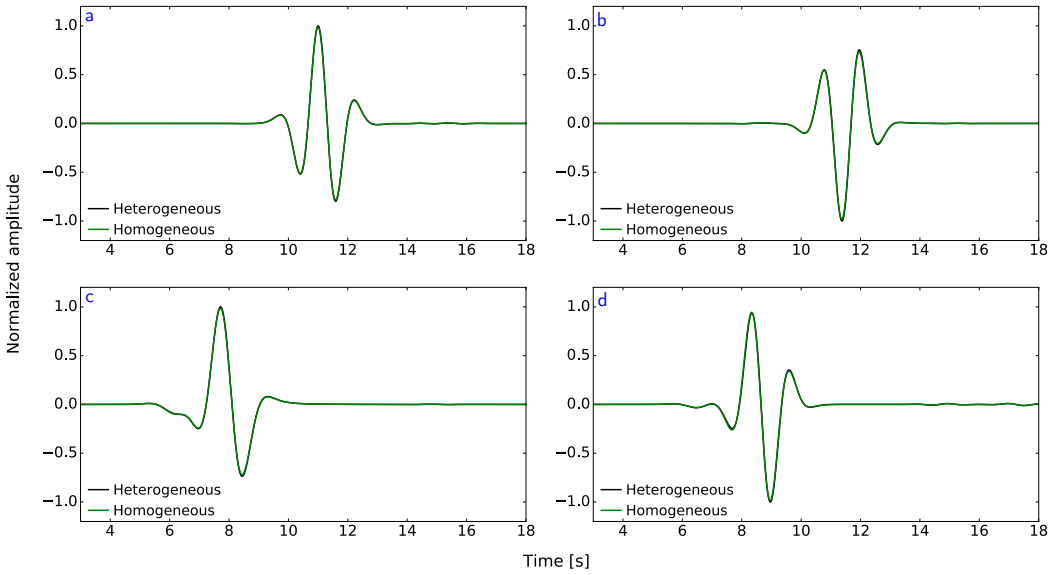

Fig. G.2.: Vertical displacements for the four events shown in Figure 5.11 at the blue receiver shown in Figure G.1. Displacements in the heterogeneous media are shown in black and displacements in the homogeneous media are shown in green.

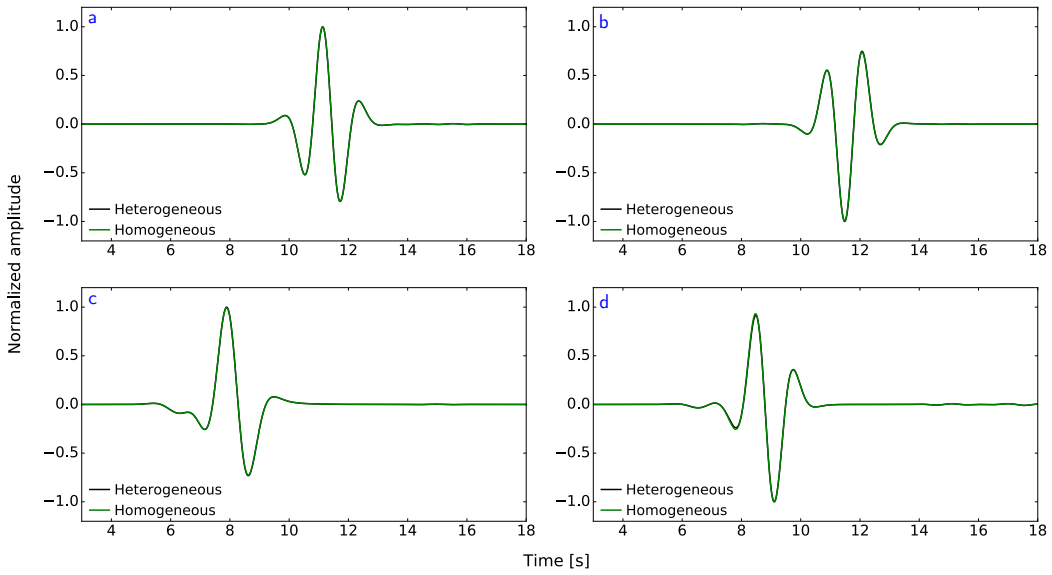

Fig. G.3.: Vertical displacements for the four events shown in Figure 5.11 at the red receiver shown in Figure G.1. Displacements in the heterogeneous media are shown in black and displacements in the homogeneous media are shown in green.

Inversion with strains

H

Here, we follow the setup of Chapter 6 to inspect FWI with strains.

We start with calculating the Frechlet derivatives using the adjoint source. Following Chapter 6, the gradient of the misfit function for the gradient of displacement $\partial_n \mathbf{u}$ measured at the receiver location $\mathbf{x}_\mathrm{r}$ is given by

$$\delta\partial_n \mathbf{u} = \sum_\mathrm{r} \int_0^\mathrm{T} [\partial_n \mathbf{u}(\mathbf{x}_\mathrm{r}, t) - \partial_n \mathbf{u}^\mathrm{o}(\mathbf{x}_\mathrm{r}, t)] \; . \; \delta\partial_n \mathbf{u}(\mathbf{x}_\mathrm{r}, t)\mathrm{dt}. \tag{H.1}$$

The associated perturbation in the gradient of displacement due to perturbations $\{\delta\rho, \delta c_{jklm}\}$ in the background model is given by

$$\begin{aligned}\delta\partial_n \mathrm{u}_i(\mathbf{x}, t) = -\int_0^t \int_V \Big[&\delta\rho(\mathbf{x}') G_{ij}(\mathbf{x}, \mathbf{x}', t-t') \partial_{t'}^2 \partial_n \mathrm{u}_j(\mathbf{x}', t') + \\ &\delta c_{jklm}(\mathbf{x}') \partial'_k G_{ij}(\mathbf{x}, \mathbf{x}', t-t') \partial'_l \partial_n \mathrm{u}_m(\mathbf{x}', t') \Big] d^3\mathbf{x}' dt',\end{aligned} \tag{H.2}$$

where V denotes the model volume and $\mathbf{x}'$ denotes the source location. Substituting this in (H.1), we get,

$$\begin{aligned}\delta\phi = -\sum_\mathrm{r} \int_0^\mathrm{T} [\partial_n \mathrm{u}_i(\mathbf{x}_\mathrm{r}, t) - \partial_n \mathrm{u}_i^\mathrm{o}(\mathbf{x}_\mathrm{r}, t)] \int_0^t \int_V \Big[&\delta\rho(\mathbf{x}') G_{ij}(\mathbf{x}_\mathrm{r}, \mathbf{x}', t-t') \partial_{t'}^2 \mathrm{u}_j(\mathbf{x}', t') + \\ &\delta c_{jklm}(\mathbf{x}') \partial'_k G_{ij}(\mathbf{x}_\mathrm{r}, \mathbf{x}', t-t') \partial'_l \mathrm{u}_m(\mathbf{x}', t') \Big] d^3\mathbf{x}' dt',\end{aligned} \tag{H.3}$$

Using reciprocity of the Green's function, we have

$$\partial'_l G_{ij}(\mathbf{x}_\mathrm{r}, \mathbf{x}', t-t') = \partial'_l G_{ji}(\mathbf{x}', \mathbf{x}_\mathrm{r}, t-t').$$

This means for ε_{ii} strains in 2D, the adjoint source $f^\dagger$ is given by

$$\boldsymbol{f}^\dagger = \sum_\mathrm{r} \delta(t)\delta(\mathbf{x} - \mathbf{x}_\mathrm{r}) \begin{bmatrix} 1 & 0 \\ 0 & 0 \end{bmatrix}.$$

For ε_{jj} strains in 2D, the adjoint source $f^\dagger$ is given by

$$\boldsymbol{f}^\dagger = \sum_{\mathrm{r}} \delta(t)\delta(\mathbf{x}-\mathbf{x}_{\mathrm{r}}) \begin{bmatrix} 0 & 0 \\ 0 & 1 \end{bmatrix}.$$

Similarly, for ε_{ij} strains in 2D, the adjoint source $f^\dagger$ is given by

$$\boldsymbol{f}^\dagger = \sum_{\mathrm{r}} \delta(t)\delta(\mathbf{x}-\mathbf{x}_{\mathrm{r}}) \begin{bmatrix} 0 & \frac{1}{2} \\ \frac{1}{2} & 0 \end{bmatrix}.$$

Here, carry out two tests. In the first test, the receiver placement is far away from the heterogeneity. In the second test, the receiver placement is close to the heterogeneity such that the strain data are affected by it. Since we have not implemented inversion with strain and correctors yet, we do not carry out the third test like we did for rotations in Chapter 6. But the results will undoubtedly be similar.

The target model for these inversions is shown in Figure 6.1.

Just like in Chapter 6, our inversions start from an entirely homogeneous model whose V_p, V_s and ρ are 5 kms^{-1}, 2.8 kms^{-1} and 3.0 kgm^{-3} respectively. The inversion area is 18×18 km^2 and extends slightly beyond the heterogeneity. It is divided into 36×36 elements, and for each element, the elastic tensor $\mathbf{c}$ and density ρ are inverted. For the forward problem, we use number of Gauss-Lobatto-Legendre (nGLL) 4 while for the inversion, we use nGLL 1. This ensures that the discretization errors are different. Furthermore, the mesh chosen for inversion cannot accurately represent the small-scale structure (the element size for the inversion is ∼0.22 λ_m, while the size of individual heterogeneity is ∼0.18 λ_m) and this ensures that we are not injecting prior information through our mesh. Consequently, we avoid any inversion crime.

After convergence, the final model is homogenized using the method described in Chapter 2, and choose ε=2 to focus on long wavelength results. We project the anisotropic tensor $\mathbf{c}$ to the nearest isotropic tensor $\mathbf{c}^{\mathrm{iso}}$ fol-

lowing Browaeys and Chevrot (2004). Subsequently, V_p, V_s and the total anisotropy are defined as follows:

$$V_p = \sqrt{\frac{c^{iso}_{1111}}{\rho}},$$

$$V_s = \sqrt{\frac{c^{iso}_{1212}}{\rho}},$$

$$\text{anisotropy} = \sqrt{\frac{\sum_{ijkl}(c^{iso}_{ijkl} - c_{ijkl})^2}{\sum_{ijkl}(c^{iso}_{ijkl})^2}}.$$

Note that in 2D, the number of data for strain is 1.5 times the number of data for displacement and 3 times the number of data for rotation.

H.1 Receivers far away from the heterogeneity

The starting model is shown in Figure H.1 along with the receiver locations. The inversion domain is given by the black inner squares.

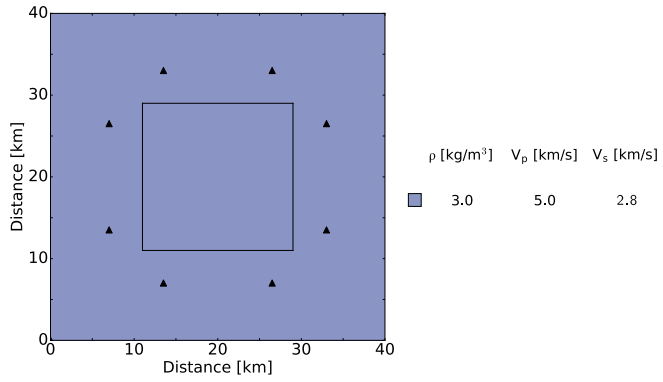

Fig. H.1.: Starting model used in the inversion in Section H.1. The triangles show the location of the receivers. All boundaries are absorbing. The inner square shows the inversion area.

For the inversion, the improvement in misfit reduction is 98%. Results are shown in Figure H.2 for V_p, V_s, ρ and anisotropy. Also shown are the respective values along two-cross sections in the model. The values along the vertical cross-section are shown on the right (red lines) and the values along

the horizontal cross-section are shown just below (red lines). Also shown are the respective values in the target model (green lines).

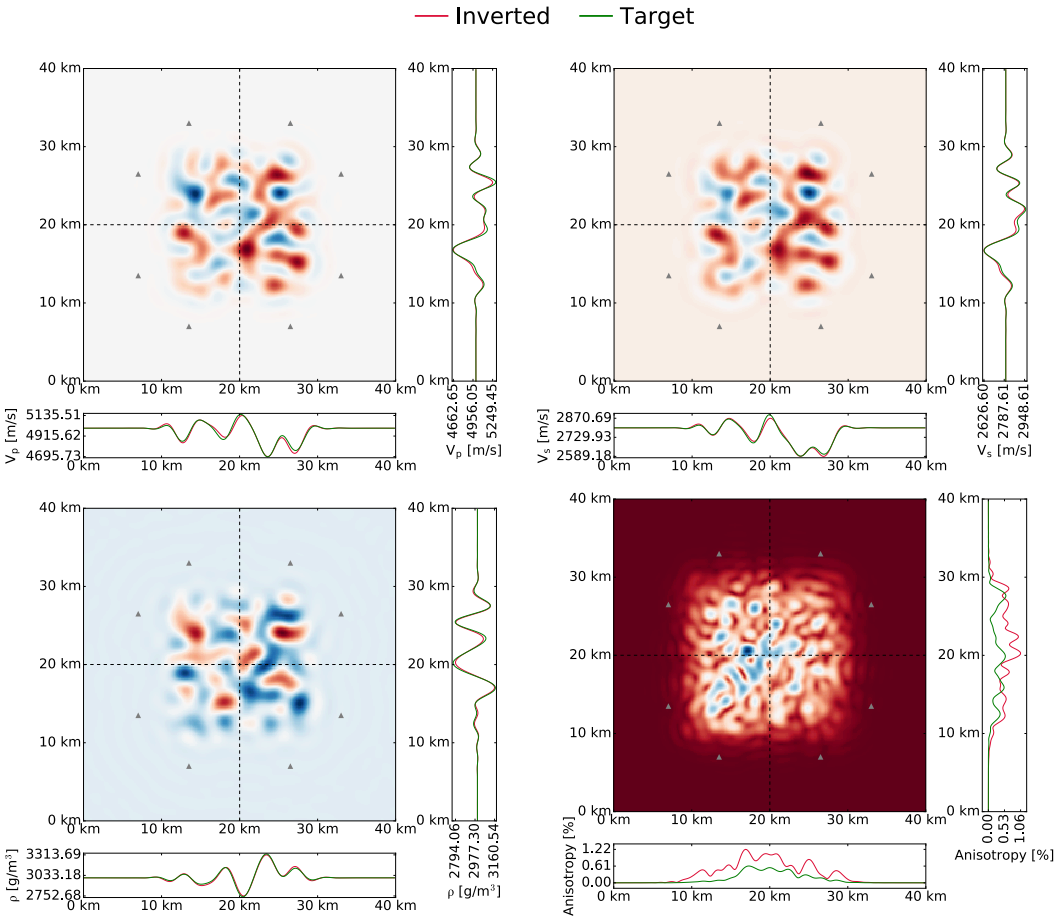

Fig. H.2.: Results of the first test. Clockwise from top left: V_p, V_s, anisotropy and ρ. The receiver locations are shown by the grey and the starting model was entirely homogeneous. For each result, cross-section along the horizontal dotted line is shown below and cross-section along the vertical dotted line is shown to its right. Also shown in green are the respective cross-sections along the target model.

From the cross-sections in Figure H.2, it can be seen that the inversion from strains are in agreement with the target model.

Validation

To validate our model recovered from inversion, we place a receiver at a new location and compare the displacements and strains in the model to those in the target model. The receiver and source positions are shown by the diamond and the star respectively in the left panel of Figure H.3.

Measurements are shown on the right panel. Measurements in the target model are shown in black, in the model recovered from displacement are shown in green, and in the model recovered from strain are shown in red. The amplitudes have been normalized.

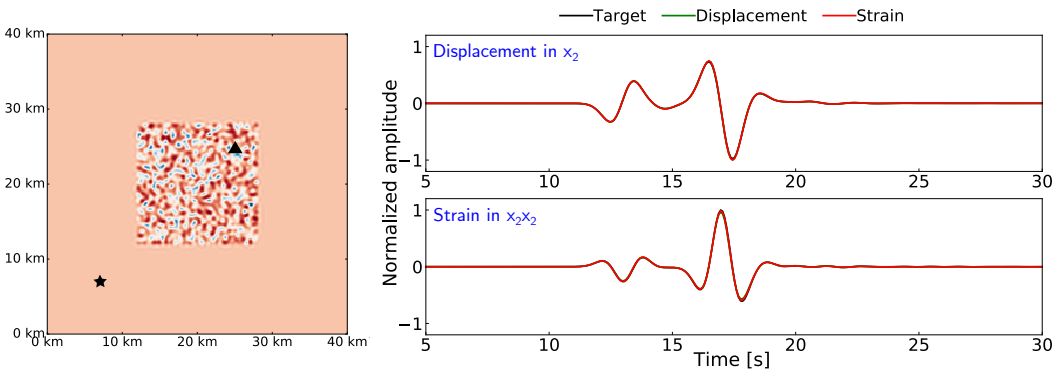

Fig. H.3.: Validating the inverted models. Left: Source-receiver configuration. The source location is given by the star and the receiver location is given by the triangle. Right: Vertical displacements (top) and vertical strains (bottom). Measurements in the target model are shown in black, in the model inverted from displacements are shown in green in the model inverted from strain are shown in red.

From the right panel in H.3, we can see both recovered models are able to achieve the measurements in the target model, meaning that both inversions are reliable.

H.2 Receivers close to the heterogeneity

The starting model is shown in Figure H.4 along with the receiver locations. The inversion domain is given by the black inner squares.

For the inversion, the improvement in misfit reduction is 98%. Results are shown in Figure H.5 for V_p, V_s, ρ and anisotropy. Also shown are the respective values along two-cross sections in the model. The values along the vertical cross-section are shown on the right (red lines) and the values along the horizontal cross-section are shown just below (red lines). Also shown are the respective values in the target model (green lines).

From the cross-sections in Figure H.5, it can be seen that the inversion from strains are not in agreement with the target model.

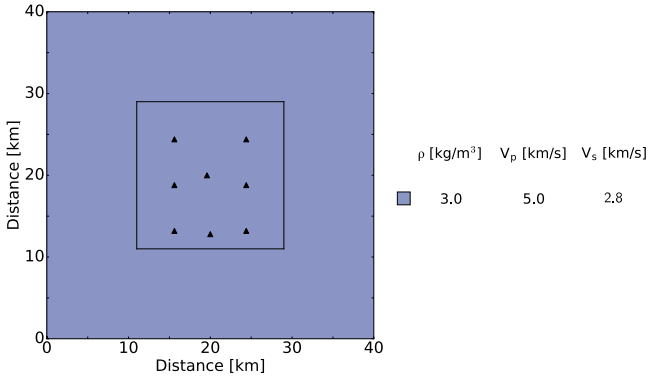

Fig. H.4.: Starting model used in the inversion in Section H.2. The triangles show the location of the receivers. All boundaries are absorbing. The inner square shows the inversion area.

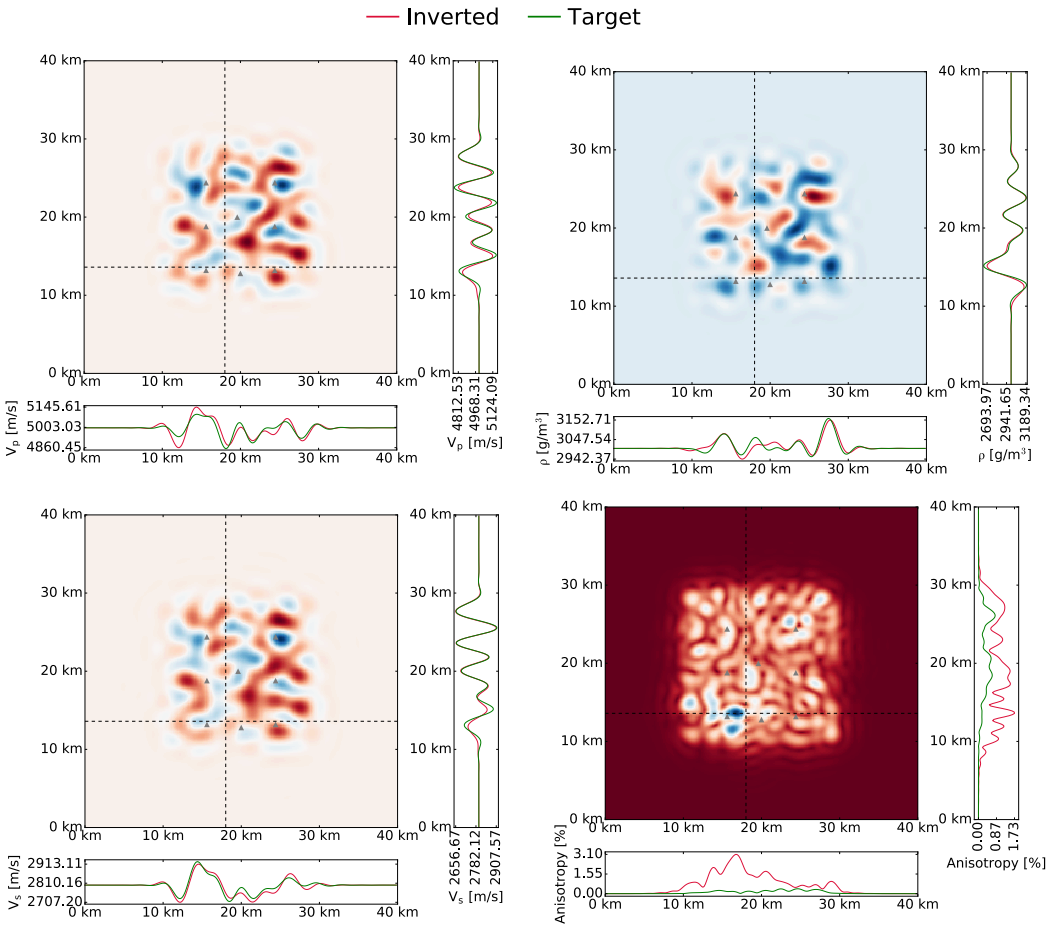

Fig. H.5.: Results of the second test. Clockwise from top left: V_p, V_s, anisotropy and ρ. The receiver locations are shown by the grey and the starting model was entirely homogeneous. For each result, cross-section along the horizontal dotted line is shown below and cross-section along the vertical dotted line is shown to its right. Also shown in green are the respective cross-sections along the target model.

Validation

To validate our model recovered from inversion, we place a receiver at a new location and compare the displacements and strains in the model to those in the target model. The receiver and source positions are shown by the diamond and the star respectively in the left panel of Figure H.6. Measurements are shown on the right panel. Measurements in the target model are shown in black, in the model recovered from displacement are shown in green, and in the model recovered from strain are shown in red. The amplitudes have been normalized.

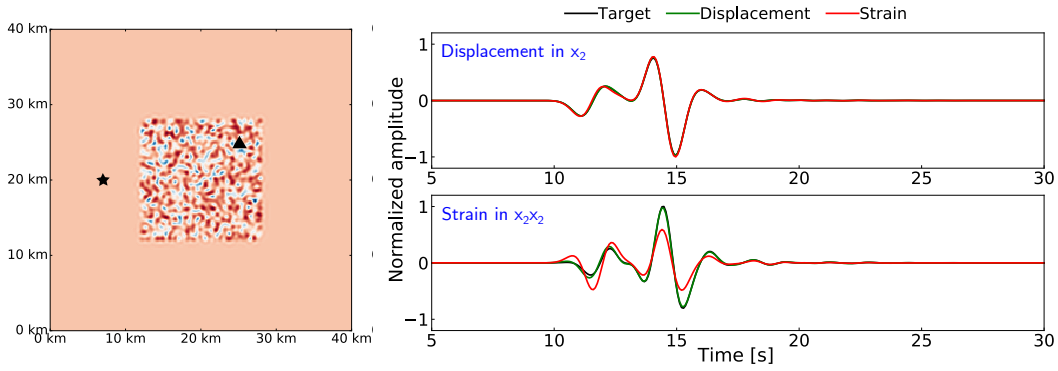

Fig. H.6.: Validating the inverted models. Left: Source-receiver configuration. The source location is given by the star and the receiver location is given by the triangle. Right: Vertical displacements (top) and vertical strains (bottom). Measurements in the target model are shown in black, in the model inverted from displacements are shown in green in the model inverted from strain are shown in red.

From the right panel in H.6, we can see that the model derived from strain does not achieve the measurements in the target model. Therefore, unlike the model recovered from displacement, the model recovered from strain is not reliable.

List of Figures

I Le problème direct xv

II Les observables sismiques. 1) Translation, 2) Déformation, et 3) Rotation. xv

III Le problème inverse xvii

IV Le concept d'homogénéisation illustré sur une partie du modèle Marmousi2 xx

V Haut : domaines 2D utilisés dans la Section II. Les deux domaines font 20×20 km^2. Toutes les limites sont absorbantes. L'étoile indique l'emplacement de la source et les diamants indiquent l'emplacement de quatre récepteurs. À gauche : milieu entièrement homogène. À droite : Une hétérogénéité de 200×200 m^2, placée au centre, est indiquée par le carré (pas à l'échelle).
En bas : V_p, V_s et ρ à l'hétérogénéité. La longueur de la longueur d'onde minimale pour la simulation est indiquée dans le panneau le plus à gauche. xxii

VI A gauche : Mesures dans le milieu homogène. A droite : Mesures dans le milieu hétérogène. Les deux milieux sont représentés sur la Figure V.
En partant du haut, les déplacements verticaux, les vitesses verticales, les accélérations verticales, les cisaillements et les rotations sont indiqués. Les facteurs d'échelle pour chaque panneau sont indiqués en haut à gauche. xxiv

VII A gauche : domaine 2D utilisé dans la Section III. Le domaine est de 20×20 km^2 et l'hétérogénéité au centre, pas à l'échelle, est de 200×200 m^2. Les étoiles indiquent l'emplacement des sources et le diamant celui du récepteur. Toutes les limites sont absorbantes. Au centre : Zoom sur l'hétérogénéité. A droite : V_p, V_s et ρ dans le domaine. Les vitesses P et S dans le domaine extérieur sont de 5 kms^{-1} et 3.2 kms^{-1}, et les vitesses de chaque élément à l'intérieur de l'hétérogénéité sont de $\pm50\%$ par rapport au domaine environnant. xxx

VIII Rotations. Panneaux a, b, c : Les trois événements utilisés pour l'inversion du correcteur. Panneau d : L'événement utilisé comme validation en applicant ce correcteur. Il est représenté sur fond bleu pour indiquer qu'il n'a pas été utilisé pour l'inversion. Les rotations hétérogènes et homogénéisées sont indiquées en noir et en vert respectivement. Les rotations qui ont été corrigées à l'aide du tenseur de couplage **J** sont indiquées en rouge. . . . xxxii

IX Rotations. Panneaux a, b, c : Les trois événements utilisés pour l'inversion du correcteur. Panneau d : L'événement utilisé comme validation en applicant ce correcteur. Il est représenté sur fond bleu pour indiquer qu'il n'a pas été utilisé pour l'inversion. Les rotations hétérogènes et homogènes sont indiquées en noir et en vert respectivement. Les rotations qui ont été corrigées à l'aide du tenseur de couplage **J** sont indiquées en rouge. xxxii

X Vitesses de rotation de l'axe vertical. Haut : 201611131102A Île du Sud, Nouvelle-Zélande. Un des 32 événements qui servent au calcul du tenseur de couplage **J** par inversion. Milieu : 201210280304A Îles de la Reine-Charlotte. Un événement de l'ensemble des données de validation. En bas : 201006121926A Îles Nicobar. Également un événement de l'ensemble des données de validation. Les événements de l'ensemble des données de validation sont représentés sur fond bleu pour indiquer que ces événements n'ont pas été utilisés pour l'inversion.
Les données, les vitesses de rotation synthétiques et corrigées sont indiquées en noir, vert et rouge respectivement. xxxv

XI En haut : modèle cible brut, en bas : modèle cible homogénéisé avec $\varepsilon = 2$. Le domaine est 40×40 km^2 et l'hétérogénéité au centre est 16×16 km^2. Les étoiles indiquent l'emplacement des sources. Toutes les limites sont absorbantes. A gauche : V_p, au centre : V_s et à droite : ρ dans le domaine. Les vitesses P et S dans le domaine extérieur sont de 5 kms^{-1} et de 3.2 kms^{-1}, et les vitesses pour chaque élément à l'intérieur de l'hétérogénéité sont de $\pm$40% par rapport au domaine environnant. xxxvi

XII Modèle de départ utilisé dans l'inversion de la Section IV. Les triangles indique l'emplacement des récepteurs. Toutes les limites sont absorbantes. Le carré intérieur montre la zone d'inversion. xxxviii

XIII Résultats du premier test. A gauche : inversion avec seulement des déplacements, à droite : inversion avec seulement des rotations. En partant du haut, V_p, V_s, ρ et anisotropie sont affichés. Pour chaque résultat, la coupe transversale le long de la ligne pointillée horizontale est indiquée en dessous et la coupe transversale le long de la ligne pointillée verticale est indiquée à droite. Les coupes transversales respectives le long du modèle cible sont également indiquées en vert. xxxix

XIV Validation des modèles récupérés. A gauche : Configuration source-récepteur. L'emplacement de la source est donné par l'étoile et l'emplacement du récepteur est donné par le triangle. A droite : Déplacements verticaux (en haut) et rotations (en bas). Les mesures dans le modèle cible sont indiquées en noir, celles dans le modèle récupéré à partir des déplacements sont indiquées en vert, celles dans le modèle récupéré à partir des rotations sont indiquées en rouge. xl

XV Modèle de départ utilisé dans l'inversion de la section IV. Les triangles indique l'emplacement des récepteurs. Toutes les limites sont absorbantes. Le carré intérieur montre la zone d'inversion. xl

XVI Résultats du premier test. A gauche : inversion avec seulement des déplacements, à droite : inversion avec seulement des rotations. En partant du haut, V_p, V_s, ρ et anisotropie sont affichés. Pour chaque résultat, la coupe transversale le long de la ligne pointillée horizontale est indiquée en dessous et la coupe transversale le long de la ligne pointillée verticale est indiquée à droite. Les coupes transversales respectives le long du modèle cible sont également indiquées en vert. xli

XVII Validation des modèles récupérés. A gauche : Configuration source-récepteur. L'emplacement de la source est donné par l'étoile et l'emplacement du récepteur est donné par le triangle. A droite : Déplacements verticaux (en haut) et rotations (en bas). Les mesures dans le modèle cible sont indiquées en noir, celles dans le modèle récupéré à partir des déplacements sont indiquées en vert, et celles dans le modèle récupéré à partir des rotations sont indiquées en rouge. xlii

1.1 The forward problem 2

1.2 Left: initial position of a particle within the body. Right: its position at a time t. 3

1.3 The seismic observables. 1) Translation, 2) Strain, and 3) Rotation. 5
1.4 The inverse problem 7

2.1 The concept of homogenization illustrated on a part of the Marmousi2 model 12
2.2 Cartoon showing the relation between λ, λ_m, $\mathbf{x}$ and $\mathbf{y}$. 16
2.3 All scales. 17
2.4 Separation into large-scales (top) and small-scales (bottom). . . 18

3.1 Top: 2D domains used in Section 3.2.1. Both domains are 20×20 km^2. All boundaries are absorbing. The star shows the location of the source and the diamonds show the locations of four receivers. Left: Entirely homogeneous medium. Right: A heterogeneity of 200×200 m^2, placed at the centre, is shown by the square (not to scale).
Bottom: V_p, V_s and ρ at the heterogeneity. The length of the minimum wavelength for the simulation is shown in the leftmost panel. 26
3.2 Left: Measurements in the homogeneous medium. Right: Measurements in the medium with the heterogeneity. The two media are shown in Figure 3.1.
Starting from top, vertical displacements, vertical velocities, vertical accelerations, shear strains and rotations are shown. The scaling factors for each panel are shown on the top left. 27
3.3 Top: 2D domains used in Section 3.2.2. Both domains are 20×20 km^2. All boundaries are absorbing. The star shows the location of the source and the diamonds show the locations of three receivers. Left: Entirely homogeneous medium. Right: A heterogeneity of 200×200 m^2, placed at the centre, is shown by the square (not to scale).
Bottom: V_p, V_s and ρ at the heterogeneity. The length of the minimum wavelength for the simulation is shown in the leftmost panel. 29
3.4 Left: Measurements in the homogeneous medium. Right: Measurements in the medium with the heterogeneity. The two media are shown in Figure 3.3.
Starting from top, horizontal displacements, horizontal velocities, horizontal accelerations, shear strains at Receiver 2 and rotations at Receiver 2 are shown. The scaling factors for each panel are shown on the top left. 30

4.1 Left: 2D domain used in Section 4.3.1. The domain is 20×20 km^2 and the heterogeneity at the centre, not to scale, is 200×200 m^2. The stars show the location of the sources and the diamond shows the location of the receiver. All boundaries are absorbing. Middle: Zoom in into the heterogeneity. Right: V_p, V_s and ρ in the domain. The P and S velocities in the outer domain are 5 kms^{-1} and 3.2 kms^{-1}, and velocities for each element inside the heterogeneity are ±50% of the surrounding domain. 39

4.2 Rotations. Panels a, b, c: Three events used for inversion of the corrector. Panel d: The event used as validation using this corrector. It is shown on blue to indicate that it has not been used for the inversion.
Heterogeneous and homogenized rotations are shown in black and green respectively. Rotations that have been corrected using the coupling tensor **J** are shown in red. 42

4.3 Rotations. Panels a, b, c: Three events used for inversion of the corrector. Panel d: The event used as validation using this corrector. It is shown on blue to indicate that it has not been used for the inversion.
Heterogeneous and homogeneous rotations are shown in black and green respectively. Rotations that have been corrected using the coupling tensor **J** are shown in red. 42

4.4 Top: 3D domain used in Section 4.3.2. The domain is 40×40×10 km^3, and the heterogeneity at the centre, not to scale, is 1334×1334×222 m^3. The stars show the location of the sources and the diamond shows the location of the receiver. All but top boundary are absorbing.
Bottom: Zoom in into the heterogeneity from the top showing the V_p, V_s and ρ in the domain. The P and S velocities in the outer domain are 5 kms^{-1} and 3.2 kms^{-1}, and velocities for each element inside the heterogeneity are chosen randomly and independently, but within 25% of the surrounding domain. . . . 43

4.5 Rotations around the vertical axis. Panels a, b, c: Three events used for inversion of the corrector. Panel d: The event used as validation using this corrector. It is shown on blue to indicate that it has not been used for the inversion.
Heterogeneous and homogenized rotations are shown in black and green respectively. Rotations that have been corrected using the coupling tensor **J** are shown in red. 44

4.6 Rotations around the vertical axis. Panels a, b, c: Three events used for inversion of the corrector. Panel d: The event used as validation using this corrector. It is shown on blue to indicate that it has not been used for the inversion.
Heterogeneous and homogeneous rotations are shown in black and green respectively. Rotations that have been corrected using the coupling tensor **J** are shown in red. 44
4.7 Rotation rates around the vertical axis. Top: 201611131102A South Island, New Zealand. One of the 32 events from the inversion data set that are used to invert for the coupling tensor **J**. Middle: 201210280304A Queen Charlotte Islands. An event from the validation data set. Bottom: 201006121926A Nicobar Islands. Also an event from the validation data set. The events from the validation data set are shown on blue to indicate that these events have not been used for the inversion.
Data, synthetic and corrected rotation rates are given in black, green and red respectively. 47
4.8 Left: location of the receivers used for the finite difference. Right: Location of the seismometer ROTZ (top) and WET (bottom). . . 49
4.9 Rotation rates around the vertical axis. Top: 201103110546A Near East Coast of Honsh. One of the 6 events from the inversion data set that are used to invert for the coupling tensor $\mathbf{J}^{\dagger}\mathbf{G}$. Bottom: 200909291748A Samoa Islands Region. An event from the validation data set. It is shown on blue to indicate that this event has not been used for the inversion.
Observed, array-derived and corrected rotation rates are given in black, green and red respectively. 50

5.1 Top: 3D domain used in Section 5.2.1. The domain is $40\times40\times10$ km^3, and the heterogeneity at the centre, not to scale, is $1334\times1334\times222$ m^3. The star shows the location of the source. The location of the receivers is shown in Figure 5.2. All but top boundary are absorbing.
Bottom: Zoom in into the heterogeneity from the top showing the V_p, V_s and ρ in the domain. The P and S velocities in the outer domain are 5 kms^{-1} and 3.2 kms^{-1}, and velocities for each element inside the heterogeneity are chosen randomly and independently, but within 25% of the surrounding domain. . . . 55

5.2 Zoom in on the surface of the 3D domain shown in Figure 5.1. The receiver locations are shown by the triangles. Background color shows the P-wave velocity. 56
5.3 Snapshot of the movie for the numerical example. Horizontal displacement $u_{x_1}(x_1, x_2)$ is shown on the left and the spatial gradient $u'_{x_2}(x_1, x_2)$ is shown on the right. The two panels below show the displacement and spatial gradient recorded at a receiver, which is marked in the upper panels by the black triangle. 57
5.4 Receivers of the US Transportable Array used in Section 5.2.2. The inset zooms in on the relative location of the receivers. The source location is shown by the beachball. 59
5.5 Snapshot of the movie for the US Transportable Array. Vertical displacement $u_Z(E, N)$ is shown on the left and its spatial gradient $u'_Z(E, N)$ is shown on the right. The two panels below show the displacement and spatial gradient recorded at the receiver L15A, which is marked in the upper panels by the black triangle. 60
5.6 Snapshot of the movie for the part of US Transportable Array. Vertical displacement $u_Z(E, N)$ is shown on the left and its spatial gradient $u'_Z(E, N)$ is shown on the right. The two panels below show the displacement and spatial gradient recorded at the receiver L15A, which is marked in the upper panels by the black triangle. 61
5.7 Right: Receivers of the Sage Brush Nodal Flats Experiment used in Section 5.2.2. The source location is shown by the red star. Left: Zoom in showing the relative location of the receivers. . . 62
5.8 Snapshot of the movie for the Sage Brush Nodal Flats Experiment. Vertical displacement $u_Z(E, N)$ is shown on the left and its spatial gradient $u'_Z(E, N)$ is shown on the right. The two panels below show the displacement and spatial gradient recorded at the receiver R2010, which is marked in the upper panels by the black triangle. 63
5.9 Left: Receivers of the Sweetwater Array used in Section 5.2.2. The source is shown by the red star. Right: Zoom in on the relative location of the receivers. 64
5.10 Snapshot of the movie for the Sweetwater Array. Vertical displacement $u_Z(E, N)$ is shown on the left and the spatial gradient $\partial N u'_Z(E, N)$ is shown on the right. The two panels below show the displacement and spatial gradient recorded at the receiver 6B446, which is marked in the upper panels by the black triangle. 65

5.11 Top: 3D domain used in Section 5.3.1. The domain is 40×40×10 km^3, and the heterogeneity at the centre, not to scale, is 1334×1334×222 m^3. The stars show the location of the sources. The location of the receivers is shown in Figure 5.12. All but top boundary are absorbing.
Bottom: Zoom into the heterogeneity from the top showing the V_p, V_s and ρ in the domain. The P and S velocities in the outer domain are 5 kms^{-1} and 3.2 kms^{-1}, and velocities for each element inside the heterogeneity are chosen randomly and independently, but within 25% of the surrounding domain. . . . 67
5.12 Zoom in on the surface of the 3D domain shown in Figure 5.11. The receiver locations are shown by the diamonds. Background color shows the P-wave velocity. 68
5.13 One of the components of the coupling tensor **J** for the 1225 receivers. 68

6.1 Top: Raw target model, bottom: homogenized target model with $\varepsilon = 2$. The domain is 40×40 km^2 and the heterogeneity at the centre is 16×16 km^2. The stars show the location of the sources. All boundaries are absorbing. Right: V_p, middle: V_s and left: ρ in the domain. The P and S velocities in the outer domain are 5 kms^{-1} and 3.2 kms^{-1}, and velocities for each element inside the heterogeneity are ±40% of the surrounding domain. 75
6.2 Left: An example of data for displacement (red line) and realisations with noise (grey lines). Right: An example of data for rotation (red line) and realisations with noise (grey lines) . . . 79
6.3 Starting model used in the inversion in Section 6.3.1. The triangles show the location of the receivers. All boundaries are absorbing. The inner square shows the inversion area. 82
6.4 Starting model used in the inversion in Section 6.3.2. The triangles show the location of the receivers. All boundaries are absorbing. The inner square shows the inversion area. 83
6.5 Results of the first test. Left: Inversion with only displacements, right: inversion with only rotations. Starting from top, V_p, V_s, ρ and anisotropy are shown. For each result, cross-section along the horizontal dotted line is shown below and cross-section along the vertical dotted line is shown to its right. Also shown in green are the respective cross-sections along the target model. 86

6.6 Results of inversion with only rotations and 16 receivers. Clockwise from top left: V_p, V_s, anisotropy and ρ. The receiver locations are shown by the grey and the starting model was entirely homogeneous. For each result, cross-section along the horizontal dotted line is shown below and cross-section along the vertical dotted line is shown to its right. Also shown in green are the respective cross-sections along the target model. 87
6.7 Validating the recovered models. Left: Source-receiver configuration. The source location is given by the star and the receiver location is given by the triangle. Right: Vertical displacements (top) and rotations (bottom). Measurements in the target model are shown in black, in the model recovered from displacements are shown in green in the model recovered from rotation are shown in red. 88
6.8 Covariance matrices for the first test. Left: inversion with only displacements, right: inversion with only rotations. 89
6.9 Resolution analysis. Starting from left, the variance in resolution for displacement, the resolution for inversion with displacement, the resolution for inversion with rotation and the variance in resolution for rotation are shown. Starting from top are the corresponding figures for c_{1111}, c_{1122}, c_{1112}, c_{2222}, c_{2212}, c_{1212}, and ρ. 90
6.10 Results of the second test. Left: Inversion with only displacements, right: inversion with only rotations. Starting from top, V_p, V_s, ρ and anisotropy are shown. For each result, cross-section along the horizontal dotted line is shown below and cross-section along the vertical dotted line is shown to its right. Also shown in green are the respective cross-sections along the target model. 91
6.11 Results of inversion with only rotations and 16 receivers. Clockwise from top left: V_p, V_s, anisotropy and ρ. The receiver locations are shown by the grey and the starting model was entirely homogeneous. For each result, cross-section along the horizontal dotted line is shown below and cross-section along the vertical dotted line is shown to its right. Also shown in green are the respective cross-sections along the target model. 92

6.12 Validating the recovered models. Left: Source-receiver configuration. The source location is given by the star and the receiver location is given by the triangle. Right: Vertical displacements (top) and rotations (bottom). Measurements in the target model are shown in black, in the model recovered from displacements are shown in green in the model recovered from rotation are shown in red. 93
6.13 Results of the third test. Left: Inversion with only displacements, right: inversion with only rotations. Starting from top, V_p, V_s, ρ and anisotropy are shown. For each result, cross-section along the horizontal dotted line is shown below and cross-section along the vertical dotted line is shown to its right. Also shown in green are the respective cross-sections along the target model. 95
6.14 Results of inversion with only rotations and 16 receivers. Clockwise from top left: V_p, V_s, anisotropy and ρ. The receiver locations are shown by the grey and the starting model was entirely homogeneous. For each result, cross-section along the horizontal dotted line is shown below and cross-section along the vertical dotted line is shown to its right. Also shown in green are the respective cross-sections along the target model. 96
6.15 Validating the recovered models. Left: Source-receiver configuration. The source location is given by the star and the receiver location is given by the triangle. Right: Vertical displacements (top) and rotations (bottom). Measurements in the target model are shown in black, in the model recovered from displacements are shown in green in the model recovered from rotation are shown in red. 96

A.1 Original receiver setup. 117
A.2 Receiver setup after transformation. 118

C.1 Vertical displacements for the four events shown in Figures 4.2 and 4.3. Displacements in the heterogeneous media are shown in black, displacements in the homogeneous media are shown in green and displacements in the homogenized media are shown in red. 120

C.2 Vertical displacements for the four events shown in Figures 4.5 and 4.6. Displacements in the heterogeneous media are shown in black, displacements in the homogeneous media are shown in green and displacements in the homogenized media are shown in red. 121
C.3 Vertical displacements measured at WET for the three events shown in Figure 4.7. Observed displacements are shown in black and displacements computed in PREM are shown in green. Top: 201611131102A South Island, New Zealand. Middle: 201210280304A Queen Charlotte Islands. Bottom: 201006121926A Nicobar Islands. 122
C.4 Velocities along the East component for the two events shown in Figure 4.9. Observed velocities at stations ROTZ, WET and GRC1 are shown in black, green and red respectively. Top: 201103110546A Near East Coast of Honsh. Bottom: 200909291748A Samoa Islands Region. 122

D.1 The source receiver geometry for the events in Section 4.4.1. The 32 events used for the inversion are shown in red, while the events that were used for validation are shown in blue and green. The event in blue is the 201210280304A Queen Charlotte Islands while the event shown in green is the 201006121926A Nicobar Islands. The blue triangle shows the location of the receiver. 123
D.2 The source receiver geometry for the events in Section 4.4.2. The 6 events used for the inversion are shown in red, while the event that was used for validation is shown in blue. The blue triangles show the location of the three receivers. 124

E.1 Top: Displacement measured by the receiver L15A of the Transportable Array due to the Mw7.7 Sea of Okhotsk event. Middle: Displacement measured at the receiver R2010 of the Sage Brush Nodal Flats Experiment due to the MW4.2 Southern California event. Bottom: Displacement measured by the receiver 6B446 of the Sweetwater Array due to the mb4.5 Oklahoma event. . . 125

F.1 Left: the K-NET/KiK-net. Middle: Hi-net. Right: F-net. 126
F.2 The Southern California Seismic Network. 127
F.3 Left: the AlpArray, right: the Long Beach Array. 127

G.1 Zoom in on the surface of the 3D domain shown in Figure 5.11. The receiver locations are shown by the diamonds. Background color shows the P-wave velocity. 128
G.2 Vertical displacements for the four events shown in Figure 5.11 at the blue receiver shown in Figure G.1. Displacements in the heterogeneous media are shown in black and displacements in the homogeneous media are shown in green. 129
G.3 Vertical displacements for the four events shown in Figure 5.11 at the red receiver shown in Figure G.1. Displacements in the heterogeneous media are shown in black and displacements in the homogeneous media are shown in green. 129

H.1 Starting model used in the inversion in Section H.1. The triangles show the location of the receivers. All boundaries are absorbing. The inner square shows the inversion area. 132
H.2 Results of the first test. Clockwise from top left: V_p, V_s, anisotropy and ρ. The receiver locations are shown by the grey and the starting model was entirely homogeneous. For each result, cross-section along the horizontal dotted line is shown below and cross-section along the vertical dotted line is shown to its right. Also shown in green are the respective cross-sections along the target model. 133
H.3 Validating the inverted models. Left: Source-receiver configuration. The source location is given by the star and the receiver location is given by the triangle. Right: Vertical displacements (top) and vertical strains (bottom). Measurements in the target model are shown in black, in the model inverted from displacements are shown in green in the model inverted from strain are shown in red. 134
H.4 Starting model used in the inversion in Section H.2. The triangles show the location of the receivers. All boundaries are absorbing. The inner square shows the inversion area. 135
H.5 Results of the second test. Clockwise from top left: V_p, V_s, anisotropy and ρ. The receiver locations are shown by the grey and the starting model was entirely homogeneous. For each result, cross-section along the horizontal dotted line is shown below and cross-section along the vertical dotted line is shown to its right. Also shown in green are the respective cross-sections along the target model. 135

H.6 Validating the inverted models. Left: Source-receiver configuration. The source location is given by the star and the receiver location is given by the triangle. Right: Vertical displacements (top) and vertical strains (bottom). Measurements in the target model are shown in black, in the model inverted from displacements are shown in green in the model inverted from strain are shown in red. 136

DOCTORAT ECOLOGIE BRETAGNE GEOSCIENCES LOIRE AGRONOMIE ALIMENTATION

UNIVERSITÉ DE NANTES

Titre : **Gradients de champ d'ondes et hétérogénéités à petite échelle**

Mots clés : gradients de champ d'onde, rotation, déformation, homogénéisation, hétérogénéités à petite échelle

Résumé : Comme toutes les sources sismiques produisent non seulement des translations mais aussi ses gradients, c'est-à-dire des déformations et des rotations, ces trois mouvements sont également cruciaux en sismologie. Seule la mesure de tous ces mouvements permet d'accéder complètement au mouvement du sol.

Toutefois, contrairement aux translations, les déformations et les rotations sont affectées par des hétérogénéités locales à petite échelle, telles que des inhomogénéités géologiques, des topographies de surface et des cavités. Dans ce travail, nous étudions l'effet des hétérogénéités à petite échelle sur les gradients de champ d'onde dans le contexte de problèmes à la fois direct et inverse.

Dans le contexte du problème direct, nous montrons que les structures à petite échelle peuvent affecter la phase, l'amplitude et le temps de parcours des gradients de champ d'onde. Cependant, l'effet des structures à petite échelle sur un récepteur donné peut être capté par un tenseur **J**, qui ne dépend pas de la source et du temps. Par conséquent, **J** peut être déterminé par une inversion linéaire. Une fois trouvé, il peut également être utilisé pour corriger tous les futurs gradients de champ d'onde au niveau de ce récepteur.

Dans le contexte du problème inverse, nous montrons que les déformations et les rotations n'apportent pas d'améliorations substantielles aux inversions complètes de la forme d'onde. Elles peuvent récupérer le même modèle que celui des déplacements lorsque le nombre de données est suffisant (pour les rotations) et lorsque les récepteurs sont placés loin des hétérogénéités (pour les déformations et les rotations). Lorsque les récepteurs sont placés près des hétérogénéités, le modèle récupéré à partir des gradients de champ d'onde n'est pas correct.

Title: **Wavefield gradients and small-scale heterogeneities**

Keywords: wavefield gradients, rotation, strain, homogenization, small-scale heterogeneities

Abstract: Since all seismic sources produce not only translations but also its gradients, i.e strains and rotations; all three motions are equally crucial in seismology. Only with the measurement of all these motions can ground motion be completely accessed.

Unlike translations, however, strains and rotations are shown to be affected by local small-scale heterogeneities, such as geological inhomogeneities, surface topographies, and cavities. In this work, we study the effect of small-scale heterogeneities on wavefield gradients in the context of both forward and inverse problems.

In the context of the forward problem, we show that small-scale structures can affect phase, amplitude, and travel time of the wavefield gradients. However, the effect of small-scale structures at any given receiver can be captured by a tensor **J**, which does not depend on source and time. Therefore, **J** can be determined through linear inversion. Once found, it can also be used to correct all future wavefield gradients at that receiver.

In the context of the inverse problem, we show that strains and rotations do not bring substantial improvements to full waveform inversions. They can recover the same model that is recovered from displacements when the number of data is sufficient (for rotations) and when the receivers are placed far away from heterogeneities (for both strains and rotations). When the receivers are placed near heterogeneities, the model recovered from wavefield gradients is not correct.